Volume 3 | Issue 1 January 2023

MICROSTRUCTURES

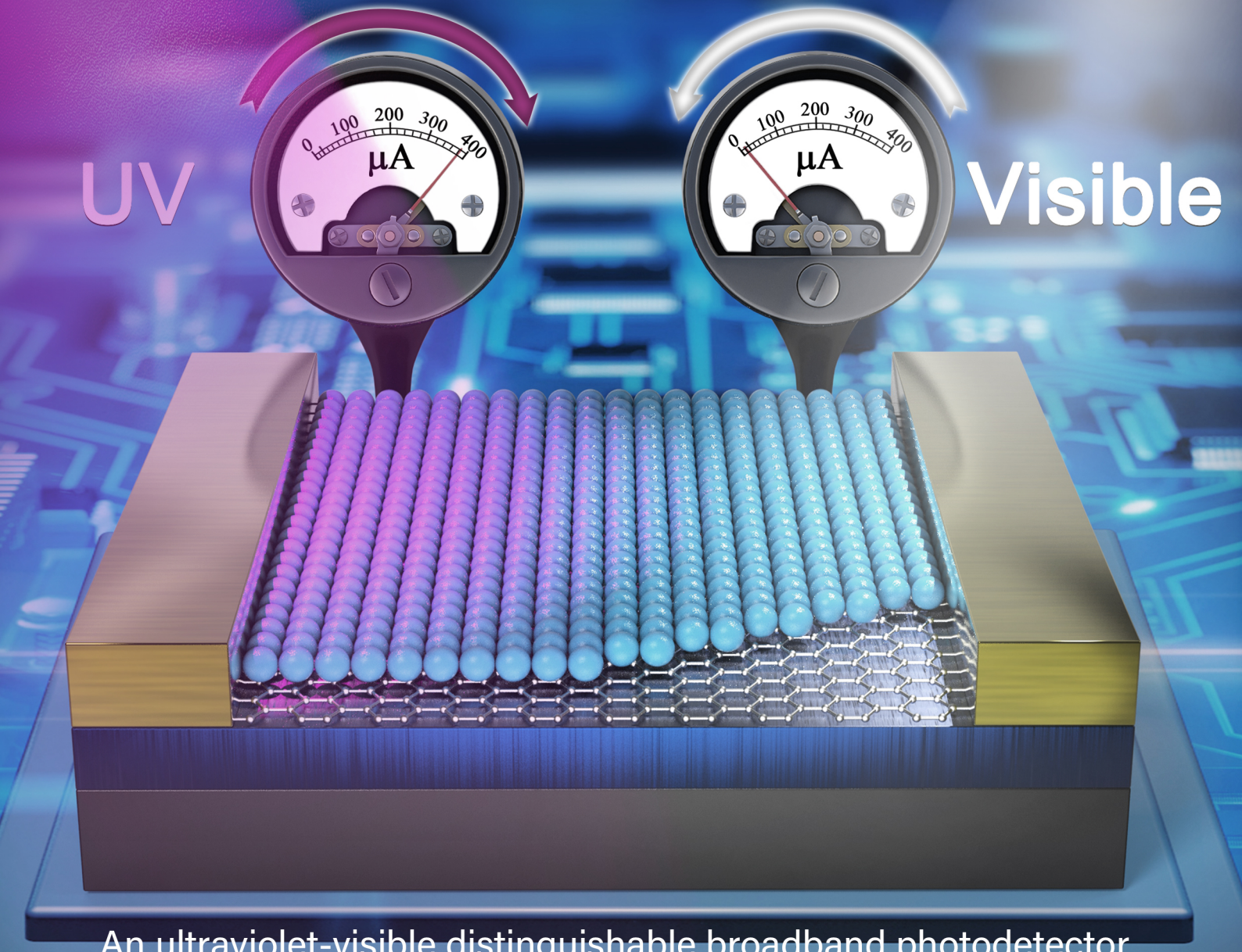

An ultraviolet-visible distinguishable broadband photodetector based on the positive and negative photoconductance effects of a graphene/ZnO quantum dot heterostructure

Xun Yang, Shaobo Cheng*, Chongxin Shan*

Open Access
ISSN 2770-2995 (Online)
www.microstructj.com

EDITORIAL BOARD

GENERAL INFORMATION

About the Journal

Microstructures, ISSN 2770-2995 (Online), is a peer-reviewed and continuously published online journal with print on demand compilation of articles published. The journal's full text is available online at www.jcmtjournal.com. The journal allows free access (Open Access) to its contents and permits authors to self-archive final accepted version of Microstructure, which is the nature, quantity and distribution of structural elements or phases that make up materials, determines the properties of materials. Understanding microstructure–properties relationships is critical for the design of materials. With the increase of demand and investment in new materials around the globe, there has been a great deal of interest in the exploration and manipulation of microstructure in materials science and engineering.

Information for Authors

Manuscripts should be prepared in accordance with Author Instructions.
Please check www.microstructj.com/pages/view/author_instructions for details.
All manuscripts should be submitted online at https://oaemesas.com/login?JournalId=microstructures.

Copyright

Permissions

For information on how to request permissions to reproduce articles/information from this journal, please visit www.microstructj.com.

Disclaimer

The information and opinions presented in the journal reflect the views of the authors and not of the journal or its Editorial Board or the Publisher. Publication does not constitute endorsement by the journal. Neither the *Microstructures* nor its publishers nor anyone else involved in creating, producing or delivering the *Microstructures* or the materials contained therein, assumes any liability or responsibility for the accuracy, completeness, or usefulness of any information provided in the *Microstructures*, nor shall they be liable for any direct, indirect, incidental, special, consequential or punitive damages arising out of the use of the *Microstructures*. The *Microstructures*, nor its publishers, nor any other party involved in the preparation of material contained in the *Microstructures* represents or warrants that the information contained herein is in every respect accurate or complete, and they are not responsible for any errors or omissions or for the results obtained from the use of such material. Readers are encouraged to confirm the information contained herein with other sources.

Publisher

OAE Publishing Inc.
245 E Main Street st112, Alhambra, CA 91801, USA
Website: www.oaepublish.com

Contacts

E-mail: editorialoffice@microstructj.com
Website: www.microstructj.com

Microstructures

CONTENTS

Volume 3 / Issue 1 / January 2023 /

Liu *et al. Microstructures* 2023;3:2023001
DOI: 10.20517/microstructures.2022.23

Microstructures

Review

Open Access

Check for updates

Modulation of photogenerated holes for enhanced photoelectrocatalytic performance

Naiyun Liu, Yixian Liu, Yunliang Liu, Yaxi Li, Yuanyuan Cheng, Haitao Li

Institute for Energy Research, School of Chemistry and Chemical Engineering, Jiangsu University, Zhenjiang 212013, Jiangsu, China.

Correspondence to: Prof. Haitao Li, Institute for Energy Research, School of Chemistry and Chemical Engineering, Jiangsu University, Zhenjiang 212013, Jiangsu, China. E-mail: liht@ujs.edu.cn

How to cite this article: Liu N, Liu Y, Liu Y, Li Y, Cheng Y, Li H. Modulation of photogenerated holes for enhanced photoelectrocatalytic performance. *Microstructures* 2023;3:2023001. https://dx.doi.org/10.20517/microstructures.2022.23

Received: 3 Sep 2022 **First Decision:** 21 Sep 2022 **Revised:** 5 Oct 2022 **Accepted:** 21 Oct 2022 **Published:** 1 Jan 2023

Academic Editors: Yunhau Ng, Shujun Zhang **Copy Editor:** Fangling Lan **Production Editor:** Fangling Lan

Abstract

Utilizing clean energy derived from photoelectrocatalytic reactions is expected to be an excellent choice to fundamentally solve the problem of the human energy crisis. Photoelectrochemical (PEC) cell can effectively promote charge separation and improve solar energy conversion efficiency since it combines the advantages of photocatalysis and electrocatalysis. However, the hole transfer and subsequent oxidation reaction in the PEC process are slow, resulting in the rapid recombination of photogenerated electron-hole pairs and low PEC performance. The half-oxidation reaction involving photogenerated holes is the bottleneck of PEC water splitting. Therefore, hole modulation has been an important research area in the field of catalysis. However, compared with electron modulation, research on hole modulation is limited and still faces great challenges. It is therefore of great significance to develop effective modulation strategies for photogenerated holes. This review summarizes the hole modulation strategies developed in the last five years, including hole sacrificial agents, nanostructural modification, heterostructure construction and cocatalyst modification. Hole modulation dynamics studies, such as transient absorption spectroscopy, time-resolved photoluminescence spectroscopy, transient photovoltage and scanning electrochemical microscopy, are also summarized. Moreover, relevant conclusions and an outlook are proposed.

Keywords: Photoelectrocatalysis, hole modulation, charge separation, interfacial kinetics

INTRODUCTION

Solar energy is clean, renewable, sustainable and abundant. Currently, solar energy conversion and storage have become important options to solve the global energy shortage and environmental pollution challenges[1-3]. Semiconductor-based photocatalysis for splitting water into hydrogen is a renewable and sustainable technology for direct solar-to-chemical energy conversion. However, the relatively low solar energy conversion efficiency limits its practical applications[4-6]. The main semiconductor photocatalytic process can be divided into three steps: (i) the catalyst absorbs photons equal to or greater than the energy of its bandgap width and generates electron-hole pairs by excitation; (ii) photogenerated electron-hole separation and transfer to the semiconductor surface; (iii) transfer to the reactive species to undergo surface reactions (surface complex or effective reactions). The solar energy conversion efficiency is determined by these steps. To improve the efficiency of the photocatalytic process, it is necessary to effectively enhance the separation and transportation of photogenerated charges and simultaneously make the charges migrate to the surface and further initiate the surface reactions of the chemical compounds. During the photocatalytic water splitting process, the hydrogen evolution reaction usually takes place simultaneously with the oxygen evolution reaction (OER). It is noteworthy that the OER becomes the bottleneck of photocatalytic water decomposition because it involves multiple proton- and electron-transfer steps.

The generation rate of holes depends on the illumination light intensity, light absorption and charge separation of the photoelectrode, while the consumption rate of holes depends on the rate of surface charge recombination and hole transfer into solution. However, the water oxidation reaction involving photogenerated holes is much slower than the recombination process. Figure 1 shows a schematic illustration of the processes of semiconductor-based photoelectrocatalytic water splitting and the associated reaction timescales. The accumulated holes not only lead to an increase in the recombination rate of the catalyst, resulting in a reduction in catalytic activity, but also oxidize the catalyst itself, leading to a decrease in catalyst stability and deactivation. Since the discovery of water splitting catalyzed by a single-crystal TiO_2 photoelectrode in 1972, photoelectrochemical (PEC) catalysis based on semiconductor photoelectrodes has attracted extensive attention for solar-to-energy conversion[7-9]. PEC water splitting combines photocatalysis and electrocatalysis, which can effectively promote charge separation and improve solar energy utilization[9]. Furthermore, a series of studies have been carried out on semiconductor materials used as photocatalytic OER photoanodes, including transition metal oxides, hydroxides, nitrides and selenides, metal-organic frameworks (MOFs) and non-metallic polymer semiconductor graphitic carbon nitrides ($g\text{-}C_3N_4$)[10,11]. However, due to the slow hole transfer and subsequent oxidation reactions, the kinetic mismatch between the bulk charge carrier lifetime and the interfacial catalytic timescale results in high electron-hole recombination rates, thus limiting the PEC performance. Furthermore, the water oxidation reaction is also necessary as a counter reaction for electron-involved half reactions[12-14], such as the CO_2 and NH_3 reduction reactions. Therefore, intensive efforts need to be focused on the improvement of the half OER regarding materials, systems, and so on. Understanding how to suppress the recombination of electron-hole pairs and improve the subsequent oxidation reaction rate is the main research direction in the PEC catalysis reaction. Hole modulation to accelerate the kinetics of photogenerated hole transfer and the hole-involved surface oxidation reaction has significant potential for addressing these issues[15,16].

Noble metal oxides, such as RuO_2 and IrO_2, are the most commonly selected materials to modulate photogenerated holes to enhance PEC performance[17]. However, the high cost of noble metals is not sustainable for practical implementation. Therefore, developing low-cost and efficient photogenerated hole modulation candidates that can rapidly initiate oxidation half-reactions has become an urgent challenge in this field. Regarding hole modulation, by designing and modifying the materials that match the valence band energy level of the photoelectrode semiconductor, the photogenerated holes can be efficiently

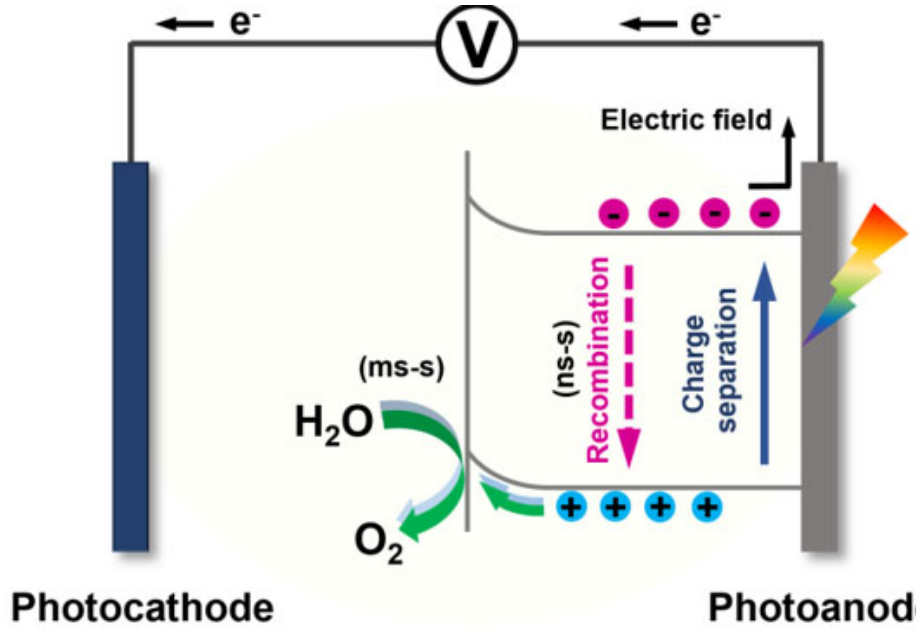

Figure 1. Schematic illustration of the processes of photoinduced charge separation, recombination, transfer and the final catalytic reaction in semiconductor-based photoelectrocatalytic water splitting and the associated reaction timescales.

extracted and the recombination of photogenerated electron-hole pairs can be suppressed. Catalytic regulation to ensure that the holes in the valence band have sufficient potential to oxidize the target molecule is an alternative method[18,19]. Thus, the effective separation and transport of photogenerated carriers on the surface can be improved and the charges can effectively participate in the surface reaction, which can effectively improve the PEC efficiency. In 2019, Sun *et al.* reviewed the development of photogenerated hole modulation in PEC catalysis for solar fuel production, with a focus on surface polarization strategies[15]. So far, the recent advancements in PEC catalysts have yet to be reviewed clearly. Compared to electron modulation, limited research work has been contributed to the field of hole modulation.

This review focuses on the hole modulation of semiconductor-based photoelectrocatalysts in the last five years. The studies of modulation strategies and dynamics form two main sections. The PEC performance is sensitive to the electrode surface structure. In this review, the modulation strategies section covers the recent advances in the design strategies of photoelectrocatalysts with excellent PEC performance through hole modulation, including hole sacrificial agents, nanostructural modification, heterostructure construction and cocatalyst modification [Figure 2]. In the cocatalyst modification section, recent progress on low-cost carbon-based materials is highlighted. The analysis of the transport process of photogenerated holes on the surface is helpful for the design and synthesis of efficient photoelectrocatalysts. Therefore, this review also emphasizes various techniques for studying hole modulation dynamics, such as transient absorption spectroscopy, time-resolved photoluminescence spectroscopy, transient photovoltage and scanning electrochemical microscopy. Moreover, relevant conclusions and outlooks are proposed. This review will trigger the design and construction of efficient photoelectrocatalysts.

HOLE MODULATION STRATEGIES IN PHOTOELECTROCATALYSIS

To suppress photogenerated electron-hole recombination and accelerate hole-to-solution transfer, methods such as introducing hole sacrificial agents, nanostructural modification, heterostructure construction and

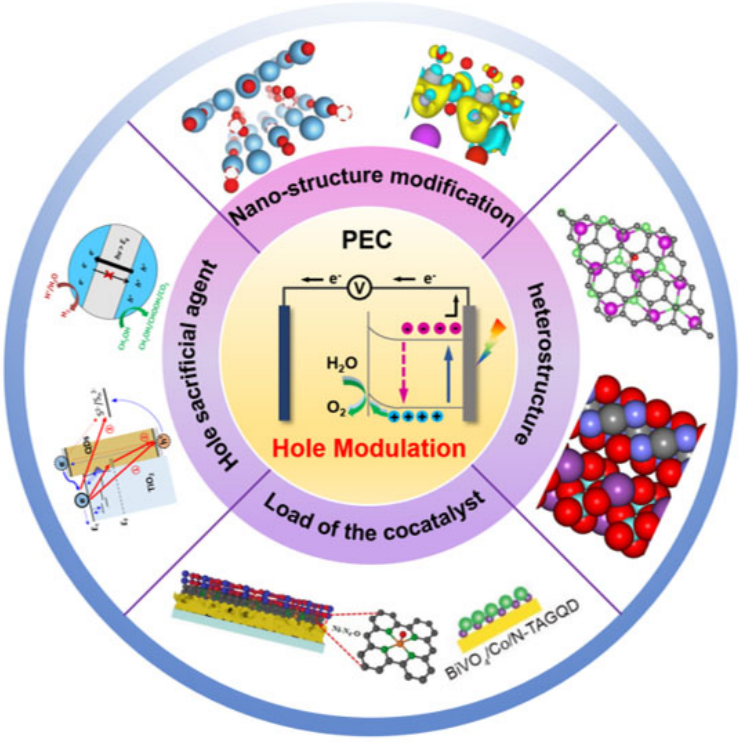

Figure 2. Schematic diagram of photogenerated hole modulation strategies in photoelectrocatalysis.

cocatalyst loading have been developed. The modification of nanostructure regulates the electrostatic field on the surface of the catalyst and promotes the migration of holes. The construction of a heterojunction can realize hole extraction through charge transfer between two semiconductor materials with different energy level positions. The loading of a cocatalyst can effectively extract the photogenerated holes and carry out surface reactions by means of energy level matching with the valence band of the semiconductor.

Hole sacrificial agents

In PEC catalysis, the photogenerated holes migrate to the active site and then accumulate, which affects the subsequent hole migration. The consumption of holes can ensure that the subsequent holes continue to migrate and improve the PEC efficiency. Commonly used sacrificial agents in PEC systems include Na_2S-Na_2SO_3[20,21], triethanolamine (TEOA)[22,23] and H_2O_2[24-26] and these have been widely used to evaluate interfacial charge transfer properties. Thorne *et al.* measured the photocurrent-voltage curves of a hematite photoanode and found that the photoanode with H_2O_2 as hole scavengers has lower onset potential values[24]. This means that there will be fewer photogenerated holes accumulated on the surface of the photoanode after inducing hole scavengers[24]. Unfortunately, the introduction of excess sacrificial agents not only increases the cost but also results in secondary chemical pollution[27]. Alternatively, it is also an important research direction to transform sacrificial agents into value-added chemicals through selective organic synthesis reactions and to cooperate with electrons in the reduction reaction[28]. However, this process remains a major challenge. According to the current research background, researchers mainly prefer to develop efficient PEC catalysts without the use of sacrificial agents.

Nanostructural modification

As mentioned above, researchers are currently working on developing efficient PEC catalysts that do not use sacrificial agents. PEC performance is sensitive to the electrode surface structure. The valence band

edges of some semiconductors are commonly more positive than the thermodynamic potential for the OER, leading to a high oxidation potential for holes in the valence band. The modulation of holes is a feasible method to enhance photocatalytic performance. Researchers have tuned the electronic structure of the semiconductor by introducing heteroatoms, as well as introducing defect states to adjust the atomic structure to increase the charge separation efficiency and further carry out the surface reaction.

Heteroatom doping

The introduction of impurity states through heteroatom doping with, for example, metal cations, S, C, N and O in semiconductors provides the opportunity of trapping photogenerated electrons or holes, so that the photogenerated electrons and holes will be located in different regions, respectively[29,30]. This strategy can reduce the overlap of photogenerated electrons and holes and improve charge transport and separation[31,32]. Zhang *et al.* introduced non-metallic N atoms into $NiFeO_x$ catalysts and used them as cocatalysts to modify a $BiVO_4$ photoanode, in which the O sites in $NiFeO_x$ and $BiVO_4$ were partially replaced by low-electronegativity N atoms, leading to their electronic reconfiguration[18]. The morphological and structural characterization of the $BiVO_4$/N:$NiFeO_x$ photoanodes with a rough flocculent structure is shown in Figure 3A-D. The weak electron-attracting capacity of N atoms leads to electron enrichment on Fe and Ni. The electron injection from Ni atoms into the V sites in the $BiVO_4$ lattice is beneficial for improving the stability of oxygen evolution, while the Fe sites can effectively attract holes to promote the PEC activity. The final obtained $BiVO_4$/N:$NiFeO_x$ exhibited an excellent photocurrent density of 6.4 mA·cm^{-2} at 1.23 V (*vs.* a reversible hydrogen electrode (RHE)) under light [Figure 3E]. The half-cell applied bias photon-to-current efficiency of the $BiVO_4$/N:$NiFeO_x$ photoanode (1.9% at 0.73 V *vs.* a RHE) was also much higher than that of $BiVO_4$/$NiFeO_x$ (1.1% at 0.8 V *vs.* a RHE) and pristine $BiVO_4$ (0.29% at 0.96 V *vs.* a RHE), as shown in Figure 3F[18].

Meng *et al.* synthesized two-dimensional (2D) atomically thin $Zn_{10}In_{16}S_{34}$ nanosheet arrays and achieved oxygen doping and Zn and S vacancies at the surface through low-temperature heat treatment[33]. The excessive surface defect states were then passivated by an ultrathin Al_2O_3 layer. The obtained photoelectrode showed remarkably enhanced PEC OER performance due to the fast electron-hole pair separation and prolonged lifetime of the carriers[33]. However, improper chemical doping may alter the crystal form of the semiconductor and reduce the lifetime of holes, thereby increasing the kinetic challenge of driving catalysis[10,34]. In addition, the control of the concentration and distribution of heteroatom doping on the surface of the photoanode catalysts remains challenging.

Defect engineering

Defect engineering can efficiently modulate the electronic structure and surface properties of a catalyst to reduce the reaction energy barrier for PEC performance. Oxygen vacancies are the most common defects[35]. Any treatment that changes the chemical environment of the catalyst (temperature annealing, treatment under different atmospheres during growth, laser irradiation, and so on) can lead to the formation of these oxygen defect states[36,37]. Zhang *et al.* fabricated a $BiVO_4$ catalyst modified with a FeNiOOH cocatalyst rich in oxygen vacancies ($BiVO_4$/Vo-FeNiOOH) through a simple and economical $NaBH_4$ reduction method[38]. The introduced oxygen vacancies accelerate hole transfer and promote efficient electron-hole pair separation, leading to a negative shift in the starting potential and OER acceleration. The achieved photocurrent of the $BiVO_4$/Vo-FeNiOOH catalyst was more than four times that of pure $BiVO_4$ due to the introduction of oxygen vacancies in the system[38]. Li *et al.* successfully prepared $Bi_7O_9I_3$ microspheres rich in oxygen vacancies by a solvothermal method assisted by an ionic liquid[39]. Compared with $Bi_7O_9I_3$ with fewer oxygen vacancies after annealing, the valence band maximum position of $Bi_7O_9I_3$ with rich oxygen vacancies shifted upward, which resulted in better photooxidation ability for the

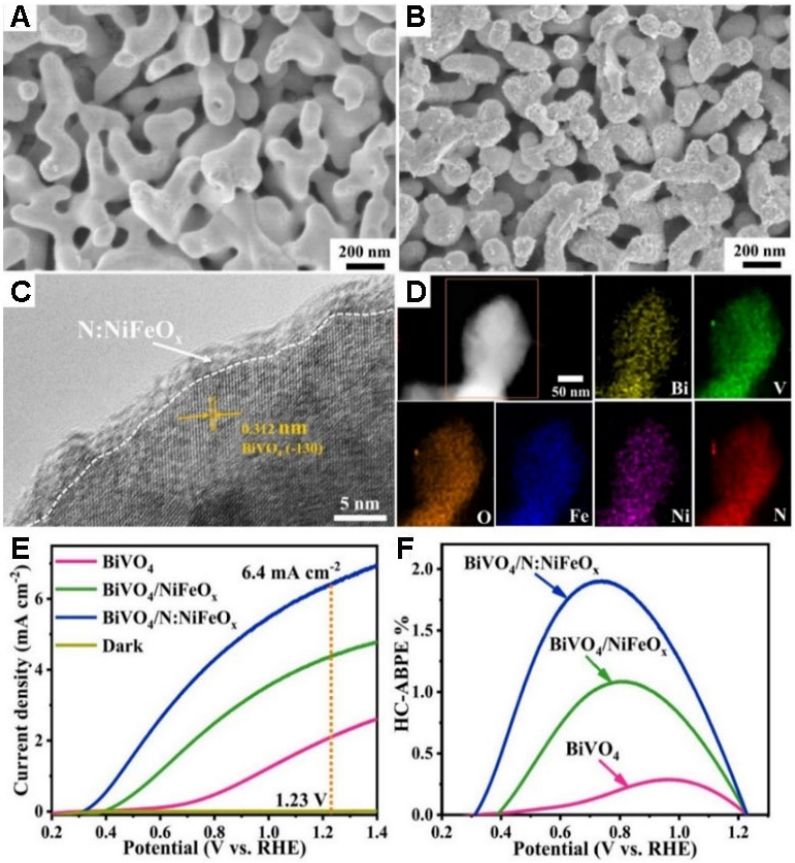

Figure 3. (A-D) Morphological and structural characterization, (E) linear sweep voltammograms and (F) half-cell applied bias photon-to-current efficiency results of $BiVO_4$/N:$NiFeO_x$ photoanodes[18].

photogenerated holes and higher separation efficiency for the photogenerated carriers, thus promoting the photocatalytic removal of oxygen and photocatalytic pollutants[39].

In addition to oxygen vacancies, the introduction of other vacancies can also prolong and migrate the photogenerated carriers to the surface to participate in the reactions[33]. Zhao *et al.* introduced S vacancies to a CdS photoanode surface through H_2O_2 etching and adjusted the vacancy concentration by controlling the etching time[40]. The photocurrent density of the CdS nanorods etched by H_2O_2 for 35 s reached 3.09 mA·cm^{-2}, which was 6.5 times higher than for CdS[40]. Ma *et al.* prepared a WO_3 overlayer with dual oxygen and tungsten vacancies on a WO_3 photoanode by a solution-based process[41]. The obtained mesoporous WO_3 achieved a cathodic shift of the onset potential and enhanced photocurrent for the OER[41]. Although significant progress has been made in improving PEC performance by introducing defects, many issues remain unresolved. For example, surface oxygen vacancies favor the final performance of water-splitting photoanodes because they improve charge separation by narrowing the space-charge layer. In general, however, bulk oxygen vacancies are detrimental because they enhance recombination kinetics, thereby reducing the PEC performance. In addition, the concentration of oxygen vacancies also has an effect on the performance. To improve the PEC performance, the optimization of defect density is necessary[42]. However, similar to the heteroatom doping engineering discussed above, control of the defect concentration and distribution in photoanodes remains a challenge.

Construction of heterostructures

In addition to the nanostructural modification of photoanodes, a highly conductive and active semiconductor can also be used directly on the photoanode surface to form a heterojunction photoelectrode. The construction of heterojunctions can effectively separate the photoelectron holes by satisfying the appropriate energy level positions between the two semiconductors (p-n/n-n)[43,44]. For low-energy light-induced holes, Z-type nanocomposites have been successfully constructed by coupling suitable band gap semiconductors[45]. Photoanodes with Z-type electronic transfer result in enhanced light-harvesting properties and charge separation. For a g-C_3N_4/semiconductor composite, the photogenerated electrons of the semiconductor transfer to the valence band of g-C_3N_4 and then recombine with the photogenerated holes derived from g-C_3N_4. Therefore, the photogenerated electrons on g-C_3N_4 and the photogenerated holes on modified oxides have strong reducing and oxidizing properties. This can lead to charge separation and improve the PEC activity of the catalyst. MOFs with a large surface area are also used in PEC systems. The construction of MOF-based heterojunctions can increase the internal electric field by the conjugated π electrons in the linkers [Figure 4]. Wang *et al.* fabricated Z-scheme heterostructures of TiO_2 nanorods (NRs) coated by MOFs and obtained UiO-66@TiO_2 and UiO-67@TiO_2 photoanodes. Compared with pristine TiO_2, UiO-66@TiO_2 and UiO-67@TiO_2 showed enhanced photocurrent density in the PEC water oxidation process[25].

For a type-II heterojunction, the semiconductor photoanode will be combined with a semiconductor that has a relatively low valence band position. The photogenerated electrons in the conduction band of the modified semiconductor will be transferred to the photoanode. The photogenerated holes in the semiconductor anode will be transferred to the modified semiconductor and further induce the transfer of holes. Different type-II heterojunction photoanodes, such as WO_3/$BiVO_4$, ZnO/$BiVO_4$, ZnO/Fe_2O_3, TiO_2/ZnO, and so on, have been reported with remarkable PEC performance. Maity *et al.* fabricated a one-dimensional n-ZnO/p-$ZnCo_2O_4$ nanoheterojunction photoanode[46]. In this type-II heterojunction photoanode, the $ZnCo_2O_4$ surface overlayer passivated the surface states of ZnO nanorods, thereby significantly reducing the recombination of photogenerated electron-hole pairs. The generated holes from the ZnO nanorods can migrate rapidly to the surface of $ZnCo_2O_4$ and initiate the OER. Compared with the pristine ZnO photoanode, the n-ZnO/p-$ZnCo_2O_4$ nanoheterojunction photoanode achieved a significant increase in photocurrent density[46]. N-type semiconductors with suitable band edges for water oxidation have also been coupled with photoanodes to improve the PEC water splitting performance. Ho *et al.* constructed an epitaxial Fe_2TiO_5/ZnO nanodendrite heterojunction array photoanode. Due to the decoupled light harvesting and hole transport paths, the photocurrent density was greatly improved[47]. Type-II heterojunctions are widely used for hole modulation. The construction of the heterojunction reduces the chance of photogenerated carrier recombination, thereby improving the energy conversion efficiency of PEC catalysts. In addition to these, in order to fully reveal and exploit the advantages of heterostructures, more in-depth fundamental research, especially on the understanding of interfacial properties, is required.

Loading of cocatalysts

Coupling semiconductor photoanodes with good electrocatalytic OER cocatalysts is a common strategy to enhance the charge transfer efficiency from the semiconductor to the electrolyte and improve the oxidation kinetics[48]. The addition of OER catalysts can significantly inhibit the surface recombination of photogenerated charge carriers and reduce the accumulation of holes on the electrode surface. Moreover, some OER cocatalysts have been reported to passivate the photoanode surface to prevent corrosion of the photoanode, thereby improving its stability under operating conditions. Noble metal oxides, such as RuO_2 and IrO_2, are the most commonly used hole transfer cocatalysts, which can effectively reduce the overpotential of oxidation reactions[17]. However, due to the high cost of these catalysts, the development of

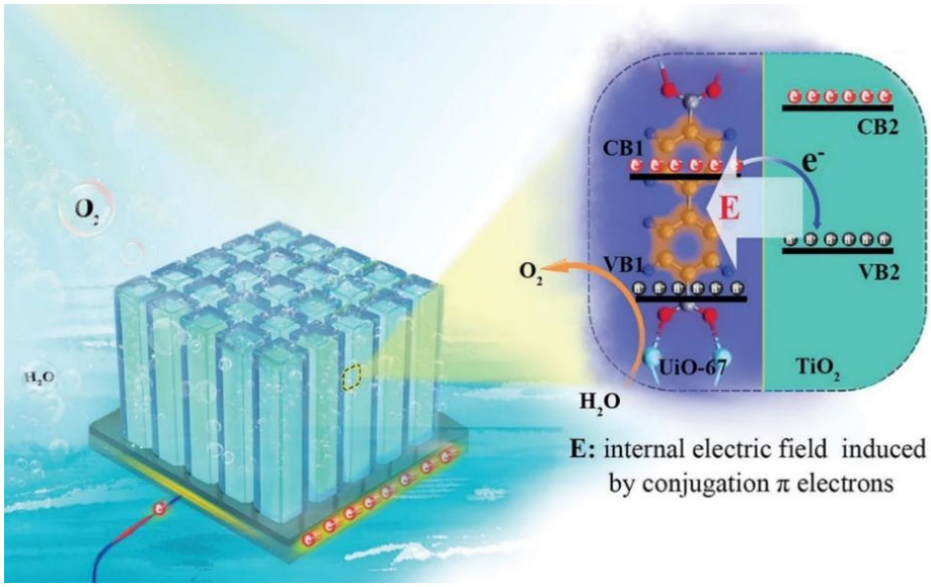

Figure 4. Schematic diagram of conjugated π electrons in a MOF (UiO-67) inducing an internal electric field to promote the charge transfer, followed by the Z-scheme mechanism[25].

abundant and low-cost cocatalysts is indispensable.

Transition metal-based catalysts

To replace high-cost precious metals and their oxides for OER cocatalysts, many transition metal-based catalysts have been investigated extensively for improving PEC kinetics, including transition metal oxides (e.g., Co_3O_4[49], CoO_x[50] and NiO[51]), transition metal hydroxides (e.g., NiOOH[52], CoOOH[53] and FeOOH[54]) and transition metal phosphates (e.g., Fe-Pi[55] and Co-Pi[56]). However, despite these impressive achievements, the role of the cocatalysts in photoanodes is still under debate. Traditional cocatalysts as OER electrocatalysts increase the oxidation rate of water by reducing the activation energy of the four-electron oxidation process, which is the rate-determining step in the water splitting process. Some researchers have reported that the role of the cocatalyst is to rapidly trap the hole, thereby reducing recombination at the semiconductor surface. Li *et al.* demonstrated a citrate-assisted deposition method, in which Ni-Fe hydroxide was overlaid on a Fe_2O_3 nanowire photoanode [Figure 5A][57]. As shown by TEM images [Figure 5B and C], the Fe_2O_3 sample was coated with a Ni-Fe hydroxide layer (~5 nm thick). In the photoanode, Ni-Fe hydroxide as the OER catalyst is beneficial for hole migration and surface passivation and reduces electron-hole recombination on the Fe_2O_3 surface. Therefore, the obtained composite photoanode exhibited a turn-on potential as low as 0.53 V *vs.* a RHE. Compared to that of the pristine Fe_2O_3 photoanode, the turn-on potential had a large cathodic shift of 300 mV[57]. In addition, by loading a cocatalyst, the water oxidation kinetics can also be regulated to tune the product. Zhang *et al.* tuned the surface hole oxidation reaction kinetics of $BiVO_4$ by modifying it with SnO_2 rich in oxygen vacancies (SnO_{2-x}/$BiVO_4$)[58]. In contrast to pure $BiVO_4$, the modified $BiVO_4$ photoanode showed that in the process of water oxidation, the complete reaction of H_2O_2 and O_2 evolution was transformed into H_2O_2 evolution and OH radicals (OH·), accompanied by the inhibition of H_2O_2 decomposition through the hole re-oxidation process. The SnO_{2-x}/$BiVO_4$ photoanode achieved an average FE of 86% for the release of H_2O_2, thereby enabling highly selective water oxidation for producing H_2O_2[58].

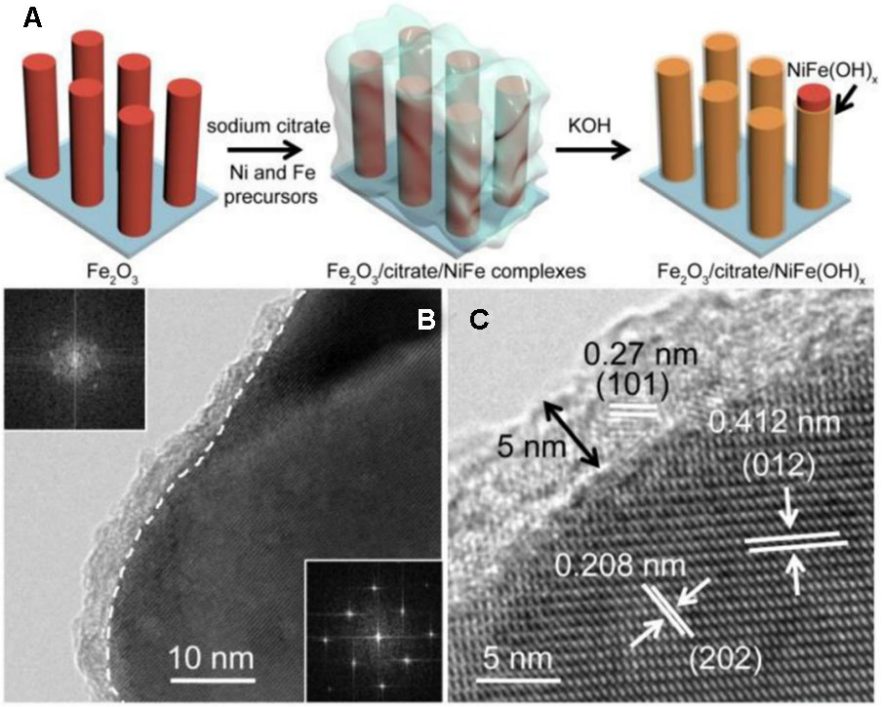

Figure 5. (A) Schematic illustration of depositing NiFe hydroxide overlays on an Fe_2O_3 nanowire photoanode. (B and C) Lattice-resolved TEM images of a NiFe hydroxide-coated Fe_2O_3 nanowire photoanode[57].

Carbon-based materials

Carbon-based materials have been widely investigated as cocatalysts for PEC catalysis due to their abundance, low cost and variety[59]. Carbon-based nanomaterials, such as graphene[60], carbon nanotubes (CNTs)[61] and carbon dots (CDs)[62], offer multiple benefits in PEC systems. For example, they not only facilitate light harvesting but also act as channels for charge transport, thereby facilitating enhanced PEC activity due to synergistic effects and electrical coupling[63]. The high charge-carrier mobility of graphene and CNTs makes them promising candidates for high-mobility charge. However, the reports on those materials are mainly for electron modulation and rarely for hole modulation. Zhao *et al.* fabricated a WO_3 nanosheet array/silane/graphene oxide (WO_3 NS/silane/GO)-based photoanode[64]. On the photoanode, the silane molecules act as hole collection sites and drive the fast transfer of the collected holes to the GO. As a hole transfer channel, GO can immediately promote holes to participate in chemical reactions at the electrode-electrolyte interface, resulting in stable and continuous charge carrier separation and transfer. The results showed that the photocurrent of the WO_3 NS/silane/GO electrode (1.25 $mA{\cdot}cm^{-2}$ at 1.23 V *vs.* a RHE) can be enhanced by a factor of 1.8 compared to the pristine WO_3 NS (0.69 $mA{\cdot}cm^{-2}$) electrode[64].

Compared to the above-mentioned carbon materials, CDs exhibit unique PEC properties, including photoluminescence and photoinduced electron transport and storage, and have been widely used as photoelectrocatalytic cocatalysts[65,66]. A large number of studies have reported CDs as cocatalysts for electron regulation. In recent years, some works have also reported the application of CDs in hole regulation. Liang *et al.* reported a CD-modified Co_3O_4/In_2O_3 composite photocatalyst for an efficient photo-driven CO_2 reduction reaction[67]. CDs can be obtained by the electrolysis of graphite rods. The preparation process of CDs is simple and compared with the noble metal Ru, the economic cost of CDs is negligible [Figure 6A]. Through analysis by transient photoelectric technology, it was found that the CDs in the composite not only participated in the electron transfer process but also in the hole transfer process

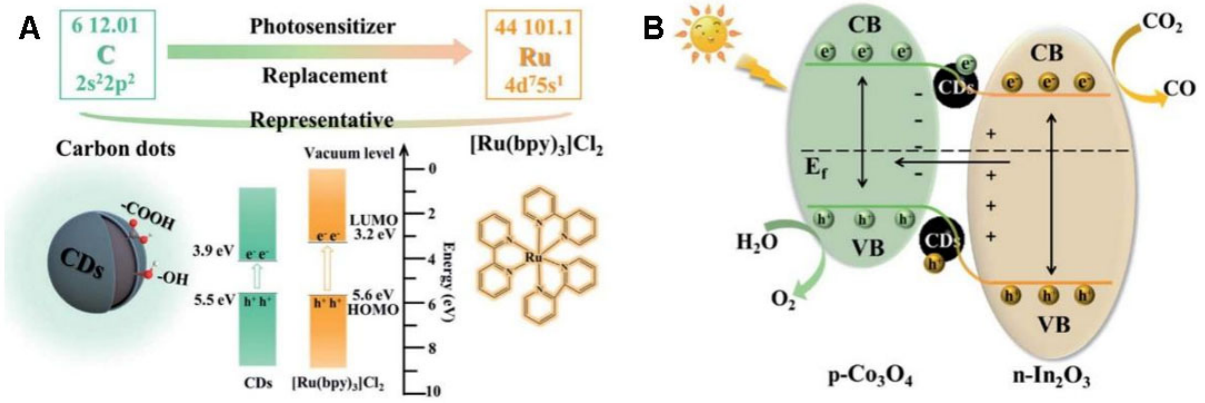

Figure 6. (A) Schematic comparison of carbon and noble metal Ru regarding resource consumption and economic cost. (B) Proposed mechanism of CD/Co_3O_4/In_2O_3 composite for water oxidation and CO_2 reduction reaction[67].

[Figure 6B][67,68]. The current density of the obtained CDs/Co_3O_4/In_2O_3 composite was increased compared with that of the Co_3O_4/In_2O_3 heterostructure. Ye *et al.* loaded CDs between a $BiVO_4$ core and a NiOOH/FeOOH shell[69]. Through the analysis of the transfer efficiency of $BiVO_4$, CD/$BiVO_4$, NiOOH/FeOOH/$BiVO_4$ and NiOOH/FeOOH/CD/$BiVO_4$ samples, the kinetic facility of transfer of the surface reached holes into the solution can be compared. The results showed that the CDs in the catalyst not only broadened the light absorption range but also facilitated the transfer of holes from the $BiVO_4$ core to the NiOOH/FeOOH shell, thus accelerating the OER kinetics[69]. Wang *et al.* obtained FAT through formic acid-treated dicyandiamide and modified it with CDs to achieve CD/FAT catalysts[70]. Wang *et al.* observed that CDs could extract holes in FAT with an efficiency of nearly 75% on a sub-microsecond timescale, leading to the reduction of the electron-hole recombination rate and a larger photoelectron density[70]. The CD/FAT catalysts exhibited the efficient selective reduction of CO_2 to methanol under neutral conditions[70].

In addition to accelerating the extraction of holes and inhibiting the recombination of photogenerated carriers, CDs also appear to accelerate the kinetics of the oxidation reaction[71]. Zhou *et al.* designed a FeOOH/$BiVO_4$ photoanode and then co-modified CDs to obtain a CD/FeOOH/$BiVO_4$ composite[72]. The modified photoanode had a lower overpotential and higher photocurrent. The maximum incident photon-to-current conversion efficiency of the composite catalyst was 6.70 and 1.86 times higher than that of the $BiVO_4$ and FeOOH/$BiVO_4$ electrodes, respectively. Zhou *et al.* reported that these results were due to the joint influence of three effects: (i) the coordinated catalysis of CDs and FeOOH significantly improves the OER kinetics due to the introduction of oxygen vacancies; (ii) the heterojunction between CDs and $BiVO_4$ suppresses the bulk charge recombination effectively; (iii) CDs effectively promote the harvesting of ultraviolet and visible light[72]. Wang *et al.* synthesized nitrogen-doped CDs with a phenolic group (N-TACDs) from tannic acid[73]. The N-TACDs were then deposited on a $BiVO_4$ photoanode via metal-ligand complexation[73]. The N-TACDs can act as hole-storage layers to improve the charge separation efficiency and also improve the catalytic activity with a suitable band position.

CDs have many unique advantages as cocatalysts, as they can facilitate light harvesting and act as agents for photogenerated charge transfer. Furthermore, CDs can also serve as active centers, providing more electrochemically active sites through inherent structural defects, abundant surface/edge functional groups and heteroatom doping. The physical and chemical properties of CDs, such as size, defects, dopants and functional groups, strongly influence their PEC performance. Therefore, in order to realize the wide application of CDs, the controlled synthesis of CDs with specific structures is necessary. Furthermore, to

understand the origin and decay of activity, more control experiments are required to investigate the effect of CD structure on PEC performance.

Organic hole transfer materials

Currently, because of the tunable electrical properties of organic semiconductors or organic molecular materials, the construction of inorganic/organic composite photoanode has attracted increasing attention. Organic long-chain polymer hole transport materials are widely used in solar cells, such as spiro-OMeTAD (2,2′,7,7′-tetrakis(N,N-p-dimethoxyphenylamino)-9,9′-spirobifluorene) and PTAA (poly-[bis(4-phenyl)(2,4,6-trimethylphenyl)amine])[74]. In addition, some research has shown that polyimide polymers have high thermal and chemical stability. Polyimide film electrodes with the semiconductor characteristics of a narrow band gap and suitable band structure have good catalytic ability and stability for the OER in strongly alkaline electrolytes. Thus, the integration of semiconductors with functional polymer layers can be used to achieve efficient and stable photoelectrodes under alkaline conditions. Gao *et al.* coated a metal-free poly(p-phenylene pyromellitimide) (PI) film on a $BiVO_4$ photoanode by in-situ polymerization[75]. The PI film not only acts as a good OER catalytic layer but also promotes the transfer of photogenerated holes on the surface of the photoanode. The photocurrent density of the obtained PI/$BiVO_4$ was increased by ~2.5 times compared to a pristine $BiVO_4$ photoanode[75]. Gu *et al.* reported a metal-free bifunctional polyaniline (PANI)/CD electrocatalyst capable of producing hydrogen under light, in which PANI as a p-type semiconductor was used to solve the problem of insufficient protons[76].

Small molecular materials that are soluble in water or polar solvents are more suitable for photoelectric catalytic systems. Currently, many research works have reported that organic hole-transporting molecular materials can be used to modify photoanodes as cocatalysts for hole modulation to improve charge separation efficiencies, such as ferrocene ligands, phenothiazine (PTZ) and trifluoroacetic acid[77-80]. A suitable hole-accepting ligand should satisfy the energy requirement for continuous hole transfer and interact closely with the photoelectrode to enable ultrafast hole transfer. Niu *et al.* systematically studied the role of carbazole-derived hole transport molecules anchoring on the surface of a CdS QD/TiO_2 film[80]. As shown in Figure 7, dithiol-functionalized carbazole and a ruthenium coordination compound (RubdaS) were used as a hole transfer molecule and OER catalyst, respectively. These results demonstrated the importance of hole transport molecules for rapid hole transfer. A series of hole transport molecules, including carbazole, triphenylamine (TPA) and PTZ, were further anchored on the surface of a $BiVO_4$/CdS photoanode. The photogenerated holes from the photoanode can be extracted rapidly by these molecules. Among these different hole transport molecules, the obtained $BiVO_4$/CdS-TPA/CoBi exhibited an ultralow onset potential of 0.15 V *vs.* a RHE and the highest photocurrent density of 5.2 mA/cm^2[81]. Wu *et al.* reported the transfer kinetics of photogenerated holes in CdS nanorods (NRs) by PTZ molecules adsorbed on the surface[82]. In the presence of PTZ, the trapped holes are transferred to the PTZ to form PTZ^+ radical cations and this hole transfer rate is found to be much faster than the slow electron-trapping hole recombination in CdS NRs. This proved that the adsorbed PTZ can effectively extract trapped holes in CdS NRs[82]. In addition, Li *et al.* fabricated CdSe QDs modified with PTZ hole-accepting ligands and found that the PTZ modification of the CdSe QDs could significantly enhance the PEC H_2 evolution efficiency[83].

RESEARCH METHODS FOR KINETICS OF HOLE TRANSFER

In the semiconductor photocatalytic process, the lifetimes of the kinetic processes, such as migration, transport and recombination, generally range from a few nanoseconds to a few microseconds, whereas the timescales of photocatalytic reaction process are microseconds to seconds. Therefore, to effectively study the transport and transfer of charges in photoelectrodes, time-resolved analytical testing techniques are necessary.

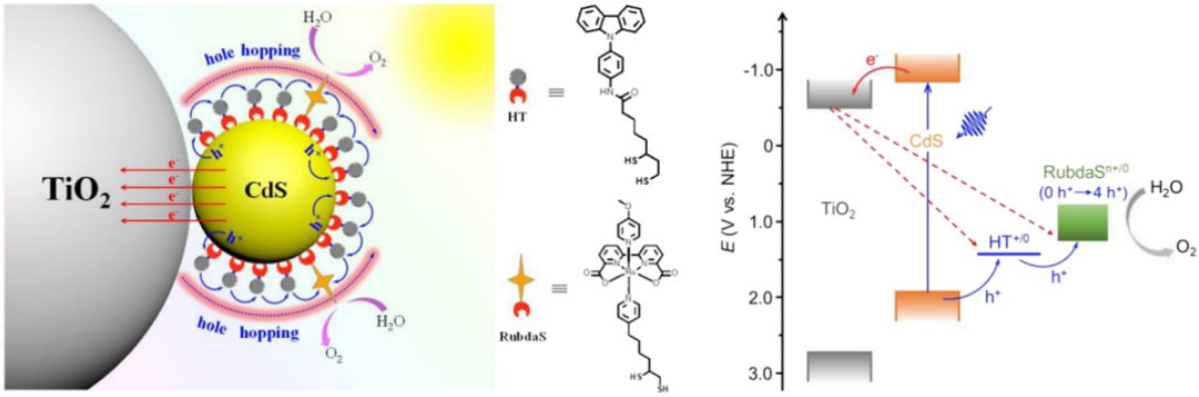

Figure 7. Simplified interfacial hole hopping scheme for integrated photoanode[80].

Transient absorption spectroscopy (TAS)

Time-resolved spectroscopy is a new field developed by pulse technology combined with weak and transient signal detection methods, focusing on the investigation of the interaction between light and the sample. TAS is a pump-probe time-resolved technique that has been widely used to investigate dynamic processes. TAS can directly obtain information on the molecular ground, excited, oxidation and reduction states at different relaxation times and is therefore an effective means to explore the kinetics of charge transfer[84]. Tamaki *et al.* studied the intrinsic dynamics of electron-hole pairs in the range from femtoseconds to picoseconds and found that the holes could be trapped on the nanoparticle surfaces rapidly while the electrons were slowly trapped in the bulk phase with long lifetimes[85]. Wang *et al.* used TAS to fundamentally understand the charge carrier dynamics of hole-accepting CDs as cocatalysts[71]. The transient absorption spectra of g-C_3N_4 measured with and without Ag^+ electron scavengers showed that the signal observed at 510 nm was mainly attributed to photogenerated holes, while the wide signal at 700 nm was attributed to photogenerated electrons. The amplitude of ^{m}CDs/CN at 700 nm was higher than that of pure CN, indicating that the holes were transferred to ^{m}CDs efficiently and the number of long-lived electrons in CN was increased.

For heterostructured systems, Lian *et al.* synthesized CdS/ZnS core/mesoporous-shell (CdS@mZnS) heterostructures with superior photocatalytic activity[86]. TAS and the time-resolved microwave conductivity revealed efficient photoinduced hole transfer from the CdS core to the ZnS shell. The long-lived photoinduced charge separation (> 2.4 ms) via defect-mediated hole transfer resulted in good catalytic activity and stability for CdS@mZnS[86]. Andrews *et al.* also demonstrated sub-picosecond hole-transfer kinetics in β-$Sn_{0.23}V_2O_5$/CdSe heterostructures by TAS measurements[87]. The three-dimensional TA color maps of β-$Sn_{0.23}V_2O_5$ nanowires and β-$Sn_{0.23}V_2O_5$/CdSe heterostructures were acquired. The bare β-$Sn_{0.23}V_2O_5$ nanowires have two broad induced absorption bands at 500-600 and 650-750 nm, assigned to excited holes in the mid-gap state and β-$Sn_{0.23}V_2O_5$ electrons in the conduction band, respectively. The results demonstrated that the β-$Sn_{0.23}V_2O_5$/CdSe heterostructures have rapid excited-state charge transfer kinetics[87].

Time-resolved photoluminescence (TRPL) spectroscopy

In addition to TAS, TRPL spectroscopy is another effective means to probe electron transfer kinetics[88]. With the development of science and technology, the temporal resolution of fluorescence spectroscopy has reached the femtosecond scale (< 100 fs). Direct hole transfer rate tests can be carried out by adding a small amount of hole sacrificial agent to the catalyst with the corresponding carrier lifetime achieved by TRPL spectroscopy. Yu *et al.* tested the lifetime of photogenerated carriers of InP/ZnS-S QDs using TRPL

spectroscopy[89]. A range of carrier lifetimes can be obtained by the stepwise addition of electron and hole sacrificial agents (N^{i2+}/H_2A) [Figure 8A and B]. The final electron and hole transfer rates were obtained by fitting the obtained data, indicating a calculated electron transfer rate from InP/ZnS-S QDs to Ni^{2+} of 7.64×10^8 s^{-1}·mM^{-1} and a hole transfer rate from InP/ZnS-S QDs to H_2A of 1.25×10^8 s^{-1}·mM^{-1} [Figure 8C and D][89]. Fan *et al.* tested the static photoluminescence quenching and trap-state photoluminescence decay curves of CdSe and CdSe with surface S^{2-} (CdSe-nS) QDs with the sacrificial agent isopropyl alcohol[90]. After the TRPL measurements of CdSe QDs with different molar ratios of S^{2-} ions, it was found that the corresponding hole transfer rate increased with increasing molar ratios of S^{2-} ions and was saturated at $n = 75$. The TRPL measurements showed that the S^{2-} ligands were beneficial for hole transfer[90].

Transient photoelectric technology (TPV)

TPV is also an effective technique for determining interfacial charge transfer kinetics and photoelectron extraction in composites. In contrast to TAS and TRPL, TPV is a characterization technology that excites the catalysts in a photoelectrode by an optical signal and measures the dynamic process of the electrical signal inside the composite materials. Zhang *et al.* reported SnO_{2-x} overlay-coated $BiVO_4$ (SnO_{2-x}/$BiVO_4$) and investigated its hole migration via TPV[58]. The photoanode provided positive TPV signals, meaning that the surface migration behavior of photoinduced holes occurred. Compared with pure $BiVO_4$, the SnO_{2-x}/$BiVO_4$ photoanode had the highest TPV signal intensity, indicating that the coated SnO_{2-x} overlay facilitated the photoinduced holes to reach the photoanode surface. In addition, the prolonged delay time of the photovoltage signal for both the SnO_2/$BiVO_4$ and SnO_{2-x}/$BiVO_4$ photoanodes indicated the existence of long-lived holes as a result of the reduction in surface recombination[58]. Kang *et al.* reported a metal-free dual-function photo-assisted catalyst of PANI/CDs for overall water splitting[62]. It was found that the addition of CDs reduced the recombination rate of photogenerated carriers. The number of photogenerated electrons consumed in the catalytic reaction could be calculated by integrating the tested TPV curves. It was found that the photocurrent intensity of PANI/CDs in 5 vol.‰ KOH (pH = 8.5)/ACN (v/v) was much higher than that in ACN solution, which may be due to the participation of photogenerated holes in the OER, resulting in increasing photocurrent intensity[76].

Electrochemical impedance spectroscopy (EIS)

Different from the above photophysical methods, electrochemical methods can directly record information, such as the photocurrent and photocurrent-potential (i-V) curves of PEC reactions. Photocurrent responses can reveal the separation efficiency of photogenerated electron-hole pairs. Among the electrochemical methods, EIS, through transient measurements, can be employed to investigate interfacial processes, such as redox reactions at the interfaces and the migration of electroactive species[91,92]. EIS measurements are based on the perturbation signals with a set of sine voltages or current signals at different frequencies. Currently, EIS analysis is a relatively well-established method for investigating PEC systems[93].

Abbas *et al.* studied the hole transfer pathway in a TiO_2 photoanode sensitized by Au nanoclusters using EIS[94]. Through the analysis of the Nyquist plots obtained as a function of applied potentials under light, the possible charge transfer mechanism in the photoelectrode can be achieved. From the low-frequency semicircle in the Nyquist plots at low bias potentials, the hole transfer process can be analyzed. The EIS studies confirmed that when $Au_{15}(SG)_{13}$ and $Au_{18}(SG)_{14}$ were employed, hole transfer occurred through the HOMO level of the nanoclusters and when $Au_{25}(SG)_{18}$ was used, the hole transfer proceeded with the surface traps in TiO_2[94]. In EIS, the charge transfer resistance (R_{ct}) of the photoanode is sensitive to surface processes and can be used to analyze the transfer of photogenerated holes. Kolay *et al.* investigated the charge recombination rate in a CdS-sensitized TiO_2 photoanode by modifying CDs through EIS and found that the R_{ct} has a strong dependence on illumination but a low dependence on voltage[95]. This implies that

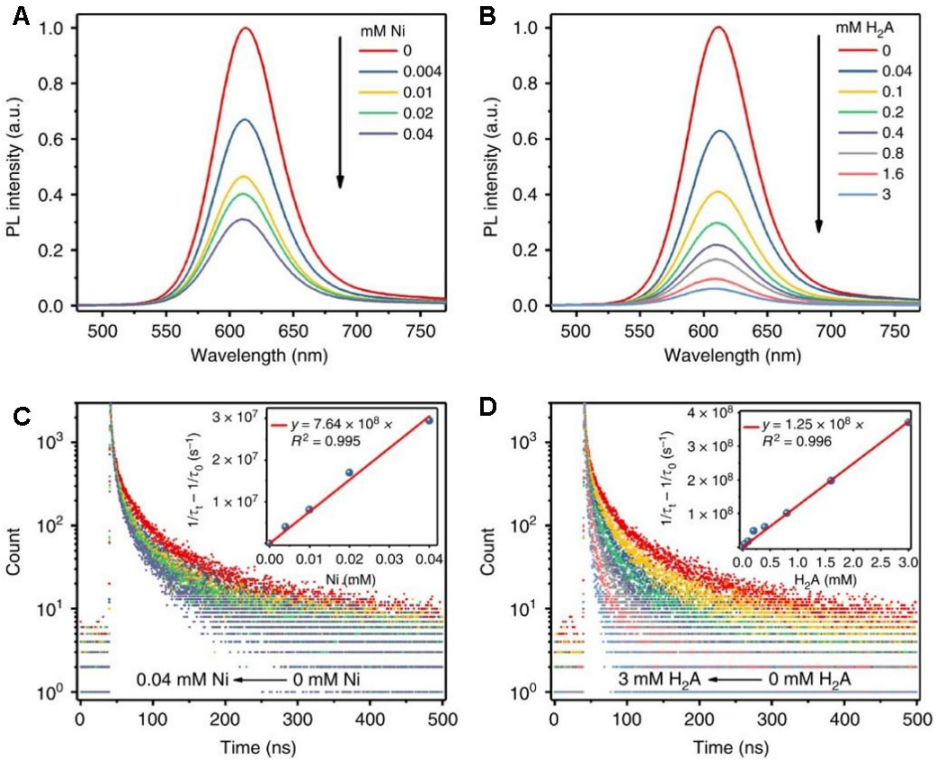

Figure 8. Steady state and time-resolved photoluminescence quenching experiment of InP/ZnS-S QDs (525 nm, 15 min). Static photoluminescence quenching for InP/ZnS-S QDs in water after addition of different amounts of Ni^{2+} (A) and H_2A (B). PL decay curves of InP/ZnS-S QDs after addition of different amounts of Ni^{2+} (C) and H_2A (D), respectively[89].

charge transfer is influenced by photogenerated holes[95].

Peter *et al.* characterized the competition between photogenerated carrier transfer and the recombination of an α-Fe_2O_3 electrode using photoelectrochemical impedance spectroscopy (PEIS)[96,97]. The variation of EIS with electrodes for different layered α-Fe_2O_3 films was also recorded. The PEIS response of the α-Fe_2O_3 electrode exhibits characteristic transmission line behavior in the high-frequency part. Peter *et al.* speculated that this may be due to the slow hole transport, probably between adjacent surface iron species[96,97]. Moreover, Peter *et al.* studied the effects of introducing Mn on the surface carrier dynamics of the hematite nanorods through intensity-modulated photocurrent spectroscopy (IMPS)[98]. In contrast to EIS, IMPS measurements control the intensity of light on the electrode. In IMPS, the upper quadrant semicircle corresponds to the competition between charge transfer and recombination and the lower quadrant semicircle corresponds to the RC attenuation of the system [Figure 9]. Compared to the pristine hematite, the radius of the low-frequency semicircle (upper quadrant) of the Mn-doped hematite decreased and the hole transfer efficiency improved. The IMPS result revealed that the introduction of Mn not only increased the hole transfer rate constant but also reduced the surface recombination rate constant[98].

In addition, for the development of the PEC performance, understanding the interactions between ions in the electric double layer and charge carriers is critical. EIS measurements can also be used to study the surface ion adsorption. Zheng *et al.* showed that the capacitance at the interface of an InSe/graphene photoanode and the solution under illumination was ~2.3 times greater than that in the dark[99]. The result showed an interaction between the photogenerated holes and OH^- species, which further enhanced the concertation of OH^- surface adsorption and improved the PEC performance[99].

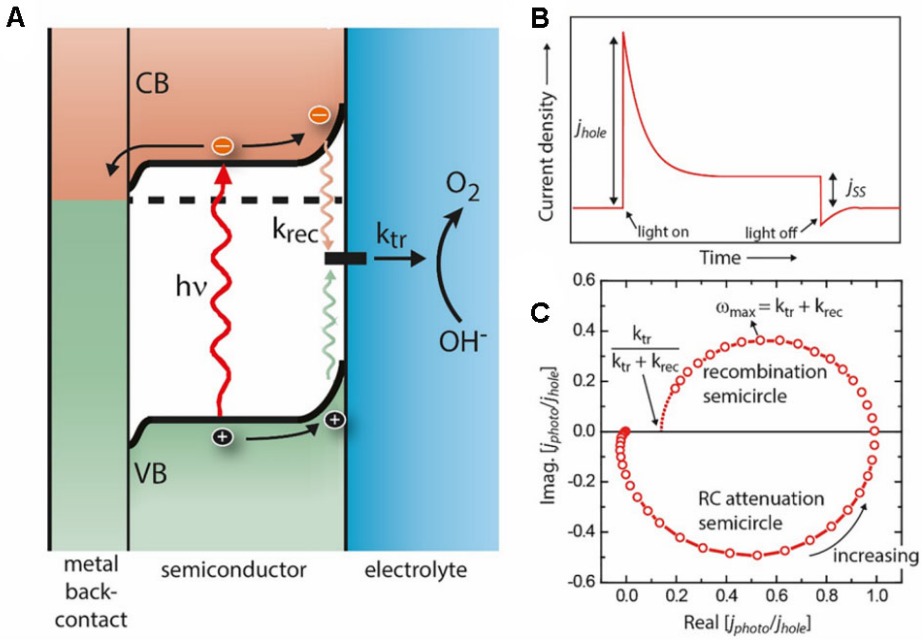

Figure 9. (A) Schematic of competition between hole transfer (k_{tr}) and recombination (k_{rec}). (B) A typical photocurrent of a photoanode in an electrolyte. (C) A typical example of a complex photocurrent or IMPS spectrum[98].

Scanning electrochemical microscopy (SECM)

Furthermore, it is of great significance to measure the interfacial processes of photoanodes at the microscopic scale. SECM is a scanning probe technique for electrical analysis, which can obtain information on substrate topography and localized electrochemical activity[100]. The concept of SECM is to place the ultramicroelectrode (diameter of < 25 μm) near the surface of the photoanode (or substrate) and to probe the changes in the concentration of active molecules in the electrolyte to investigate its chemical properties. Therefore, it is a powerful tool for imaging microelectrochemical activity and studying the kinetic behavior of reactive species under in-situ liquid-phase reaction conditions. In addition, the ultramicroelectrode can be scanned locally in the *x, y* or *z* direction through a piezoelectric actuator or stepper motor, so SECM can also be used to investigate spatial electrochemical information. SECM has also been used to explore the OER interfacial hole migration kinetics of composite photocatalytic systems [Figure 10A]. Zhang *et al.* studied the effect of oxygen vacancies on the hole transfer behavior of a $BiVO_4/V_O$-FeNiOOH catalyst through SECM. SECM was employed at a UV-vis/SECM platform by the feedback mode[38]. Under visible-light irradiation, the current at the UME increases, which is mainly caused by photogenerated holes participating in the oxidation process of the active species [Figure 10B]. The results show that the kinetics of hole transfer in different photoanodes was in the order of: $BiVO_4/V_O$-FeNiOOH $BiVO_4$/FeNiOOH $BiVO_4$ [Figure 10C and D], confirming that the strategy of introducing oxygen vacancies on the cocatalyst can improve the photogenerated charge transfer ability and further suppress the interfacial recombination[38].

The interfacial kinetic data of photogenerated holes can be further achieved through theoretical model simulations after obtaining different approaching curves. Liu *et al.* fabricated a CD-modified TiO_2 (CD/TiO_2) anode and investigated the regeneration kinetics of the CD sensitizer, i.e., the rate constant of the hole transfer from the oxidized CDs to the solution[101]. In this work, SECM measurements were performed by examining the ultramicroelectrode (UME) feedback current related to the change in the active species concentration under short-circuit conditions. The active species was chosen as I_3^-/I^- in acetonitrile. Under illumination (475 nm), the photoexcited state of the CDs injected electrons into the conduction band of

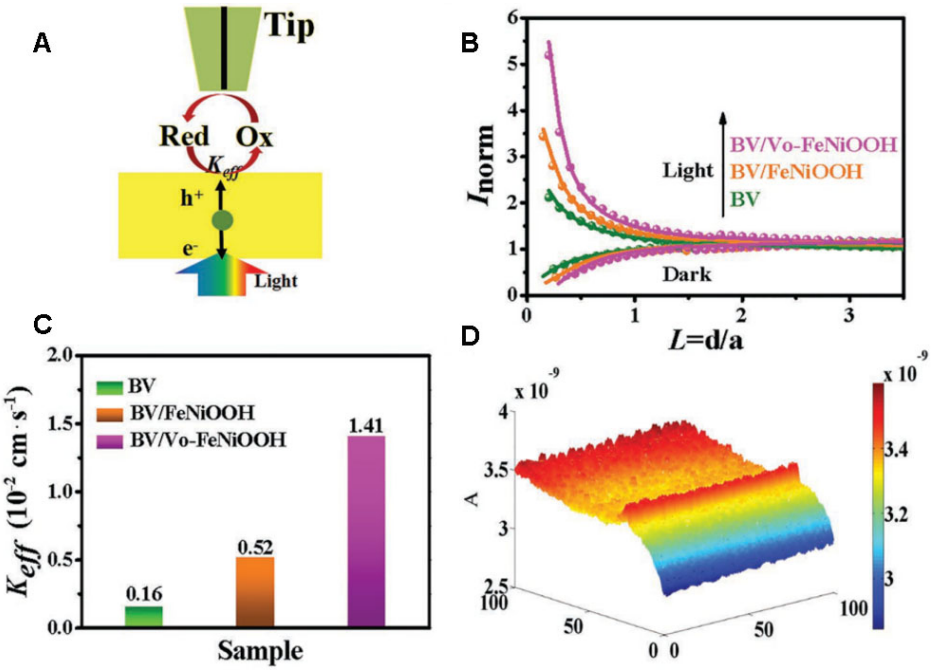

Figure 10. (A) Principle of SECM setup. (B) Probe approach curves and (C) rate constants (K_{eff}) of $BiVO_4$-based photoanodes. (D) SECM image (100 × 100 μm^2) of $BiVO_4$/Vo-FeNiOOH photoanode surface under light[38].

TiO_2. As the UME approaches the substrate, the oxidation state (CDs^+) generated is regenerated by reacting with I^- in the electrolyte. Furthermore, the regeneration rate constant of CDs was achieved by fitting and analyzing the approaching curves obtained by testing different concentrations of active species and light intensities[101]. SECM can also be used to further study the back-transfer behavior (electron participation process) and dye regeneration (hole participation process) at the interface between the photoanode and electrolyte for the effect of cocatalysts on the separation of electron-hole pairs. Yu *et al.* used SECM to study the surface kinetics of a $BiVO_4$/NiFe-LDH composite photocatalyst[102]. It was found that the rate constant ratio of photogenerated surface holes and electrons reacting with the active species (k_{h+}/k_{e-}) was five times higher than that of $BiVO_4$. The results indicate that the NiFe-LDH cocatalyst can significantly inhibit electron back transfer and ultimately reduce surface recombination[102].

CONCLUSIONS

In this review, the strategies of hole modulation to improve solar-to-energy conversion efficiency are outlined. The modulation of holes facilitates the efficient separation of photogenerated carriers and accelerates the subsequent oxidation reactions. The catalysts in photoanodes with different compositions and structures show different reactivity. Hole modulation strategies, including hole sacrificial agents, nanostructural modification, heterostructure construction and cocatalyst modification, are effective methods to suppress electron-hole pair recombination and enhance PEC performance. The design of catalysts to modulate holes is summarized and the application of low-cost carbon materials as cocatalysts in hole modulation is highlighted. In addition, some kinetic techniques have also been summarized to analyze the transport and transfer kinetics of photogenerated holes. Although some achievements have been made, understanding how to acquire highly active PEC photoanodes via the rational design and regulation of fine structures and interfaces remains a significant challenge. The effects of the compositions and structures of the photoanode on the photogenerated charge migration and PEC properties need to be studied more thoroughly.

In these discussions, we have focused on designing and developing PEC catalysts for efficient solar-to-energy conversion. However, there are still many significant challenges that need to be addressed in order to make catalysts economically competitive. First, the PEC process involves the transport of charges and the coupling of subsequent reactions. The rate at which the photogenerated holes transfer to the semiconductor surface is effectively matched with the rate of transferring into the solution, enabling the efficient utilization of the photogenerated charges. Therefore, it is important to develop research methods to effectively distinguish the kinetic processes for the achievement of rate matching. Second, if the spatially separated photogenerated charges cannot be overlapped and synergized with the catalytic sites, it will lead to the recombination of the photogenerated charges, thereby reducing the PEC efficiency. The development of high-resolution characterization instruments can effectively promote the design of efficient PEC catalysts.

DECLARATIONS

Authors' contributions

Conceptualization, investigation, writing - original draft: Liu N
Writing - review & editing: Liu Y (Yixian Liu), Liu Y (Yunliang Liu), Li Y, Cheng Y
Writing - review & editing, supervision, funding acquisition: Li H

Availability of data and materials

Not applicable.

Financial support and sponsorship

This work was supported by the National Natural Science Foundation of China (Grants 52072152, 51802126), the Jiangsu University Jinshan Professor Fund and the Jiangsu Specially-Appointed Professor Fund, Open Fund from Guangxi Key Laboratory of Electrochemical Energy Materials.

Conflicts of interest

All authors declared that there are no conflicts of interest.

Ethical approval and consent to participate

Not applicable.

Consent for publication

Not applicable.

REFERENCES

1. Fang Y, Hou Y, Fu X, Wang X. Semiconducting polymers for oxygen evolution reaction under light illumination. *Chem Rev* 2022;122:4204-56. DOI PubMed
2. Kranz C, Wächtler M. Characterizing photocatalysts for water splitting: from atoms to bulk and from slow to ultrafast processes. *Chem Soc Rev* 2021;50:1407-37. DOI PubMed
3. Morikawa T, Sato S, Sekizawa K, Suzuki TM, Arai T. Solar-driven CO_2 reduction using a semiconductor/molecule hybrid photosystem: from photocatalysts to a monolithic artificial leaf. *Acc Chem Res* 2022;55:933-43. DOI PubMed
4. Pan J, Shen S, Chen L, Au C, Yin S. Core-shell photoanodes for photoelectrochemical water oxidation. *Adv Funct Mater* 2021;31:2104269. DOI PubMed
5. Thalluri SM, Bai L, Lv C, Huang Z, Hu X, Liu L. Strategies for semiconductor/electrocatalyst coupling toward solar-driven water splitting. *Adv Sci* 2020;7:1902102. DOI PubMed PMC
6. Niu F, Wang D, Li F, Liu Y, Shen S, Meyer TJ. Hybrid photoelectrochemical water splitting systems: from interface design to system assembly. *Adv Energy Mater* 2020;10:1900399. DOI

7. Fujishima A, Honda K. Electrochemical photolysis of water at a semiconductor electrode. *Nature* 1972;238:37-8. DOI PubMed
8. Zhao E, Du K, Yin PF, et al. Advancing photoelectrochemical energy conversion through atomic design of catalysts. *Adv Sci* 2022;9:e2104363. DOI PubMed PMC
9. Marwat MA, Humayun M, Afridi MW, et al. Advanced catalysts for photoelectrochemical water splitting. *ACS Appl Energy Mater* 2021;4:12007-31. DOI
10. Corby S, Rao RR, Steier L, Durrant JR. The kinetics of metal oxide photoanodes from charge generation to catalysis. *Nat Rev Mater* 2021;6:1136-55. DOI
11. Yao T, An X, Han H, Chen JQ, Li C. Photoelectrocatalytic materials for solar water splitting. *Adv Energy Mater* 2018;8:1800210. DOI
12. Zhuang Z, Li Y, Yu R, et al. Reversely trapping atoms from a perovskite surface for high-performance and durable fuel cell cathodes. *Nat Catal* 2022;5:300-10. DOI
13. Zhuang Z, Huang J, Li Y, Zhou L, Mai L. The holy grail in platinum-free electrocatalytic hydrogen evolution: molybdenum-based catalysts and recent advances. *ChemElectroChem* 2019;6:3570-89. DOI
14. Huang J, Zhuang Z, Zhao Y, et al. Back-gated van der waals heterojunction manipulates local charges toward fine-tuning hydrogen evolution. *Angew Chem Int Ed Engl* 2022;61:e202203522. DOI PubMed
15. Sun R, Zhang Z, Li Z, Jing L. Review on photogenerated hole modulation strategies in photoelectrocatalysis for solar fuel production. *ChemCatChem* 2019;11:5875-84. DOI
16. Rahman MZ, Edvinsson T, Gascon J. Hole utilization in solar hydrogen production. *Nat Rev Chem* 2022;6:243-58. DOI
17. Sahoo PP, Mikolášek M, Hušeková K, et al. Si-based metal-insulator-semiconductor structures with RuO_2-(IrO_2) films for photoelectrochemical water oxidation. *ACS Appl Energy Mater* 2021;4:11162-72. DOI
18. Zhang B, Yu S, Dai Y, et al. Nitrogen-incorporation activates $NiFeO_x$ catalysts for efficiently boosting oxygen evolution activity and stability of $BiVO_4$ photoanodes. *Nat Commun* 2021;12:6969. DOI PubMed PMC
19. Wang J, Liao T, Wei Z, Sun J, Guo J, Sun Z. Heteroatom-doping of non-noble metal-based catalysts for electrocatalytic hydrogen evolution: an electronic structure tuning strategy. *Small Methods* 2021;5:e2000988. DOI PubMed
20. Liu G, Yang Y, Li Y, et al. Band structure engineering toward low-onset-potential photoelectrochemical hydrogen production. *ACS Mater Lett* 2020;2:1555-60. DOI
21. Li F, Benetti D, Zhang M, Feng J, Wei Q, Rosei F. Modulating the 0D/2D interface of hybrid semiconductors for enhanced photoelectrochemical performances. *Small Methods* 2021;5:e2100109. DOI PubMed
22. Tashakory A, Karjule N, Abisdris L, Volokh M, Shalom M. Mediated growth of carbon nitride films via spray-coated seeding layers for photoelectrochemical applications. *Adv Sustain Syst* 2021;5:2100005. DOI
23. Karjule N, Singh C, Barrio J, et al. Carbon nitride-based photoanode with enhanced photostability and water oxidation kinetics. *Adv Funct Mater* 2021;31:2101724. DOI
24. Thorne JE, Jang JW, Liu EY, Wang D. Understanding the origin of photoelectrode performance enhancement by probing surface kinetics. *Chem Sci* 2016;7:3347-54. DOI PubMed PMC
25. Wang X, Sun W, Tian Y, et al. Conjugated π electrons of MOFs drive charge separation at heterostructures interface for enhanced photoelectrochemical water oxidation. *Small* 2021;17:e2100367. DOI PubMed
26. Dotan H, Sivula K, Grätzel M, Rothschild A, Warren SC. Probing the photoelectrochemical properties of hematite (α-Fe_2O_3) electrodes using hydrogen peroxide as a hole scavenger. *Energy Environ Sci* 2011;4:958-64. DOI
27. Jiang P, Yu K, Yuan H, et al. Encapsulating Ag nanoparticles into ZIF-8 as an efficient strategy to boost uranium photoreduction without sacrificial agents. *J Mater Chem A* 2021;9:9809-14. DOI
28. Zhang T, Lu S. Sacrificial agents for photocatalytic hydrogen production: effects, cost, and development. *Chem Catalysis* 2022;2:1502-5. DOI
29. Shen S, Lindley SA, Chen X, Zhang JZ. Hematite heterostructures for photoelectrochemical water splitting: rational materials design and charge carrier dynamics. *Energy Environ Sci* 2016;9:2744-75. DOI
30. Prasad U, Young JL, Johnson JC, et al. Enhancing interfacial charge transfer in a WO_3/$BiVO_4$ photoanode heterojunction through gallium and tungsten co-doping and a sulfur modified Bi_2O_3 interfacial layer. *J Mater Chem A* 2021;9:16137-49. DOI
31. Sun D, Zhang X, Shi A, et al. Metal-free boron doped g-C3N5 catalyst: efficient doping regulatory strategy for photocatalytic water splitting. *Appl Surface Sci* 2022;601:154186. DOI
32. Nyarige JS, Paradzah AT, Krüger TPJ, Diale M. Mono-Doped and Co-Doped nanostructured hematite for improved photoelectrochemical water splitting. *Nanomaterials* 2022;12:366. DOI PubMed PMC
33. Meng L, Rao D, Tian W, Cao F, Yan X, Li L. Simultaneous manipulation of O-doping and metal vacancy in atomically thin $Zn_{10}In_{16}S_{34}$ nanosheet arrays toward improved photoelectrochemical performance. *Angew Chem Int Ed Engl* 2018;57:16882-7. DOI PubMed
34. Yang R, Zhu R, Fan Y, Hu L, Chen Q. In situ synthesis of C-doped $BiVO_4$ with natural leaf as a template under different calcination temperatures. *RSC Adv* 2019;9:14004-10. DOI PubMed PMC
35. Wen L, Li X, Zhang R, et al. Oxygen vacancy engineering of MOF-derived Zn-doped Co_3O_4 nanopolyhedrons for enhanced electrochemical nitrogen fixation. *ACS Appl Mater Interfaces* 2021;13:14181-8. DOI PubMed
36. Wang S, Wang X, Liu B, et al. Vacancy defect engineering of $BiVO_4$ photoanodes for photoelectrochemical water splitting. *Nanoscale* 2021;13:17989-8009. DOI PubMed
37. Pan JB, Wang BH, Wang JB, et al. Activity and stability boosting of an oxygen-vacancy-rich $BiVO_4$ photoanode by NiFe-MOFs thin

layer for water oxidation. *Angew Chem Int Ed Engl* 2021;60:1433-40. DOI PubMed

38. Zhang R, Ning X, Wang Z, et al. Significantly promoting the photogenerated charge separation by introducing an oxygen vacancy regulation strategy on the FeNiOOH Co-catalyst. *Small* 2022;18:e2107938. DOI PubMed
39. Ji M, Chen R, Di J, et al. Oxygen vacancies modulated Bi-rich bismuth oxyiodide microspheres with tunable valence band position to boost the photocatalytic activity. *J Colloid Interface Sci* 2019;533:612-20. DOI PubMed
40. Zhao Q, Liu Z, Guo Z, Ruan M, Yan W. The collaborative mechanism of surface S-vacancies and piezoelectric polarization for boosting CdS photoelectrochemical performance. *Chem Eng J* 2022;433:133226. DOI
41. Ma M, Zhang K, Li P, Jung MS, Jeong MJ, Park JH. Dual Oxygen and tungsten vacancies on a WO3 Photoanode for enhanced water oxidation. *Angew Chem Int Ed Engl* 2016;55:11819-23. DOI PubMed
42. Fernández-climent R, Giménez S, García-tecedor M. The role of oxygen vacancies in water splitting photoanodes. *Sustain Energy Fuels* 2020;4:5916-26. DOI
43. Xu W, Tian W, Meng L, Cao F, Li L. Interfacial chemical bond-modulated z-scheme charge transfer for efficient photoelectrochemical water splitting. *Adv Energy Mater* 2021;11:2003500. DOI
44. Li J, Yuan H, Zhang W, et al. Advances in Z-scheme semiconductor photocatalysts for the photoelectrochemical applications: A review. *Carbon Energy* 2022;4:294-331. DOI
45. Mane P, Bae H, Burungale V, et al. Interface-engineered Z-scheme of $BiVO_4$/g-C_3N_4 photoanode for boosted photoelectrochemical water splitting and organic contaminant elimination under solar light. *Chemosphere* 2022;308:136166. DOI PubMed
46. Maity D, Karmakar K, Pal D, Saha S, Khan GG, Mandal K. One-dimensional p-$ZnCo_2O_4$/n-ZnO nanoheterojunction photoanode enabling photoelectrochemical water splitting. *ACS Appl Energy Mater* 2021;4:11599-608. DOI
47. Ho W, Chen J, Wu J. Epitaxial, energetic, and morphological synergy on photocharge collection of the Fe_2TiO_5/ZnO nanodendrite heterojunction array photoelectrode for photoelectrochemical water oxidation. *ACS Sustain Chem Eng* 2021;9:8868-78. DOI
48. Hao J, Zhuang Z, Cao K, et al. Unraveling the electronegativity-dominated intermediate adsorption on high-entropy alloy electrocatalysts. *Nat Commun* 2022;13:2662. DOI PubMed PMC
49. Dong G, Hu H, Huang X, Zhang Y, Bi Y. Rapid activation of Co_3O_4 cocatalysts with oxygen vacancies on TiO_2 photoanodes for efficient water splitting. *J Mater Chem A* 2018;6:21003-9. DOI
50. Cao X, Wang Y, Lin J, Ding Y. Ultrathin CoO_x nanolayers derived from polyoxometalate for enhanced photoelectrochemical performance of hematite photoanodes. *J Mater Chem A* 2019;7:6294-303. DOI
51. Li H, Yin M, Li X, Mo R. Enhanced photoelectrochemical water oxidation performance in bilayer TiO_2/α-Fe_2O_3 Nanorod Arrays Photoanode with Cu:NiO_x as hole transport layer and Co-Pi as Cocatalyst. *ChemSusChem* 2021;14:2331-40. DOI
52. Wei J, Zhou C, Xin Y, Li X, Zhao L, Liu Z. Cooperation effect of heterojunction and co-catalyst in $BiVO_4$/Bi_2S_3/NiOOH photoanode for improving photoelectrochemical performances. *New J Chem* 2018;42:19415-22. DOI
53. Zhang B, Huang X, Hu H, Chou L, Bi Y. Defect-rich and ultrathin CoOOH nanolayers as highly efficient oxygen evolution catalysts for photoelectrochemical water splitting. *J Mater Chem A* 2019;7:4415-9. DOI
54. Wang T, Long X, Wei S, et al. Boosting hole transfer in the fluorine-doped hematite photoanode by depositing ultrathin amorphous FeOOH/CoOOH Cocatalysts. *ACS Appl Mater Interfaces* 2020;12:49705-12. DOI PubMed
55. Vo T, Tai Y, Chiang C. Novel hierarchical ferric phosphate/bismuth vanadate nanocactus for highly efficient and stable solar water splitting. *Appl Catalysis B Environ* 2019;243:657-66. DOI
56. Klahr B, Gimenez S, Fabregat-Santiago F, Bisquert J, Hamann TW. Photoelectrochemical and impedance spectroscopic investigation of water oxidation with "Co-Pi"-coated hematite electrodes. *J Am Chem Soc* 2012;134:16693-700. DOI PubMed
57. Li M, Liu T, Yang Y, et al. Zipping Up NiFe(OH)x-encapsulated hematite to achieve an ultralow turn-on potential for water oxidation. *ACS Energy Lett* 2019;4:1983-90. DOI
58. Zhang K, Liu J, Wang L, et al. Near-complete suppression of oxygen evolution for photoelectrochemical H_2O oxidative H_2O_2 synthesis. *J Am Chem Soc* 2020;142:8641-8. DOI PubMed
59. Liu Z, Du Y, Zhang P, Zhuang Z, Wang D. Bringing catalytic order out of chaos with nitrogen-doped ordered mesoporous carbon. *Matter* 2021;4:3161-94. DOI
60. Kaplan A, Yuan Z, Benck JD, et al. Current and future directions in electron transfer chemistry of graphene. *Chem Soc Rev* 2017;46:4530-71. DOI PubMed
61. Rai S, Ikram A, Sahai S, Dass S, Shrivastav R, Satsangi VR. CNT based photoelectrodes for PEC generation of hydrogen: a review. *Inter J Hydrog Energy* 2017;42:3994-4006. DOI
62. Kang Z, Lee ST. Carbon dots: advances in nanocarbon applications. *Nanoscale* 2019;11:19214-24. DOI PubMed
63. Ali M, Pervaiz E, Sikandar U, Khan Y. A review on the recent developments in zirconium and carbon-based catalysts for photoelectrochemical water-splitting. *Inter J Hydrog Energy* 2021;46:18257-83. DOI
64. Zhao Z, Zheng L, Hu W, Zheng H. Synergistic effect of silane and graphene oxide for enhancing the photoelectrochemical water oxidation performance of WO3NS arrays. *Electrochimica Acta* 2018;292:322-30. DOI
65. Đorđević L, Arcudi F, Cacioppo M, Prato M. A multifunctional chemical toolbox to engineer carbon dots for biomedical and energy applications. *Nat Nanotechnol* 2022;17:112-30. DOI PubMed
66. Zhai Y, Zhang B, Shi R, et al. Carbon dots as new building blocks for electrochemical energy storage and electrocatalysis. *Advan Energy Mater* 2022;12:2103426. DOI
67. Liang Q, Yan X, Li Z, et al. Replacing Ru complex with carbon dots over MOF-derived Co_3O_4/In_2O_3 catalyst for efficient solar-

driven CO_2 reduction. *J Mater Chem A* 2022;10:4279-87. DOI

68. Li F, Liu Y, Chen Q, et al. Transient photovoltage study of the kinetics and synergy of electron/hole co-extraction in MoS2/Ag-In-Zn-S/carbon dot photocatalysts for promoted hydrogen production. *Chem Eng J* 2022;439:135759. DOI
69. Ye K, Wang Z, Gu J, et al. Carbon quantum dots as a visible light sensitizer to significantly increase the solar water splitting performance of bismuth vanadate photoanodes. *Energy Environ Sci* 2017;10:772-9. DOI
70. Wang Y, Godin R, Durrant JR, Tang J. Efficient Hole trapping in carbon dot/oxygen-modified carbon nitride heterojunction photocatalysts for enhanced methanol production from CO_2 under neutral conditions. *Angew Chem Int Ed Engl* 2021;60:20811-6. DOI PubMed PMC
71. Wang Y, Liu X, Han X, et al. Unique hole-accepting carbon-dots promoting selective carbon dioxide reduction nearly 100% to methanol by pure water. *Nat Commun* 2020;11:2531. DOI PubMed PMC
72. Zhou T, Chen S, Wang J, et al. Dramatically enhanced solar-driven water splitting of BiVO4 photoanode via strengthening hole transfer and light harvesting by co-modification of CQDs and ultrathin β-FeOOH layers. *Chem Eng J* 2021;403:126350. DOI
73. Choi Y, Bae S, Kim B, Ryu J. Atomically-dispersed cobalt ions on polyphenol-derived nanocarbon layers to improve charge separation, hole storage, and catalytic activity of water-oxidation photoanodes. *J Mater Chem A* 2021;9:13874-82. DOI
74. Rombach FM, Haque SA, Macdonald TJ. Lessons learned from spiro-OMeTAD and PTAA in perovskite solar cells. *Energy Environ Sci* 2021;14:5161-90. DOI
75. Gao B, Wang T, Li Y, et al. Boosting the stability and photoelectrochemical activity of a $BiVO_4$ photoanode through a bifunctional polymer coating. *J Mater Chem A* 2021;9:3309-13. DOI
76. Gu X, Chen Z, Li Y, et al. Polyaniline/carbon dots composite as a highly efficient metal-free dual-functional photoassisted electrocatalyst for overall water splitting. *ACS Appl Mater Interfaces* 2021;13:24814-23. DOI PubMed
77. Li F, Liu Y, Mao B, et al. Carbon-dots-mediated highly efficient hole transfer in I-III-VI quantum dots for photocatalytic hydrogen production. *Appl Catalysis B Environ* 2021;292:120154. DOI
78. Liu Y, Zhou X, Shen C, et al. Hydrogen-bonding-assisted charge transfer: significantly enhanced photocatalytic H_2 evolution over g-C_3N_4 anchored with ferrocene-based hole relay. *Catal Sci Technol* 2018;8:2853-9. DOI
79. Olshansky JH, Balan AD, Ding TX, Fu X, Lee YV, Alivisatos AP. Temperature-dependent hole transfer from photoexcited quantum dots to molecular species: evidence for trap-mediated transfer. *ACS Nano* 2017;11:8346-55. DOI PubMed
80. Niu F, Zhou Q, Liu R, Hu K. Photoinduced hole hopping across CdS quantum dot surfaces for photoelectrochemical water oxidation. *ACS Appl Energy Mater* 2022;5:1244-51. DOI
81. Niu F, Zhou Q, Han Y, et al. Rapid hole extraction based on cascade band alignment boosts photoelectrochemical water oxidation efficiency. *ACS Catal* 2022;12:10028-38. DOI
82. Wu K, Du Y, Tang H, Chen Z, Lian T. Efficient extraction of trapped holes from colloidal CdS nanorods. *J Am Chem Soc* 2015;137:10224-30. DOI PubMed
83. Li XB, Liu B, Wen M, et al. Hole-accepting-ligand-modified CdSe QDs for dramatic enhancement of photocatalytic and photoelectrochemical hydrogen evolution by solar energy. *Adv Sci* 2016;3:1500282. DOI PubMed PMC
84. Forster M, Cheung DWF, Gardner AM, Cowan AJ. Potential and pitfalls: on the use of transient absorption spectroscopy for in situ and operando studies of photoelectrodes. *J Chem Phys* 2020;153:150901. DOI PubMed
85. Tamaki Y, Furube A, Murai M, Hara K, Katoh R, Tachiya M. Dynamics of efficient electron-hole separation in TiO_2 nanoparticles revealed by femtosecond transient absorption spectroscopy under the weak-excitation condition. *Phys Chem Chem Phys* 2007;9:1453-60. DOI PubMed
86. Lian Z, Sakamoto M, Kobayashi Y, et al. Anomalous photoinduced hole transport in type I core/mesoporous-shell nanocrystals for efficient photocatalytic H_2 evolution. *ACS Nano* 2019;13:8356-63. DOI PubMed
87. Andrews JL, Cho J, Wangoh L, et al. Hole extraction by design in photocatalytic architectures interfacing CdSe quantum dots with topochemically stabilized tin vanadium oxide. *J Am Chem Soc* 2018;140:17163-74. DOI PubMed
88. Taheri MM, Elbert KC, Yang S, et al. Distinguishing electron and hole dynamics in functionalized CdSe/CdS core/shell quantum dots using complementary ultrafast spectroscopies and kinetic modeling. *J Phys Chem C* 2021;125:31-41. DOI
89. Yu S, Fan XB, Wang X, et al. Efficient photocatalytic hydrogen evolution with ligand engineered all-inorganic InP and InP/ZnS colloidal quantum dots. *Nat Commun* 2018;9:4009. DOI PubMed PMC
90. Fan XB, Yu S, Wang X, et al. Susceptible surface sulfide regulates catalytic activity of CdSe quantum dots for hydrogen photogeneration. *Adv Mater* 2019;31:e1804872. DOI PubMed
91. Bredar ARC, Chown AL, Burton AR, Farnum BH. Electrochemical impedance spectroscopy of metal oxide electrodes for energy applications. *ACS Appl Energy Mater* 2020;3:66-98. DOI
92. Gimenez S, Dunn HK, Rodenas P, et al. Carrier density and interfacial kinetics of mesoporous TiO2 in aqueous electrolyte determined by impedance spectroscopy. *J Electroanal Chem* 2012;668:119-25. DOI
93. Cui J, Daboczi M, Regue M, et al. 2D bismuthene as a functional interlayer between $BiVO_4$ and NiFeOOH for enhanced oxygen-evolution photoanodes. *Adv Funct Mater* 2022:2207136-48. DOI
94. Abbas MA, Bang JH. Anomalous transition of hole transfer pathways in gold nanocluster-sensitized TiO_2 photoelectrodes. *ACS Energy Lett* 2020;5:3718-24. DOI
95. Kolay A, Kokal RK, Kalluri A, et al. New antimony selenide/nickel oxide photocathode boosts the efficiency of graphene quantum-dot co-sensitized solar cells. *ACS Appl Mater Interfaces* 2017;9:34915-26. DOI PubMed

96. Wijayantha KG, Saremi-Yarahmadi S, Peter LM. Kinetics of oxygen evolution at α-Fe2O3 photoanodes: a study by photoelectrochemical impedance spectroscopy. *Phys Chem Chem Phys* 2011;13:5264-70. DOI PubMed
97. Cummings CY, Marken F, Peter LM, Wijayantha KG, Tahir AA. New insights into water splitting at mesoporous α-Fe_2O_3 films: a study by modulated transmittance and impedance spectroscopies. *J Am Chem Soc* 2012;134:1228-34. DOI PubMed
98. Peter LM, Wong LH, Abdi FF. Revealing the influence of doping and surface treatment on the surface carrier dynamics in hematite nanorod photoanodes. *ACS Appl Mater Interfaces* 2017;9:41265-72. DOI PubMed
99. Zheng H, Lu Y, Ye KH, et al. Atomically thin photoanode of InSe/graphene heterostructure. *Nat Commun* 2021;12:91. DOI PubMed PMC
100. Bard AJ, Faulkner LR. Scanning electrochemical microscopy, 2nd ed.; New York: Marcel Dekker. 2001.
101. Liu N, Qin Y, Han M, et al. Investigation of regeneration kinetics of a carbon-dot-sensitized metal oxide semiconductor with scanning electrochemical microscopy. *ACS Appl Energy Mater* 2018;1:1483-8. DOI
102. Yu Z, Huang Q, Jiang X, et al. Effect of a cocatalyst on a photoanode in water splitting: a study of scanning electrochemical microscopy. *Anal Chem* 2021;93:12221-9. DOI PubMed

Zhao *et al. Microstructures* 2023;3:2023002
DOI: 10.20517/microstructures.2022.21

Microstructures

Research Article

Open Access

$BaTiO_3$-$NaNbO_3$ energy storage ceramics with an ultrafast charge-discharge rate and temperature-stable power density

Peiyao Zhao, Longtu Li, Xiaohui Wang

State Key Laboratory of New Ceramics and Fine Processing, School of Materials Science and Engineering, Tsinghua University, Beijing 100084, China.

Correspondence to: Prof. Xiaohui Wang, State Key Laboratory of New Ceramics and Fine Processing, School of Materials Science and Engineering, Tsinghua University, Beijing 100084, China. E-mail: wxh@tsinghua.edu.cn

How to cite this article: Zhao P, Li L, Wang X. $BaTiO_3$-$NaNbO_3$ energy storage ceramics with an ultrafast charge-discharge rate and temperature-stable power density. *Microstructures* 2023;3:2023002. https://dx.doi.org/10.20517/microstructures.2022.21

Received: 26 Aug 2022 **First Decision:** 28 Sep 2022 **Revised:** 11 Oct 2022 **Accepted:** 28 Oct 2022 **Published:** 5 Jan 2023

Academic Editors: Shiqing Deng, Ruzhong Zuo, Shujun Zhang **Copy Editor:** Fangling Lan **Production Editor:** Fangling Lan

Abstract

Dielectric capacitors with ultrafast charge-discharge rates are extensively used in electrical and electronic systems. To meet the growing demand for energy storage applications, researchers have devoted significant attention to dielectric ceramics with excellent energy storage properties. As a result, the awareness of the importance of the pulsed discharge behavior of dielectric ceramics and conducting characterization studies has been raised. However, the temperature stability of pulsed discharge behavior, which is significant for pulsed power applications, is still not given the necessary consideration. Here, we systematically investigate the microstructures, energy storage properties and discharge behaviors of nanograined (1-*x*)$BaTiO_3$-*x*$NaNbO_3$ ceramics prepared by a two-step sintering method. The 0.60$BaTiO_3$-0.40$NaNbO_3$ ceramics with relaxor ferroelectric characteristics possess an optimal discharge energy density of 3.07 J cm^{-3}, a high energy efficiency of 92.6%, an ultrafast discharge rate of 39 ns and a high power density of 100 MW cm^{-3}. In addition to stable energy storage properties in terms of frequency, fatigue and temperature, the 0.60$BaTiO_3$-0.40$NaNbO_3$ ceramics exhibit temperature-stable power density, thereby illustrating their significant potential for power electronics and pulsed power applications.

Keywords: $BaTiO_3$-$NaNbO_3$, energy storage properties, charge-discharge rate, temperature-stable power density

INTRODUCTION

Dielectric capacitors, as fundamental components in high-power energy storage and pulsed power systems, play an important role in many applications, including hybrid electric vehicles, portable electronics, medical devices and electromagnetic weapons, due to their high power density, ultrafast charge-discharge rates and long lifetimes[1-6]. However, most current commercial polymer dielectric capacitors and multilayer ceramic capacitors (MLCCs) possess somewhat low energy densities of < 1-2 J cm^{-3}, which results in them occupying relatively large volumes and/or weights in devices[7-10]. The development of third-generation semiconductors and the need for device miniaturization have resulted in an urgent demand for high-energy-density dielectric capacitors[1,11].

Under an applied voltage, the dielectric materials in dielectric capacitors polarize to store energy[1,12,13]. Their energy storage properties can be calculated through polarization-electric field (*P-E*) loops, namely, $W_c = \int_0^{P_{max}} E dP$, $W_d = \int_{P_r}^{P_{max}} E dP$ and $\eta = W_d/W_c$, where W_c and W_d are the charge and discharge energy density, respectively, P_{max} and P_r are the maximum and remnant polarization, respectively, and η is the energy efficiency[14-16]. Among all dielectric materials, relaxor ferroelectrics with high P_{max}, low P_r, high breakdown strength (E_b) and slim *P-E* loops have been investigated extensively for their excellent energy storage properties[17-22]. The polar nanoregions in relaxor ferroelectrics can switch rapidly under an applied electric field, which significantly reduces loss and results in high η[23-28]. In addition, the excellent fatigue and temperature stability of the pulsed discharge behavior and energy storage properties are highly desirable for dielectric capacitors operating in harsh environments, i.e., aerospace fields and oil-well drilling[29-32]. Many strategies have been utilized to enhance the temperature stability of dielectric materials in recent years, including multiscale optimization[27], composite strategy design[28], unmatched temperature range design[33] and special sintering methods[34]. However, the temperature stability of pulsed discharge behavior is not given sufficient attention in current research into dielectric materials.

In this study, we prepare nanograined (1-*x*)$BaTiO_3$-*x*$NaNbO_3$ ceramics, which possess relaxor ferroelectric characteristics with a good *P-E* relationship (high P_{max}, low P_r and slim *P-E* loops) and high E_b, using a solid-state reaction method. The 0.60$BaTiO_3$-0.40$NaNbO_3$ ceramics exhibit an optimal W_d of 3.07 J cm^{-3} and a high η of 92.6% under 38.1 MV m^{-1} at ambient temperature. Stable energy storage properties in terms of frequency (0.1-100 Hz), fatigue (10^6 cycles) and temperature (25-120 °C) are also achieved. Moreover, the ceramics possess an ultrafast discharge rate of 39 ns and a high power density of 100 MW cm^{-3}. The variation of the power density is less than 15% from 25 to 140 °C. All these results suggest that 0.60$BaTiO_3$-0.40$NaNbO_3$ ceramics are ideal candidates for energy storage applications in pulsed power systems.

MATERIALS AND METHODS

(1-*x*)$BaTiO_{3-x}NaNbO_3$ ((1-*x*)BT-*x*NN) dielectric ceramics with x = 0.35, 0.40, 0.45 and 0.50 were prepared through a conventional solid-state method. According to the stoichiometric ratio of (1-*x*)BT-*x*NN ceramics, $BaCO_3$, TiO_2, Na_2CO_3 and Nb_2O_5 powders with analytical grade, as the raw materials, were weighed and ball milled with ethanol for 24 h. The mixed powders were then dried at 80 °C and calcined at 950-1030 °C for 5 h in the closed alumina crucibles to avoid the volatilization of Na. Afterward, the calcined (1-*x*)BT-*x*NN powders were ground with a polyvinyl butyraldehyde solution (PVB, 10 wt.%) and uniaxially pressed into cylinders with a diameter of 8 mm and a thickness of 0.5 mm under a pressure of 2 MPa. The cylinders were heated at 600 °C for 5 h to remove the PVB binder and then sintered with a two-step sintering method[35,36] (all samples were heated to 1250-1350 °C for 1-10 min and then cooled down to 1100-1150 °C for 3-5 h).

The ambient-temperature X-ray diffraction profiles of the (1-*x*)BT-*x*NN ceramics were obtained using a Rigaku 2500 X-ray diffractometer (Rigaku, Tokyo, Japan) with Cu Kα radiation and λ = 1.5418 Å. The surface microstructures of the ceramics after thermally etching at 1050 °C for 0.5 h were characterized using scanning electron microscopy (SEM, MERLIN VP Compact, Zeiss Ltd., Germany) at 15 kV. To measure the ferroelectric properties and pulsed discharge behaviors, the compact ceramics were polished down to 180-200 μm in thickness and then gold electrodes with a radius of 1.5 mm were sputtered on both surfaces. The *P-E* loops were measured using a TF ANALYZER 2000E ferroelectric measurement system (aixACCT Systems GmbH, Aachen, Germany) under different frequencies (0.1-100 Hz) and various temperatures (25-140 °C). The dielectric properties were measured under a frequency range of 1 kHz to 1 MHz and a temperature range of -150 to 300 °C using an impedance analyzer (E4980A, Agilent Technologies, USA). The overdamped and underdamped pulsed discharge behavior was measured using a charge-discharge platform (CFD-001, Gogo Instruments Technology, Shanghai, China) with a resistor-capacitance load circuit. More details regarding the resistor-capacitance circuit measurement system are given in Supplementary Figure 1.

RESULTS AND DISCUSSION

The ambient-temperature X-ray diffraction profiles of the (1-*x*)BT-*x*NN ceramics are displayed in Figure 1. All samples exhibit typical perovskite structures with traces of a $Ba_6Ti_7Nb_9O_{42}$ secondary phase (PDF#47-0522). The approximate amounts of $Ba_6Ti_7Nb_9O_{42}$ phases are displayed in Supplementary Table 1 and are less than 5% in all (1-*x*)BT-*x*NN ceramics. The (200) peaks between 45° and 46° without splitting suggest that all samples are mainly pseudocubic phases at room temperature. The cell parameters of (1-*x*)BT-*x*NN ceramics decrease with increasing NN content [Supplementary Table 2], which is mainly because the radius of Na^+ (1.39 Å) is smaller than that of Ba^{2+} (1.61 Å). The SEM images of the surface and cross-section microstructures of the (1-*x*)BT-*x*NN ceramics are displayed in Figure 2 and Supplementary Figure 2. There are no obvious pores in the (1-*x*)BT-*x*NN ceramics, suggesting that all samples possess high relative density. The grain size distributions [Supplementary Figure 3] are counted by the Feret diameters of more than 250 grains from the SEM images, and they show that all the ceramics possess nanograins with average grain sizes of 180-280 nm. The grain size tends to increase with NN content and the distribution moves toward larger sizes. Generally, fine grains are conducive to achieving high E_b and η. The elemental distribution results of the 0.60BT-0.40NN ceramics are shown in Supplementary Figure 4, where it can be seen that all the elements are uniformly distributed in the ceramics.

The temperature-dependent (150-300 °C) dielectric properties of the (1-*x*)BT-*x*NN ceramics were measured at various frequencies [Figure 3] and indicated prototypical relaxor ferroelectric characteristics. The dielectric constants of all the (1-*x*)BT-*x*NN ceramics at room temperature are ~1000-1200 and the $Ba_6Ti_7Nb_9O_{42}$ phases are considered to have paraelectric characteristics. Hence, the $Ba_6Ti_7Nb_9O_{42}$ phases may not significantly affect the dielectric characteristics of the ceramics. It can be found that the dielectric constant and the Curie temperature increase with increasing NN content. All the (1-*x*)BT-*x*NN ceramics exhibit low dielectric loss of less than 0.012 between -100 and 200 °C. Generally, the modified Curie-Weiss law, $1/\varepsilon - 1/\varepsilon_m = (T - T_m)^\gamma/C$, is utilized to describe the dielectric characteristics of relaxor ferroelectrics, where ε and ε_m are the dielectric constant and maximum value of ε, respectively, T and T_m are the corresponding temperatures, C is the Curie constant and γ is used to describe the degree of diffuseness. The γ value varies from one for typical ferroelectrics to two for ideal relaxor ferroelectrics[24,37]. The fitted γ values of all the ceramics are shown in Figure 4 and are between 1.686 and 1.766 at 1 MHz, thereby manifesting strong relaxation behavior. This strong relaxation behavior causes the (1-*x*)BT-*x*NN ceramics to respond rapidly under an applied electric field, resulting in high η.

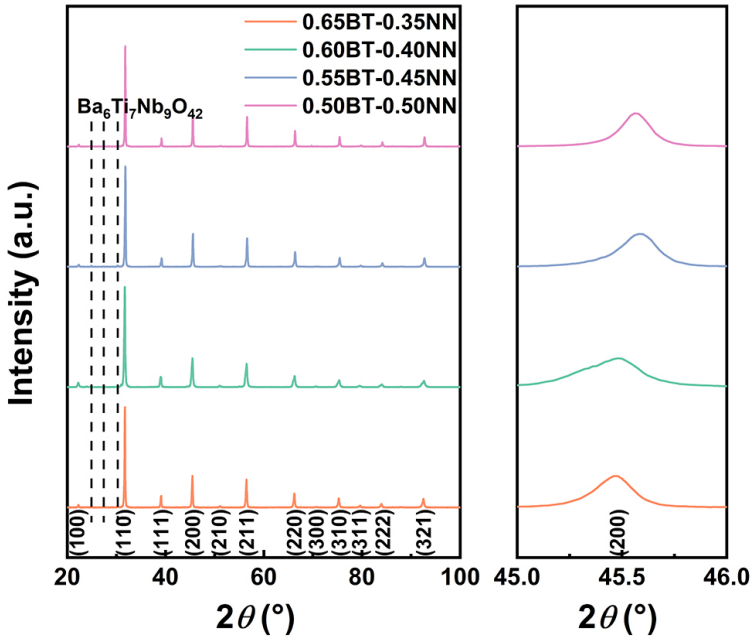

Figure 1. X-ray diffraction profiles of (1-*x*)BT-*x*NN ceramics.

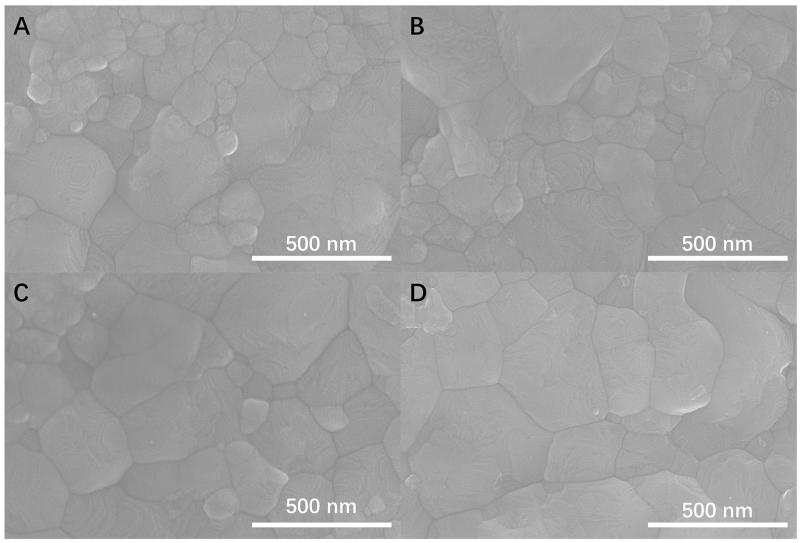

Figure 2. Surface microstructure images of (A) 0.65BT-0.35NN; (B) 0.60BT-0.40NN; (C) 0.55BT-0.45NN; and (D) 0.50BT-0.50NN.

The unipolar *P-E* loops of all ceramics measured at 25 °C and 20 MV m^{-1} are shown in Figure 5A, with all ceramics exhibiting slim *P-E* loops. Among these, the 0.55BT-0.45NN ceramics possess the largest P_{max} and P_{max} - P_r values [Figure 5B], leading to high W_d. However, due to the lower P_r, relatively larger P_{max} - P_r value and the highest E_b [Figure 5B and C], a W_d of 3.07 J cm^{-3} and a high η of 92.6% are achieved in the 0.60BT-0.40NN ceramics at 38.1 MV m^{-1}, which are the optimum energy storage properties among all the (1-*x*)BT-*x*NN ceramics at 25 °C [Figure 5D]. Figure 6 exhibits the energy storage properties as a function of the applied electric field. All BT-NN ceramics possess high E_b between 32.7 and 38.1 MV m^{-1} and high η between 87.5% and 93.0%. The corresponding current-field curves of the (1-*x*)BT-*x*NN ceramics are shown

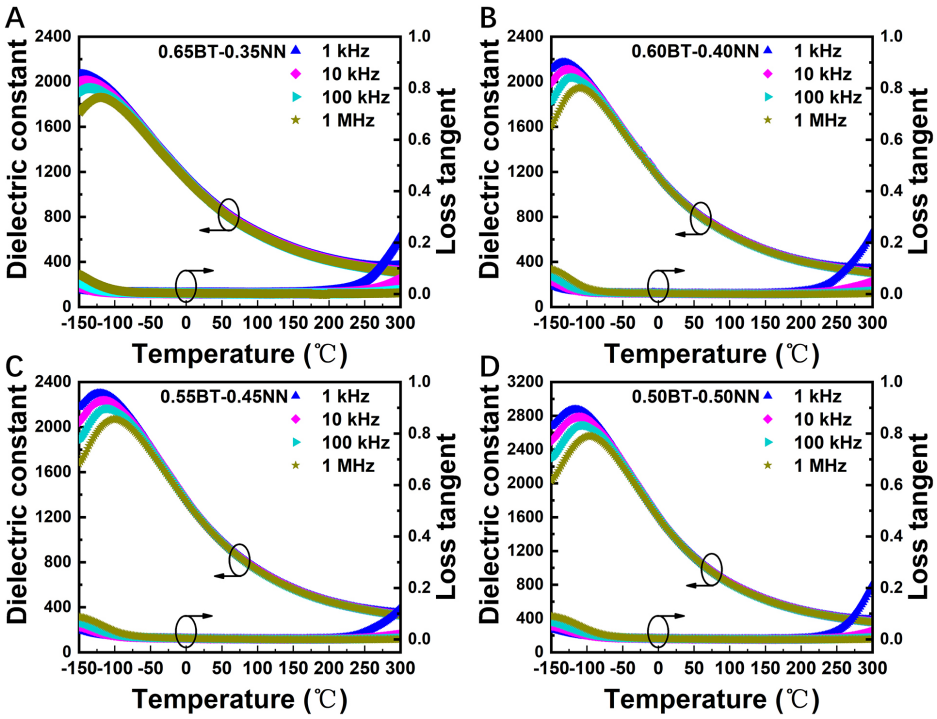

Figure 3. Temperature-dependent dielectric properties measured at 1 kHz to 1 MHz for (A) 0.65BT-0.35NN; (B) 0.60BT-0.40NN; (C) 0.55BT-0.45NN; and (D) 0.50BT-0.50NN.

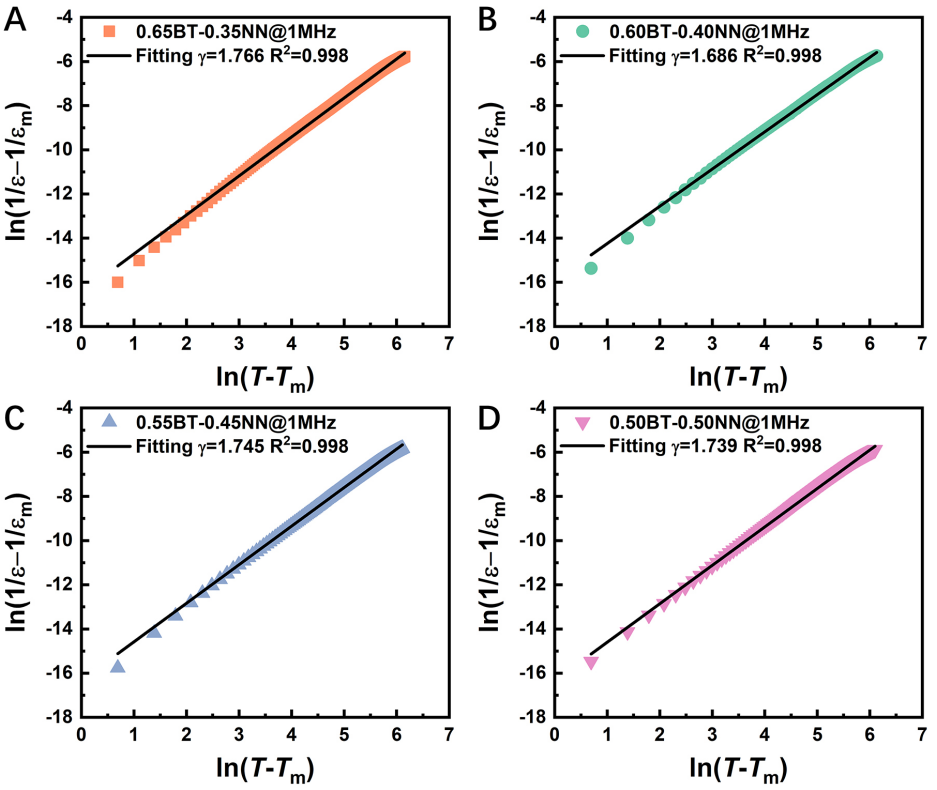

Figure 4. Fitted γ values for (A) 0.65BT-0.35NN; (B) 0.60BT-0.40NN; (C) 0.55BT-0.45NN; and (D) 0.50BT-0.50NN.

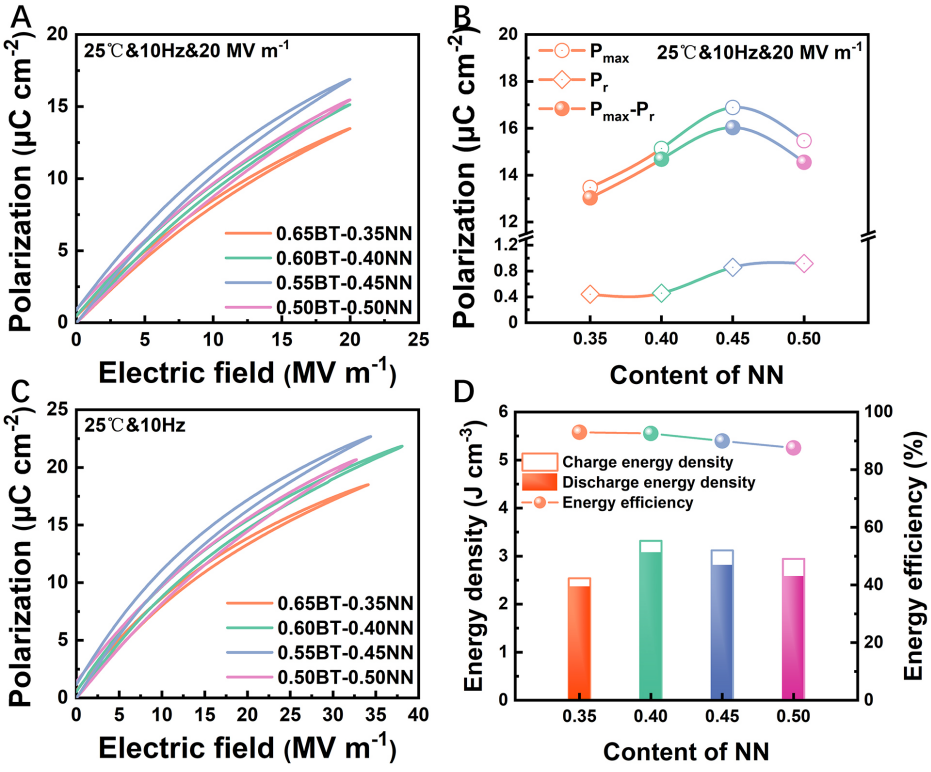

Figure 5. (A) Unipolar *P-E* loops for (1-*x*)BT-*x*NN ceramics at 25 °C, 20 MV m^{-1} and 10 Hz. (B) P_{max}, P_r and P_{max} - P_r as a function of NN content. (C) Unipolar *P-E* loops at 25 °C, maximum applied electric field and 10 Hz. (D) Energy storage properties as a function of NN content.

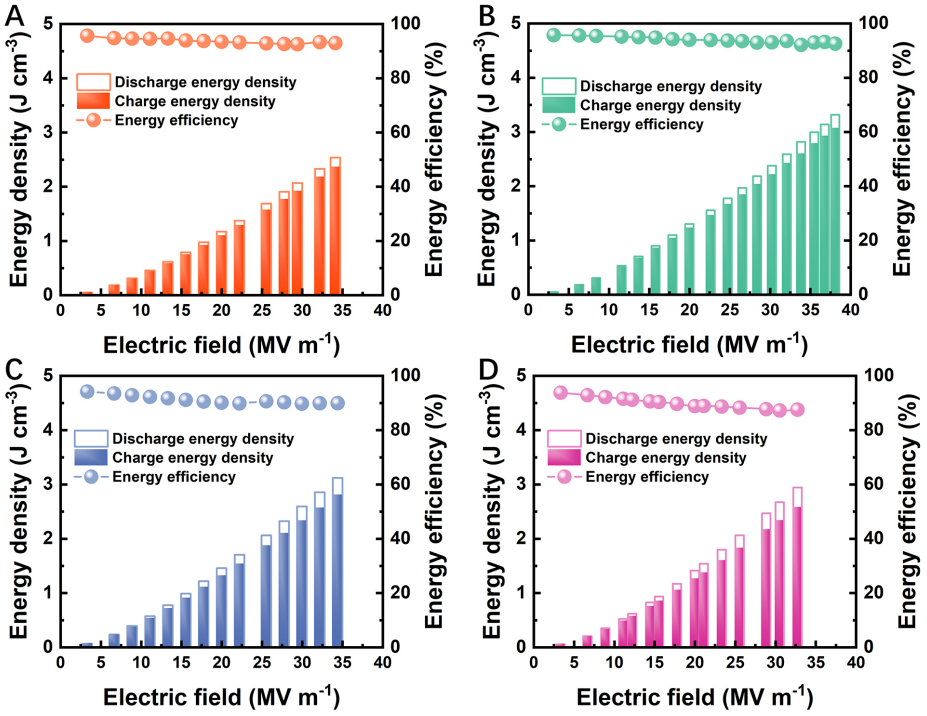

Figure 6. Energy storage properties at 25 °C and 10 Hz for (A) 0.65BT-0.35NN; (B) 0.60BT-0.40NN; (C) 0.55BT-0.45NN; and (D) 0.50BT-0.50NN.

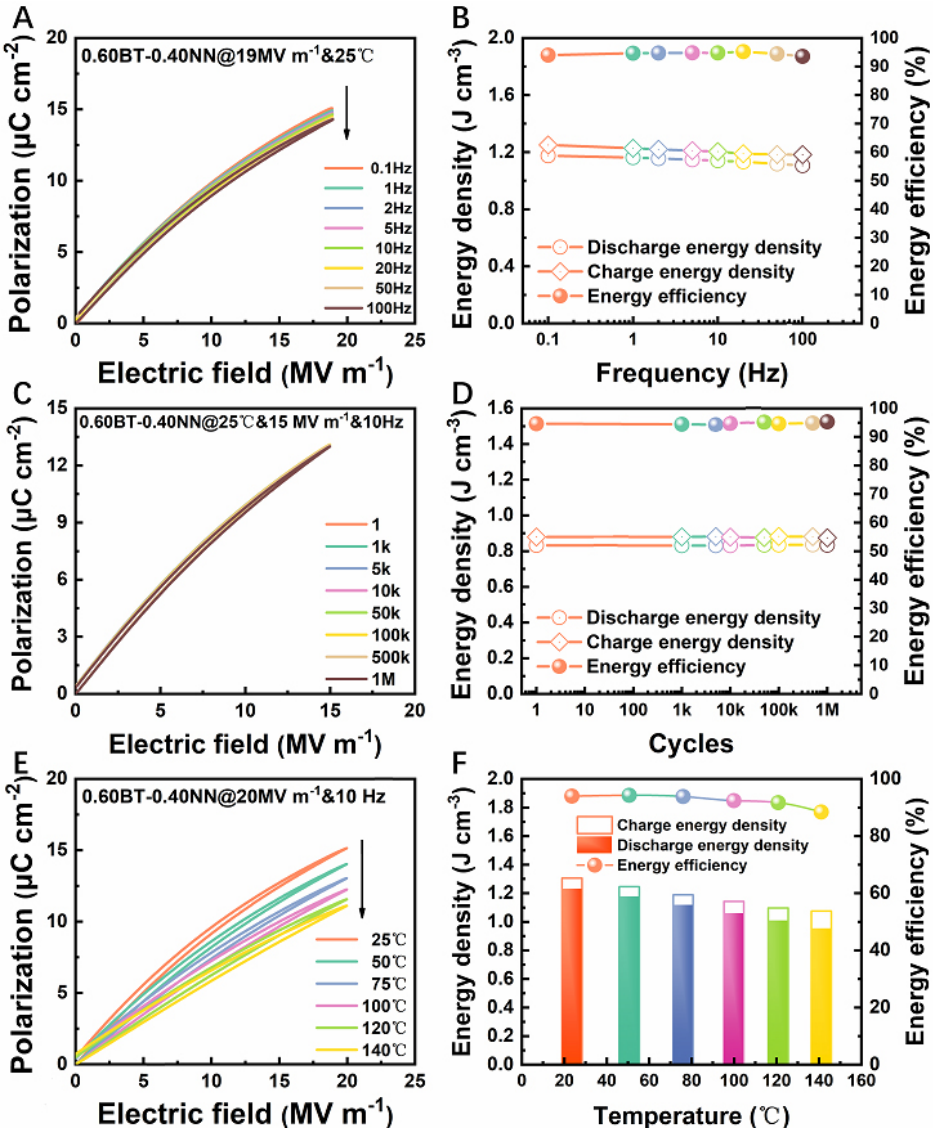

Figure 7. (A) Unipolar *P-E* loops of 0.60BT-0.40NN ceramics measured under 19 MV m^{-1} at various frequencies, (C) under 15 MV m^{-1} at different cycles and (E) under 20 MV m^{-1} at various temperatures. Corresponding (B) frequency-dependent, (D) fatigue-dependent and (F) temperature-dependent energy storage properties.

in Supplementary Figure 5, confirming the high η. Noticeably, the η of the 0.60BT-0.40NN ceramics decreases slightly with increasing E and shows a slight variation of < 4% within the whole electric field range tested, which is conducive to high η energy storage applications.

Given that the stability of the energy storage properties for dielectric materials is crucial in practical applications, the frequency, fatigue and temperature stabilities of the energy storage properties for the 0.60BT-0.40NN ceramics are characterized in Figure 7. The P_{max} of the 0.60BT-0.40NN ceramics only decreases from 15.1 to 14.3 μC cm^{-2} with increasing frequency from 0.1 to 100 Hz, while the P_r remains almost unchanged [Figure 7A]. Hence, the variations in W_d and η are less than 6.0% and 1.2%, respectively [Figure 7B]. The stable frequency-dependent energy storage properties are realized because the polar nanoregions can switch rapidly under the applied electric field[38]. To evaluate the fatigue stability, the unipolar *P-E* loops under 15 MV m^{-1} are characterized for 10^6 cycles [Figure 7C]. Fortunately, the *P-E* loops

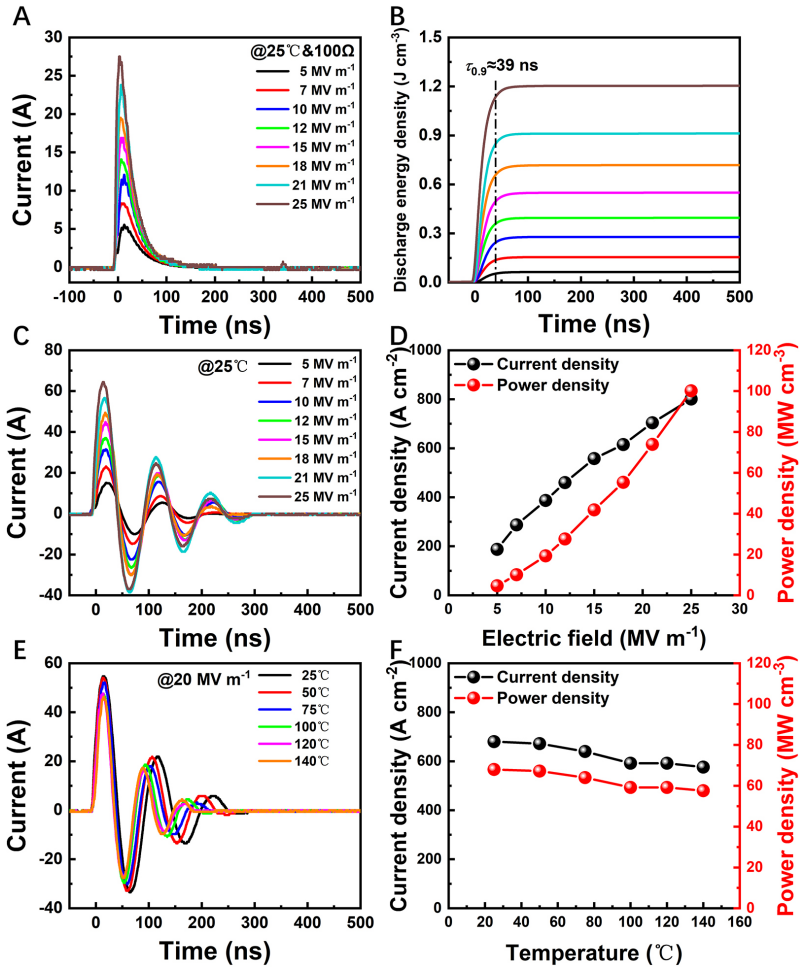

Figure 8. (A) Overdamped pulsed discharge current curves under various *E* values and (B) corresponding W_d as a function of time. Undamped pulsed discharge current curves (C) at 25 °C under various *E* values and (E) at 20 MV m^{-1} under various temperatures and (D and F) corresponding C_D and P_D values.

have no noticeable change and the variations in W_d and η are less than 0.6% and 0.7%, respectively [Figure 7D]. Figure 7E exhibits the unipolar *P-E* loops measured under 20 MV m^{-1} at various temperatures. It can be found that the P_{max} of the 0.60BT-0.40NN ceramics is consistent with the trend of the ε and gradually decreases with increasing temperature. The reduction in P_{max} results in a decrease in W_d, while the η stays over 90% when the temperature is up to 120 °C. Figure 7F shows the energy storage properties (W_d and η) of the 0.60BT-0.40NN ceramics with increasing temperature from 25 to 120 °C, revealing good temperature stability.

In practical applications, dielectric capacitors charge and discharge at the microsecond or nanosecond timescale[1]. The W_d and η calculated by the *P-E* loops cannot reflect the true energy storage properties[39], so a resistor-capacitance circuit is constructed to evaluate the discharge behavior of the 0.60BT-0.40NN ceramics. Figure 8A displays the overdamped pulsed discharge electric current-time (*I-t*) curves at various *E* values. The corresponding W_d can be calculated using $W_d = \int I(t)^2 R dt/V$, where *R* and *V* are the load resistor (here *R* = 100 Ω) and the effective volume of the sample, respectively[40]. The discharge rate is usually described by the discharge time corresponding to the 90% stored W_d value, which is abbreviated as $\tau_{0.9}$. As the *E* increases, the current peak and W_d also increase. Finally, the W_d reaches 1.21 J cm^{-3} at 25 MV m^{-1}

[Figure 8B]. In general, the W_d calculated by the *I-t* curve is always lower than that calculated by the *P-E* loop because the characterization mechanisms with different measurement frequencies[1] and dielectric material losses differ[41]. The $\tau_{0.9}$ of the 0.60BT-0.40NN ceramics is ~39 ns [Figure 8B]. The ultrafast discharge rate comes from the low hysteresis polarization response and the relaxor characteristic. This makes the 0.60BT-0.40NN ceramics more competitive in high-power applications[38,42]. Moreover, the undamped pulsed discharge current curves at 25 °C under various *E* values are displayed in Figure 8C. From the current curves, we can calculate the current density (C_D) and power density (P_D) from $C_D = I_{max}/S$ and $P_D = EI_{max}/2S$, where I_{max} and S represent the maximum value of the undamped pulsed discharge current curves and the electrode area, respectively[26]. The C_D and P_D of the 0.60BT-0.40NN ceramics at 25 MV m^{-1} are 801 A cm^{-2} and 100 MW cm^{-3}, respectively [Figure 8D]. More importantly, from the undamped pulsed discharge current curves at 20 MV m^{-1} under various temperatures [Figure 8E], it can be found that the variations of C_D and P_D are ~15% from 25 to 140 °C [Figure 8F], which suggests that the 0.60BT-0.40NN ceramics have significant potential for pulsed power system applications.

CONCLUSIONS

In summary, the 0.60BT-0.40NN ceramics with relaxor ferroelectric characteristics have an optimal W_d of 3.07 J cm^{-3}, a high η of 92.6%, a high P_D of 100 MW cm^{-3} and an ultrafast $\tau_{0.9}$ of 39 ns. Moreover, they exhibit stable energy storage properties in terms of frequency (0.1-100 Hz), fatigue (10^6 cycles) and temperature (25-120 °C), as well as temperature-stable power density (25-140 °C). These ideal energy storage properties and pulsed discharge behavior make the 0.60BT-0.40NN ceramics more promising for high-stability energy storage MLCCs in pulsed power system applications.

DECLARATIONS

Author's contributions

Sample fabrication and characterization: Zhao P
Data analysis and interpretation: Li L, Wang X
Preparation of the manuscript and discussion: Zhao P, Li L, Wang X

Availability of data and materials

Data can be deposited into data repositories or published as supplementary information in the journal.

Financial support and sponsorship

This work was supported by Shuimu Tsinghua Scholar Program, Key-Area Research and Development Program of Guandong Province (No. 2019B090912003), National Natural Science Foundation of China (No. 52032005), High-end MLCC Key Project Supported by Guangdong Fenghua Advanced Technology Holding Co., Ltd.

Conflicts of interest

All authors declared that there are no conflicts of interest.

Ethical approval and consent to participate

Not applicable.

Consent for publication

Not applicable.

REFERENCES

1. Zhao P, Cai Z, Wu L, et al. Perspectives and challenges for lead-free energy-storage multilayer ceramic capacitors. *J Adv Ceram* 2021;10:1153-93. DOI
2. Wang G, Lu Z, Li Y, et al. Electroceramics for high-energy density capacitors: current status and future perspectives. *Chem Rev* 2021;121:6124-72. DOI PubMed PMC
3. Palneedi H, Peddigari M, Hwang G-T, Jeong D-Y, Ryu J. High-performance dielectric ceramic films for energy storage capacitors: progress and outlook. *Adv Funct Mater* 2018;28:1803665. DOI
4. Li Q, Chen L, Gadinski MR, et al. Flexible high-temperature dielectric materials from polymer nanocomposites. *Nature* 2015;523:576-9. DOI PubMed
5. Whittingham MS. Materials challenges facing electrical energy storage. *MRS Bull* 2008;33:411-9. DOI
6. Li J, Shen Z, Chen X, et al. Grain-orientation-engineered multilayer ceramic capacitors for energy storage applications. *Nat Mater* 2020;19:999-1005. DOI PubMed
7. Xu R, Feng Y, Wei X, Xu Z. Analysis on nonlinearity of antiferroelectric multilayer ceramic capacitor (MLCC) for energy storage. *IEEE Trans Dielect Electr Insul* 2019;26:2005-11. DOI
8. Love GR. Energy storage in ceramic dielectrics. *J Am Ceram Soc* 1990;73:323-8. DOI
9. Jow TR, MacDougall FW, Ennis JB, et al. Pulsed power capacitor development and outlook. In 2015 IEEE Pulsed Power Conference (PPC); 2015, pp. 1-7. DOI
10. Wang Y, Zhou X, Chen Q, Chu BJ, Zhang QM. Recent development of high energy density polymers for dielectric capacitors. *IEEE Trans Dielect Electr Insul* 2010;17:1036-42. DOI
11. Kim J, Saremi S, Acharya M, et al. Ultrahigh capacitive energy density in ion-bombarded relaxor ferroelectric films. *Science* 2020;369:81-4. DOI PubMed
12. Liu Z, Lu T, Ye J, et al. Antiferroelectrics for energy storage applications: a review. *Adv Mater Technol* 2018;3:1800111. DOI
13. Hong K, Lee TH, Suh JM, Yoon S-H, Jang HW. Perspectives and challenges in multilayer ceramic capacitors for next generation electronics. *J Mater Chem C* 2019;7:9782-802. DOI
14. Li F, Zhai J, Shen B, Zeng H. Recent progress of ecofriendly perovskite-type dielectric ceramics for energy storage applications. *J Adv Dielect* 2019;8:1830005. DOI
15. Zhang H, Wei T, Zhang Q, et al. A review on the development of lead-free ferroelectric energy-storage ceramics and multilayer capacitors. *J Mater Chem C* 2020;8:16648-67. DOI
16. Yao Z, Song Z, Hao H, et al. Homogeneous/inhomogeneous-structured dielectrics and their energy-storage performances. *Adv Mater* 2017;29:1601727. DOI PubMed
17. Ogihara H, Randall CA, Trolier-McKinstry S. High-energy density capacitors utilizing $0.7BaTiO_3$-$0.3BiScO_3$ ceramics. *J Am Ceram Soc* 2009;92:1719-24. DOI
18. Wang Z, Kang R, Liu W, et al. $(Bi_{0.5}Na_{0.5})TiO_3$-based relaxor ferroelectrics with medium permittivity featuring enhanced energy-storage density and excellent thermal stability. *Chem Eng J* 2022:427. DOI
19. Yang L, Kong X, Cheng Z, Zhang S. Ultra-high energy storage performance with mitigated polarization saturation in lead-free relaxors. *J Mater Chem A* 2019;7:8573-80. DOI
20. Yang L, Kong X, Cheng Z, Zhang S. Enhanced energy density and electric cycling reliability via MnO_2 modification in sodium niobate-based relaxor dielectric capacitors. *J Mater Res* ;2021, 36:1214-1222. DOI
21. Wang X, Huan Y, Zhao P, et al. Optimizing the grain size and grain boundary morphology of $(K,Na)NbO_3$-based ceramics: Paving the way for ultrahigh energy storage capacitors. *J Mater* 2021;7:780-9. DOI
22. Zhao P, Wang H, Wu L, et al. High-performance relaxor ferroelectric materials for energy storage applications. *Adv Energy Mater* 2019;9:1803048. DOI
23. Pan H, Li F, Liu Y, et al. Ultrahigh-energy density lead-free dielectric films via polymorphic nanodomain design. *Science* 2019;365:578-82. DOI PubMed
24. Yuan Q, Li G, Yao F-Z, et al. Simultaneously achieved temperature-insensitive high energy density and efficiency in domain engineered $BaTiO_3$-$Bi(Mg_{0.5}Zr_{0.5})O_3$ lead-free relaxor ferroelectrics. *Nano Energy* 2018;52:203-10. DOI
25. Wu L, Wang X, Li L. Lead-free $BaTiO_3$-$Bi(Zn_{2/3}Nb_{1/3})O_3$ weakly coupled relaxor ferroelectric materials for energy storage. *RSC Adv* 2016;6:14273-82. DOI
26. Zhou M, Liang R, Zhou Z, Dong X. Superior energy storage properties and excellent stability of novel $NaNbO_3$-based lead-free ceramics with A-site vacancy obtained via a Bi_2O_3 substitution strategy. *J Mater Chem A* 2018;6:17896-904. DOI
27. Zhao P, Cai Z, Chen L, et al. Ultra-high energy storage performance in lead-free multilayer ceramic capacitors via a multiscale optimization strategy. *Energy Environ Sci* 2020;13:4882-90. DOI
28. Zhao P, Chen L, Li L, Wang X. Ultrahigh energy density with excellent thermal stability in lead-free multilayer ceramic capacitors via composite strategy design. *J Mater Chem A* 2021;9:25914-21. DOI
29. Chen L, Wang H, Zhao P, et al. Effect of MnO_2 on the dielectric properties of Nb-doped $BaTiO_3$-$(Bi_{0.5}Na_{0.5})TiO_3$ ceramics for X9R

MLCC applications. *J Am Ceram Soc* 2018;102:2781-90. DOI

30. Hui K, Chen L, Cen Z, et al. KNN based high dielectric constant X9R ceramics with fine grain structure and energy storage ability. *J Am Ceram Soc* 2021;104:5815-25. DOI
31. Li T, Qiao Z, Zuo R. X9R-type $Ag_{1-3x}Bi_xNbO_3$ based lead-free dielectric ceramic capacitors with excellent energy-storage properties. *Ceram Int* 2022;48:2533-7. DOI
32. Zhu C, Cai Z, Luo B, et al. High temperature lead-free BNT-based ceramics with stable energy storage and dielectric properties. *J Mater Chem A* 2020;8:683-92. DOI
33. Yang Z, Du H, Jin L, et al. Realizing high comprehensive energy storage performance in lead-free bulk ceramics via designing an unmatched temperature range. *J Mater Chem A* 2019;7:27256-66. DOI
34. Cai Z, Zhu C, Wang H, et al. High-temperature lead-free multilayer ceramic capacitors with ultrahigh energy density and efficiency fabricated via two-step sintering. *J Mater Chem A* 2019;7:14575-82. DOI
35. Chen I-W, XH W. Sintering dense nanocrystalline ceramics without final-stage grain growth. *Nature* 2000;404:168. DOI PubMed
36. Wang XH, Deng X-Y, Bai H-L, et al. Two-step sintering of ceramics with constant grain-size, II: $BaTiO_3$ and Ni-Cu-Zn ferrite. *J Am Ceram Soc* 2006;89:438-43. DOI
37. Shen Z, Wang X, Luo B, Li L. $BaTiO_3$-$BiYbO_3$ perovskite materials for energy storage applications. *J Mater Chem A* 2015;3:18146-53. DOI
38. Zhu C, Cai Z, Guo L, et al. Simultaneously achieved ultrastable dielectric and energy storage properties in lead-free $Bi_{0.5}Na_{0.5}TiO_3$-based ceramics. *ACS Appl Energy Mater* 2022;5:1560-70. DOI
39. Yang L, Kong X, Li F, et al. Perovskite lead-free dielectrics for energy storage applications. *Prog Mater Sci* 2019;102:72-108. DOI
40. Hao X. A review on the dielectric materials for high energy-storage application. *J Adv Dielectr* 2013;03:1330001. DOI
41. Li J, Li F, Xu Z, Zhang S. Multilayer lead-free ceramic capacitors with ultrahigh energy density and efficiency. *Adv Mater* 2018;30:1802155. DOI PubMed
42. Yang D, Gao J, Shu L, et al. Lead-free antiferroelectric niobates $AgNbO_3$ and $NaNbO_3$ for energy storage applications. *J Mater Chem A* 2020;8:23724-37. DOI

Zhang. *Microstructures* 2023;3:2023003
DOI: 10.20517/microstructures.2022.38

Microstructures

Commentary

Open Access

High entropy design: a new pathway to promote the piezoelectricity and dielectric energy storage in perovskite oxides

Shujun Zhang

Institute for Superconducting and Electronic Materials, Australian Institute for Innovative Materials, University of Wollongong, Wollongong, NSW 2500, Australia.

Correspondence to: Prof. Shujun Zhang, Institute for Superconducting and Electronic Materials, Australian Institute for Innovative Materials, University of Wollongong, Wollongong, NSW 2500, Australia. E-mail: shujun@uow.edu.au

How to cite this article: Zhang S. High entropy design: a new pathway to promote the piezoelectricity and dielectric energy storage in perovskite oxides. *Microstructures* 2023;3:2023003. https://dx.doi.org/10.20517/microstructures.2022.38

Received: 2 Nov 2022 **Accepted:** 7 Nov 2022 **Published:** 6 Jan 2023

Academic Editor: Xiaozhou Liao **Copy Editor:** Fangling Lan **Production Editor:** Fangling Lan

Commentary to publications by Prof. Jun Chen, University of Science and Technology Beijing, E-mail: junchen@ustb.edu.cn (10.1038/s41467-022-30821-7; 10.1016/j.actamat.2022.118115).

Intrinsic polarization is an important property that distinguishes ferroelectric materials from others. Tuning the polarization configuration is crucial for promoting the electric performance, including the piezoelectric and dielectric properties. For example, the traditional strategy of constructing phase boundaries, including morphotropic phase boundaries (MPBs) and polymorphic phase boundaries (PPBs), is usually adopted to tune the polarization configuration with coexisting multiple ferroelectric phases to cause a more flexible polarization configuration than that of a single phase, resulting in higher ferroelectricity or piezoelectricity[1-5]. To enhance the energy storage performance of ferroelectrics, macrodomains with an ordered configuration due to long-range polarization are generally broken by tuning the polarization configuration to nanodomains or polar nanoregions (PNRs)[6-8]. These approaches, however, have limited degrees of freedom in further tuning the polarization configuration and improving electrical performance. "High entropy" is a new materials design strategy developed in the 1980s-1990s, but only recently realized in high-entropy alloys in 2004 by Yeh *et al.*[9], and was gradually extended into the fields of metal carbides and oxides[10,11]. Its excellent high-entropy effect increases the disorder of a system by forming solid solutions of multi-component elements, effectively controlling various properties benefiting from the entropy-

dominated phase stabilization, atomic disorder with lattice distortion, sluggish diffusion kinetics and property synergy from multiple components[12-16]. Recently, Chen's group proposed a high-entropy strategy to successfully promote piezoelectric and energy storage performance in perovskite oxide ceramics by tuning the polarization configuration [*Acta Mater.* 236 (2022) 118115 - high entropy piezoelectrics $Pb(Ni,Sc,In,Ti,Nb)O_3$[17]; *Nat. Commun.* 13 (2022) 3089 - high entropy dielectric $(K,Na,Li,Ba,Bi)(Nb,Sc,Hf,Zr,Ta,Sb)O_3$[18]], opening up new ideas for high-entropy piezoelectrics and high-entropy energy storage materials.

It is well known that different elements have different valence states, ionic radii, electronic configurations, electronegativity and polarizabilities. In recent studies, the high-entropy concept has been tuned to enable various elements, such as Ni^{2+}, Mg^{2+}, Sc^{3+}, Yb^{3+}, In^{3+}, Zr^{4+}, Hf^{4+}, Ti^{4+}, and Nb^{5+}, to simultaneously occupy equivalent lattice sites, such as *B*-sites, in perovskites to enhance the local polarization fluctuation as much as possible, achieving the effect of increasing entropy[17]. After introducing multiple components, as shown in Figure 1A, large-scale transition regions (green color) that are spread out over the whole area demonstrate the high flexibility of this unique polarization configuration. An almost even distribution of polarization angles (θ) over the whole range of 0-45° can be observed in the statistical results [Figure 1B], breaking the constraints of crystallographic symmetry and promoting the polarization rotation under excitation by an electric field[19]. From another perspective, the unique polarization configuration can be considered as coexisting multiple monoclinic phases with different θ values on the atomic scale, which play a bridge-like role between the polarizations of different phases[20], facilitating the flexible rotation between different phases under electric fields. Benefiting from this unique polarization configuration caused by increasing configuration entropy, an ultrahigh piezoelectric coefficient (d_{33}) of ~1210 pC/N can be achieved in the multi-component perovskite ceramics [Figure 1C].

A local diverse polarization configuration can greatly enhance the polarization response rate under electric fields, leading to high W_{rec} and efficiency η in energy storage capacitors[21]. Chen's group introduced the high-entropy concept into KNN-based ceramics and designed "local polymorphic distortion" to tune the local diverse polarization configuration with coexisting rhombohedral - orthorhombic - tetragonal - cubic (R-O-T-C) multiphase nanoclusters [Figure 1D][18]. Notably, the cations (Li^{+}, Ba^{2+}, Bi^{3+}, Sc^{3+}, Hf^{4+}, Zr^{4+}, Ta^{5+}, Sb^{5+}) introduced by the high entropy strategy take into account the substitution on *A*-sites and *B*-sites in perovskites, greatly enhancing the occupancy disorder and perturbation of the polarization. Meanwhile, the cations are also considered as additives used to tailor the phase transition temperatures T_{R-O}, T_{O-T}, and T_{T-C} to construct room-temperature R-O-T-C multiphase nanoclusters coexisting at the local scale. Compared with the dielectrics with single-phase and coexisting two-phase polarization configuration, the high-entropy sample exhibited smaller and more diverse PNRs with weak correlation embedded in the nonpolar cubic phase, providing higher η and delayed polarization saturation under electric fields. In addition, different types of oxygen octahedral distortions exist in different nanophases, which would introduce coexisting multiple randomly-distributed oxygen octahedral tilts, further breaking the local polarization order. As a result, high-entropy designed KNN-based ceramics with local polymorphic distortion achieved breakthroughs in the ultrahigh W_{rec} (≥ 10 J cm^{-3}) and ultrahigh η (≥ 90%) for lead-free ceramics for the first time [Figure 1E]. The results demonstrate that high-entropy design opens a new avenue to enhance electrical performance by tuning the polarization configuration.

The multiple components introduced by high entropy can cause significant local compositional disorder and random fields, resulting in flexible and diverse local polarization configurations in both high-entropy piezoelectrics and high-entropy energy storage dielectrics. It has to be mentioned that the various elements introduced by the high-entropy strategy endow the material with more performance control freedom and

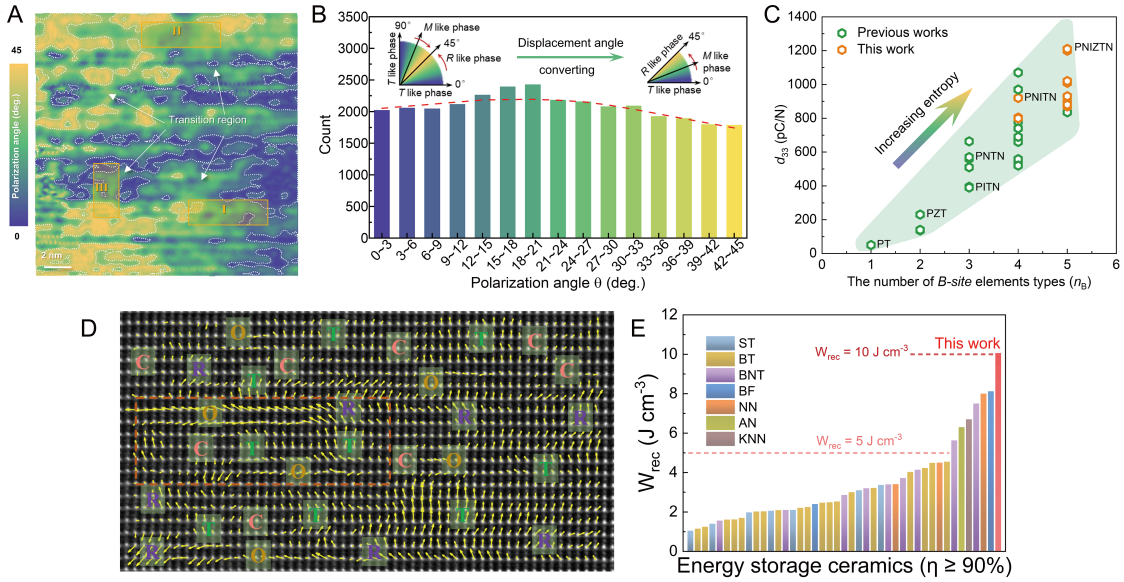

Figure 1. (A) Contour map of the distribution of polarization angles (θ). (B) Statistics of the distribution of θ in the range of 0°-45°, extracted from over 30, 000 polarization vectors. (C) Strong correlation between d_{33} and the number of *B*-site element types (n_B) for a series of PbBO_3-based solid solutions. Reproduced with permission from[17], Copyright 2022, Elsevier. (D) Atomic-resolution high-angle annular dark field - scanning transmission electron microscopy (HAADF STEM) polarization vector image along $[110]_c$. (E) Comparison of the recoverable energy storage density, W_{rec} (efficiency, $\eta \geq 90\%$), of (K,Na)NbO_3 (KNN)-based high-entropy ceramic with other representative lead-free bulk ceramics with $W_{rec} \geq 1$ J cm^{-3}. Reproduced with permission from[18], Copyright 2022, Nature Publishing Group.

control methods, rather than a single ferroelectric/piezoelectric performance improvement. We believe that high-entropy design will become an important way to enhance the electrical properties of perovskite materials, enriching the design of material components thanks to the rapid development of machine learning and materials genome engineering.

DECLARATIONS

Authors' contributions

The author contributed solely to the article.

Availability of data and materials

Not applicable.

Financial support and sponsorship

None.

Conflicts of interest

The author declared that there are no conflicts of interest.

Ethical approval and consent to participate

Not applicable.

Consent for publication

Not applicable.

REFERENCES

1. Liu W, Ren X. Large piezoelectric effect in Pb-free ceramics. *Phys Rev Lett* 2009;103:257602. DOI PubMed
2. Jaffe B, Roth RS, Marzullo S. Piezoelectric properties of lead zirconate-lead titanate solid-solution ceramics. *J Appl Phys* 1954;25:809-10. DOI
3. Tao H, Wu H, Liu Y, et al. Ultrahigh performance in lead-free piezoceramics utilizing a relaxor slush polar state with multiphase coexistence. *J Am Chem Soc* 2019;141:13987-94. DOI PubMed
4. Shrout TR, Zhang SJ. Lead-free piezoelectric ceramics: alternatives for PZT? *J Electroceram* 2007;19:113-26. DOI
5. Fu J, Zuo Z. Structural evidence for the polymorphic phase boundary in NKN based perovskites close to the rhombohedral-tetragonal phase coexistence zone. *Acta Mater* 2020;195:1903338. DOI
6. Qi H, Xie A, Tian A, Zuo R. Superior energy-storage capacitors with simultaneously giant energy density and efficiency using nanodomain engineered $BiFeO_3$-$BaTiO_3$-$NaNbO_3$ lead-free bulk ferroelectrics. *Adv Energy Mater* 2020;195:571-8. DOI
7. Chen L, Long F, Qi H, Liu H, Deng S, Chen J. Outstanding energy storage performance in high-hardness $(Bi_{0.5}K_{0.5})TiO_3$-based lead-free relaxors via multi-scale synergistic design. *Adv Funct Mater* 2022;32:2110478. DOI
8. Li F, Zhang S, Damjanovic D, Chen L, Shrout T. Local structural heterogeneity and electromechanical responses of ferroelectrics: learning from relaxor ferroelectrics. *Adv Funct Mater* 2018;29:1801504. DOI
9. Yeh JW, Chen SK, Lin SJ, et al. Nanostructured high-entropy alloys with multiple principal elements: novel alloy design concepts and outcomes. *Adv Eng Mater* 2004;6:299-303. DOI
10. Rost CM, Sachet E, Borman T, et al. Entropy-stabilized oxides. *Nat Commun* 2015;6:8485. DOI PubMed PMC
11. Sarker P, Harrington T, Toher C, et al. High-entropy high-hardness metal carbides discovered by entropy descriptors. *Nat Commun* 2018;9:4980. DOI PubMed PMC
12. Lim X. Mixed-up metals make for stronger, tougher, stretchier alloys. *Nature* 2016;533:306-7. DOI PubMed
13. George EP, Raabe D, Ritchie RO. High-entropy alloys. *Nat Rev Mater* 2019;4:515-34. DOI
14. Oses C, Toher C, Curtarolo S. High-entropy ceramics. *Nat Rev Mater* 2020;5:295-309. DOI
15. Cantor B, Chang I, Knight P, Vincent A. Microstructural development in equiatomic multicomponent alloys. *Mater Sci Eng A* 2004;375-377:213-8. DOI
16. Yang BB, Zhang Y, Pan H, et al. High-entropy enhanced capacitive energy storage. *Nat Mater* 2022;21:1074-80. DOI PubMed
17. Liu Y, Yang J, Deng S, et al. Flexible polarization configuration in high-entropy piezoelectrics with high performance. *Acta Mater* 2022;236:118115. DOI
18. Chen L, Deng S, Liu H, Wu J, Qi H, Chen J. Giant energy-storage density with ultrahigh efficiency in lead-free relaxors via high-entropy design. *Nat Commun* 2022;13:3089. DOI PubMed PMC
19. Li F, Lin D, Chen Z, et al. Ultrahigh piezoelectricity in ferroelectric ceramics by design. *Nat Mater* 2018;17:349-54. DOI PubMed
20. Viehland D. Symmetry-adaptive ferroelectric mesostates in oriented $Pb(BI_{1/3}BII_{2/3})O_3$-$PbTiO_3$ crystals. *J Appl Phys* 2000;88:4794. DOI
21. Chen L, Wang N, Zhang Z, et al. Local diverse polarization optimized comprehensive energy storage performance in lead-free superparaelectrics. *Adv Mater* 2022;34:e2205787. DOI PubMed

Valiev. *Microstructures* 2023;3:2023004
DOI: 10.20517/microstructures.2022.25

Microstructures

Technical Note

Open Access

Check for updates

Nanostructural design of superstrong metallic materials by severe plastic deformation processing

Ruslan Z. Valiev[1,2]

[1]Ufa University of Science and Technology, Ufa 450008, Russia.
[2]Saint Petersburg State University, St. Petersburg 199034, Russia.

Correspondence to: Prof. Ruslan Z. Valiev, Ufa University of Science and Technology, 12 K. Marx Str., Ufa 450008, Russia. E-mail: ruslan.valiev@ugatu.su

How to cite this article: Valiev RZ. Nanostructural design of superstrong metallic materials by severe plastic deformation processing. *Microstructures* 2023;3:2023004. https://dx.doi.org/10.20517/microstructures.2022.25

Received: 7 Sep 2022 **First Decision:** 23 Sep 2022 **Revised:** 10 Oct 2022 **Accepted:** 2 Nov 2022 **Published:** 10 Jan 2023

Academic Editors: Daolun Chen, Yandong Wang **Copy Editor:** Fangling Lan **Production Editor:** Fangling Lan

Abstract

Ultrafine-grained (UFG) metallic materials processed by severe plastic deformation (SPD) techniques often exhibit significantly higher strengths than those calculated by the well-known Hall-Petch equation. These higher strengths result from the fact that SPD processing not only forms the UFG structure but also leads to the formation of other nanostructural features, including dislocation substructures, nanotwins and nanosized second-phase precipitations, which further contribute to the hardening. Moreover, the analysis of strengthening mechanisms in recent studies demonstrates an important contribution to the hardening due to phenomena related to the structure of grain boundaries as a non-equilibrium state and the presence of grain boundary segregations. Herein, the principles of the nanostructural design of metallic materials for superior strength using SPD processing are discussed.

Keywords: Nanostructural design, severe plastic deformation, ultrafine-grained materials, superior strength

INTRODUCTION

Although several factors determine the strength properties of pure metals and alloys, the average grain size usually plays a significant role in their mechanical properties[1,2]. In particular, the dependence of the strength of polycrystalline materials on the average grain size d is usually described by the Hall-Petch equation, according to which the yield stress σ_{YS} is depicted as follows:

$$\sigma_{YS} = \sigma_0 + k_{HP} d^{-1/2} \quad (1)$$

where σ_0 is the lattice friction stress and k_{HP} is the Hall-Petch coefficient. According to Equation (1), the strength of the material increases with decreasing average grain size.

Based on this connection, there is significant interest in achieving ultrafine-grained (UFG) structures in metallic materials with an average grain size of less than 1 μm and predominantly high-angle grain boundaries, which may be implemented by using severe plastic deformation (SPD) processing techniques[3-5].

For this purpose, at present, the most popular SPD processing techniques are equal-channel angular pressing (ECAP) and high-pressure torsion (HPT). The deformation processing of materials by SPD was the first key step that initiated comprehensive studies of the mechanical properties of bulk nanomaterials and is now the basis for their innovative applications (see reviews and books on this topic)[5-10].

The past two decades have witnessed detailed analyzes of the effect of reducing the grain size to the nanoscale on the strength of materials. Although many studies have observed an increase in strength with decreasing grain size following Equation (1), this relationship is often violated for nanosized grains (less than 100 nm). Thus, the Hall-Petch curve deviates from the linear relationship at lower stress values and its slope k_{HP} becomes negative (curve 1, Figure 1)[2]. This problem has been extensively analyzed in many experimental and theoretical studies. In addition, several recent studies have shown that UFG materials may exhibit significantly higher strengths than that predicted by the Hall-Petch relation for the range of ultrafine grains (curve 2, Figure 1)[5,6]. The nature of such superstrength may be related to the influence of various nanostructural features observed in SPD-processed metals and alloys located in the grain interior (dislocation substructures, nanosized particles of secondary phases and nanotwins) and at grain boundaries[10].

In this regard, the task herein is to analyze the nature of the superstrength of UFG materials and various strengthening mechanisms, including both the known ones related to the presence of nanoparticles and other nanostructural features and the new ones related to the influence of grain boundary structures in UFG materials.

EXPERIMENTAL OBSERVATIONS

In the last decade, a number of studies on the strength properties of various nanostructured metals and alloys, including Al alloys[11,12], steels[13,14] and titanium materials[15], have been performed in our laboratory in collaboration with colleagues from other institutions. In all cases, a significant increase in the strength of the material was observed during grain refinement by SPD techniques, with yield stress values significantly exceeding the values calculated by the Hall-Petch equation. This is illustrated in Figure 2[11] for the yield stress values of the UFG Al alloys 1570 and 7475 with grain sizes of ~100 nm, which are significantly higher than the Hall-Petch ratio calculations for closely related Al alloys with similar grain sizes.

It is important that in all these and our other works[16-19], the formation of nanoclusters and solute segregations at grain boundaries was observed along with the formation of the UFG structure. This is clearly seen, for example, when studying the SPD-processed alloys with the use of three-dimensional atom probe tomography [Figure 3][12], as well as in Figure 4, which demonstrates observations of the nanostructural features of the alloy 7075 after HPT at two different temperatures (room temperature and 200 °C)[20].

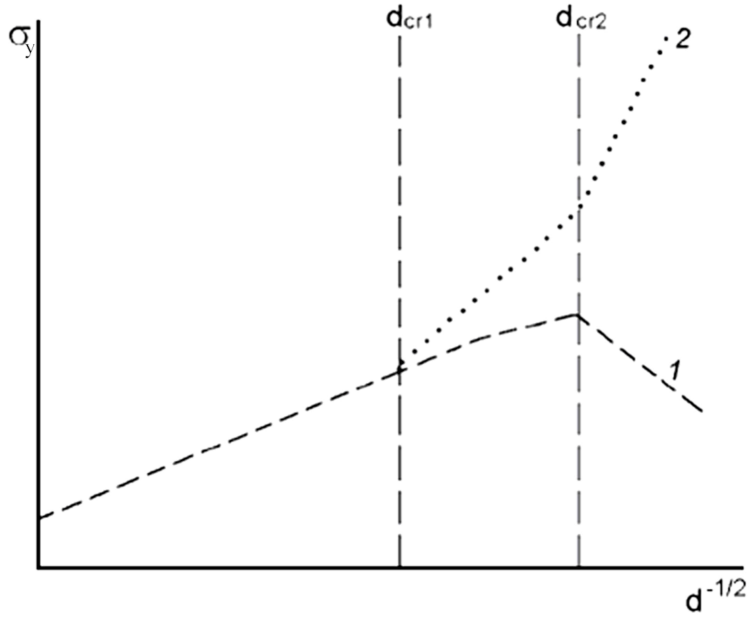

Figure 1. Two types of Hall-Petch slopes within different characteristic length scales: d_{cr1} - grain size, below which the contribution of nanostructural features (nanoparticles, substructure and others) becomes significant in the strengthening of SPD-processed materials; d_{cr2} - grain size, below which the contribution of grain boundary segregation and non-equilibrium grain boundaries becomes significant in UFG materials. Reproduced with permission, Copyright 2013, John Wiley and Sons[5].

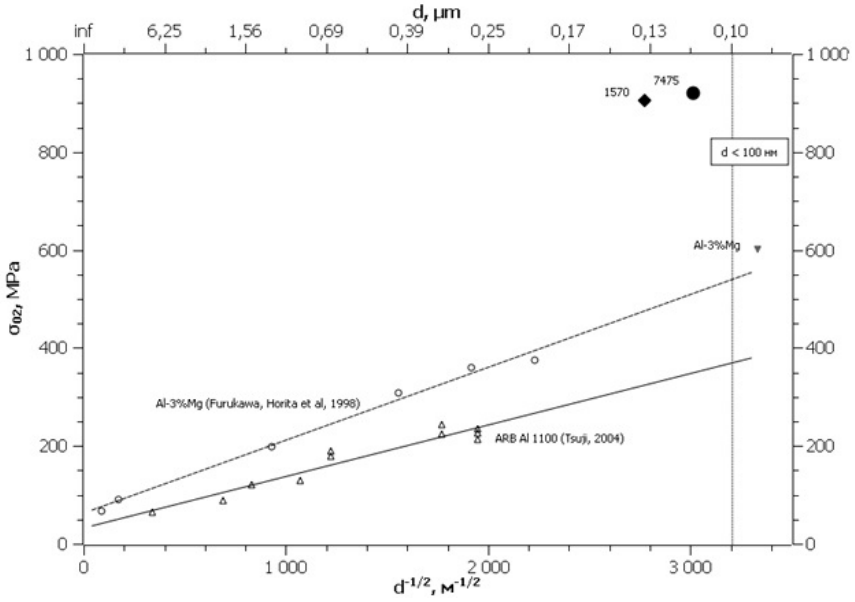

Figure 2. Hall-Petch relationships for Al 1100 and Al-3%Mg supported by the yield stress of nanostructured alloys Al-3%Mg, 1570 and 7475. Reproduced with permission, Copyright 2010, Elsevier[11].

This study pays special attention to experiments achieving a high-strength state in commercially pure (CP) Ti Grade 4 subjected to processing by ECAP and HPT. The material (composition, wt.% Fe - 0.5, O - 0.4, C - 0.08, N - 0.05, H_2 - 0.015 and Ti - base) is favored by medical professionals for its biocompatibility and is a popular material for medical applications. CP Ti is widely used for implants because its strength is crucial

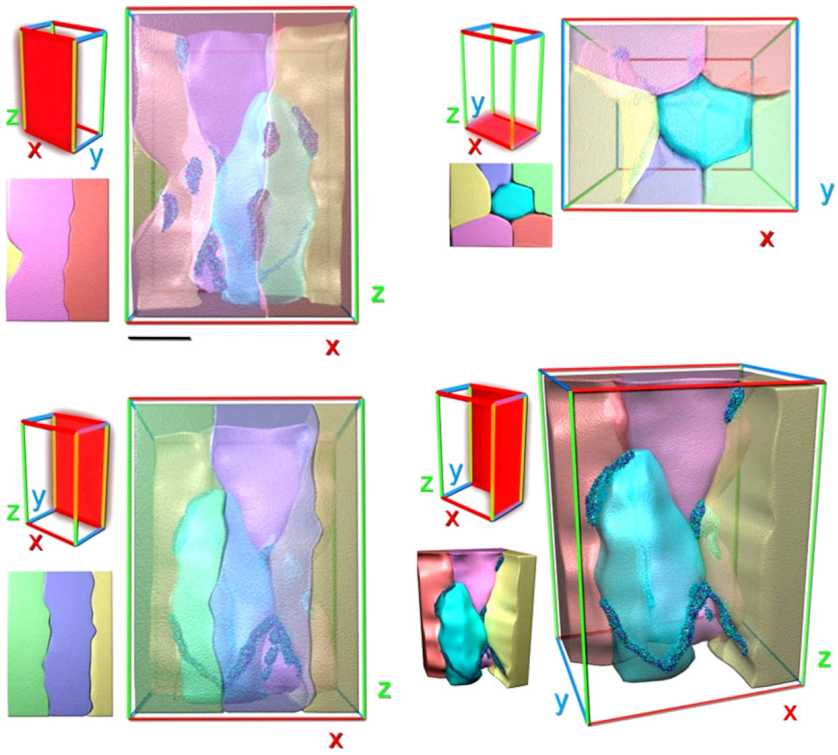

Figure 3. Tomographic view of nanostructural architecture in HPT 7075 alloy. Lineal and node solute structures are observed to occur at grain boundary interfaces and junctions. Reproduced with permission, Copyright 2010, Nature Publishing Group[12].

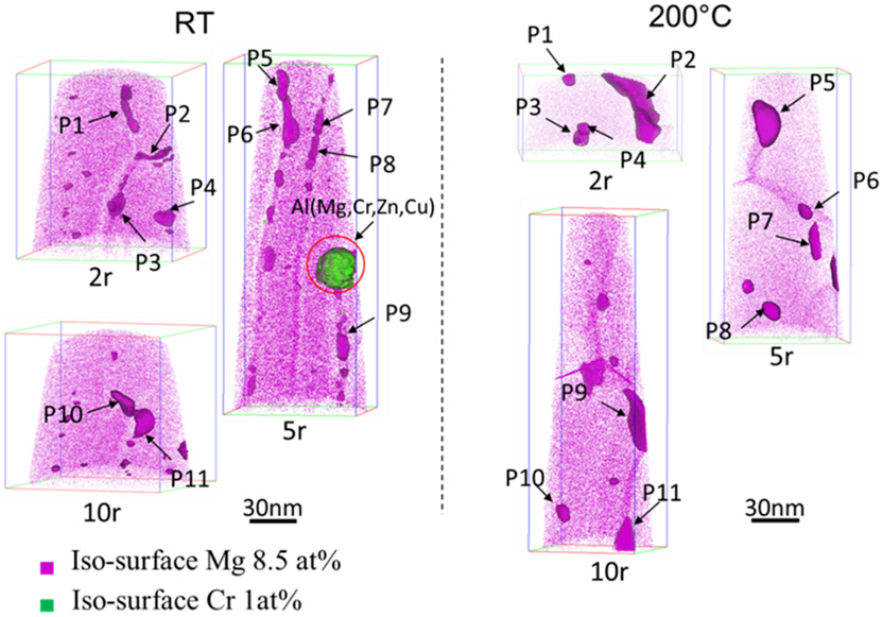

Figure 4. Three-dimensional reconstructed Mg atom maps of AA7075 samples processed by HPT in different conditions, with precipitates defined by iso-concentration surfaces at 8.5 at.% Mg (in pink) and 1.0 at.% Cr (in green). Reproduced with permission, Copyright 2018, Elsevier[20].

for manufacturing implants of improved design with increased osseointegration[21]. The details of Ti Grade 4

processing, including HPT in different regimes and annealing procedures [Table 1], are provided in our previous work[22]. Table 1 also shows the structural parameters of Ti measured by X-ray and TEM analysis after processing.

Figure 5 shows the stress-strain engineering curves of the samples during tensile tests. In the initial state, the character of the curve is typical for the materials obtained by hot rolling. After reaching the yield point, a gradual increase in stresses to maximum values is observed, followed by a decrease due to strain localization. The character of the curve changes significantly after HPT. A decrease in the uniform strain, a significant increase in the strength parameters and a decrease in ductility are observed. High-temperature annealing of the deformed state leads to the development of recrystallization and complete leveling of the hardening effect from the formation of the UFG structure and distortions of the crystal lattice. Additional HPT leads to a rapid increase in the material strength but a significant loss of ductility. However, subsequent annealing at 350 °C to relieve the stresses provides an increase in ductility while maintaining high strength. A summary of the changes in mechanical properties is presented in Table 2.

As seen from Tables 1 and 2, the structural parameters of CP Ti Grade 4 differ significantly in various states and therefore may contribute differently to the strength properties of the material.

The contributions of various microstructural parameters to the overall strength of the material are important to be calculated for establishing the basic mechanisms of hardening after the combined deformation-heat treatment of CP Ti Grade 4, as well as for understanding the nature of its superstrength state. Following Refs.[2,5,9,23], the calculation may be realized by considering the additive contribution of such strengthening mechanisms as grain boundary (σ_{gb}), dislocation (σ_{dis}), solid solution (σ_{ss}) and dispersion (σ_{Or}) strengthening to the flow stress:

$$\sigma_{total} = \sigma_0 + \sigma_{gb} + \sigma_{dis} + \sigma_{ss} + \sigma_{Or} \quad (2)$$

where $\sigma_0 \approx 80$ MPa and is the frictional stress of the crystal lattice in Ti[15,24].

Following the known relations for these strengthening mechanisms [such as grain boundary hardening (Hall-Petch strengthening), dislocation hardening, solid solution and dispersion hardening (Orowan equation)] and considering the microstructural data in Table 2, the contributions of different strengthening mechanisms to UFG Ti strength were calculated. Their comparison with experimental data from mechanical tests is provided in Table 3.

Various strengthening mechanisms contribute to the strength of UFG Ti. However, their contributions in the state with the highest strength (σ_T = 1340 MPa) are noticeably less than this value, which means that the deformation of UFG Ti in such a state may also be affected by a different strengthening mechanism. Similar conclusions have been made for other UFG metallic materials, including Al alloys[11,12] and a number of steels[13,14]. Such a strengthening mechanism may be related to the state of grain boundaries in UFG materials, their non-equilibrium structure containing grain boundary dislocations and the grain boundary segregation of alloying elements[10,25].

Recent model calculations in Ref.[26] show [Figure 6] that the formation of segregations of impurities or alloying elements at grain boundaries may significantly inhibit the dislocation nucleation at grain boundaries, thereby contributing to the additional hardening of UFG materials. Simultaneously, computer simulations[27,28] and experimental studies[11,12,14,17-19] provide convincing evidence of the formation of grain

Table 1. Structural parameters of CP Ti Grade 4 after various processing regimes

State	Average grain size, d, μm	Total dislocation density, ρ, m^{-2}	Size of second-phase particles, r, nm	Volume fraction of second-phase particles, f, %
Hot rolled	10.00 ± 2.00	≈ $2.4*10^{14}$	10^3	2-3
HPT	0.12 ± 0.03	≈ $2.1*10^{15}$	-	< 1
HPT + 700	5.00 ± 1.00	≈ $2.2*10^{14}$	35 ± 7	4-5
HPT + 700 + HPT	0.09 ± 0.03	≈ $1.6*10^{15}$	-	< 1
HPT + 700 + HPT + 350	0.12 ± 0.04	≈ $2.3*10^{14}$	18 ± 10	7-8

Table 2. Mechanical properties of Ti Grade 4 in various structural states

State	Microhardness, HV	$\sigma_{0.2}$, MPa	σ_B, MPa	ε, %
Hot rolled	237 ± 2	500	680	23.9 ± 1.4
HPT	353 ± 7	1020	1170	8.9 ± 1.2
HPT + 700	266 ± 5	600	720	30.8 ± 2.0
HPT + 700 + HPT	423 ± 8	1200	1340	0.9 ± 0.4
HPT + 700 + HPT + 350	433 ± 3	1340	1510	9.5 ± 2.0

$\sigma_{0.2}$: Yield stress; σ_B: tensile strength; ε: elongation to failure.

Table 3. Calculated contributions of various strengthening mechanisms to the strength of UFG Ti Grade 4 and experimental data on yield strength values for all analyzed states

State	σ_T, MPa	$\sigma_{T\,calc}$, MPa	σ_0, MPa	σ_{gb}, MPa	σ_{dis}, MPa	σ_{ss}, MPa	σ_{Or}, MPa	σ_{SL}, MPa
Hot rolled	500	480	80	140	150	110	0	0
HPT	1020	980		350	440		0	0
HPT+700	600	600		200	140		70	0
HPT + 700 + HPT	1200	1170		400	380		0	200
HPT + 700 + HPT + 350	1340	830		340	150		150	0

boundary segregations during the formation of UFG structures in metallic materials using SPD techniques. However, their nature and morphology are closely related to the processing regimes.

CONCLUSION

Recent studies show that the strength of UFG materials processed by SPD techniques is traditionally much higher than that predicted by the Hall-Petch relation. The physical nature of this phenomenon is related to the fact that the strength properties of UFG materials result not only from the presence of ultrafine grains but also from other nanostructural features, including the formation of subgrain dislocation structures, nanotwins, nanosized second-phase precipitations and the grain boundary structure, their non-equilibrium nature and the presence of grain boundary segregations of impurities or alloying elements. The latter factor is very important since it may contribute significantly to the strength of UFG materials. Moreover, the segregations at grain boundaries can also affect the ductility of such metals and alloys. In particular, as has recently been shown, the presence of grain boundary Zn in Al alloys with ultrafine grains leads to the phenomenon of superplasticity at lower temperatures[27]. In this regard, the nature of grain boundary segregations and their behavior in deformation mechanisms is a relevant and exciting problem. The coming years may witness the study of strengthening mechanisms and their control using SPD techniques to become a relevant trend in the development of metallic materials with not only very high strength but also ductility and other enhanced mechanical properties.

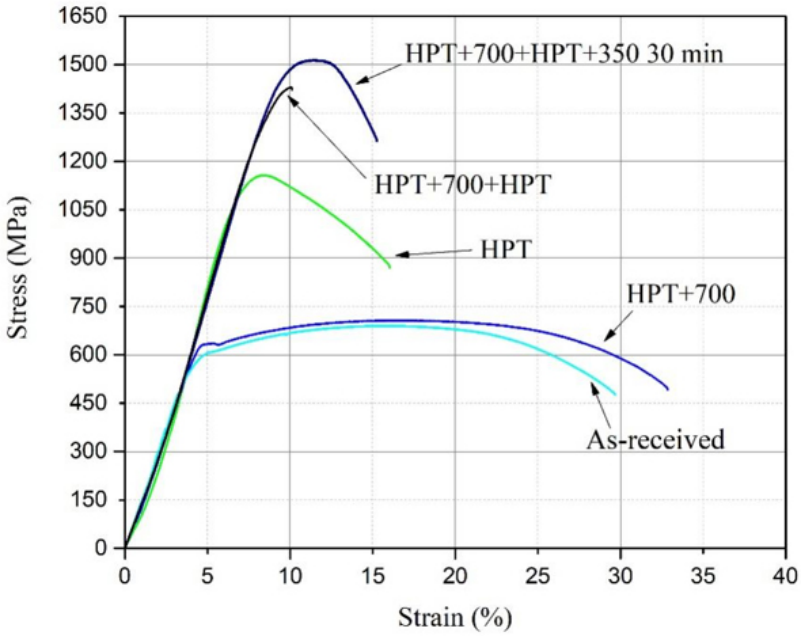

Figure 5. Engineering stress-strain curves of Ti Grade 4 after various treatments.

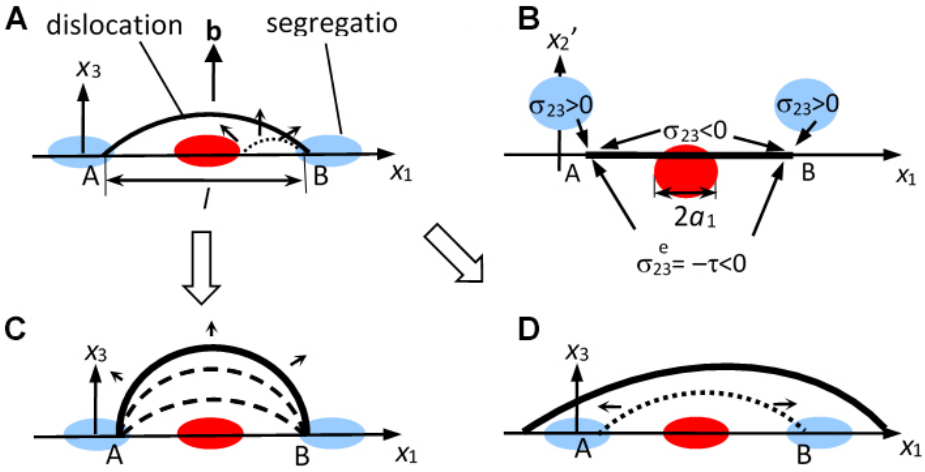

Figure 6. Expansion of a dislocation loop in the presence of segregations. The blue and red ovals denote the segregations that hinder and promote loop expansion, respectively. (A and B) Dislocation loop ends, A and B, which nucleate and expand under the action of the applied load, are pinned by segregations. (A) Projection on dislocation glide plane illustrating segregation-induced pinning. (B) Projection on grain boundary plane illustrating the fact that a segregation can either promote or hinder dislocation loop expansion, depending on the sign of the x2-coordinate of its center. (C) Dislocation loop expansion realized via its bow-out, thereby increasing the applied load if segregation-induced pinning is strong. (D) If pinning is weak, loop expansion is realized via the unpinning and lateral motion of points A and B. Reproduced with permission, Copyright 2019, Elsevier[26].

DECLARATIONS

Acknowledgments

Author acknowledges the support in part from Russian Science Foundation (Grant No. 22-19-00445) and in part by the Ministry of Science and Higher Education of Russian Federation (Agreement No. 075-15-2022-1114 as of 06/30/2022. The Author also appreciates the Ministry of Science and Higher Education of the Russian Federation, the contract 075-15-2021-709, unique identifier of the project RF-2296.61321X0037, for

discussion of the results.

Authors' contribution
The author contributed solely to the article.

Availability of data and materials
The data and related materials of this study are available from the corresponding author on reasonable request.

Financial support and sponsorship
This work was supported by Russian Science Foundation (Grant No. 22-19-00445).

Conflicts of interest
The Author declare that there are no conflicts of interest.

Ethical approval and consent to participate
Not applicable.

Consent for publication
Not applicable.

REFERENCES
1. Gleiter H. Nanostructured materials: basic concepts and microstructure. *Acta Mater* 2000;48:1-29. DOI
2. Meyers M, Mishra A, Benson D. Mechanical properties of nanocrystalline materials. *Prog Mater Sci* 2006;51:427-556. DOI
3. Valiev R, Islamgaliev R, Alexandrov I. Bulk nanostructured materials from severe plastic deformation. *Prog Mater Sci* 2000;45:103-89. DOI
4. Zehetbauer MJ, Zhu YT. (eds.). Bulk nanostructured materials. Weinheim, Germany: Wiley, 2009.
5. Valiev RZ, Zhilyaev AP, Langdon TG. Bulk nanostructured materials: fundamentals and applications. Hoboken: TMS-Wiley, 2014.
6. Firstov SA, Rogul TG, Shut OA. Transition from microstructures to nanostructures and ultimate hardening. *Funct Mater* 2009;16:364-373.
7. Horita Z, Edalati K. Severe plastic deformation for nanostructure controls. *Mater Trans* 2020;61:2241-7. DOI
8. Edalati K, Bachmaier A, Beloshenko VA, et al. Nanomaterials by severe plastic deformation: review of historical developments and recent advances. *Mater Res Lett* 2022;10:163-256. DOI
9. Ovid'ko I, Valiev R, Zhu Y. Review on superior strength and enhanced ductility of metallic nanomaterials. *Prog Mater Sci* 2018;94:462-540. DOI
10. Valiev RZ, Straumal B, Langdon TG. Using severe plastic deformation to produce nanostructured materials with superior properties. *Annu Rev Mater Res* 2022;52:357-82. DOI
11. Valiev R, Enikeev N, Murashkin M, Kazykhanov V, Sauvage X. On the origin of the extremely high strength of ultrafine-grained Al alloys produced by severe plastic deformation. *Scripta Mater* 2010;63:949-52. DOI
12. Liddicoat PV, Liao XZ, Zhao Y, et al. Nanostructural hierarchy increases the strength of aluminium alloys. *Nat Commun* 2010;1:63. DOI PubMed
13. Karavaeva MV, Kiseleva SK, Ganeev AV, et al. Superior strength of carbon steel with an ultrafine-grained microstructure and its enhanced thermal stability. *J Mater Sci* 2015;50:6730-8. DOI
14. Kim JG, Enikeev NA, Seol JB, et al. Superior strength and multiple strengthening mechanisms in nanocrystalline TWIP steel. *Sci Rep* 2018;8:11200. DOI PubMed PMC
15. Semenova I, Salimgareeva G, Da Costa G, Lefebvre W, Valiev R. Enhanced strength and ductility of ultrafine-grained Ti processed by severe plastic deformation. *Adv Eng Mater* 2010;12:803-7. DOI
16. Valiev R, Enikeev N, Langdon TG. Towards superstrength of nanostructured metals and alloys, produced by SPD. *Kovove Mater* 2021;49:1-9.
17. Abramova M, Enikeev N, Valiev R, et al. Grain boundary segregation induced strengthening of an ultrafine-grained austenitic stainless

steel. *Mater Lett* 2014;136:349-52. DOI

18. Sauvage X, Wilde G, Divinski S, Horita Z, Valiev R. Grain boundaries in ultrafine grained materials processed by severe plastic deformation and related phenomena. *Mater Sci Eng A* 2012;540:1-12. DOI
19. Sauvage X, Ganeev A, Ivanisenko Y, Enikeev N, Murashkin M, Valiev R. Grain boundary segregation in UFG alloys processed by severe plastic deformation: grain boundary segregation in UFG. *Adv Eng Mater* 2012;14:968-74. DOI
20. Zhang Y, Jin S, Trimby PW, et al. Dynamic precipitation, segregation and strengthening of an Al-Zn-Mg-Cu alloy (AA7075) processed by high-pressure torsion. *Acta Mater* 2019;162:19-32. DOI
21. Valiev RZ, Sabirov I, Zemtsova EG, Parfenov EV, Dluhoš L, Lowe TC. Nanostructured commercially pure titanium for development of miniaturized biomedical implants. In Froes F, Qian M, editors. Titanium in medical and dental applications. 1st ed. Sawston: Woodhead Publishing, 2018. p. 393-417.
22. Rezyapova L, Valiev R, Sitdikov V, Valiev R. Study of second phase precipitates in nanostructured commercially pure titanium. *Lett Mater* 2021;11:345-50. DOI
23. Balasubramanian N, Langdon TG. The Strength-grain size relationship in ultrafine-grained metals. *Metall Mater Trans A* 2016;47:5827-38. DOI
24. Luo P, Hu Q, Wu X. Quantitatively analyzing strength contribution vs grain boundary scale relation in pure titanium subjected to severe plastic deformation. *Metall Mater Trans A* 2016;47:1922-8. DOI
25. Valiev RZ. Superior strength in ultrafine-grained materials produced by SPD processing. *Mater Trans* 2014;55:13-8. DOI
26. Bobylev S, Enikeev N, Sheinerman A, Valiev R. Strength enhancement induced by grain boundary solute segregations in ultrafine-grained alloys. *Int J Plast* 2019;123:133-44. DOI
27. Chinh NQ, Murashkin MY, Bobruk EV, et al. Ultralow-temperature superplasticity and its novel mechanism in ultrafine-grained Al alloys. *Mater Res Lett* 2021;9:475-82. DOI
28. Petrik MV, Kuznetsov AR, Enikeev NA, Gornostyrev YN, Valiev RZ. Peculiarities of interactions of alloying elements with grain boundaries and the formation of segregations in Al-Mg and Al-Zn Alloys. *Phys Met Metallogr* 2018;119:607-12. DOI

Yang *et al. Microstructures* 2023;3:2023005
DOI: 10.20517/microstructures.2022.24

Microstructures

Research Article

Open Access

Check for updates

An ultraviolet-visible distinguishable broadband photodetector based on the positive and negative photoconductance effects of a graphene/ZnO quantum dot heterostructure

Xun Yang[#], Chao-Jun Wang[#], Shaobo Cheng, Xi-Gui Yang, Jin-Hao Zang, Chong-Xin Shan

Henan Key Laboratory of Diamond Optoelectronic Materials and Devices, Key Laboratory of Material Physics, Ministry of Education, School of Physics and Microelectronics, Zhengzhou University, Zhengzhou 450052, Henan, China.
[#]Authors contributed equally.

Correspondence to: Dr. Shaobo Cheng, Henan Key Laboratory of Diamond Optoelectronic Materials and Devices, Key Laboratory of Material Physics, Ministry of Education, School of Physics and Microelectronics, Zhengzhou University, Zhengzhou 450052, Henan, China. E-mail: chengshaobo@zzu.edu.cn; Dr. Chong-Xin Shan, Henan Key Laboratory of Diamond Optoelectronic Materials and Devices, Key Laboratory of Material Physics, Ministry of Education, School of Physics and Microelectronics, Zhengzhou University, Zhengzhou 450052, Henan, China. E-mail: cxshan@zzu.edu.cn

How to cite this article: Yang X, Wang CJ, Cheng S, Yang XG, Zang JH, Shan CX. An ultraviolet-visible distinguishable broadband photodetector based on the positive and negative photoconductance effects of a graphene/ZnO quantum dot heterostructure. *Microstructures* 2023;3:2023005. https://dx.doi.org/10.20517/microstructures.2022.24

Received: 6 Sep 2022 **First Decision:** 9 Oct 2022 **Revised:** 21 Oct 2022 **Accepted:** 25 Nov 2022 **Published:** 10 Jan 2023

Academic Editor: Zibin Chen **Copy Editor:** Fangling Lan **Production Editor:** Fangling Lan

Abstract

Broadband photodetectors covering the ultraviolet (UV) to visible range are significant for applications in communication and imaging. Broadband photodetectors with the capacity to distinguish wavelength bands are highly desirable because they can provide additional spectral information. Herein, we report a UV-visible distinguishable broadband photodetector based on a graphene/ZnO quantum dot heterostructure. The photodetector exhibits negative photoconductance under visible illumination because the adsorbents on graphene act as scattering centers to reduce the carrier mobility. In contrast, under UV illumination, the photodetector shows positive photoconductance as the photogenerated electrons in the ZnO quantum dots transfer to the graphene, thereby increasing the conductivity. Thus, the detection and distinction of UV and visible illumination can be realized by utilizing the opposing photoconductivity changes. These results offer inspiration for the design of multifunctional broadband photodetectors.

Keywords: Graphene, ZnO, positive photoconductance, negative photoconductance, broadband photodetector

INTRODUCTION

Photodetectors, which convert optical to electrical signals, play a key role in optoelectronic systems[1-6]. In contrast to photodetectors that respond only to a specific wavelength range, broadband photodetectors can detect light over a broad spectral range and it is therefore essential to various techniques, including image sensing, optical communications, environmental monitoring, and so on[7-9]. Broadband photodetectors responding to light over a wide spectral range from ultraviolet (UV) to infrared have been developed from a variety of materials, such as two-dimensional (2D) materials, perovskites, organic semiconductors, and so on. However, the specific band of the incident light usually cannot be distinguished[10-13]. Therefore, broadband photodetectors with the capacity to distinguish different wavelength bands are highly desirable and can provide additional spectral information. For instance, UV-visible distinguishable broadband photodetectors are required for astronomical detection, information storage and other applications[1,14-16]. However, it is challenging to detect and distinguish UV and visible light using a single photodetector.

Graphene is a promising material for broadband photodetectors due to its wide-range absorption spectrum and high carrier mobility[17-22]. More interestingly, both positive and negative photoconductance responses have been reported for graphene photodetectors[23-25]. Ordinarily, light with photon energy larger than the band gap generates carriers in the valence and conduction bands of a semiconductor material, thereby increasing the conductivity. Such positive photoconductance (PPC) has been observed in most photodetectors[26,27]. In contrast to PPC, the conductivity in some low-dimensional materials may decrease under illumination, i.e., negative photoconductance (NPC)[24,28-30]. This abnormal phenomenon has been observed in photodetectors based on graphene, InAs nanowires, ZnS nanoparticles, carbon nanotubes, monolayer MoS_2, and so on[23,30-32]. NPC in graphene is related to surface adsorbents, which act as scattering centers and decrease the carrier mobility under light illumination, leading to a decrease in conductivity[33,34]. In contrast, graphene photodetectors with PPC and high responsivity can also be obtained from van der Waals heterostructures composed of graphene and other materials[7,35]. The opposing photoconductivity changes of photodetectors with PPC and NPC can be easily distinguished[36]. Therefore, UV-visible distinguishable broadband photodetectors may be realized by integrating the two different response mechanisms in the same photodetector.

Here, we present a UV-visible distinguishable photodetector composed of graphene and zinc oxide (ZnO) quantum dots (QDs). Bare graphene shows NPC under illumination from the UV to visible region. To make the response in the UV and visible region distinguishable, ZnO QDs are coated onto graphene to convert the NPC response under UV illumination to a PPC response. ZnO is chosen to absorb UV illumination due to its wide bandgap (3.3 eV, ~376 nm), low cost and abundant nanostructures[37-42]. Moreover, given that the surface states of ZnO are sensitive to the environment, the applications of ZnO photodetectors may further be extended to the chemical, medical and biological fields[43-48]. In the graphene/ZnO QD van der Waals heterostructure, electrons generated in the ZnO QDs by UV light can transfer to the graphene and enhance its conductivity, resulting in PPC in the UV region. Furthermore, the graphene/ZnO QD photodetector retains the NPC response in the visible region because the ZnO QDs do not absorb visible light. In this context, the graphene/ZnO QD photodetector shows PPC under UV light and NPC under visible light, thereby realizing the detection and distinction of UV and visible illumination simultaneously.

RESULTS AND DISCUSSION

Before investigating the spectral response characteristics of the graphene/ZnO QD photodetector, we first study the photoresponsive behavior of the bare graphene device. A schematic diagram of the bare graphene photodetector is displayed in Figure 1A. In this structure, graphene functions as the charge transport channel as well as the light-absorbing medium. The Raman spectrum of graphene is shown in Figure 1B. The two predominant peaks located at 1583 and 2680 cm^{-1} can be attributed to the graphene G- and 2D-bands, respectively. The small peak at 1344 cm^{-1} is the D-band Raman peak of graphene, related to defects or disorders in the hybrid structure[49,50]. The intensity ratio between the 2D and G peaks is ~0.6, indicating that the graphene is bilayer[51]. Figure 1C demonstrates the photoresponsive behavior of the bare graphene device under UV and visible illumination at a source-drain voltage (V_{DS}) of 0.2 V and a gate voltage (V_G) of 0 V. Under illumination at all wavelengths, the source-drain current (I_{DS}) gradually decreases within 1000 s, indicating persistent NPC. The persistent NPC in graphene derives from the adsorbents (O_2 or OH^- groups) at its surface, which induce p-type conductance and act as scattering centers under illumination, thereby reducing its conductance[24,52]. The decrease in free carrier mobility of graphene under illumination can also be confirmed by Hall measurements. In dark conditions, the hole mobility of graphene is 1050 $cm^2\ V^{-1}\ s^{-1}$, which decreases to 910 $cm^2\ V^{-1}\ s^{-1}$ under 365 nm UV illumination. After the light is switched off, the I_{DS} recovers slowly. For instance, after 4000 s, the current under 365 nm illumination only recovers to 24%[53]. It is notable that both the saturated current and transition time vary with the incident light wavelength, which is related to the wavelength-dependent absorption characteristics of graphene[24,54]. Figure 1D shows the responsivity of the graphene photodetector *vs.* the excitation wavelength. The responsivity is defined as $R = (I_{ph}\text{-}I_{dark})/(P_{ph}*S)$, where I_{ph} is I_{DS} under illumination, I_{dark} is I_{DS} in the dark environment, P_{ph} is the incident light intensity density and S is the active area of the device. The negative responsivity values represent the NPC behavior of the photodetector. The absolute value of the responsivity increases as the excitation wavelength decreases.

To make the response of the photodetector to UV illumination distinguishable from that to visible illumination, the graphene is coated with ZnO QDs to form a graphene/ZnO QD photodetector, as shown in Figure 2A. Figure 2B presents the transmission electron microscopy (TEM) image of the ZnO QDs, which show a typical diameter of ~5 nm. The HRTEM image clearly identifies lattice fringes with a spacing of 0.26 nm, corresponding to the (002) plane of hexagonal wurtzite ZnO[55]. Figure 2C shows the XRD pattern of the ZnO QDs. There are six characteristic peaks, corresponding to the (100), (101), (102), (110), (103) and (200) planes of the hexagonal wurtzite structure of the ZnO QDs (P63mc, $a = b = 0.325$ nm, $c = 0.521$ nm, JCPDS Card No. 80-007). Figure 2D-F show the XPS survey, O 1s and Zn 2p spectra of the ZnO QDs. The O 1s spectrum is composed of three peaks at 530.8, 532.0 and 534.0 eV, corresponding to Zn-O, O-C=O and C-O-C/OH bonds, respectively[56]. The XPS spectrum for Zn 2p shows two peaks at 1023.4 and 1046.5 eV, which can be attributed to Zn $2p_{3/2}$ and Zn $2p_{1/2}$, respectively, thereby confirming the divalent state of Zn. Figure 2G shows the Raman spectrum of the graphene/ZnO QDs. In addition to the peaks from graphene, there are three obvious peaks at 99, 418 and 640 cm^{-1}, which derive from the E2(low), E1(TO) and multi-phonon modes of ZnO, respectively[57,58]. Figure 2H presents the absorption of the graphene/ZnO QDs, which show an absorption edge at ~376 nm, corresponding to the bandgap of ZnO. The absorption in the visible region is due to scattering by the ZnO QDs.

Figure 3A shows the response characteristics of the graphene/ZnO QD photodetector under UV (upper panel) and visible (lower panel) illumination. NPC behavior can be observed under visible illumination, similar to that of the bare graphene photodetector. However, under UV illumination, the I_{DS} increases gradually, indicating PPC response to UV illumination. After the light is switched off, the I_{DS} recovers to its original level slowly. The current under 650 nm illumination recovers to 21% after 1400 s, while the current

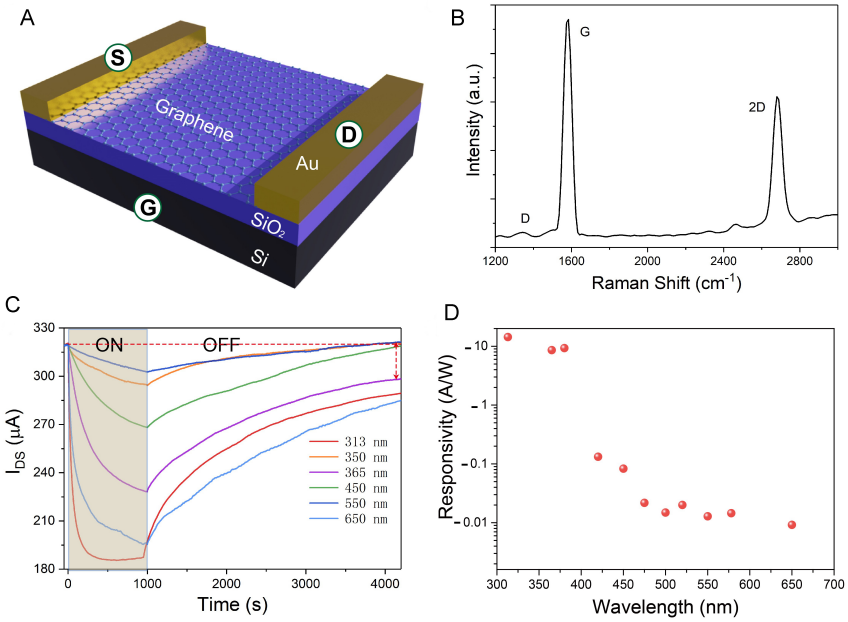

Figure 1. Bare graphene photodetector. (A) Schematic diagram of device structure (device area is 100 μm in length and 1200 μm in width defined as the area between the two electrodes). (B) Raman spectrum of graphene. (C) Photoelectric on/off response under illumination in the UV to visible range (*VDS* = 0.2 V and *VG* = 0 V). (D) Responsivity at different wavelengths.

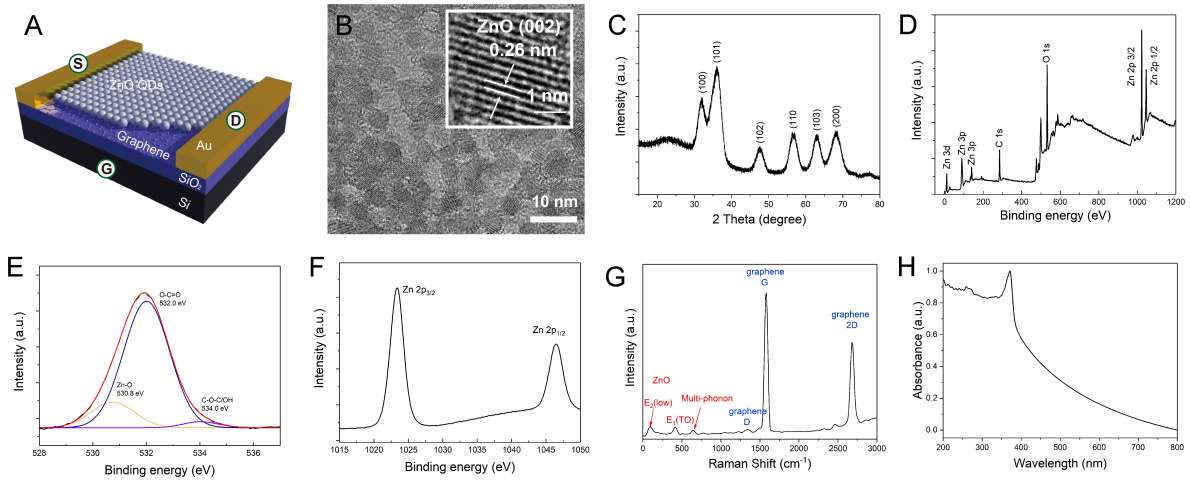

Figure 2. Graphene/ZnO QD heterostructure. (A) Schematic diagram of graphene/ZnO QD heterostructure. (B) TEM image of ZnO QDs. Inset shows HRTEM image of a single ZnO QD. (C) XRD pattern of ZnO QDs. (D) XPS survey spectrum and high-resolution spectra of (E) O 1s and (F) Zn 2p for ZnO QDs. (G) Raman and (H) absorption spectra of graphene/ZnO QDs.

under 313 nm illumination recovers to 4% after 700 s. The opposing photoconductance changes under UV and visible illumination confirm the spectrum-selective detection of the graphene/ZnO QD device. Figure 3B and C show the time-dependent response curves of the graphene/ZnO QD photodetector under 365 and 460 nm illumination, respectively. The light sources are turned on and off periodically to investigate the reproducibility of the photoresponse. Both the PPC and NPC responses are repeatable. However, the baselines change slightly after multicycle testing, which may derive from catalytic modification of the graphene.

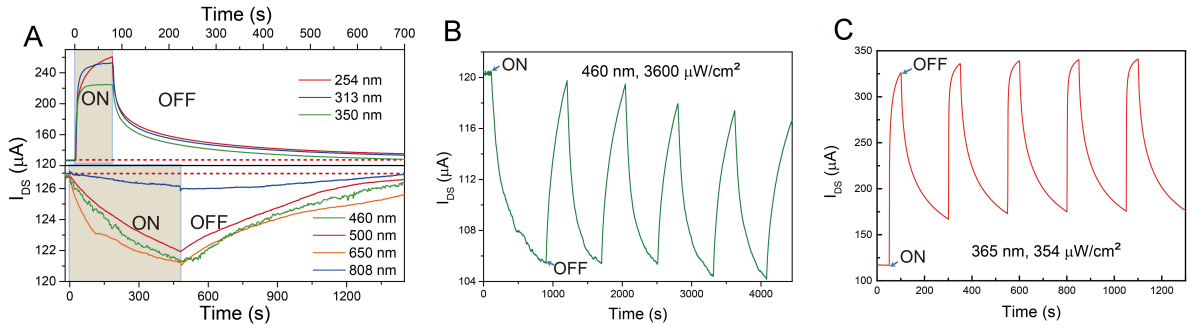

Figure 3. Graphene/ZnO QD photodetector. (A) Photocurrent response under UV and visible illumination (*VDS* = 0.2 V and *VG* = 0 V). Time-dependent photoresponse of photodetector under (B) 460 and (C) 365 nm illumination (*VDS* = 0.2 V and *VG* = 0 V).

Figure 4A and B plot the responsivity of the graphene/ZnO QD photodetector as a function of light intensity. The responsivity decreases with the light intensity and the data can be fitted using $R \propto E^{\beta-1}$, where E is the light intensity and β is a constant[25]. The constant β values under visible (460 nm) and UV (365 nm) illumination are fitted to be 0.46 and 0.12, respectively. The different β values suggest different trap states for NPC under visible illumination and PPC under UV illumination[59].

To obtain a better understanding of the response mechanism of the graphene/ZnO QD photodetector, we measured the transfer curves under UV (365 nm) and visible (460 nm) illumination, as shown in Figure 5A and B, respectively. In dark conditions, the transfer curve shows typical ambipolar transfer characteristics with the Dirac point at 1.7 V, due to the p-type doping effects from surface adsorbents. Under 460 nm illumination, the transfer curve shifts down, confirming the NPC response of the photodetector. Moreover, the Dirac point shifts gradually to 2.0 V with the incident light intensity increasing to 128 μW/cm^2, indicating that the photogenerated electrons are trapped, which is also regarded as the photogating effect[59]. In contrast, the Dirac point moves to about -0.9 V under 365 nm illumination. The negative Dirac point indicates that the p-type conductivity of graphene turns into n-type conductivity because the photogenerated electrons in the ZnO QDs transfer to the graphene[42,60]. The electron transfer mechanism can be understood using the schematic diagram in Figure 5C. Under illumination with photon energy larger than the bandgap of ZnO, electrons and holes are generated in the ZnO QDs. The photogenerated holes are trapped by surface hole traps formed by adsorbed oxygen ions, which are sufficient due to the high surface-to-volume ratio of the ZnO QDs[15,42,61,62]. Furthermore, the photogenerated electrons transfer to the graphene, which are numerous enough to compensate for the holes in the graphene and convert the p- to n-type conductivity. Hall measurements also show that the hole sheet density and mobility of graphene coated with ZnO QDs in the dark are 6.39×10^{12} cm^{-2} and 360 cm^2 V^{-1} s^{-1}, respectively. The carrier mobility is smaller than that of the bare graphene (1050 cm^2 V^{-1} s^{-1}) due to scattering by the ZnO QDs. Under the illumination of 365 nm light with an intensity of 20 μW/cm^2, the graphene exhibits n-type conductivity with an electron sheet density of 1.6×10^{13} cm^{-2} and a mobility of 150 cm^2 V^{-1} s^{-1}. The significant increase in carrier density under UV illumination results in an increase in conductivity, namely, PPC.

Figure 5D shows the responsivity spectrum of the graphene/ZnO QD photodetector accompanied by the absorption spectrum of the ZnO QDs. The absorption edge of the ZnO QDs (376 nm) is denoted by the vertical dashed line. It is apparent that the graphene/ZnO QD photodetector shows PPC under illumination with photon energy larger than the bandgap of the ZnO QDs, because a large amount of photon-generated electrons transfer from the ZnO QDs to the graphene, thereby increasing the conductivity. Furthermore, under illumination with photon energy smaller than the bandgap of the ZnO QDs, photoinduced impurity

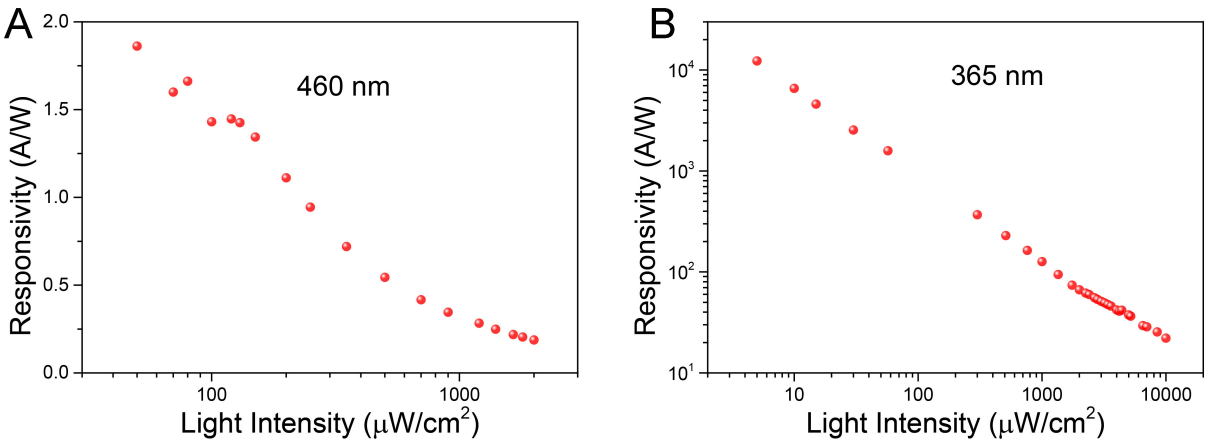

Figure 4. Responsivity of graphene/ZnO QD photodetector as a function of light intensity for (A) 460 and (B) 365 nm illumination.

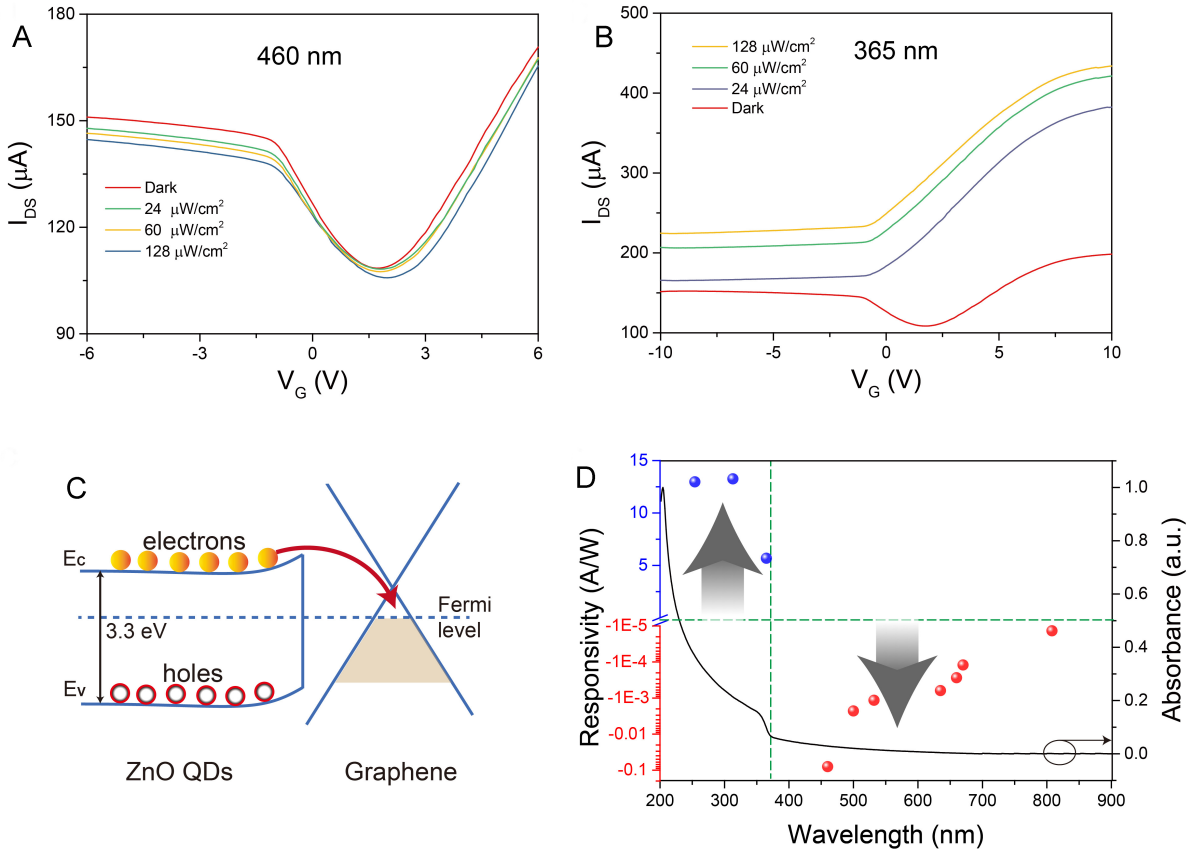

Figure 5. Photoresponsive behavior of graphene/ZnO QD photodetector. Transfer curves under (A) 460 and (B) 365 nm illumination (*VDS* = 0.2 V). (C) Schematic diagram of charge transfer process between ZnO QDs and graphene. (D) Responsivity spectrum of graphene/ZnO QD photodetector and absorption spectrum of ZnO QDs.

scattering plays the leading role, resulting in NPC. Thus, in this context, the NPC response of the graphene for UV illumination can be converted to a PPC response, thereby realizing the detection and distinction of UV and visible light using a single graphene/ZnO QD photodetector.

CONCLUSIONS

In conclusion, we have demonstrated a UV-visible distinguishable broadband photodetector utilizing the NPC and PPC response in a graphene/ZnO QD heterostructure. The photoresponsive mechanism of the photodetector under visible illumination is attributed to adsorbents on the graphene, which act as scattering centers in illumination conditions to decrease the conductivity. In contrast, under UV illumination, the photogenerated electrons in the ZnO QDs could transfer to the graphene, leading to an increase in conductivity. Thus, the current of the graphene/ZnO QDs photodetector decreases under visible illumination and increases under UV illumination, which can be used to detect and distinguish UV and visible illumination. Our results may expand the application area of broadband photodetectors.

MATERIALS AND METHODS

Device Fabrication: Graphene was grown on copper foils via a chemical vapor deposition method and transferred to Si(n+)/SiO_2 (300 nm) substrates via the solution method. Then, two Ti/Au electrodes were prepared onto the graphene by thermal evaporation using a mask. Another Ti/Au electrode was deposited on the Si substrate as a gate electrode [Figure 1A]. The device active area is 100 μm in length and 1200 μm in width defined as the area between the two electrodes. ZnO QDs were synthesized by a traditional sol-gel method using zinc acetate and KOH as reactants. To fabricate the graphene/ZnO QD photodetector, the ZnO QDs dispersed in an ethanol solution (2 mg/mL) were spin-coated over the graphene at 2000 rpm for 20 s and baked at 70 °C for 10 min. This process was repeated three times to ensure that the graphene was covered by sufficient ZnO QDs. The final thickness of the ZnO QD film is ~120 nm.

Device Characterization: The electrical transport characteristics of the device were studied using a semiconductor characterization system (Keithley 4200-SCS). Handhold lasers and LEDs with different wavelengths were employed as the light sources. The X-ray diffraction (XRD) pattern of the ZnO QDs was obtained using a diffractometer (X'Pert Pro, PANalytical). The Raman spectra were recorded using an SOL instrument spectrometer (Confotec MR520) using a 532-nm laser as the excitation source. X-ray photoelectron spectroscopy (XPS) spectra were carried out using an XPS spectrometer (Thermo ESCALAB 250) and calibrated based on the C 1s peak at 284.8 eV. The absorption spectra of the ZnO QDs were measured using a spectrophotometer (Hitachi UH4150). The morphology of the ZnO QDs was investigated using transmission electron microscopy (TEM, JEOL 2100). All the photoresponsive measurements were carried out at room temperature and in air.

DECLARATIONS

Authors' contributions

Design, writing review and editing: Yang X, Cheng S, Shan CX
Data analysis: Yang X, Yang XG, Cheng S
Data acquisition: Yang X, Wang CJ
Sample fabrication: Wang CJ, Zang JH

Availability of data and materials

Not applicable.

Financial support and sponsorship

This work was supported by National Natural Science Foundation of China (Nos. 62271450, 12174348) and Henan Center for Outstanding Overseas Scientists (No. GZS201903).

Conflicts of interest

All authors declared that there are no conflicts of interest.

Ethical approval and consent to participate

Not applicable.

Consent for publication

Not applicable.

REFERENCES

1. Du S, Lu W, Ali A, et al. A broadband fluorographene photodetector. *Adv Mater* 2017;29:1700463. DOI PubMed
2. Clifford JP, Konstantatos G, Johnston KW, Hoogland S, Levina L, Sargent EH. Fast, sensitive and spectrally tuneable colloidal-quantum-dot photodetectors. *Nat Nanotechnol* 2009;4:40-4. DOI PubMed
3. Patel M, Kumar M, Kim J. Polarity flipping in an isotype heterojunction (p-SnS/p-Si) to enable a broadband wavelength selective energy-efficient photodetector. *J Mater Chem C* 2018;6:6899-904. DOI
4. Bao C, Yang J, Bai S, et al. High performance and stable all-inorganic metal halide perovskite-based photodetectors for optical communication applications. *Adv Mater* 2018;30:e1803422. DOI PubMed
5. Li Y, Shi Z, Li X, Shan C. Photodetectors based on inorganic halide perovskites: materials and devices. *Chinese Phys B* 2019;28:017803. DOI
6. Guo Q, Pospischil A, Bhuiyan M, et al. Black phosphorus mid-infrared photodetectors with high gain. *Nano Lett* 2016;16:4648-55. DOI PubMed
7. Liu CH, Chang YC, Norris TB, Zhong Z. Graphene photodetectors with ultra-broadband and high responsivity at room temperature. *Nat Nanotechnol* 2014;9:273-8. DOI PubMed
8. Rogalski A. Infrared detectors: status and trends. *Prog Quantum Electron* 2003;27:59-210. DOI
9. Clark J, Lanzani G. Organic photonics for communications. *Nat Photon* 2010;4:438-46. DOI
10. Ding N, Wu Y, Xu W, et al. A novel approach for designing efficient broadband photodetectors expanding from deep ultraviolet to near infrared. *Light Sci Appl* 2022;11:91. DOI PubMed PMC
11. Li C, Wang H, Wang F, et al. Ultrafast and broadband photodetectors based on a perovskite/organic bulk heterojunction for large-dynamic-range imaging. *Light Sci Appl* 2020;9:31. DOI PubMed PMC
12. Yao J, Yang G. 2D material broadband photodetectors. *Nanoscale* 2020;12:454-76. DOI PubMed
13. Nanda Kumar Reddy N, Godavarthi S, Mohan Kumar K, et al. Evaluation of temperature dependent electrical transport parameters in Fe_3O_4/SiO_2/n-Si metal-insulator-semiconductor (MIS) type Schottky barrier heterojunction in a wide temperature range. *J Mater Sci Mater Electron* 2019;30:8955-66. DOI
14. Chesnokov S, Dolzhenko D, Ivanchik I, Khokhlov D. Far infrared high-performance lead telluride-based photodetectors for space-born applications. *Infrared Phys Technol* 1994;35:23-31. DOI
15. Kind H, Yan HQ, Messer B, Law M, Yang PD. Nanowire ultraviolet photodetectors and optical switches. *Adv Mater* 2002;14:158-60. DOI
16. Schaffer M, Mitkas P. Requirements and constraints for the design of smart photodetector arrays for page-oriented optical memories. *IEEE J Select Topics Quantum Electron* 1998;4:856-65. DOI
17. Hu W, Li Q, Chen X, Lu W. Recent progress on advanced infrared photodetectors. *Acta Phys Sin* 2019;68:35. DOI
18. Long M, Wang P, Fang H, Hu W. Progress, challenges, and opportunities for 2D material based photodetectors. *Adv Funct Mater* 2019;29:1803807. DOI
19. Zhang X, John S. Broadband light-trapping enhancement of graphene absorptivity. *Phys Rev B* 2019:99. DOI
20. Jia W, Ren P, Tian Y, Fan C. Dynamically tunable optical properties in graphene-based plasmon-induced transparency metamaterials. *Chinese Phys B* 2019;28:026102. DOI
21. Xia C, Xue B, Wang T, Peng Y, Jia Y. Interlayer coupling effects on Schottky barrier in the arsenene-graphene van der Waals heterostructures. *Appl Phys Lett* 2015;107:193107. DOI
22. Du H, Jia Y, Sun Q, Guo Z. Single vacancy defects diffusion at the initial stage of graphene growth: a first-principles study. *Phys Lett A* 2015;379:1270-3. DOI
23. Cui B, Xing Y, Han J, et al. Negative photoconductivity in low-dimensional materials. *Chinese Phys B* 2021;30:028507. DOI
24. Biswas C, Güneş F, Duong DL, et al. Negative and positive persistent photoconductance in graphene. *Nano Lett* 2011;11:4682-7. DOI PubMed
25. Sun Z, Liu Z, Li J, Tai GA, Lau SP, Yan F. Infrared photodetectors based on CVD-grown graphene and PbS quantum dots with

ultrahigh responsivity. *Adv Mater* 2012;24:5878-83. DOI PubMed
26. Nakanishi H, Bishop KJ, Kowalczyk B, et al. Photoconductance and inverse photoconductance in films of functionalized metal nanoparticles. *Nature* 2009;460:371-5. DOI PubMed
27. Hayden O, Agarwal R, Lieber CM. Nanoscale avalanche photodiodes for highly sensitive and spatially resolved photon detection. *Nat Mater* 2006;5:352-6. DOI PubMed
28. Han Y, Zheng X, Fu M, et al. Negative photoconductivity of InAs nanowires. *Phys Chem Chem Phys* 2016;18:818-26. DOI PubMed
29. Wei P, Chattopadhyay S, Yang M, et al. Room-temperature negative photoconductivity in degenerate InN thin films with a supergap excitation. *Phys Rev B* 2010:81. DOI
30. Chen X, Xu Y, Zhou D, et al. Solar-blind photodetector with high avalanche gains and bias-tunable detecting functionality based on metastable phase α-Ga_2O_3/ZnO Isotype Heterostructures. *ACS Appl Mater Interfaces* 2017;9:36997-7005. DOI
31. Wu JY, Chun YT, Li S, et al. Broadband MoS_2 field-effect phototransistors: ultrasensitive visible-light photoresponse and negative infrared photoresponse. *Adv Mater* 2018;30:1705880. DOI PubMed
32. Yang Y, Peng X, Kim HS, et al. Hot carrier trapping induced negative photoconductance in inas nanowires toward novel nonvolatile memory. *Nano Lett* 2015;15:5875-82. DOI PubMed
33. Tielrooij KJ, Song JCW, Jensen SA, et al. Photoexcitation cascade and multiple hot-carrier generation in graphene. *Nat Phys* 2013;9:248-52. DOI
34. Nomura K, MacDonald AH. Quantum hall ferromagnetism in graphene. *Phys Rev Lett* 2006;96:256602. DOI PubMed
35. Kong WY, Wu GA, Wang KY, et al. Graphene-β-Ga_2O_3 heterojunction for highly sensitive deep UV Photodetector application. *Adv Mater* 2016;28:10725-31. DOI PubMed
36. Haque MA, Li J, Abdelhady AL, et al. Transition from positive to negative photoconductance in doped hybrid perovskite semiconductors. *Adv Opt Mater* 2019;7:1900865. DOI
37. Yang X, Ni P, Jing P, et al. Room temperature electrically driven ultraviolet plasmonic lasers. *Adv Opt Mater* 2019;7:1801681. DOI
38. Yang X, Shan CX, Ni PN, et al. Electrically driven lasers from van der Waals heterostructures. *Nanoscale* 2018;10:9602-7. DOI PubMed
39. Lu Y, Shi Z, Shan C, Shen D. ZnO-based deep-ultraviolet light-emitting devices. *Chinese Phys B* 2017;26:047703. DOI
40. Shi ZF, Xu TT, Wu D, et al. Semi-transparent all-oxide ultraviolet light-emitting diodes based on ZnO/NiO-core/shell nanowires. *Nanoscale* 2016;8:9997-10003. DOI PubMed
41. Shi ZF, Sun XG, Wu D, et al. High-performance planar green light-emitting diodes based on a PEDOT:PSS/$CH_3NH_3PbBr_3$/ZnO sandwich structure. *Nanoscale* 2016;8:10035-42. DOI PubMed
42. Guo W, Xu S, Wu Z, Wang N, Loy MM, Du S. Oxygen-assisted charge transfer between ZnO quantum dots and graphene. *Small* 2013;9:3031-6. DOI PubMed
43. Liu X, Yang Y, Xing X, Wang Y. Grey level replaces fluorescent intensity: fluorescent paper sensor based on ZnO nanoparticles for quantitative detection of Cu_{2+} without photoluminescence spectrometer. *Sensor Actuat B Chem* 2018;255:2356-66. DOI
44. Barui AK, Veeriah V, Mukherjee S, et al. Zinc oxide nanoflowers make new blood vessels. *Nanoscale* 2012;4:7861-9. DOI PubMed
45. Kim K, Kim H, Choi K, Kim H, Lee J. ZnO hierarchical nanostructures grown at room temperature and their C_2H_5OH sensor applications. *Sensor Actuat B Chem* 2011;155:745-51. DOI
46. Pichat P. Powder photocatalysts: characterization by isotopic exchanges and photoconductivity; potentialities for metal recovery, catalyst preparation and water pollutant removal. In Schiavello M. editor, Photocatalysis and environment: trends and applications. Dordrecht: Springer Netherlands. 1988. pp 399-424.
47. Tan Y, Qiao Q, Weng T, et al. Self-powered photodetector based on poly(3-hexylthiophene)/Zinc oxide quantum dots Organic-inorganic hybrid heterojunction. *Chem Phys Lett* 2022;806:140033. DOI
48. Zhou YH, Zhang ZB, Xu P, Zhang H, Wang B. UV-visible photodetector based on I-type heterostructure of ZnO-QDs/monolayer MoS_2. *Nanoscale Res Lett* 2019;14:364. DOI PubMed PMC
49. Zhang J, Zhang X, Ding Y, Zhu Y. ZnO/graphene/Ag composite as recyclable surface-enhanced Raman scattering substrates. *Appl Opt* 2016;55:9105-12. DOI PubMed
50. Zhang BY, Liu T, Meng B, et al. Broadband high photoresponse from pure monolayer graphene photodetector. *Nat Commun* 2013;4:1811. DOI PubMed
51. Zhou H, Qiu C, Yu F, et al. Thickness-dependent morphologies and surface-enhanced raman scattering of Ag deposited on n-layer graphenes. *J Phys Chem C* 2011;115:11348-54. DOI
52. Wang Q, Tu Y, Ichii T, et al. Decoration of reduced graphene oxide by gold nanoparticles: an enhanced negative photoconductivity. *Nanoscale* 2017;9:14703-9. DOI PubMed
53. Bhatt V, Kumar M, Kim J, Chung H, Yun J. Persistent photoconductivity in Al-doped ZnO photoconductors under air, nitrogen and oxygen ambiance: role of oxygen vacancies induced DX centers. *Ceram Int* 2019;45:8561-70. DOI
54. Wang Y, Ni Z, Liu L, et al. Stacking-dependent optical conductivity of bilayer graphene. *ACS Nano* 2010;4:4074-80. DOI PubMed
55. Fernando JFS, Zhang C, Firestein K, Nerkar JY, Golberg DV. ZnO quantum dots anchored in multilayered and flexible amorphous carbon sheets for high performance and stable lithium ion batteries. *J Mater Chem A* 2019;7:8460-71. DOI
56. Zhou Z, Pourhashem S, Wang Z, Duan J, Zhang R, Hou B. Distinctive roles of graphene oxide, ZnO quantum dots, and their nanohybrids in anti-corrosion and anti-fouling performance of waterborne epoxy coatings. *Chem Eng J* 2022;439:135765. DOI
57. Nowak E, Szybowicz M, Stachowiak A, et al. A comprehensive study of structural and optical properties of ZnO bulk crystals and

polycrystalline films grown by sol-gel method. *Appl Phys A* 2020:126. DOI

58. Kim HH, Lee Y, Lee YJ, et al. Realization of excitation wavelength independent blue emission of ZnO quantum dots with intrinsic defects. *ACS Photonics* 2020;7:723-34. DOI
59. Han J, Wang J, Yang M, et al. Graphene/Organic semiconductor heterojunction phototransistors with broadband and bi-directional photoresponse. *Adv Mater* 2018;30:e1804020. DOI PubMed
60. Williams G, Kamat PV. Graphene-semiconductor nanocomposites: excited-state interactions between ZnO nanoparticles and graphene oxide. *Langmuir* 2009;25:13869-73. DOI PubMed
61. Li QH, Gao T, Wang YG, Wang TH. Adsorption and desorption of oxygen probed from ZnO nanowire films by photocurrent measurements. *Appl Phys Lett* 2005;86:123117. DOI
62. Fan Z, Chang P, Lu JG, et al. Photoluminescence and polarized photodetection of single ZnO nanowires. *Appl Phys Lett* 2004;85:6128-30. DOI

Xiao *et al. Microstructures* 2023;3:2023006
DOI: 10.20517/microstructures.2022.26

Microstructures

Review

Open Access

Environmental embrittlement behavior of high-entropy alloys

Bo Xiao[1,2,3], Shaofei Liu[2], Jianyang Zhang[1], Yinghao Zhou[1,2], Qian Li[1], Jinxiong Hou[1], Weicheng Xiao[1,2], Jixun Zhang[1], Yilu Zhao[4], Chain Tsuan Liu[1,3], Lianyong Xu[5], Tao Yang[1,3]

[1]Department of Materials Science and Engineering, Mechanical Behavior Division of Shenyang National Laboratory for Materials Science, City University of Hong Kong, Hong Kong 999077, China.
[2]Center for Advanced Nuclear Safety and Sustainable Development, City University of Hong Kong, Hong Kong 999077, China.
[3]Hong Kong Institute for Advanced Study, City University of Hong Kong, Hong Kong 999077, China.
[4]School of Materials Science and Engineering, Harbin Institute of Technology (Shenzhen), Shenzhen 518055, Guangdong, China.
[5]School of Materials Science and Engineering, Tianjin University, Tianjin 300350, China.

Correspondence to: Prof. Tao Yang, Department of Materials Science and Engineering, Mechanical Behavior Division of Shenyang National Laboratory for Materials Science, City University of Hong Kong, Hong Kong 999077, China. E-mail: taoyang6@cityu.edu.hk

How to cite this article: Xiao B, Liu S, Zhang J, Zhou Y, Li Q, Hou J, Xiao W, Zhang J, Zhao Y, Liu CT, Xu L, Yang T. Environmental embrittlement behavior of high-entropy alloys. *Microstructures* 2023;3:2023006. https://dx.doi.org/10.20517/microstructures.2022.26

Received: 18 Sep 2022 **First Decision:** 11 Oct 2022 **Revised:** 21 Oct 2022 **Accepted:** 14 Nov 2022 **Available online:** 10 Jan 2023

Academic Editors: Huijun Li, Shujun Zhang **Copy Editor:** Fangling Lan **Production Editor:** Fangling Lan

Abstract

High entropy alloys (HEAs), as a new class of structural materials, have attracted extensive interest from numerous metallurgical scientists and engineers. Benefiting from their unique microstructural features and outstanding mechanical performance, HEAs have shown significant potential for applications in many engineering fields, even under extreme conditions. In particular, when exposed to hydrogen and/or intermediate-temperature environments, these HEAs inevitably suffer from severe environmental embrittlement (EE) issues, e.g., hydrogen embrittlement (HE) and intermediate-temperature embrittlement (ITE), resulting in serious premature intergranular failure. In this work, we critically review the state-of-the-art advances of EE in previously reported HEA systems. Particular focus is given to novel strategies to enhance the resistance to EE in different HEAs. Two critical embrittlement phenomena, namely, HE and ITE, are highlighted separately. Finally, we provide perspectives on future research directions and opportunities for EE-resistant HEAs.

Keywords: High-entropy alloys (HEAs), environmental embrittlement (EE), hydrogen embrittlement, intermediate-temperature embrittlement, EE-resistant HEAs

INTRODUCTION

High-performance structural materials with promising strength and ductility combinations are highly desirable for a wide range of engineering applications[1-4]. Distinct from traditional single-principal-element-guided materials, like steels[5-8], aluminum alloys[9,10], titanium alloys[11,12] and Co/Ni-based superalloys[13-17], the multiple-principal-element paradigm has significantly motivated the rapid development of a new class of metallic structural materials, namely, high-entropy alloys (HEAs), which are also known as multi-principal-component and chemically complex alloys[18-22].

Given their extraordinary physical, thermal and mechanical properties[23-25], emerging HEAs have been expected to benefit many potential engineering applications in the aerospace, automotive, nuclear power, petrochemical and electronic manufacturing fields, as well as many other industries[26-28]. Like most conventional metallic alloys[29,30], HEAs unavoidably face enormous challenges regarding environmental embrittlement (EE) failure, which is critical to the safety and reliability of engineering structures. Intermediate-temperature embrittlement (ITE) and hydrogen embrittlement (HE) are considered to be two crucial EE issues in various advanced metallic structural materials[31-38]. Specifically, due to the synergetic effect of the local stress concentration in the vicinity of grain boundaries (GBs) and environmental GB attacks, most polycrystalline high-temperature structural alloys often undergo serious intergranular embrittlement in intermediate-temperature regimes (i.e., 600-800 °C)[39,40]. Similarly, when exposed to hydrogen environments, the deformation capability of some once ductile metallic alloys dramatically degraded, resulting in poor fracture resistance and intergranular failures[41-46]. This is because the hydrogen generally traps at the GBs and then reduces their cohesive strength. The nucleation and propagation of cracks preferentially occur at GBs during tensile deformation, consequently leading to intergranular fracture[47,48].

Notably, such undesired EE behavior, including HE and ITE, has been frequently observed in different HEA systems[39,49]. To date, many research groups have devoted their efforts to addressing EE problems in new types of HEAs and have made significant achievements. Therefore, in this study, we provide an overview of the recent important discoveries in the EE of representative HEAs. Two major types of typical EE (ITE and HE) behavior and mechanisms (or microstructural factors) are discussed separately, as schematically illustrated in Figure 1. The key strategies for improving the resistance to EE in the HEA systems are highlighted. In this review, different HEA systems are introduced and discussed, as presented in Table 1. Finally, the challenges and future research trends for the development of EE-resistant HEAs are briefly summarized.

HE MECHANISMS AND MITIGATION STRATEGIES IN HEA SYSTEMS

In this section, we summarize the significant progress made in the development of HE-resistant HEAs and the associated governing mechanisms and novel strategies.

In the past few years, numerous studies on HE resistance have been mainly focused on single-phase HEAs, such as the CoCrNi, CoNiV and FeCoCrNiMn systems[49-52]. Generally, hydrogen diffuses into alloys and can be introduced via electrochemical and gas hydrogen charging. Here, we summarize the HE behavior of HEAs in different hydrogen charging approaches. For the former case, when hydrogen is incorporated via electrochemical hydrogen charging, Soundararajan *et al.* demonstrated a relatively high HE resistance of an

Table 1. Summary of different categories of HEAs (at.%)

EE issues	HE	ITE
HEA systems	Equiatomic CoCrNi	39.9Ni-20Co-30Fe-6Al-4Ti-0.1B
	Equiatomic CoNiV	29.9Ni-30Co-13Fe-15Cr-6Al-6Ti-0.1B
	Equiatomic FeCoCrNiMn	46.23Ni-23Co-10Cr-5Fe-8.5Al-4Ti-2W-1Mo-0.15C-0.1B-0.02Zr
	97(CoCrNi)-3Mo	100-*x*(NbMoTaW)-*x*B
	Equiatomic FeCoCrNi	
	45Fe-35Mn-10Co-10Cr	
	50Fe-30Mn-10Cr-10Co	

HEAs: High entropy alloys; EE: environmental embrittlement; HE: hydrogen embrittlement; ITE: intermediate-temperature embrittlement.

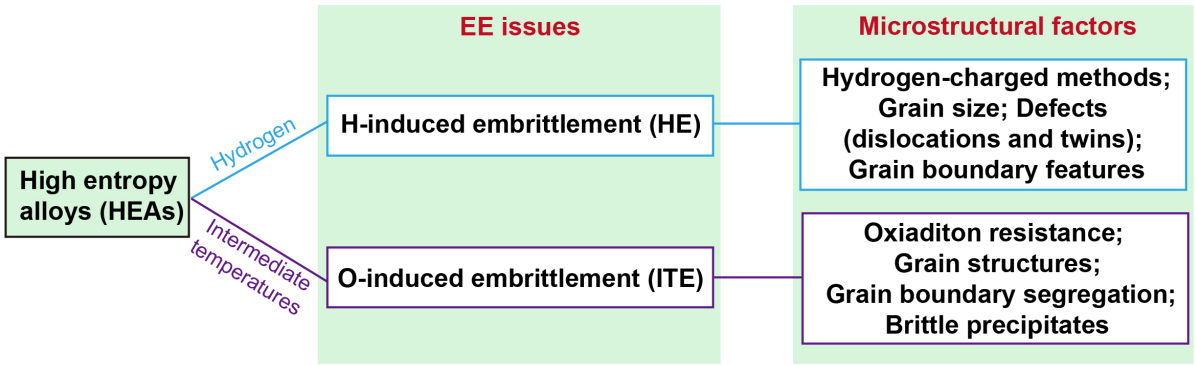

Figure 1. Schematic showing EE phenomena and associated microstructural factors. EE: Environmental embrittlement.

equiatomic CoCrNi medium entropy alloy (MEA) with ultimate tensile strength as high as ~1 GPa, as shown in Figure 2A[51]. The authors argued that the superior HE resistance is primarily attributed to the enhanced dynamic strain hardening caused by hydrogen-promoted mechanical nanotwinning [Figure 2B]. However, an inconsistent observation of this equiatomic CoCrNi MEA can be found under gas hydrogen charging, where the CoCrNi MEA displayed a pronounced ductility reduction (~70.9%) compared to the uncharged sample. Interestingly, it was further shown that boron doping (400 at. ppm) can obviously decrease the hydrogen-induced ductility loss (~45.8%) in this MEA, which is basically ascribed to the GB decoration of boron [Figure 2C-E]. The boron segregation not only significantly increases the cohesive strength of GBs but also reduces the hydrogen diffusivity along GBs, resulting in improved HE resistance[49]. Therefore, it should be noted that different hydrogen charging approaches can create distinctive mechanical responses in the same HEA. This is because hydrogen atoms are largely concentrated on the surface region of the samples via electrochemical charging, whereas hydrogen is more homogeneously distributed in the gas hydrogen-charged samples[53]. In addition to the effect of boron on the resistance to HE, it was also reported that a small addition of boron (0.2-1.6 at.%) can improve the malleability of brittle eutectic HEAs, which is primarily attributed to the transition in eutectic morphology from lamellar eutectic to dendrite eutectic. Such a transition is believed to result from the increased constitutional undercooling caused by boron additions[54].

Additionally, the HE resistance of the equiatomic CoCrNi MEA can be further enhanced via Mo doping (~3 at.%). As shown in Figure 3, Mo can promote the formation of nanotwins (NTs) in the hydrogen-charged specimen during the deformation process[55]. It was claimed that the existence of NTs can impede the local accumulation of hydrogen and disturb the continuous motion of dislocation interacting GBs, thereby inhibiting the intergranular decohesion and improving the HE resistance. Nevertheless, it is

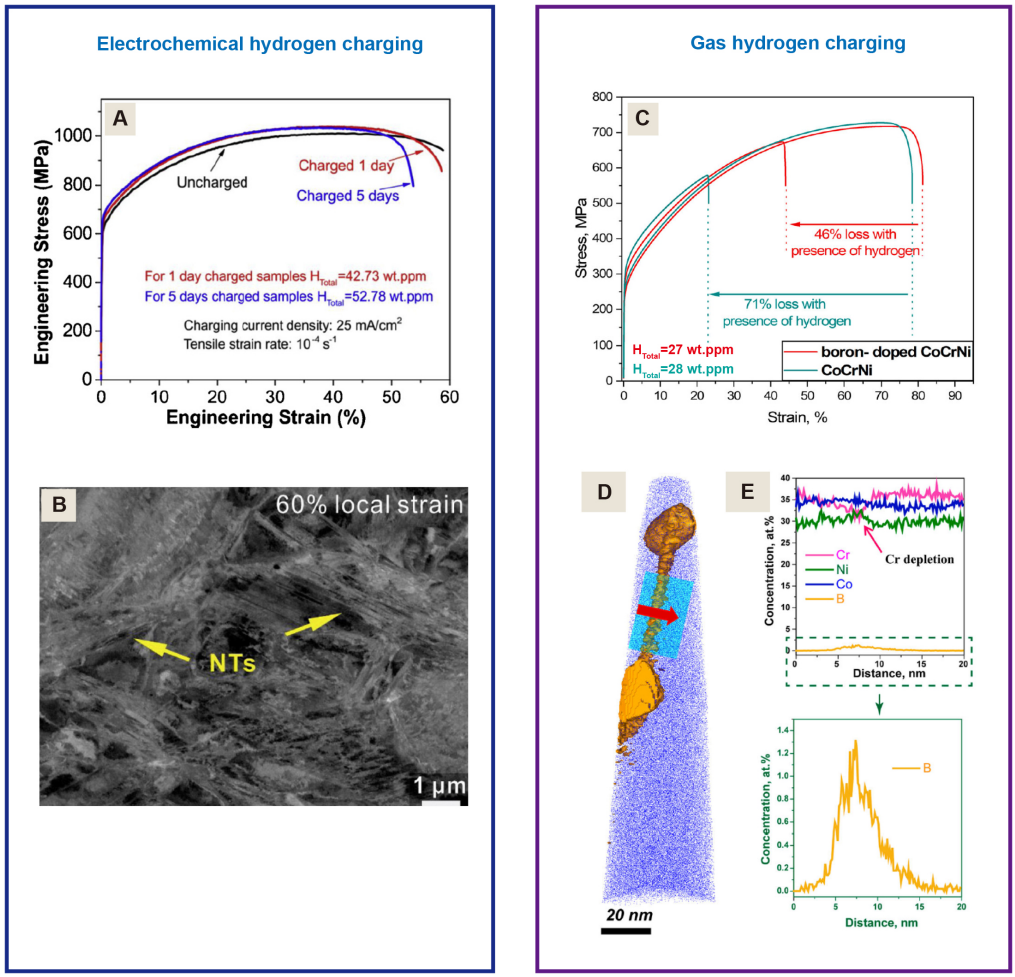

Figure 2. Tensile properties and associated mechanisms of equiatomic CoCrNi MEA under different hydrogen-charged conditions. (A) Engineering stress-strain curves under electrochemical charging. (B) Electron channeling contrast images of samples at 60% local strain levels with 5 d (52.78 wt. ppm) of hydrogen charging showing high-density NTs (Reproduced with permission[51]. Copyright 2020, Elsevier). (C) Engineering stress-strain curves of undoped and boron-doped CoCrNi MEAs under gas hydrogen charging. (D and E) Detailed reconstruction and one-dimensional composition profiles of boron-doped (400 at. ppm) CrCoNi alloy using 0.4 at.% B isosurface[49]. MEA: Medium entropy alloy; NTs: nanotwins.

noteworthy that the local chemistry of GBs has not been identified here and its effect on the improved hydrogen resistance remains elusive. More strikingly, through a combination of molecular dynamics simulations and high-resolution TEM observations, our very recent study demonstrated that an increased concentration of Fe from 2.5 to 25 at.% can effectively suppress the hydrogen-induced GB embrittlement in the Fe-Co-Cr-Ni HEA system due to the unique nanoscale segregation of Cr at the GBs. It was reported that the interfacial Cr segregation is mainly motivated by the strong repulsive force between Fe and Cr and the strong self-bonding tendency of Cr[56].

In addition to the CoCrNi MEA system, Luo *et al.* investigated the hydrogen effect on a strong and ductile CoNiV MEA under electrochemical hydrogen charging[52]. The results show that only a marginal reduction can be found in the hydrogen-charged sample, indicating the excellent HE resistance of the CoNiV MEA. Such a good combination of properties could be ascribed to four effects: (I) the single face-centered cubic (FCC) phase minimizes the local micromechanical contrast for hydrogen accumulation; (II) the solid solution elements give rise to a sluggish diffusion of hydrogen and no hydride is formed; (III) the hydrogen-

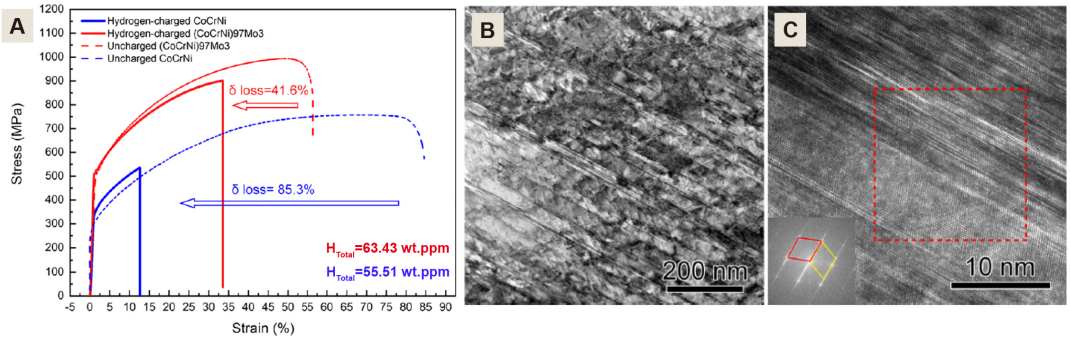

Figure 3. Superior tensile properties and deformation microstructures of hydrogen charged 97(CoCrNi)-3Mo samples. (A) Engineering stress-strain curves of Mo-doped and undoped CoCrNi alloys with and without hydrogen. (B and C) Microstructures of hydrogen-charged 97(CoCrNi)-3Mo alloy near the fracture surface showing high-density NTs. Note that hydrogen charging was performed in a 100 MPa hydrogen gas environment at 200 °C for a duration of 160 h (Reproduced with permission[55]. Copyright 2021, Elsevier). NTs: Nanotwins.

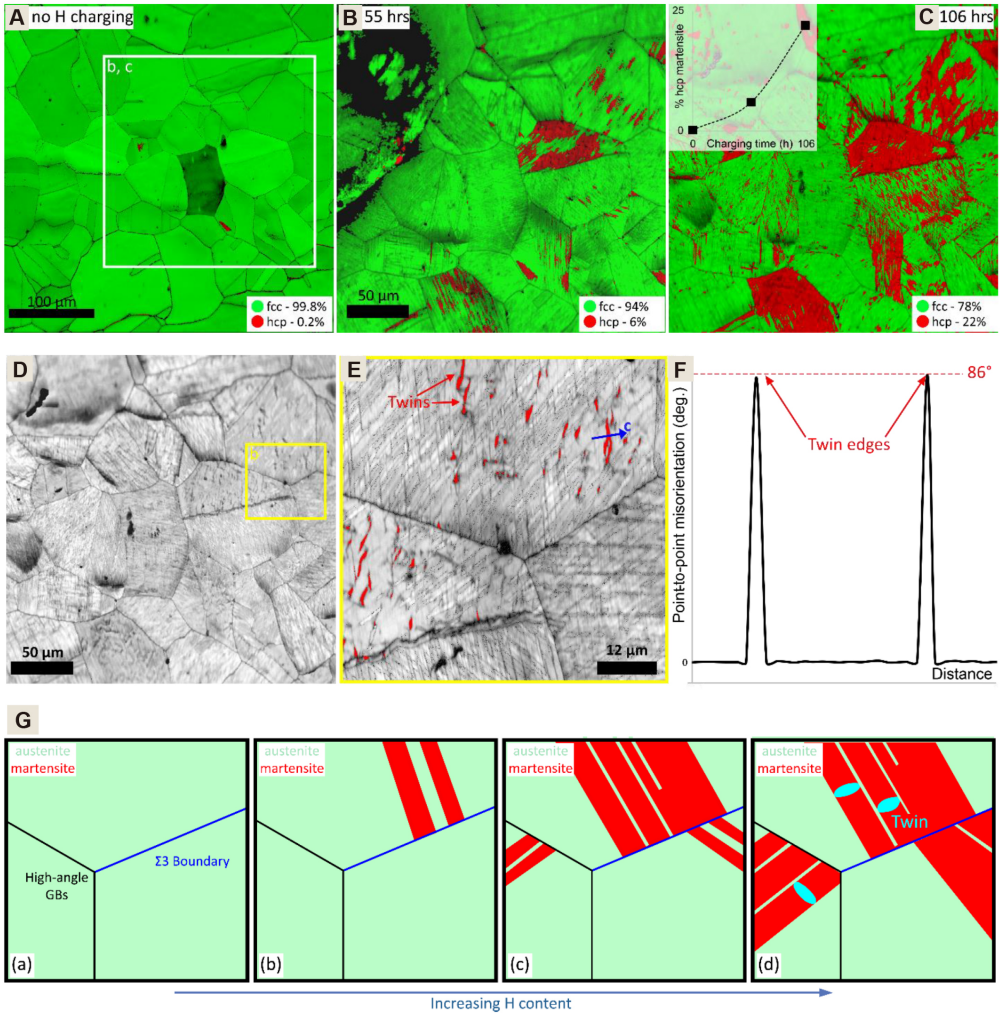

Figure 4. Hydrogen-induced phase transformations and schematic overview of metastable 45Fe-35Mn-10Co-10Cr HEA. (A-C) Electron backscatter diffraction (EBSD) phase maps of no-hydrogen charging after 55 h of hydrogen charging and 106 h of hydrogen charging. (D) Image quality map of a hydrogen-charged sample for 106 h. (E) Enlarged region with hydrogen-induced twins is highlighted in red. (F) Point-to-point misorientation across a hydrogen-induced twin[28].

induced decrease in stacking fault energy promotes the formation of NTs for increased work hardening; and (IV) the dense surface oxide film can keep the hydrogen from being absorbed and thus improves the HE resistance[52].

It is noteworthy that similar mechanisms and/or strategies (i.e., tailoring of diffusion kinetics, regulation of GB features, and so on) have been reported in other alloy systems like Al alloys and steels[57-59]. For instance, Li *et al.* simultaneously achieved the improved mechanical strength and corrosion resistance of Mg-Li-Al alloy by solid solution treatment because of the low diffusion kinetics of the solid solution phase[57]. Furthermore, the stress corrosion cracking resistance and the strength of the 7056 Al alloy with a high content of Zn were also concurrently enhanced by tailoring GB architectures (i.e., the formation of GB precipitates)[58].

In contrast to the above single-phase HEAs, Ronchi *et al.* demonstrated that hydrogen can produce a phase transformation in the metastable 45Fe-35Mn-10Co-10Cr (at.%) HEA[28]. Based on microstructural characterization [Figure 4], it was found that hydrogen induces the γ- to ε-martensite phase transformation in the metastable HEA, which preferentially occurs in the <101> and <111> oriented grains along Σ3 coincident site lattice boundaries. Additionally, high concentrations of hydrogen can promote the formation of the extension twinning within the martensite[28], which may further contribute to enhancing the HE resistance. Unfortunately, the mechanical response of the metastable HEA with hydrogen charging was not demonstrated in the study.

Additionally, the effects of hydrogen on the mechanical response and embrittlement behavior of stable and metastable HEAs (i.e., 20Fe-20Mn-20Ni-20Cr-20Co and 50Fe-30Mn-10Cr-10Co, at.%, respectively) pre-charged with 100 MPa hydrogen gases have been experimentally investigated. Figure 5A and B show the engineering stress-strain curves of the stable and metastable HEA with and without hydrogen charging, respectively. Both HEAs with hydrogen charging exhibited severe degradation in tensile plasticity. It was found that hydrogen-assisted cracking of the metastable HEA occurred via localized plasticity for both the austenite and ε-martensite phases [Figure 5C-F][60].

Moreover, regardless of electrochemical and gas hydrogen charging, the equiatomic FeCoCrNiMn HEA system shows superior resistance to HE when compared with typical steels, i.e., 304, 316L and X80[50,61,62], which is expected to be an important candidate for HE-resistant HEAs. Thereafter, extensive efforts have been devoted to further enhancing the HE resistance of the FeCoCrNiMn HEA by tailoring its architectures[50,63-65]. For example, as shown in Figure 6A, through hydrogen-induced gradient NT structures, the equiatomic FeCoCrNiMn HEA demonstrated an excellent property combination at 77 K[63]. Furthermore, the gradient-structured FeCoCrNiMn HEA shows both high yield stress (500-700 MPa) and good ductility (15%-33%) under hydrogen environments [Figure 6B], where the gradient structures containing surface NTs are introduced via the surface mechanical attrition treatment technique[66]. Additionally, it was reported that grain refinement can also contribute to improving the HE resistance of equiatomic FeCoCrNiMn and FeCoCrNi HEAs[64,65]. Specifically, the hydrogen-charged FeCoCrNiMn HEA with an average grain size of 1.9 μm exhibited a high tensile strength that was 1.5 times greater than that of the hydrogen-charged HEA with a grain size of 22 μm and there was no significant decrease in tensile elongation [Figure 6C and D][64]. Moreover, as shown in Figure 6E, incorporating the modified cellular structures by selective laser melting and annealing treatment can also effectively improve the HE resistance of the FeCoCrNiMn alloy[67]. Such excellent resistance to HE is ascribed to the delayed crack initiation and propagation by hydrogen-enhanced local plasticity with the formation of NTs and dislocation cells [Figure 6F]. These above strategies should be further explored in many other HEA systems, like CoCrNi, CoNiV, and so on.

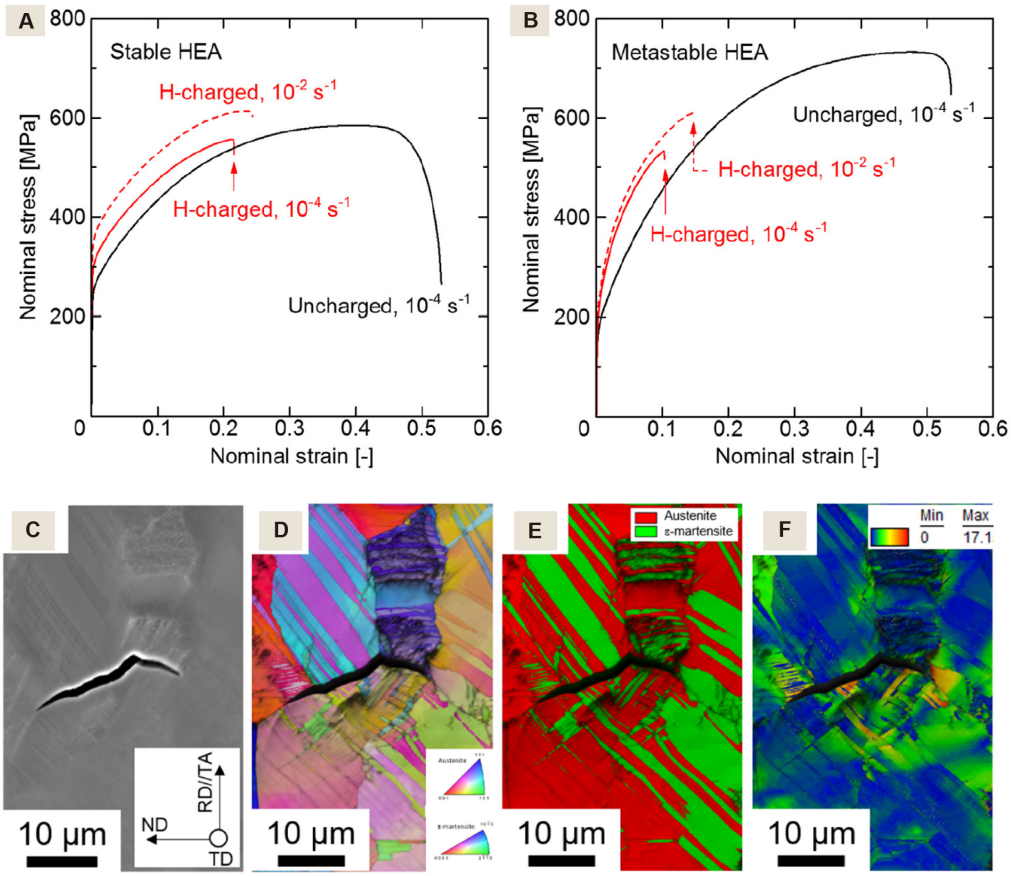

Figure 5. Tensile mechanical responses and corresponding micro-mechanisms of stable and metastable HEAs under gas hydrogen charging conditions. (A and B) Engineering stress-strain curves of stable and metastable HEAs with and without hydrogen. (C-F) Surface cracks and associated EBSD images of metastable HEA (Reproduced with permission[60].Copyright 2018, Elsevier). HEAs: High entropy alloys.

Despite the experimental evidence that HEAs exhibit excellent HE resistance, the atomic mechanisms of HE in HEA systems have further been investigated through multiscale simulations and calculations[68,69]. Zhou *et al.* presented a new theory of embrittlement in FCC metals by considering the role of hydrogen in driving an intrinsic ductile-to-brittle transition at a crack tip [Figure 7A-C][68]. This theory can be used to quantitatively predict the hydrogen concentration at which a transition to embrittlement occurs for SS304, SS316L, CoCrNi, CoNiV, CoCrFeNi and CoCrFeMnNi. For example, the predicted results show that the SS316L steel has a higher HE resistance than the CoCrFeMnNi and CoCrFeNi HEAs. The CoNiV MEA exhibits the strongest HE resistance among all the alloys [Figure 7D]. In addition, hydrogen diffusion and its interaction with dislocations also play a crucial role in the HE of HEAs. With the assistance of first-principles calculations, Xie *et al.* showed that the unique lattice distortion in HEAs causes a wide distribution of local hydrogen solution energy and the trapping of hydrogen in low-energy sites increases the diffusion barriers[69]. Furthermore, the transfer of electrons between hydrogen and metal atoms results in the reduction of unstable and stable SFEs, which contributes to the formation of deformation twins and thus increases the corresponding plasticity.

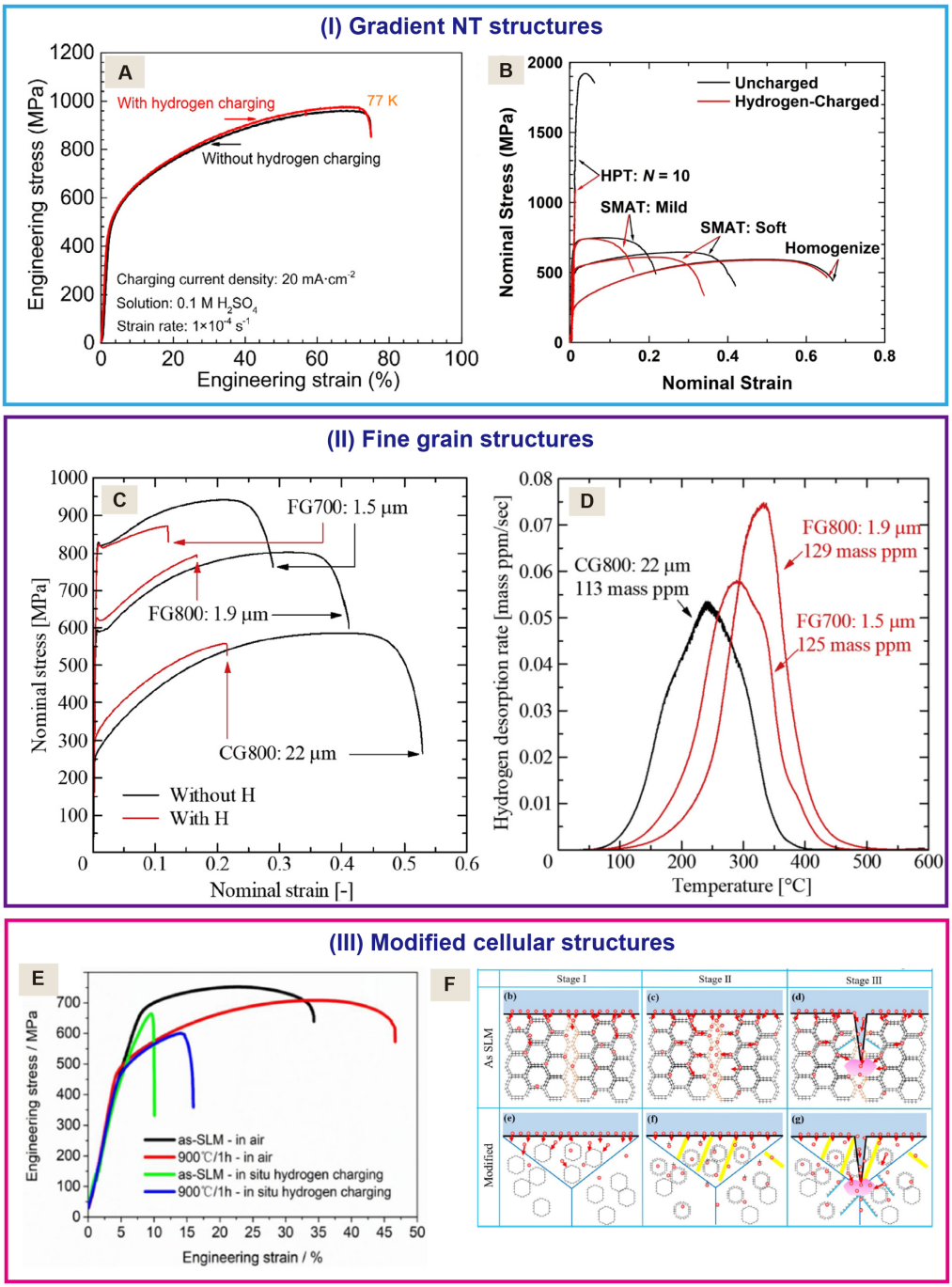

Figure 6. Enhanced HE resistance of FeCoCrNiMn HEA system via regulation of microstructural features. (A and B) Hydrogen-induced gradient NT structures (electrochemical hydrogen charging and tension) (Reproduced with permission[63]. Copyright 2018, Elsevier) (Reproduced with permission[66]. Copyright 2022, Elsevier). (C and D) Fine grain structures (gas hydrogen charging and tension) (Reproduced with permission[64]. Copyright 2019, Elsevier). (E and F) Modified cellular structures (electrochemical hydrogen charging and tension) (Reproduced with permission[67]. Copyright 2021, Elsevier). HE: Hydrogen embrittlement; HEA: high entropy alloy.

ITE MECHANISMS AND STRATEGIES FOR HEA SYSTEMS

In this section, the significant progress in the design of ITE-resistant HEAs and the associated underlying dominant mechanisms are summarized. Among recently developed HEA systems, it has been extensively

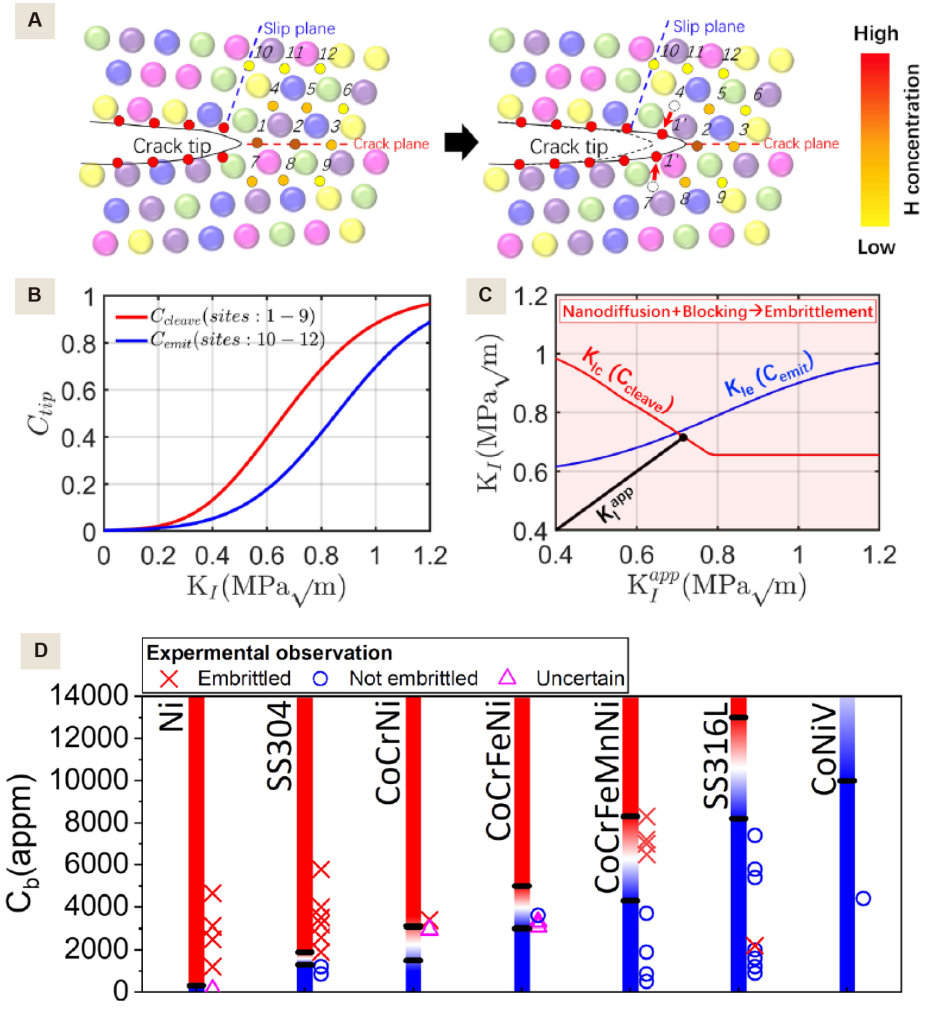

Figure 7. Mechanism and prediction of HE in various alloy systems. (A) Schematic of embrittlement process at crack tip. (B) Schematic of crack tip hydrogen concentrations C_{cleave} and C_{emit} that control embrittlement as a function of KI^{app}. (C) Predicted embrittlement due to nanodiffusion and blocking of dislocation emission: KI^{app} reaches *KIC* prior to reaching K_{Ie}. (D) Predicted embrittled and unembrittled domains of hydrogen concentration for six alloys and Ni. The transition region corresponding to the upper and lower limits of K_{Ie} is indicated by thick black lines (Reproduced with permission[68]. Copyright 2021, American Physical Society). HE: Hydrogen embrittlement.

recognized that coherent $L1_2$-type precipitate-strengthened HEAs are some of the most promising candidates for high-temperature structural applications due to their exceptional thermal and mechanical properties at a wide range of temperatures[20,70-72]. Unfortunately, like many high-strength metallic structural materials, such $L1_2$-strengthened HEAs also usually exhibit temperature-dependent premature tensile failure. As shown in Figure 8, it has been claimed that environmentally (i.e., oxygen)-assisted GB damage plays a vital role in premature intergranular failure at intermediate-temperature regimes[39,73]. Additionally, the potentially formed second phases at GBs also act as sites for crack initiation and propagation, leading to brittle intergranular fracture during tensile deformation[39].

Therefore, extensive efforts have been made to overcome this ITE issue in these $L1_2$-strengthened HEAs. Several advances have demonstrated that the ITE resistance can be effectively improved in some typical HEA systems through careful compositional optimization and structural regulation. For the former, it was found that Cr doping can introduce compact protective oxide layers in a 39.9Ni-20Co-(30-*x*)Fe-*x*Cr-6Al-

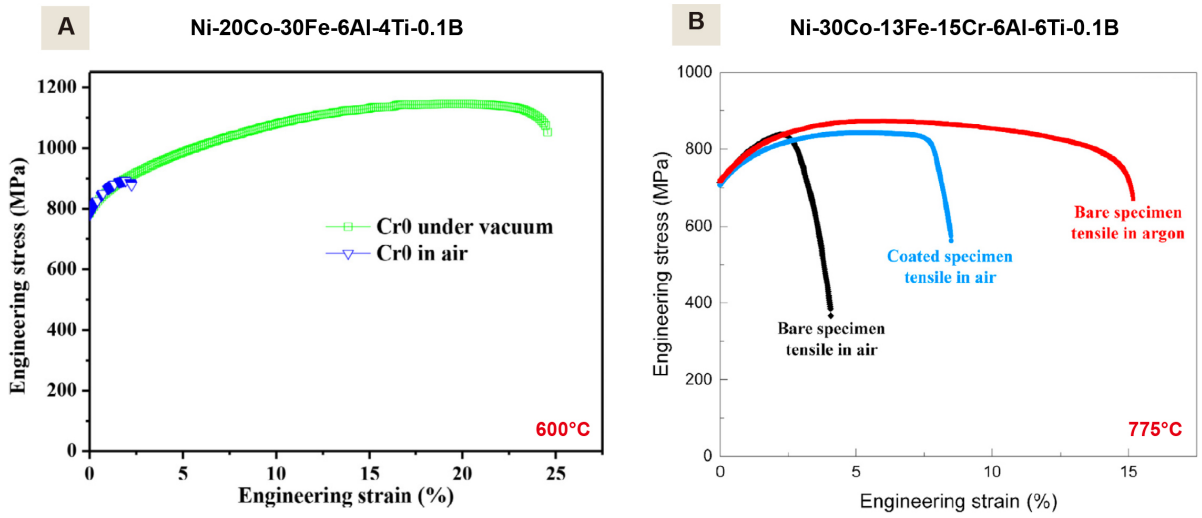

Figure 8. Oxygen-assisted failure mechanism in various HEA systems at intermediate-temperature regimes. Tensile curves of (A) Ni-20Co-30Fe-6Al-4Ti-0.1B (at.%) HEA at 600 °C in air and vacuum conditions (Reproduced with permission[73]. Copyright 2022, Elsevier) and (B) Ni-30Co-13Fe-15Cr-6Al-6Ti-0.1B (at.%) HEA at 775 °C with different surface treatments and testing environments (Reproduced with permission[39]. Copyright 2022, Elsevier). HEA: High entropy alloy.

4Ti-0.1B (at.%) HEA, which not only improves the oxidation resistance of the HEA but also hinders the inward oxygen diffusion and thus results in a substantial increase in tensile plasticity at 600 °C [Figure 9A and B][73]. This suggests that enhancing oxidation resistance via tailoring the chemical composition is a useful pathway for the innovation of ITE-resistant HEAs. Moreover, for the latter, our previous work[26] innovatively proposed a duplex-aging strategy in an $L1_2$-strengthened 39.9Ni-30Co-13Fe-15Cr-6Al-6Ti-0.1B (at.%) HEA. Such a duplex-aging strategy can controllably eliminate the intergranular brittle phases, the so-called Heusler phase, therefore achieving a distinct brittle-to-ductile transition at 700 °C, as shown in Figure 9C. More strikingly, Cao *et al.* designed a heterogeneous columnar-grained (HCG) structure in the 39.9Ni-30Co-13Fe-15Cr-6Al-6Ti-0.1B (at. %) HEA via regulating thermomechanical treatments[74]. This new type of HCG HEA exhibits superior resistance to intergranular fracture at 800 °C compared with the equiaxed counterpart with severe brittleness along GBs, which could be originated from the unique GB characteristics and distributions in the HCG HEA. Specifically, the HCG HEA shows an unusually large tensile ductility of ~18.4% combined with a high yield strength of ~652 MPa at 800 °C, as demonstrated in Figure 9D.

In addition, it is noteworthy that the serrated grain boundary (SEG) architectures can effectively solve this intergranular premature cracking issue in an $L1_2$-strengthened HEA (46.23Ni-23Co-10Cr-5Fe-8.5Al-4Ti-2W-1Mo-0.15C-0.1B-0.02Zr, at.%) at 1000 °C. This kind of HEA with SEG structures shows a brittle-to-ductile transition and achieves a superior strength as high as ~260 MPa while maintaining a uniform elongation of ~6.5% [Figure 10][75]. This finding further demonstrates that SEGs can produce enhanced resistance to intergranular crack nucleation and propagation at higher temperatures.

In addition to intergranular embrittlement in the intermediate-temperature regimes, some refractory HEAs also suffer from obvious brittleness at room temperature[76], which is essentially attributed to the GB segregation of the oxygen contaminant during fabrication, thereby weakening GB cohesion. Wang *et al.* reported that GB engineering with the addition of either metalloid B or C in a NbMoTaW refractory HEA can effectively alleviate the GB brittleness and changes the fracture morphology from intergranular to transgranular fracture[76]. The doped small-sized metalloids preferentially replace oxygen at GBs and

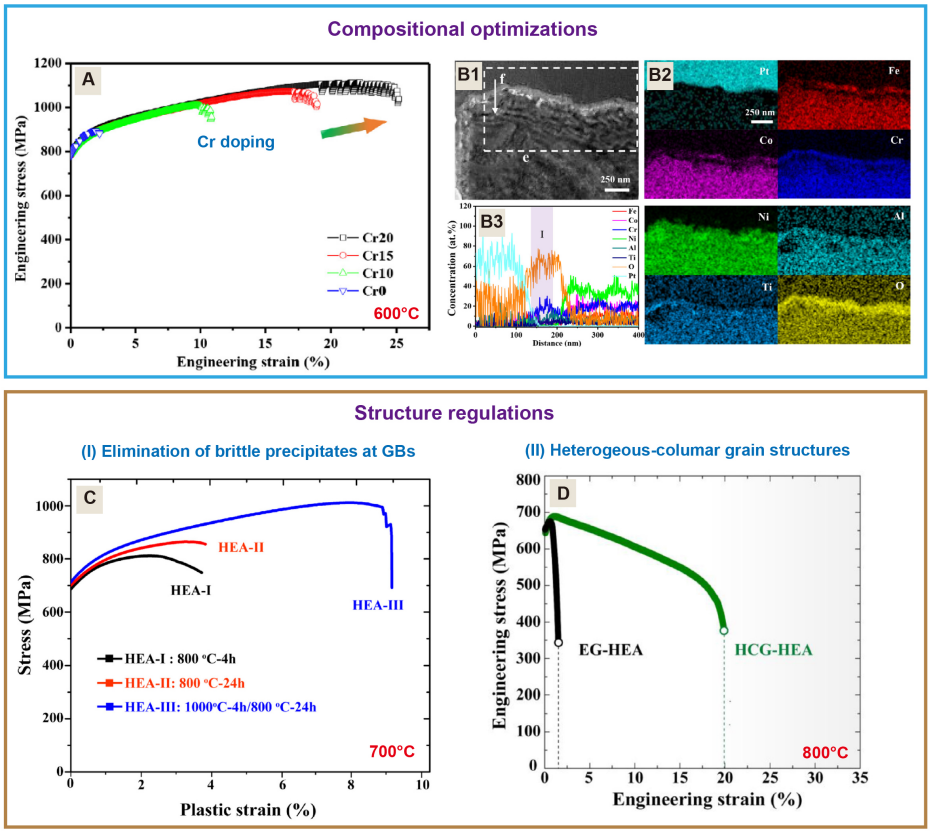

Figure 9. Overcoming ITE phenomena in $L1_2$-strengthened HEAs under tensile deformation via compositional optimization and structural regulation. (A) Cr doping enhanced tensile ductility at 600 °C. (B) Compact protective oxide layers introduced by the addition of Cr (Reproduced with permission[73]. Copyright 2022, Elsevier). (C) Elimination of brittle precipitates (Heusler phases) at GBs via a duplex-aging treatment (Reproduced with permission[26]. Copyright 2020, Elsevier). (D) Incorporation of heterogenous-columnar grain structures by controlling recrystallization durations (Reproduced with permission[74]. Copyright 2021, Elsevier). HEAs: High entropy alloys; ITE: intermediate-temperature embrittlement.

promote stronger electronic interaction with the host metals [Figure 11][76]. As earlier, a similar strategy has been reported to improve the HE resistance because of boron segregation at GBs[49].

OUTLOOK AND FUTURE WORK

As a new class of structural materials, HEAs have demonstrated distinctive microstructural architectures and promising mechanical properties, which hold significant potential for a wide of engineering applications. As summarized above, when exposed to hydrogen and/or immediate-temperature environments, these HEAs often display a serious premature embrittlement issue, like HE and/or ITE, raising enormous challenges for their practical structural applications. In this situation, more fundamental and comprehensive studies should be systematically carried out to further promote the innovation of novel high-performance HEAs together with superior EE resistance. Here, we briefly summarize several crucial issues and give some research directions on advanced structural HEAs with extraordinary EE resistance for future work.

(1) Previous efforts have been primarily focused on the development of HE-resistant steels and Al alloys[30,42,77]. The discovery of the HEAs opens a new pathway for the design of HE-resistant alloys, especially for single-phase NiCoCr and FeCoCrNiMn. However, unlike conventional alloys, such HEA

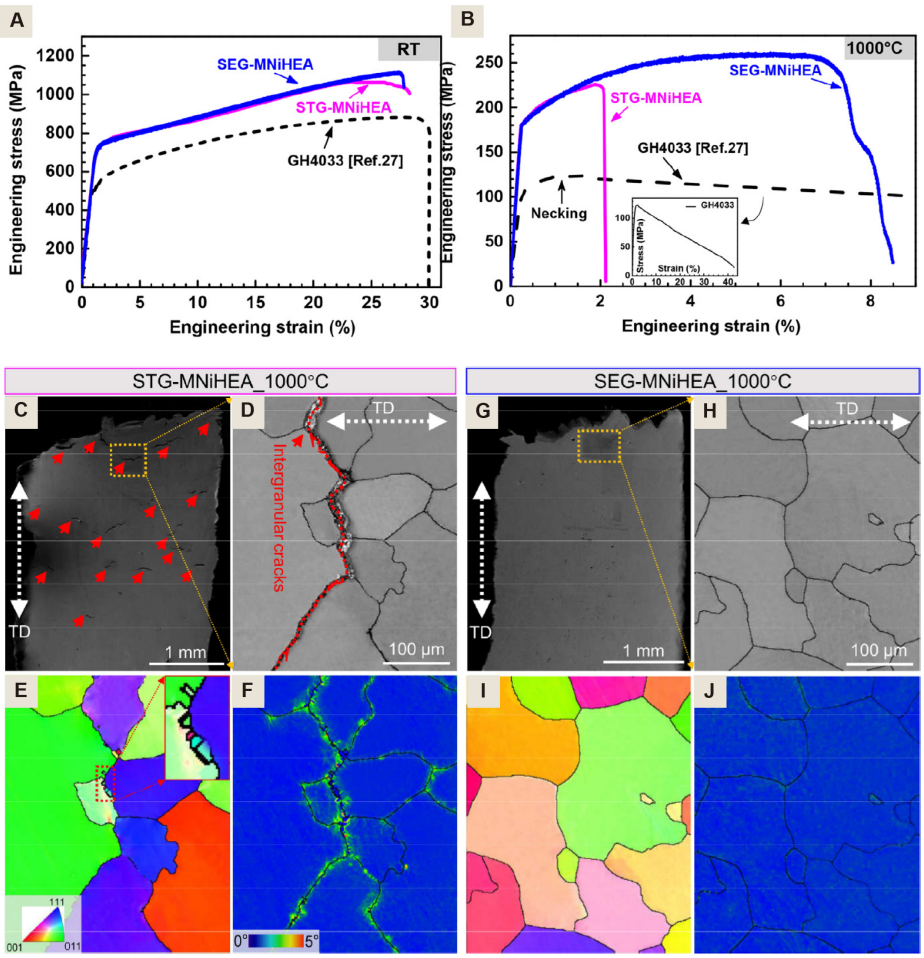

Figure 10. Tensile properties of straight grain boundary (STG)-MNiHEA and SEG-MNiHEA samples at (A) room temperature and (B) 1000 °C. Microstructures of fracture surfaces in STG-MNiHEA and SEG-MNiHEA tensioned at 1000 °C: (C and G) scanning electron microscopy images; (D and H) EBSD band contrast maps; (E and I) inverse pole figure map; (F and J) Kernal-angle misorientation maps (Reproduced with permission[75]. Copyright 2021, Elsevier).

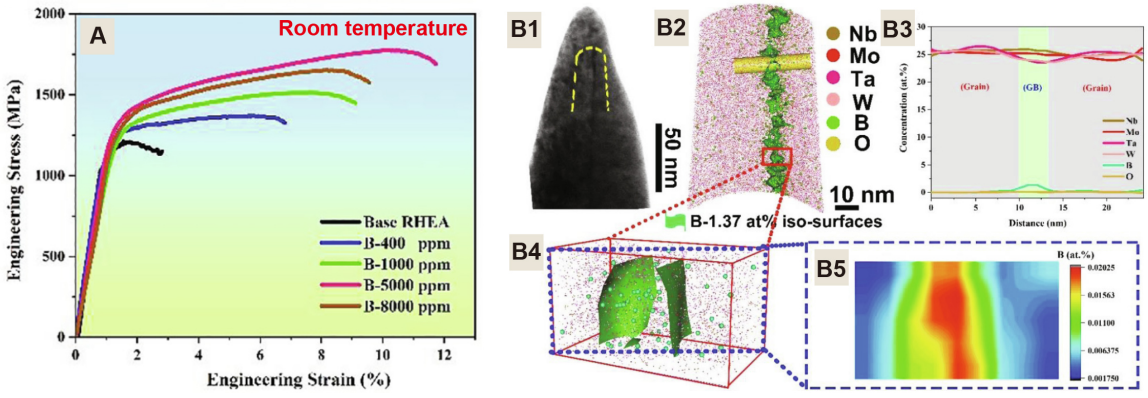

Figure 11. (A) Stress-strain curves of as-cast base refractory HEA (black) and doped HEAs with different contents of boron at room temperature under compression. (B) One-dimensional concentration profiles across a GB for the 5000 ppm (0.5 at.%) doped refractory HEA (Reproduced with permission[76]. Copyright 2022, Elsevier). HEAs: High entropy alloys.

systems exhibit complex structures and substantial compositional constitutions, which could significantly influence hydrogen diffusion and the associated mechanical responses. Therefore, the effects of structures (i.e., phase structures, vacancies and dislocations) and constitutions (substitutional and interstitial atoms) in HEAs on hydrogen-induced mechanical behavior and the underlying mechanisms should be carefully studied. Notably, a quantitative model has been proposed by Nag *et al.* and Kamachali *et al.*, which demonstrated that the solute-solute interactions and internal stresses can significantly affect the thermodynamic properties and strengthening mechanisms of HEA systems[78,79]. If the H atoms are incorporated into the HEAs with highly-diverse chemistries, the effects of complex chemistry on the mechanical responses and deformation mechanisms in the HEAs with H atoms should be experimentally and theoretically carried out. The role of complex chemistry in the formation of "surfaces" in crack formation and propagation also needs to be explored.

(2) As earlier demonstrated, hydrogen atoms are preferentially partitioned into GBs and then reduce the cohesive strength of GBs. Therefore, the structural features of GBs play a key role in determining the HE resistance of alloys. Based on this, it could be an effective routine to achieve enhanced HE resistance in HEAs via elaborately designing the GB architectures (e.g., introducing precipitates at GBs and creating GB segregation). Therefore, further research should be focused on the innovative design of novel GB structures in the HEAs.

(3) For HE-resistant materials, hydrogen local concentration is a critical parameter in governing the resistance to HE. When exposed to hydrogen environments for sufficient durations, a low hydrogen concentration stems basically from low hydrogen solubility and sluggish hydrogen diffusion in most metallic alloy systems. Therefore, the effect of a specific element on hydrogen solubility and hydrogen diffusion in different HEA systems should be systematically investigated. We believe that studies along this direction could help to significantly accelerate the design of HEAs that are intrinsically resistant to HE.

(4) It is well known that atomic-scale microstructural traps can substantially limit hydrogen diffusion. For instance, Chen *et al.* showed that hydrogen can be trapped in the core of finely dispersed V-Mo-Nb carbides in ferritic steels[30]. Furthermore, it was also reported that hydrogen concentration is observed at carbon-rich dislocations and incoherent interfaces between niobium carbides and the surrounding steel[80]. Therefore, it could be an effective strategy to enhance the resistance to HE in HEAs via engineering hydrogen traps, i.e., nanoscale carbides and low-energy dislocation nanostructures[81]. In addition, state-of-the-art microstructural characterization techniques like cryogenic atom probe tomography should be employed to directly observe the hydrogen distribution of HEA systems.

(5) Similar to Ni-based superalloys, $L1_2$-strengthened HEAs have shown significant promise in high-temperature applications. However, it has been recognized that oxygen-assisted GB damage plays an important role in the ITE issue. Therefore, improving oxidation resistance may be an efficient avenue that can hinder the oxygen-accelerated GB damage. Furthermore, as earlier reported, serrated GBs and columnar-like grains can effectively address the ITE issues. It should be noted that such unique GB structures can greatly reduce the diffusion kinetics of the oxygen and then delay intergranular cracking. As a result, careful tailoring of GB features should be carried out to further improve the resistance to ITE in HEAs. In contrast, it has been recognized that creating hydrogen traps and reducing diffusion kinetics can effectively improve the resistance to HE. We expect that $L1_2$-strengthened HEAs with unique GB features are also highly HE resistant, owing to the suppressed diffusion kinetics (serrated GBs and columnar-like grains) and high-density hydrogen traps ($L1_2$/matrix interfaces).

(6) At the present time, studies are mainly focused on the static tensile properties of the HEAs with hydrogen charging and intermediate temperatures. More importantly, the dynamic mechanical properties (fatigue, creep and fatigue/creep crack propagation) should be evaluated under *in-situ* hydrogen gas charging environments and intermediate temperatures. Subsequently, associated physical-based lifetime prediction models of HEAs should be developed. These studies are expected to ensure the reliability and safety of EE-resistant HEAs in engineering applications.

CONCLUSIONS

HEAs have received growing interest from metallurgical scientists and engineers due to their special microstructures and superb mechanical properties, which can potentially be used in many important engineering fields, including aerospace, nuclear power and chemical processing applications. In the present work, we have critically reviewed the recent major achievements in EE behavior and the associated underlying mechanisms of HEAs. In particular, two critical EE phenomena (HE and ITE) have been separately summarized. The representative HE- and ITE-resistant HEAs and the corresponding micro-mechanisms have been discussed in detail. Although some advances have been achieved, research on this topic is only just starting to develop at present and there are numerous unaddressed critical issues. In future work, to further accelerate the design of novel HEAs with superior resistance to HE and/or ITE, significant efforts should be made to fundamentally elucidate the hydrogen (oxygen) diffusion behavior and associated static/dynamic mechanical responses of HEAs. In the meantime, compositional optimization and structural regulation should be systematically studied to improve the resistance to HE and ITE of HEAs. Finally, atomic-scale microstructural characterizations are required to directly observe the hydrogen distribution and better understand the HE mechanism in HEA systems.

DECLARATIONS

Authors' contributions

Organized the literature review and drafted the original version: Xiao B, Yang T
Revised the manuscript: Liu S, Zhang J, Zhou Y, Li Q, Hou J, Xiao W, Zhang J, Zhao Y, Liu CT, Xu L
Conceived and supervised the project: Yang T, Zhao Y

Availability of data and materials

Not applicable.

Financial support and sponsorship

This project was financially supported by the Hong Kong Research Grant Council (RGC) (Grant No. CityU 21205621, 11214820, 11209021, and C1017-21G), the National Natural Science Foundation of China (Grant No. 52101151 and 52101135), and the Shenzhen Science and Technology Program (Grant No. SGDX20210823104002016 and RCBS20210609103202012).

Conflicts of interest

All authors declared that there are no conflicts of interest.

Ethical approval and consent to participate

Not applicable.

Consent for publication

Not applicable.

REFERENCES

1. Jiang S, Wang H, Wu Y, et al. Ultrastrong steel via minimal lattice misfit and high-density nanoprecipitation. *Nature* 2017;544:460-4. DOI PubMed
2. Liu G, Zhang GJ, Jiang F, et al. Nanostructured high-strength molybdenum alloys with unprecedented tensile ductility. *Nat Mater* 2013;12:344-50. DOI PubMed
3. Liddicoat PV, Liao XZ, Zhao Y, et al. Nanostructural hierarchy increases the strength of aluminium alloys. *Nat Commun* 2010;1:63. DOI PubMed
4. Nutor RK, Cao Q, Wei R, et al. A dual-phase alloy with ultrahigh strength-ductility synergy over a wide temperature range. *Sci Adv* 2021;7:eabi4404. DOI PubMed PMC
5. He BB, Hu B, Yen HW, et al. High dislocation density-induced large ductility in deformed and partitioned steels. *Science* 2017;357:1029-32. DOI PubMed
6. Kong H, Jiao Z, Lu J, Liu CT. Low-carbon advanced nanostructured steels: microstructure, mechanical properties, and applications. *Sci China Mater* 2021;64:1580-97. DOI
7. Kürnsteiner P, Wilms MB, Weisheit A, Gault B, Jägle EA, Raabe D. High-strength damascus steel by additive manufacturing. *Nature* 2020;582:515-9. DOI PubMed
8. Xiao B, Xu L, Cayron C, Xue J, Sha G, Logé R. Solute-dislocation interactions and creep-enhanced Cu precipitation in a novel ferritic-martensitic steel. *Acta Mater* 2020;195:199-208. DOI
9. Zhang Q, Zhu Y, Gao X, Wu Y, Hutchinson C. Training high-strength aluminum alloys to withstand fatigue. *Nat Commun* 2020;11:5198. DOI PubMed PMC
10. Wu G, Liu C, Sun L, et al. Hierarchical nanostructured aluminum alloy with ultrahigh strength and large plasticity. *Nat Commun* 2019;10:5099. DOI PubMed PMC
11. Zhang T, Huang Z, Yang T, et al. In situ design of advanced titanium alloy with concentration modulations by additive manufacturing. *Science* 2021;374:478-82. DOI PubMed
12. Zhang J, Liu Y, Sha G, et al. Designing against phase and property heterogeneities in additively manufactured titanium alloys. *Nat Commun* 2022;13:4660. DOI PubMed PMC
13. Suzuki A, Inui H, Pollock TM. $L1_2$-strengthened cobalt-base superalloys. *Annu Rev Mater Res* 2015;45:345-68. DOI
14. Pollock TM, Dibbern J, Tsunekane M, Zhu J, Suzuki A. New co-based γ-γ′ high-temperature alloys. *JOM* 2010;62:58-63. DOI
15. Sato J, Omori T, Oikawa K, Ohnuma I, Kainuma R, Ishida K. Cobalt-base high-temperature alloys. *Science* 2006;312:90-1. DOI PubMed
16. Smith TM, Esser BD, Antolin N, et al. Phase transformation strengthening of high-temperature superalloys. *Nat Commun* 2016;7:13434. DOI PubMed PMC
17. Ju J, Shen Z, Kang M, Zhang J, Wang J. On the preferential grain boundary oxidation of a Ni-Co-based superalloy. *Corros Sci* 2022;199:110203. DOI
18. Ding Q, Zhang Y, Chen X, et al. Tuning element distribution, structure and properties by composition in high-entropy alloys. *Nature* 2019;574:223-7. DOI PubMed
19. Fan L, Yang T, Zhao Y, et al. Ultrahigh strength and ductility in newly developed materials with coherent nanolamellar architectures. *Nat Commun* 2020;11:6240. DOI PubMed PMC
20. Yang T, Zhao YL, Tong Y, et al. Multicomponent intermetallic nanoparticles and superb mechanical behaviors of complex alloys. *Science* 2018;362:933-7. DOI PubMed
21. Wei S, Kim SJ, Kang J, et al. Natural-mixing guided design of refractory high-entropy alloys with as-cast tensile ductility. *Nat Mater* 2020;19:1175-81. DOI PubMed
22. Miracle D, Senkov O. A critical review of high entropy alloys and related concepts. *Acta Mater* 2017;122:448-511. DOI
23. Feng R, Rao Y, Liu C, et al. Enhancing fatigue life by ductile-transformable multicomponent B2 precipitates in a high-entropy alloy. *Nat Commun* 2021;12:3588. DOI PubMed PMC
24. Chen S, Aitken ZH, Pattamatta S, et al. Simultaneously enhancing the ultimate strength and ductility of high-entropy alloys via short-range ordering. *Nat Commun* 2021;12:4953. DOI PubMed PMC
25. Xiao B, Luan J, Zhao S, et al. Achieving thermally stable nanoparticles in chemically complex alloys via controllable sluggish lattice diffusion. *Nat Commun* 2022;13:4870. DOI PubMed PMC
26. Yang T, Zhao Y, Fan L, et al. Control of nanoscale precipitation and elimination of intermediate-temperature embrittlement in multicomponent high-entropy alloys. *Acta Mater* 2020;189:47-59. DOI
27. Li X, Yin J, Zhang J, et al. Hydrogen embrittlement and failure mechanisms of multi-principal element alloys: A review. *J Mater Sci Technol* 2022;122:20-32. DOI
28. Ronchi MR. Hydrogen-induced transformations in metastable high entropy alloys. Available from: https://dspace.mit.edu/handle/1721.1/139329 [Last accessed on 16 Nov 2022].
29. Xu Y, Toda H, Shimizu K, et al. Suppressed hydrogen embrittlement of high-strength Al alloys by Mn-rich intermetallic compound

particles. *Acta Mater* 2022;236:118110. DOI
30. Chen YS, Haley D, Gerstl SS, et al. Direct observation of individual hydrogen atoms at trapping sites in a ferritic steel. *Science* 2017;355:1196-9. DOI PubMed
31. López Freixes M, Zhou X, Zhao H, et al. Revisiting stress-corrosion cracking and hydrogen embrittlement in 7xxx-Al alloys at the near-atomic-scale. *Nat Commun* 2022;13:4290. DOI PubMed PMC
32. Chung H, Huh J, Jung W. Intermediate temperature brittleness of Ni based superalloy Nimonic263. *Mater Charact* 2018;140:9-14. DOI
33. Jiang L, Ye X, Cui C, et al. Intermediate temperature embrittlement of one new Ni-26W-6Cr based superalloy for molten salt reactors. *Mater Sci Eng A* 2016;668:137-45. DOI
34. Yin S, Cheng G, Chang TH, Richter G, Zhu Y, Gao H. Hydrogen embrittlement in metallic nanowires. *Nat Commun* 2019;10:2004. DOI PubMed PMC
35. Song J, Curtin WA. Atomic mechanism and prediction of hydrogen embrittlement in iron. *Nat Mater* 2013;12:145-51. DOI PubMed
36. Bechtle S, Kumar M, Somerday B, Launey M, Ritchie R. Grain-boundary engineering markedly reduces susceptibility to intergranular hydrogen embrittlement in metallic materials. *Acta Mater* 2009;57:4148-57. DOI
37. Zheng L, Schmitz G, Meng Y, Chellali R, Schlesiger R. Mechanism of intermediate temperature embrittlement of Ni and Ni-based superalloys. *Crit Rev Solid State Mater Sci* 2012;37:181-214. DOI
38. Wang C, Cao QP, Wang XD, et al. Intermediate temperature brittleness in metallic glasses. *Adv Mater* 2017;29:1605537. DOI PubMed
39. Cao B, Wei D, Zhang X, et al. Intermediate temperature embrittlement in a precipitation-hardened high-entropy alloy: the role of heterogeneous strain distribution and environmentally assisted intergranular damage. *Mater Today Phys* 2022;24:100653. DOI
40. Zheng L, Chellali R, Schlesiger R, et al. Intermediate temperature embrittlement in high-purity Ni and binary Ni(Bi) alloy. *Scr Mater* 2011;65:428-31. DOI
41. Sun B, Lu W, Gault B, et al. Chemical heterogeneity enhances hydrogen resistance in high-strength steels. *Nat Mater* 2021;20:1629-34. DOI PubMed PMC
42. Zhao H, Chakraborty P, Ponge D, et al. Hydrogen trapping and embrittlement in high-strength Al alloys. *Nature* 2022;602:437-41. DOI PubMed PMC
43. Wang S, Martin ML, Sofronis P, Ohnuki S, Hashimoto N, Robertson IM. Hydrogen-induced intergranular failure of iron. *Acta Mater* 2014;69:275-82. DOI
44. Koyama M, Tasan CC, Akiyama E, Tsuzaki K, Raabe D. Hydrogen-assisted decohesion and localized plasticity in dual-phase steel. *Acta Mater* 2014;70:174-87. DOI
45. Cotterill P. The hydrogen embrittlement of metals. *Prog Mater Sci* 1961;9:205-301. DOI
46. Rogers HC. Hydrogen embrittlement of metals. *Science* 1968;159:3819. DOI
47. Mcmahon C. Hydrogen-induced intergranular fracture of steels. *Eng Fract Mech* 2001;68:773-88. DOI
48. Pouillier E, Gourgues A, Tanguy D, Busso E. A study of intergranular fracture in an aluminium alloy due to hydrogen embrittlement. *Int J Plast* 2012;34:139-53. DOI
49. Chen XH, Zhuang XQ, Mo JW, et al. Enhanced resistance to hydrogen embrittlement in a CrCoNi-based medium-entropy alloy via grain-boundary decoration of boron. *Mater Res Lett* 2022;10:278-86. DOI
50. Zhao Y, Lee D, Seok M, et al. Resistance of CoCrFeMnNi high-entropy alloy to gaseous hydrogen embrittlement. *Scr Mater* 2017;135:54-8. DOI
51. Soundararajan CK, Luo H, Raabe D, Li Z. Hydrogen resistance of a 1 GPa strong equiatomic CoCrNi medium entropy alloy. *Corros Sci* 2020;167:108510. DOI
52. Luo H, Sohn SS, Lu W, et al. A strong and ductile medium-entropy alloy resists hydrogen embrittlement and corrosion. *Nat Commun* 2020;11:3081. DOI
53. Lee J, Lee J. The effect of lattice defects induced by cathodic hydrogen charging on the apparent diffusivity of hydrogen in pure iron. *J Mater Sci* 1987;22:3939-48. DOI
54. Yin Y, Tan Q, Wang T, et al. Eutectic modification of Fe-enriched high-entropy alloys through minor addition of boron. *J Mater Sci* 2020;55:14571-87. DOI
55. Yi J, Zhuang X, He J, He M, Liu W, Wang S. Effect of Mo doping on the gaseous hydrogen embrittlement of a CoCrNi medium-entropy alloy. *Corros Sci* 2021;189:109628. DOI
56. Li Q, Mo J, Ma S, et al. Defeating hydrogen-induced grain-boundary embrittlement via triggering unusual interfacial segregation in FeCrCoNi-type high-entropy alloys. *Acta Mater* 2022;241:118410. DOI
57. Li C, Liu X, Dong L, et al. Simultaneously improved mechanical strength and corrosion resistance of Mg-Li-Al alloy by solid solution treatment. *Mater Lett* 2021;301:130305. DOI
58. Zhou L, Chen K, Chen S, Ding Y, Fan S. Correlation between stress corrosion cracking resistance and grain-boundary precipitates of a new generation high Zn-containing 7056 aluminum alloy by non-isothermal aging and re-aging heat treatment. *J Alloys Compd* 2021;850:156717. DOI
59. Pan S, Yuan J, Linsley C, Liu J, Li X. Corrosion behavior of nano-treated AA7075 alloy with TiC and TiB2 nanoparticles. *Corros Sci* 2022;206:110479. DOI
60. Ichii K, Koyama M, Tasan CC, et al. Comparative study of hydrogen embrittlement in stable and metastable high-entropy alloys. *Scr*

Mater 2018;150:74-7. DOI
61. Pu Z, Chen Y, Dai L. Strong resistance to hydrogen embrittlement of high-entropy alloy. *Mater Sci Eng A* 2018;736:156-66. DOI
62. Luo H, Li Z, Raabe D. Hydrogen enhances strength and ductility of an equiatomic high-entropy alloy. *Sci Rep* 2017;7:9892. DOI PubMed PMC
63. Luo H, Lu W, Fang X, Ponge D, Li Z, Raabe D. Beating hydrogen with its own weapon: Nano-twin gradients enhance embrittlement resistance of a high-entropy alloy. *Mater Today* 2018;21:1003-9. DOI
64. Koyama M, Ichii K, Tsuzaki K. Grain refinement effect on hydrogen embrittlement resistance of an equiatomic CoCrFeMnNi high-entropy alloy. *Int J Hydrog Energy* 2019;44:17163-7. DOI
65. Koyama M, Wang H, Verma VK, Tsuzaki K, Akiyama E. Effects of Mn content and grain size on hydrogen embrittlement susceptibility of face-centered cubic high-entropy alloys. *Metall Mater Trans A* 2020;51:5612-6. DOI
66. Mohammadi A, Novelli M, Arita M, et al. Gradient-structured high-entropy alloy with improved combination of strength and hydrogen embrittlement resistance. *Corros Sci* 2022;200:110253. DOI
67. Fu Z, Yang B, Gan K, et al. Improving the hydrogen embrittlement resistance of a selective laser melted high-entropy alloy via modifying the cellular structures. *Corros Sci* 2021;190:109695. DOI
68. Zhou X, Tehranchi A, Curtin WA. Mechanism and prediction of hydrogen embrittlement in fcc stainless steels and high entropy alloys. *Phys Rev Lett* 2021;127:175501. DOI PubMed
69. Xie Z, Wang Y, Lu C, Dai L. Sluggish hydrogen diffusion and hydrogen decreasing stacking fault energy in a high-entropy alloy. *Mater Today Commun* 2021;26:101902. DOI
70. Zhao Y, Yang T, Han B, et al. Exceptional nanostructure stability and its origins in the CoCrNi-based precipitation-strengthened medium-entropy alloy. *Mater Res Lett* 2019;7:152-8. DOI
71. Yang T, Zhao Y, Liu W, Kai J, Liu C. $L1_2$-strengthened high-entropy alloys for advanced structural applications. *J Mater Res* 2018;33:2983-97. DOI
72. Zhao Y, Yang T, Zhu J, et al. Development of high-strength Co-free high-entropy alloys hardened by nanosized precipitates. *Scr Mater* 2018;148:51-5. DOI
73. Hou J, Liu S, Cao B, et al. Designing nanoparticles-strengthened high-entropy alloys with simultaneously enhanced strength-ductility synergy at both room and elevated temperatures. *Acta Mater* 2022;238:118216. DOI
74. Cao B, Kong H, Fan L, et al. Heterogenous columnar-grained high-entropy alloys produce exceptional resistance to intermediate-temperature intergranular embrittlement. *Scr Mater* 2021;194:113622. DOI
75. Wu S, Yang T, Cao B, et al. Multicomponent Ni-rich high-entropy alloy toughened with irregular-shaped precipitates and serrated grain boundaries. *Scr Mater* 2021;204:114066. DOI
76. Wang Z, Wu H, Wu Y, et al. Solving oxygen embrittlement of refractory high-entropy alloy via grain boundary engineering. *Mater Today* 2022;54:83-9. DOI
77. Xie D, Li S, Li M, et al. Hydrogenated vacancies lock dislocations in aluminium. *Nat Commun* 2016;7:13341. DOI PubMed PMC
78. Nag S, Curtin WA. Effect of solute-solute interactions on strengthening of random alloys from dilute to high entropy alloys. *Acta Mater* 2020;200:659-73. DOI
79. Kamachali R, Wang L. Elastic energy of multi-component solid solutions and strain origins of phase stability in high-entropy alloys. *Scr Mater* 2022;206:114226. DOI
80. Chen YS, Lu H, Liang J, et al. Observation of hydrogen trapping at dislocations, grain boundaries, and precipitates. *Science* 2020;367:171-5. DOI PubMed
81. Gong P, Nutter J, Rivera-Diaz-Del-Castillo PEJ, Rainforth WM. Hydrogen embrittlement through the formation of low-energy dislocation nanostructures in nanoprecipitation-strengthened steels. *Sci Adv* 2020;6:eabb6152. DOI PubMed PMC

Li *et al. Microstructures* 2023;3:2023007
DOI: 10.20517/microstructures.2022.27

Microstructures

Research Article

Open Access

Check for updates

The influence of A/B-sites doping on antiferroelectricity of PZO energy storage films

Dongxu Li[1], Qinghu Guo[2], Minghe Cao[1], Zhonghua Yao[1,2], Hanxing Liu[1], Hua Hao[1,2]

[1]State Key Laboratory of Advanced Technology for Materials Synthesis and Processing, School of Material Science and Engineering, International School of Material Science and Engineering, Wuhan University of Technology, Wuhan 430070, Hubei, China.
[2]Foshan Xianhu Laboratory of the Advanced Energy Science and Technology Guangdong Laboratory, Xianhu Hydrogen Valley, Foshan 528200, Guangdong, China.

Correspondence to: Prof. Hua Hao, State Key Laboratory of Advanced Technology for Materials Synthesis and Processing, School of Material Science and Engineering, International School of Material Science and Engineering, Wuhan University of Technology, Wuhan 430070, Hubei, China; Foshan Xianhu Laboratory of the Advanced Energy Science and Technology Guangdong Laboratory, Xianhu Hydrogen Valley, Foshan 528200, Guangdong, China. E-mail: haohua@whut.edu.cn

How to cite this article: Li D, Guo Q, Cao M, Yao Z, Liu H, Hao H. The influence of A/B-sites doping on antiferroelectricity of PZO energy storage films. *Microstructures* 2023;3:2023007. https://dx.doi.org/10.20517/microstructures.2022.27

Received: 22 Sep 2022 **First Decision:** 2 Nov 2022 **Revised:** 13 Nov 2022 **Accepted:** 7 Dec 2022 **Published:** 10 Jan 2023

Academic Editors: Ruzhong Zuo, Shiqing Deng **Copy Editor:** Fangling Lan **Production Editor:** Fangling Lan

Abstract

Antiferroelectrics are a kind of unique dielectric materials, mainly due to their polarization behavior, and composition-induced antiferroelectricity stability also draws considerable attention. In this work, single orthorhombic phase $(Pb_{0.95}Bi_{0.05})ZrO_3$ (PBZ), $Pb(Zr_{0.95}Bi_{0.05})O_3$ (PZB), and $PbZrO_3$ (PZO) films with good density and flatten surface was prepared on Pt/Ti/SiO_2/Si substrate via sol-gel method. Compared with pure PZO films, the PBZ and PZB films possess increased switching electric field difference ΔE due to enhanced forward switching field and the late response of backward switching field. In terms of stabilizing AFE phase, changing the tolerance factor t has the similar effect as Bi-doping the A/B sites in PZO, with the modification of the A-site being more effective than that of the B-site. PBZ films achieve a high recoverable energy density (W_{rec}) of 26.4 J/cm^3 with energy efficiency (η) of 56.2% under an electric field of 1278 kV/cm, which exceeds other pure AFE materials. This work provides a fundamental understanding of the crystal structure-related antiferroelectricity of PZO materials and broadens the chemical doping route to enhance the electric properties of AFE materials.

Keywords: Antiferroelectrics, energy storage, $PbZrO_3$, thin film, switching field

INTRODUCTION

Dielectric materials, an essential part of capacitors, would generate polarization under an electric field, enabling them to be widely used in electrocaloric, actuator, and energy storage devices. According to different polarization behaviors, dielectrics can be divided into linear dielectrics (LDs), ferroelectrics (FEs), and antiferroelectrics (AFEs)[1-4]. The energy storage performances of dielectric materials could be determined by the polarization-electric field (*P*-*E*) curves as follow:

$$W_{\mathrm{rec}} = \int_{P_{\mathrm{r}}}^{P_{\mathrm{max}}} EdP \tag{1}$$

$$\eta = \frac{W_{\mathrm{rec}}}{W_{\mathrm{rec}}+W_{\mathrm{loss}}} \tag{2}$$

where W_{rec}, η, W_{loss}, $P_{max,}$ and P_r are the recoverable energy density, the energy efficiency, the dissipated energy, the maximum polarization, and the remnant polarization under an applied electric field E, respectively. Therefore, FE and AFE materials are suitable for energy storage applications due to a large P_{max}, low $P_{r,}$ and moderate E. Meanwhile, dielectric films with much larger breakdown strength E_b could attain higher energy density than their bulk counterparts[3-6].

AFE materials possess a characteristic known as a double hysteresis loop, which corresponds to four current peaks under an applied electric field. The current peaks represent the AFE-to-FE phase transition at forward switching field E_F and FE-to-AFE phase transition at backward switching field E_A, respectively[7-10]. $PbZrO_3$ (PZO), as a prototype AFE material, exhibits an apparent double hysteresis loop characteristic, while the antiferroelectricity's origin is still controversial[11,12]. Hao *et al.* used the tolerance factor (t) to evaluate the antiferroelectricity of PZO films, and later an increasing researches focus on chemical doping to adjust antiferroelectricity of Pb-based and Pb-free AFE materials using t value[13]. The equation of tolerance factor (t) of perovskite structure can be expressed as follow:

$$t = \frac{r_A + r_O}{\sqrt{2}(r_B + r_O)} \tag{3}$$

where r_A, r_B and r_O denote the ion radius of A-site, B-site, and oxygen, respectively. It is accepted that the AFE phase is stabilized at $t < 1$, and the FE phase is stabilized at $t > 1$. For example, a reduced t value can be found in La-doped PZO and Ca-doped $AgNbO_3$ materials corresponding to an enhanced E_F and E_A to stabilize the AFE phase[14,15]. In 2017, Zhao *et al.* prepared $Ag(Nb_{1-x}Ta_x)O_3$ ceramics in a similar t value and proposed that enhanced antiferroelectricity should be attributed to reduced polarizability of the B-site[10]. In addition, (Ca, Zr), (Sr, Zr) and (Ca, Hf) modified $NaNbO_3$ AFE ceramics both possess a double hysteresis loop by decreasing the value of t while keeping the value of electronegativity fixed[16-18]. It can be seen that the electric field-induced AFE phase could be affected by a tolerance factor, polarizability, and electronegativity in A/B-sites for Pb-based and Pb-free materials. In the case of only considering the tolerance factor t, whether the role of A/B-sites on influencing antiferroelectricity of PZO films exists difference.

Following the above discussion, we choose Bi^{3+} (~1.38 Å for CN = 12 and 1.03 Å for CN = 6) to replace Pb^{2+} (1.49 Å for CN = 12) and Zr^{4+} (0.72 Å for CN = 6) at A/B-sites respectively[19], compare the difference of A/B-sites on influencing antiferroelectricity of PZO, and hence fabricate $(Pb_{0.95}Bi_{0.05})ZrO_3$ (PBZ), $Pb(Zr_{0.95}Bi_{0.05})O_3$ (PZB) and pure $PbZrO_3$ (PZO) films. A schematic representation of the crystal structure of the Bi-doping PZO material can be seen in Figure 1. Based on Equation (3), calculated t values are 0.9639,

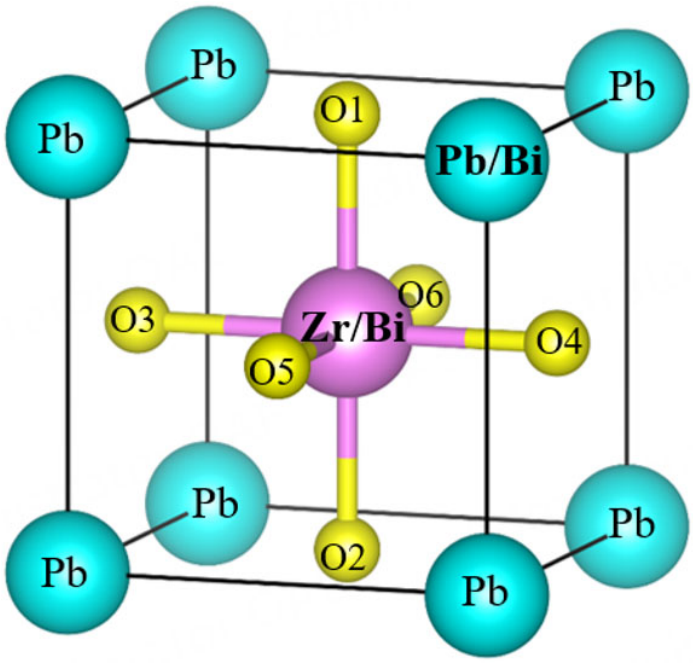

Figure 1. The schematic of 5 mol% Bi^{3+} replaces Pb^{2+} at A-site and Zr^{4+} at the B-site of PZO. PZO: $PbZrO_3$.

0.9621, and 0.9569 for PZO, PBZ, and PZB compositions, respectively. Meanwhile, a correlation between the tolerance factor *t* and the stabilized antiferroelectricity of PZO is discussed. Our work provides a new perspective in improving energy storage properties of AFE materials and prompts the development of AFE materials.

MATERIALS AND METHODS

$(Pb_{0.95}Bi_{0.05})ZrO_3$ (PBZ), $Pb(Zr_{0.95}Bi_{0.05})O_3$ (PZB), and pure $PbZrO_3$ (PZO) films were prepared on 150-nm Pt/20-nm Ti/100-nm SiO_2/Si substrate via sol-gel method. Pb $(CH_3COO)_2{\cdot}3H_2O$ (AR, 99.5 %), Bi $(NO_3)_3{\cdot}3H_2O$ (AR, 99 %), and $Zr(OCH_2CH_2CH_3)_4$ solution (70 wt%) were used as starting raw materials to prepare a stable 0.2 M precursor solution. Simultaneously, 2-methoxyethanol, acetic acid, and acetylacetone were used as solvents and stabilizers. A 10 % excess lead was added to the solvent to compensate for lead loss during the annealing process. The completed sol was spin-coated on the substrate at 4500 rpm for 30 s, pyrolyzed at 450 °C, and annealed at 650 °C to attain the desired thickness. The annealing process was achieved using an RTP-500 furnace in an air atmosphere. Finally, a P_t electrode with a diameter of ~200 μm was deposited through a magnetron sputtering system.

The crystal phase of PZO-based films was examined by grazing incident X-ray diffraction (GIXRD, Empyrean, PANalytical, Netherlands) with Cu Kα1 radiation. The cross-section morphology of the PZO-based thin films was measured using a field emission scanning electron microscope (SEM, Zeiss Ultra Plus, Germany). The surface information of thin films was collected by atomic force microscopy (AFM, Nanoscope IV, Veeco, USA). The thicknesses of PZO-based films are about 180 nm. The dielectric and ferroelectric properties of the PZO-based thin films were measured using an impendence analyzer (Agilent 4294) and a ferroelectric workstation (Precision Premier II, Radiant Technologies Inc., USA).

RESULTS AND DISCUSSION

Figure 2A shows the GIXRD patterns of PZO-based films at 2θ = 20°-60°. In the case of a PZO-based film with good crystallinity, the perovskite crystalline structure is orthorhombic phase, and no secondary phase is detectable in the range of accuracy of GIXRD technology. In order to investigate the effect of Bi doping in PZO, the enlarged patterns of PZO-based films at 2θ = 30°-31° are shown in Figure 2B. The diffraction peak (122) around 30.5° of PBZ and PZB compared to pure PZO has a slight shift towards the low angle and high angle, respectively, which demonstrates Bi successfully replaces Pb and Zr at A/B-sites. In terms of the change in diffraction peak, similar phenomena have been observed in La-doped PZO films at low content[15].

Figure 3A shows the SEM images of PZO-based films. It can be seen that all films possess good density and no pores and crack in the surface morphology. The grain size of PZB films exceeds PBZ and pure PZO films, which should be related to a reduced Pb/Zr ratio compared to PZO and PBZ. Figure 3B displays the AFM images of PZO-based films. The surface roughness R_q is 2.91 nm, 3.32 nm, and 4.04 nm for pure PZO, PBZ, and PZB films. PZO-based thin films are characterized by a smooth and flattened surface, indicating high-quality materials.

Due to the valence difference of Bi^{3+}, Pb^{2+} and Zr^{4+}, the chemical defect would be generated. The defect equation of Bi replaces Pb and Zr is given as follows:

$$2Bi_{Bi} \overset{Pb}{\rightarrow} 2Bi_{pb}^{\cdot} + V_{pb}^{''} \tag{4}$$

$$2Bi_{Bi} \overset{Zr}{\rightarrow} 2Bi_{Zr}^{'} + V_{O}^{\cdot\cdot} \tag{5}$$

It can be seen that the point defect of $V_{pb}^{''}$ and $V_{O}^{\cdot\cdot}$ could be generated when Bi acts as a donor and acceptor dopant, respectively. Figure 4 shows the room temperature frequency dependency of dielectric properties for PZO-based films. As frequency increases, the dielectric properties of PZO-based films maintain stability over the frequency range of 1 kHz-1 MHz. Figure 4A shows that the dielectric constant enhances from ~250 for PZO films to ~325 for PBZ and PZB films, which may be related to an increased point defect contribution. In addition, Figure 4B illustrates that the dielectric losses of PZO-based films are around 0.1.

Figure 5A shows the room temperature *P-E* loops of PZO-based films at an applied electric field of 800 kV/cm. PZO films exhibit an apparent double hysteresis loop. Bi-doped PZO films at A/B sites still show double hysteresis loops, but the polarization and switching fields have been changed. The polarization differences ΔP between P_{max} and P_r of PZO-based films are exhibited in Figure 5C. The P_r of all PZO-based films is unchanged, but the P_{max} of Bi-doped PZO films is lower than that of pure PZO films. Therefore, ΔP of Bi-doped PZO films cannot be enhanced effectively at the same electric field. Figure 5B shows the *I-E* loops of PZO-based films at an applied electric field of 800 kV/cm. Four current peaks correspond to the AFE-to-FE and FE-to-AFE phase transition, respectively[8,10]. Compared to pure PZO films, PBZ and PZB films both possess a lower current density and higher forward switching field E_F of 562.2 kV/cm for PBZ and 537.3 kV/cm for PZB than 413.5 kV/cm for PZO films, which illustrates Bi-doping enhances antiferroelectricity of PZO materials in some degree. As discussed above, this result may be related to a reduction in *t* value to stabilize the AFE phase. Unfortunately, the increased ΔE value sacrifices the E_F of PBZ and PZB, as shown in Figure 5D. It can be attributed to an enlarged grain size [Figure 3], which differs from the previous results. As grain size decreases, hysteresis loss in relaxor ferroelectric materials and antiferroelectric materials is reduced due to increased dipole mobility, and therefore PBZ and PZB with large grain sizes would possess a high ΔE. It can be seen that the antiferroelectricity of PZO is no positive

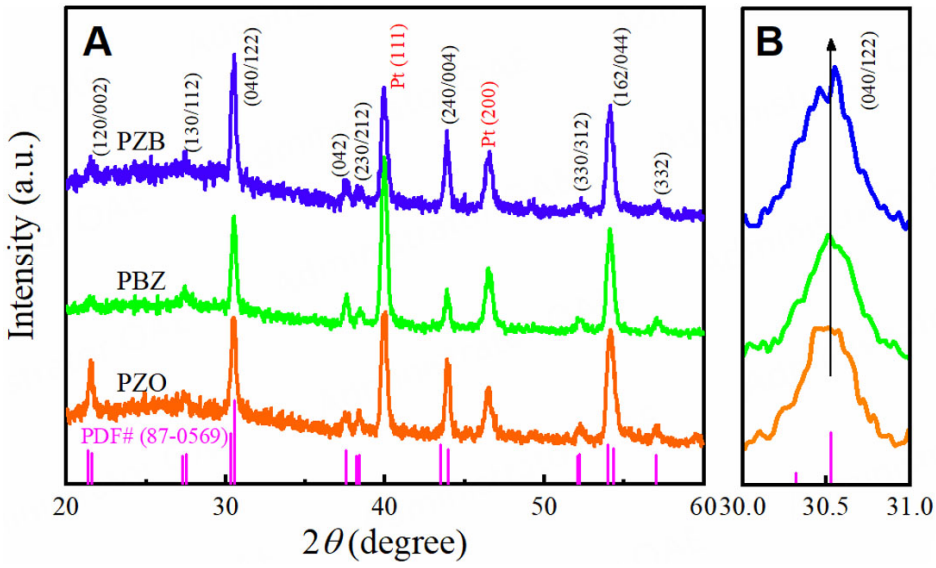

Figure 2. (A) The GIXRD patterns of PZO-based films at 2θ range from 20° to 60°. (B) The enlarged patterns at 2θ =30°-31°. GIXRD: Grazing incident X-ray diffraction; PZO: $PbZrO_3$.

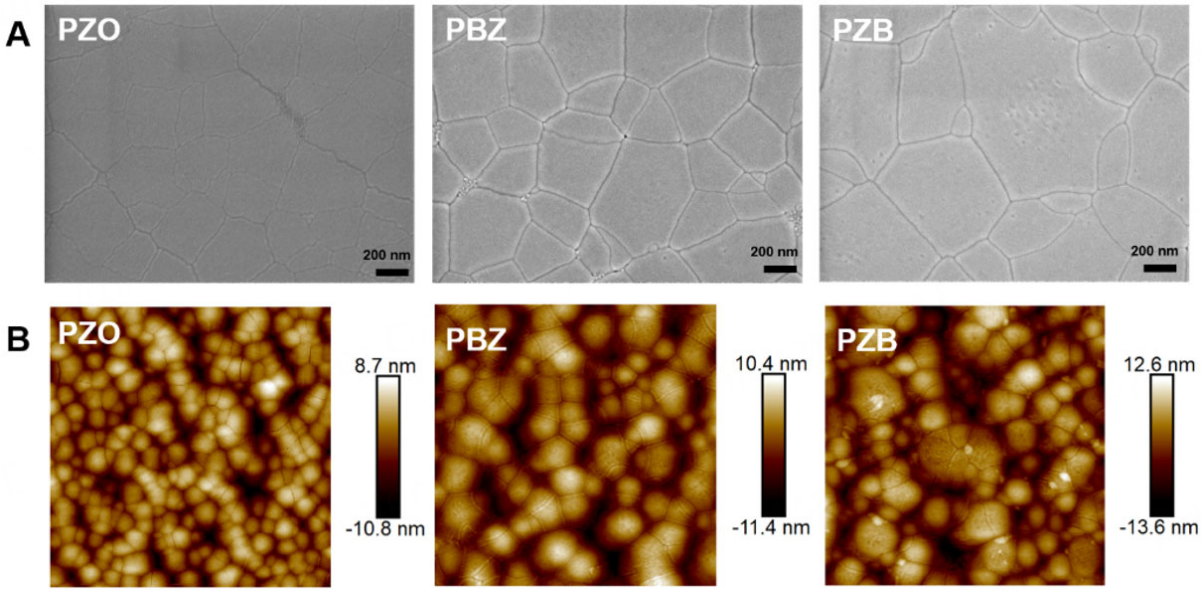

Figure 3. The (A) SEM images and corresponding (B) AFM images (5*5 μm) for PZO, PBZ, and PZB films. SEM: Scanning electron microscope; AFM: atomic force microscopy; PZO: $PbZrO_3$; PBZ: $(Pb_{0.95}Bi_{0.05})ZrO_3$; PZB: $Pb(Zr_{0.95}Bi_{0.05})O_3$.

correlation with the tolerance factor in *t* in A/B-sites doping. In addition, grain size should be taken into account when enhancing antiferroelectricity.

Figure 6A shows the *P-E* loops of pure PZO films at different electric fields. As the electric field enhances, linear hysteresis loops gradually transform into double hysteresis loops causing P_{max} to increase dramatically. With further improving the electric field, the *P-E* loops are unchanged and stay in a polarization saturation state. A detailed description of the division of regions into different states can be found in the following content. For PBZ and PZB films, the polarization saturation has a slight delay. Meanwhile, breakdown

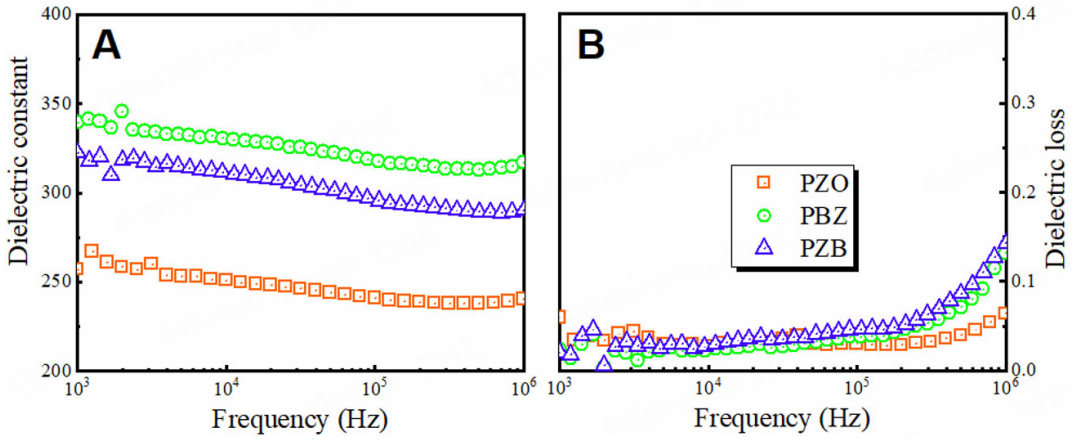

Figure 4. Frequency-dependent (A) dielectric constant and (B) dielectric loss for PZO-based films at room temperature. PZO: $PbZrO_3$.

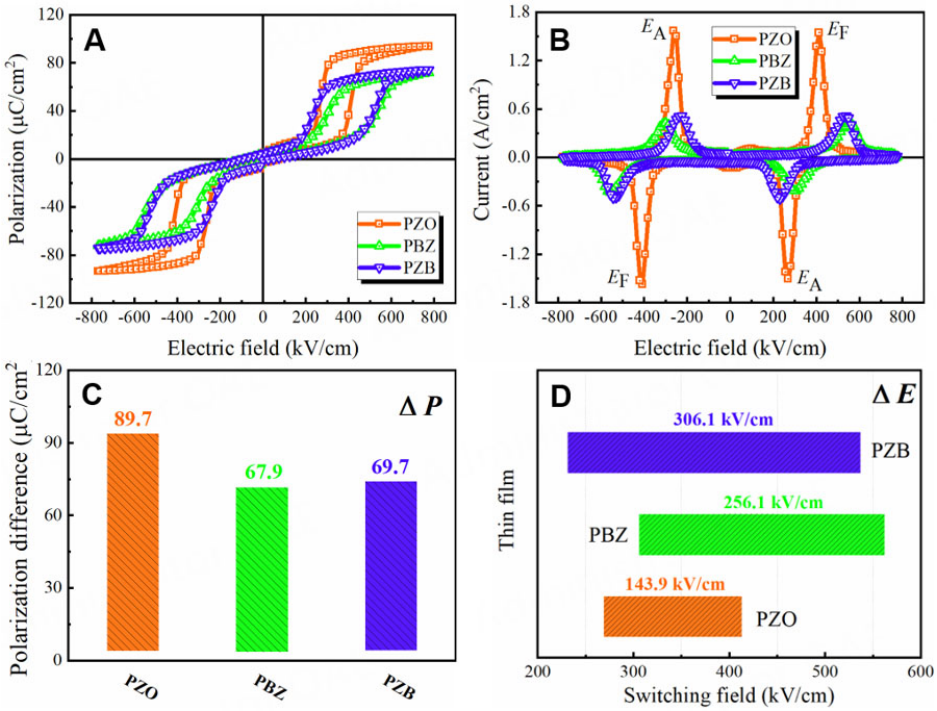

Figure 5. (A) The *P-E* loops of PZO-based films at 800 kV/cm, and corresponding (C) the polarization difference value of Δ *P* (P_{max} - P_r). (B) The *I-E* loops of PZO-based films at 800 kV/cm, and corresponding (D) the switching field value of Δ *E* (E_F - E_A). PZO: $PbZrO_3$.

strength enhances compared to pure PZO films, as exhibited in Figure 6B and C. The leakage current is a crucial parameter for evaluating dielectric film's electric properties and conduction mechanisms[20-23]. Figure 6D illustrates the leakage current for PZO-based films as a function of the electric field. It can be seen that the curve of leakage current of pure PZO films can be divided into two parts: For low electric field, the leakage conductivity belongs to the bulk-limited Ohmic mechanism. The Fowler-Nordheim tunneling (FN) mechanism dominates at high electric field. A similar phenomenon also exists in PBZ and PZB films. Note that the transition field from bulk-limited to FN mechanism gradually reduces for pure PZO, PBZ, and PZB films, which may be related to different defect types in aliovalent doping PZO at A/B sites. Compared to the lead vacancy, the oxygen vacancy may easily contribute more leakage currier; hence, the transformation field of PZB from Ohmic into FN mechanism reduces compared to PBZ.

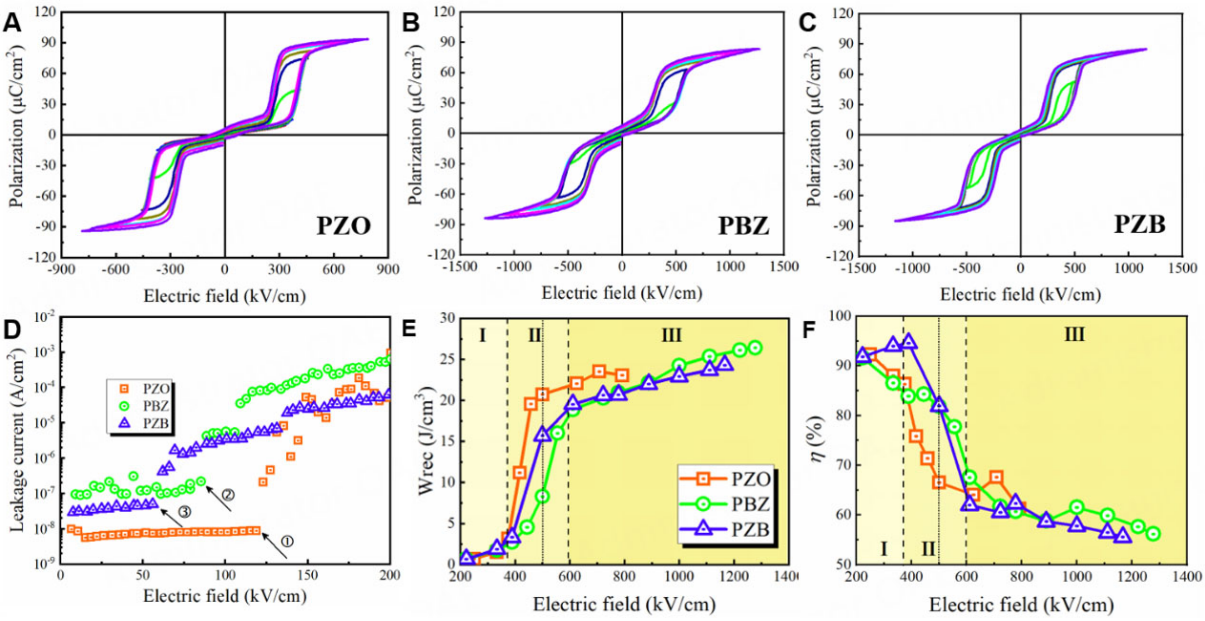

Figure 6. (A-C) The *P-E* loops of PBZ, PZB, and pure PZO films at different electric fields, respectively. (D) The leakage current functions of electric field for PZO-based films. (E) The recoverable energy density W_{rec} and (F) the energy efficiency η of PZO-based films at an applied electric field. PBZ: $(Pb_{0.95}Bi_{0.05})ZrO_3$; PZB: $Pb(Zr_{0.95}Bi_{0.05})O_3$; PZO: $PbZrO_3$.

Figure 6E shows the recoverable energy density W_{rec} as a function of the electric field for PZO-based films. Similar to other literature[24], a corresponding curve can be divided into three regions as the electric field increases. For region I, PZO-based films possess a low W_{rec} value, which should belong to the AFE phase stage with a linear polarization curve. For region II, W_{rec} of PZO-based films both sharply enhance, which should correspond to AFE-FE co-existed phase stage. Note that the dashed and dot lines represent different terminal transition fields into region III, which means Bi dope PZO would delay the polarization enhancement. The W_{rec} only slightly enhances into region III, which should be attributed to the polarization saturation phenomenon at the high electric field[25,26]. The energy efficiency η as functions of electric field for PZO-based films is displayed in Figure 6F. Similarly, the curves of η also could be divided into three regions. As the electric field enhances, the η value gradually decreases and attains a relatively 50%-60% range. PBZ films achieve a maximum W_{rec} of 26.4 J/cm^3 with a η of 56.2 %, which exceeds other reported pure AFE materials[27-29].

It is known that energy storage stability, including temperature and frequency[5,14,30], is an important parameter for evaluating the material applications, as shown in Figure 7. As temperature enhances, double hysteresis loop characteristics of PBZ films gradually transform into relaxor AFE, as shown in Figure 7A. Meanwhile, the W_{rec} gradually decreases and η value remains essentially unchanged (see Figure 7C), which should be related to the Curie temperature of PZO at about 230 °C, corresponding to the AFE-to-PE phase transition[8,31]. Figure 7B displayed frequency-dependent *P-E* loops of PBZ films at room temperature. As frequency enhances, polarization decreases and hysteresis loss also reduces. Therefore, the W_{rec} and η of PBZ films display good frequency stability, as shown in Figure 7D.

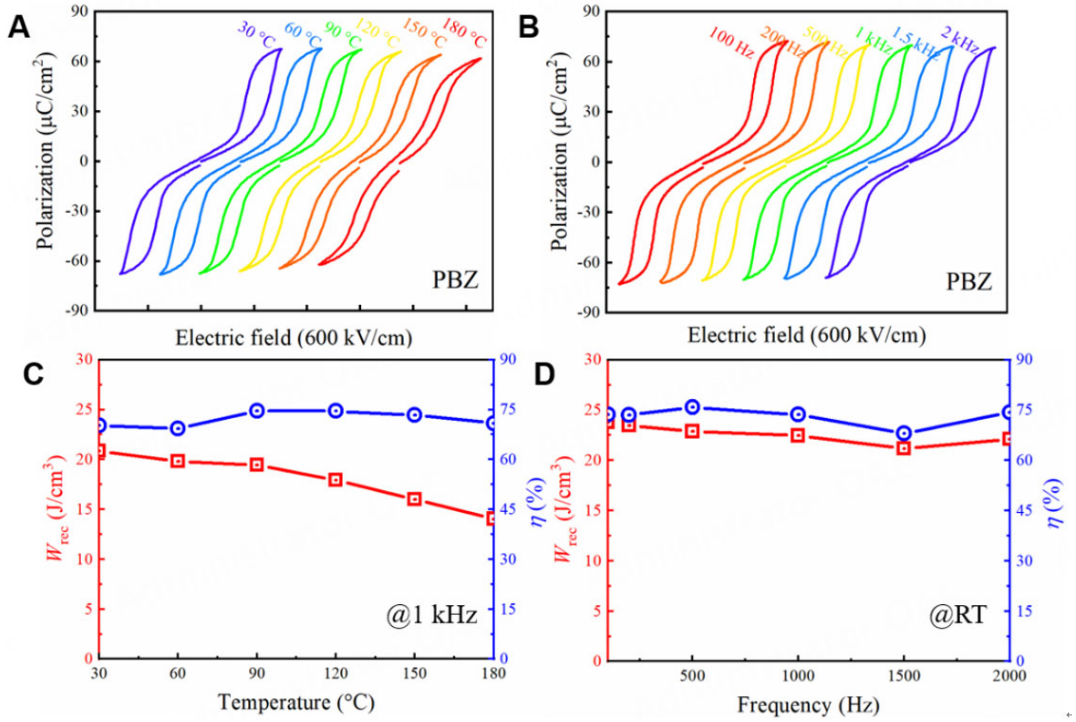

Figure 7. (A) Temperature-dependent *P-E* loops and corresponding (C) W_{rec}, η of PBZ films at 1 kHz. (B) Frequency-dependent *P-E* loops and corresponding (D) W_{rec}, η of PBZ films at room temperature. PBZ: $(Pb_{0.95}Bi_{0.05})ZrO_3$.

CONCLUSIONS

PZO, PBZ, and PZB films are prepared on Pt/Ti/SiO_2/Si substrate via the sol-gel method. Crystallized PZO-based films with orthorhombic perovskite phases exhibit low roughness and good density. The dielectric constants of the Bi-doped PZO and pure PZO films are approximately 300, and these films possess good frequency stability at room temperature. Compared to pure PZO films, ΔE value increases and ΔP decrease for PBZ and PZB films hindering the effective energy storage. A/B-site doping in influencing the antiferroelectricity of PZO has a similar effect in only considering t value, and A-site doping would be better than B-site one in energy storage properties. PBZ films achieve a high W_{rec} of 26.4 J/cm^3 with a η of 56.2 % under an applied electric field of 1278 kV/cm, accompanying a suitable temperature and frequency energy storage stabilities.

DECLARATIONS

Authors' contributions

Conceived the idea: Li D
Performed the experiments and data analysis: Li D, Guo Q, Cao M, Yao Z, Liu H, Hao H
Provided the technical support: Cao M, Yao Z, Liu H, Hao H
Wrote and reviewed the manuscript: Li D, Hao H

Availability of data and materials

Not applicable.

Financial support and sponsorship

This work was supported by Major Program of the Natural Science Foundation of China (Grant No. 51790490), Foshan Xianhu Laboratory of the Advanced Energy Science and Technology Guangdong

Laboratory (Grant No. XHT2020-011), Sanya Science and Education Innovation Park of Wuhan University of Technology (2020KF0017) and Guangdong Basic and Applied Basic Research Foundation (2022A1515010073).

Conflicts of interest

All authors declared that there are no conflicts of interest.

Ethical approval and consent to participate

Not applicable.

Consent for publication

Not applicable.

Copyright

REFERENCES

1. Yao Z, Song Z, Hao H, et al. Homogeneous/inhomogeneous-structured dielectrics and their energy-storage performances. *Adv Mater* 2017;29:1601727. DOI PubMed
2. Yang L, Kong X, Li F, et al. Perovskite lead-free dielectrics for energy storage applications. *Prog Mater Sci* 2019;102:72-108. DOI
3. Palneedi H, Peddigari M, Hwang G, Jeong D, Ryu J. High-performance dielectric ceramic films for energy storage capacitors: progress and outlook. *Adv Funct Mater* 2018;28:1803665. DOI
4. Li D, Zeng X, Li Z, et al. Progress and perspectives in dielectric energy storage ceramics. *J Adv Ceram* 2021;10:675-703. DOI
5. Pan H, Li F, Liu Y, et al. Ultrahigh-energy density lead-free dielectric films via polymorphic nanodomain design. *Science* 2019;365:578-82. DOI PubMed
6. Qi H, Xie A, Tian A, Zuo R. Superior energy-storage capacitors with simultaneously giant energy density and efficiency using nanodomain engineered $BiFeO_3$-$BaTiO_3$-$NaNbO_3$ lead-free bulk ferroelectrics. *Adv Energy Mater* 2020;10:1903338. DOI
7. Kittel C. Theory of antiferroelectric crystals. *Phys Rev* 1951;82:729-32. DOI
8. Hao X, Zhai J, Kong LB, Xu Z. A comprehensive review on the progress of lead zirconate-based antiferroelectric materials. *Prog Mater Sci* 2014;63:1-57. DOI
9. Randall CA, Fan Z, Reaney I, Chen L, Trolier-mckinstry S. Antiferroelectrics: history, fundamentals, crystal chemistry, crystal structures, size effects, and applications. *J Am Ceram Soc* 2021;104:3775-810. DOI
10. Zhao L, Liu Q, Gao J, Zhang S, Li JF. Lead-free antiferroelectric silver niobate tantalate with high energy storage performance. *Adv Mater* 2017;29:1701824. DOI PubMed
11. Tagantsev AK, Vaideeswaran K, Vakhrushev SB, et al. The origin of antiferroelectricity in $PbZrO_3$. *Nat Commun* 2013;4:2229. DOI PubMed
12. Aramberri H, Cazorla C, Stengel M, Íñiguez J. On the possibility that $PbZrO_3$ not be antiferroelectric. *NPJ Comput Mater* 2021;7:196. DOI
13. Hao X, Zhai J, Yao X. Improved energy storage performance and fatigue endurance of Sr-doped $PbZrO_3$ antiferroelectric thin films. *J Am Ceram Soc* 2009;92:1133-5. DOI
14. Luo N, Han K, Zhuo F, et al. Design for high energy storage density and temperature-insensitive lead-free antiferroelectric ceramics. *J Mater Chem C* 2019;7:4999-5008. DOI
15. Cai H, Yan S, Zhou M, et al. Significantly improved energy storage properties and cycling stability in La-doped $PbZrO_3$ antiferroelectric thin films by chemical pressure tailoring. *J Eur Ceram Soc* 2019;39:4761-9. DOI
16. Shimizu H, Guo H, Reyes-Lillo SE, Mizuno Y, Rabe KM, Randall CA. Lead-free antiferroelectric: $xCaZrO_3$-$(1-x)NaNbO_3$ system ($0<x<0.10$). *Dalton Trans* 2015;44:10763-72. DOI PubMed
17. Guo H, Shimizu H, Mizuno Y, Randall CA. Strategy for stabilization of the antiferroelectric phase (Pbma) over the metastable ferroelectric phase (P21ma) to establish double loop hysteresis in lead-free $(1-x)NaNbO_3$-$xSrZrO_3$ solid solution. *J Appl Phys* 2015;117:214103. DOI
18. Gao L, Guo H, Zhang S, Randall CA. A perovskite lead-free antiferroelectric $xCaHfO_3$-$(1-x)$ $NaNbO_3$ with induced double hysteresis loops at room temperature. *J Appl Phys* 2016;120:204102. DOI
19. Shannon RD. Revised effective ionic radii and systematic studies of interatomic distances in halides and chalcogenides. *Acta Cryst A* 1976;32:751-67. DOI
20. Chiu F. A review on conduction mechanisms in dielectric films. *Adv Mater Sci Eng* 2014;2014:1-18. DOI
21. Huang Y, Shu L, Zhang S, et al. Simultaneously achieved high-energy storage density and efficiency in $(K,Na)NbO_3$-based lead-free

ferroelectric films. *J Am Ceram Soc* 2021;104:4119-30. DOI

22. Fan Q, Ma C, Ma C, Lu R, Cheng S, Liu M. Manipulating leakage behavior via thickness in epitaxial $BaZr_{0.35}Ti_{0.65}O_3$ thin film capacitors. *Appl Phys Lett* 2020;116:192902. DOI
23. Jiang X, Lv J, Chen Z, et al. Superior energy storage $BaTiO_3$-based amorphous dielectric film with polymorphic hexagonal and cubic nanostructures. *Chem Eng J* 2022;431:133447. DOI
24. Chen X, Cao F, Zhang H, et al. Dynamic hysteresis and scaling behavior of energy density in $Pb_{0.99}Nb_{0.02}[(Zr_{0.60}Sn_{0.40})_{0.95}Ti_{0.05}]O_3$ antiferroelectric bulk ceramics. *J Am Ceram Soc* 2012;95:1163-6. DOI
25. Li D, Shen Z, Li Z, et al. Optimization of polarization behavior in (1-x)BSBNT-xNN ceramics for pulsed power capacitors. *J Mater Chem C* 2020;8:7650-7. DOI
26. Ren Y, Cheng H, Ouyang J, et al. Bimodal polymorphic nanodomains in ferroelectric films for giant energy storage. *Energy Storage Mater* 2022;48:306-13. DOI
27. Chen MJ, Ning XK, Wang SF, Fu GS. Significant enhancement of energy storage density and polarization in self-assembled $PbZrO_3$: NiO nano-columnar composite films. *Nanoscale* 2019;11:1914-20. DOI PubMed
28. Xu R, Wang M, Zhu Q, Xu Z, Feng Y, Wei X. Investigation on antiferroelectricity of $Pb_{0.97}La_{0.02}(Hf_{1-x}Ti_x)O_3$ ceramics with low Ti content ($0 \leq x \leq 0.1$). *J Am Ceram Soc* 2022;105:7438-45. DOI
29. Huang X, Zhang T, Wang W, Ge P, Tang X. Tailoring energy-storage performance in antiferroelectric $PbHfO_3$ thin films. *Mater Design* 2021;204:109666. DOI
30. Jiang X, Hao H, Zhang S, et al. Enhanced energy storage and fast discharge properties of $BaTiO_3$ based ceramics modified by $Bi(Mg_{1/2}Zr_{1/2})O_3$. *J Eur Ceram Soc* 2019;39:1103-9. DOI
31. Li YZ, Wang ZJ, Bai Y, Zhang ZD. High energy storage performance in Ca-doped $PbZrO_3$ antiferroelectric films. *J Eur Ceram Soc* 2020;40:1285-92. DOI

Liu *et al. Microstructures* 2023;3:2023008
DOI: 10.20517/microstructures.2022.31

Microstructures

Research Article

Open Access

Check for updates

Trilayer PVDF nanocomposites with significantly enhanced energy density and energy efficiency using $0.55Bi_{0.5}Na_{0.5}TiO_3$-$0.45(Sr_{0.7}Bi_{0.2})TiO_3$ nanofibers

Yuan Liu, Hang Luo, Haoran Xie, Zhida Xiao, Fan Wang, Xun Jiang, Xuefan Zhou, Dou Zhang

Powder Metallurgy Research Institute, State Key Laboratory of Powder Metallurgy, Central South University, Changsha 410083, Hunan, China.

Correspondence to: Prof./Dr. Hang Luo, Powder Metallurgy Research Institute, State Key Laboratory of Powder Metallurgy, Central South University, Changsha 410083, Hunan, China. E-mail: hangluo@csu.edu.cn; Prof./Dr. Dou Zhang, Powder Metallurgy Research Institute, State Key Laboratory of Powder Metallurgy, Central South University, Changsha 410083, Hunan, China. E-mail: dzhang@csu.edu.cn

How to cite this article: Liu Y, Luo H, Xie H, Xiao Z, Wang F, Jiang X, Zhou X, Zhang D. Trilayer PVDF nanocomposites with significantly enhanced energy density and energy efficiency using $0.55Bi_{0.5}Na_{0.5}TiO_3$-$0.45(Sr_{0.7}Bi_{0.2})TiO_3$ nanofibers. *Microstructures* 2023;3:2023008. https://dx.doi.org/10.20517/microstructures.2022.31

Received: 28 Sep 2022 **First Decision:** 24 Oct 2022 **Revised:** 5 Nov 2022 **Accepted:** 30 Nov 2022 **Published:** 11 Jan 2023

Academic Editors: Ruzhong Zuo, Shujun Zhang **Copy Editor:** Fangling Lan **Production Editor:** Fangling Lan

Abstract

The development of dielectric capacitors with high energy density and energy efficiency is of great significance in the modern electronic components market. To reduce the high energy loss of $Bi_{0.5}Na_{0.5}TiO_3$, $0.55Bi_{0.5}Na_{0.5}TiO_3$-$0.45(Sr_{0.7}Bi_{0.2})TiO_3$ (BNT-BST) nanofibers with a high aspect ratio are synthesized via electrospinning. To achieve a high energy density, the design of a symmetric trilayer nanocomposite consisting of a BNT-BST/polyvinylidene difluoride (PVDF) layer with a high dielectric constant sandwiched between two layers of pure PVDF is herein described. The trilayer structure can effectively alleviate the electric field concentration effect, resulting in a considerably enhanced breakdown strength and improved discharge energy density. The maximum discharge energy density of 17.37 J/cm^3 at 580 kV/mm could be achieved in the symmetric trilayer nanocomposite with a BNT-BST/PVDF middle layer, which is 90.5% greater than that achieved using pure PVDF (9.21 J/cm^3 at 450 kV/mm). This study presents a new case for developing dielectric capacitors with high energy density.

Keywords: Trilayer structure, electrospinning, $0.55Bi_{0.5}Na_{0.5}TiO_3$-$0.45(Sr_{0.7}Bi_{0.2})TiO_3$ nanofibers, breakdown strength, energy density

INTRODUCTION

The increasing global energy consumption and rising demand for low-carbon technologies in modern society have stimulated the development of renewable energy technology. Compared with electrochemical capacitors and batteries, dielectric capacitors have a higher power density and longer service life and are better suited for high-voltage, low-cost, and multifield applications[1-4]. Dielectric capacitors are therefore considered to be potential energy storage devices. Faced with the increased demand for the micro-nano integration of electronic components in modern society, it is technically challenging to simultaneously achieve high energy density and efficiency in dielectric capacitors[5-7].

Nanocomposite films, which integrate a ceramic filler with a high dielectric constant and a polymer matrix with a high breakdown electric field, provide novel ways for designing dielectric capacitors with high energy density[8-11]. The researchers improved the energy storage performance of nanocomposites by incorporating zero-dimensional (0D) ceramic nanoparticles, one-dimensional (1D) ceramic nanofibers, or two-dimensional (2D) ceramic nanosheet fillers into the polymer matrix[12-15]. Compared with 2D ceramic nanosheet fillers, 1D ceramic nanofibers are easier to synthesize. Compared with 0D ceramic nanoparticle fillers, the incorporation of 1D ceramic nanofibers with a high aspect ratio into a polymer matrix can considerably improve the energy storage performance of nanocomposites. Conversely, 1D ceramic nanofibers possess a greater dipole moment, which contributes to an increase in the dielectric constant. In contrast, 1D ceramic nanofibers have a smaller specific surface area and can be dispersed more uniformly in a polymer matrix, which is advantageous for alleviating electric field concentration and enhancing breakdown strength. Moreover, 1D ceramic nanofibers as fillers have a lower percolation threshold. This implies that the dielectric constant of nanocomposites will achieve its maximum value with a small amount of loading[16,17], as demonstrated by the work of Song *et al.*[18].

$Bi_{0.5}Na_{0.5}TiO_3$ (BNT) ceramic is widely used in energy storage devices owing to its high dielectric constant and powerful saturation polarization value. However, pure BNT ceramics have a rhombohedral R3c structure and high remanent polarization value at room temperature, which would significantly impede the enhancement of energy storage density and energy efficiency of BNT ceramic[19-21]. A new binary system ceramic material could be created by combining relaxor ferroelectric $Sr_{0.7}Bi_{0.2}TiO_3$ (BST) with ferroelectric BNT with extremely low remanent polarization values while maintaining the high polarization value of BNT at room temperature. For example, $0.55Bi_{0.5}Na_{0.5}TiO_3$-$0.45(Sr_{0.7}Bi_{0.2})TiO_3$ (BNT-BST) has a high saturation polarization value and low remanent polarization value, which is advantageous for improving the discharge energy density and energy efficiency of nanocomposites[22-24].

With the advantages of simple equipment, various spinnable raw materials, excellent fiber structure tunability, and strong expansion of preparation technology, electrospinning is an efficient and low-cost method for preparing nanofibers that have been rapidly developed in recent years and are widely used to produce organic, inorganic, and organic/inorganic composite nanofiber materials[25]. Polymer dielectrics with optimized multilayer structures have emerged to resolve the contradictions between nanocomposites with a high dielectric constant and high breakdown electric field. The multilayer structures use the blocking effect of the ordered interface on charge migration, which can effectively suppress the distortion of the local electric field and propagation of electrical tree branches and significantly elevate the energy storage performance of the nanocomposites[26-28], as demonstrated in our previous work[29].

In this study, BNT-BST nanofibers with a high aspect ratio and an average diameter of 280.8 nm were fabricated via electrospinning. Monolayer and symmetric trilayer polyvinylidene difluoride (PVDF)-based nanocomposites with varied BNT-BST nanofiber loadings were prepared using the solution-casting

method. Further, 0-x-0 (where x is the weight fraction of BNT-BST in the middle layer) was designed and fabricated to evaluate the breakdown strength and energy storage behavior of PVDF-based nanocomposites. The breakdown electric field increases from 450 kV/mm for pure PVDF to 580 kV/mm for the symmetric trilayer 0-2-0 sample, and the discharge energy density increases from 9.12 J/cm^3 to 17.37 J/cm^3, which is 90.5% greater than that of pure PVDF. These findings may offer a general strategy for improving the energy storage performance of dielectric capacitors for high energy/power density storage systems.

MATERIALS AND METHODS

Materials. Solutions of CH_3COOH, $CH_3OCH_2CH_2OH$, 2,4-pentanedione $C_5H_8O_2$, $Ti(CH_3(CH_2)_3O)_4$, and N,N-dimethylformamide (DMF, 99.5%) were purchased from Sinopharm Chemical Reagent Co. Polyvinylpyrrolidone (M_w = 1,300,000, Macklin), $Bi(COOCH_3)_3$ (99.9%, Macklin), $NaCOOCH_3{\cdot}3H_2O$ (AR, Aladdin), $Sr(COOCH_3)_2{\cdot}1/2H_2O$ (AR, Aladdin), and PVDF (6020, Solvay) were used.

Synthesis of 50 mL BNT-BST electrospinning precursor. Initially, 2.2196 g $Bi(COOCH_3)_3$, 0.5894 g $NaCOOCH_3{\cdot}3H_2O$, and 0.9720 g $Sr(COOCH_3)_2{\cdot}1/2H_2O$ were dissolved in a solution of 15-mL CH_3COOH and 15-mL $CH_3OCH_2CH_2OH$ and stirred at 40 °C for 30 min to generate a uniform solution A. Subsequently, 3.0033 g $C_5H_8O_2$ was added to 5.1048 g $Ti(CH_3(CH_2)_3O)_4$ and stirred at 40 °C for 30 min to generate solution B. Finally, solution B was gently added to solution A, followed by the addition of $CH_3OCH_2CH_2OH$ and vigorous stirring to bring the volume of the combination to 50 mL of solution C.

Synthesis of BNT-BST nanofibers via electrospinning. Solution C was mixed with an adequate amount of polyvinylpyrrolidone and stirred at 40 °C for 24 h to obtain solution D. The prepared solution D was placed into a disposable syringe, and the syringe was attached to the electrospinning equipment to produce nanofibers. The electrospinning environment was maintained at 40 °C, and the relative humidity was maintained at < 15%. The applied voltage was 10 kV, the solution flow rate was 1 mL/h, and the distance between the needle tip and collector was 10 cm. The nanofibers were collected on release paper, dried at 70 °C for 24 h, and then placed in a high-temperature sintering furnace at 300 °C and 700 °C, respectively, for 1 h with a heating rate of 3 °C /min.

Preparation of BNT-BST/PVDF nanocomposites via solution casting. The BNT-BST/PVDF nanocomposites were manufactured following a previously published report[29]. All nanocomposite samples had a thickness between 12 and 15 um, and each layer in the trilayer samples was ~5 um thick. The fabrication process of BNT-BST/PVDF nanocomposites with a monolayer and symmetric trilayer structure is shown in Figure 1. Further, 2 wt% BNT-BST constituted the monolayer nanocomposite, and a 0-2-0 nanocomposite with a trilayer structure was prepared by loading 2 wt% BNT-BST nanofibers as the middle layer. The final electrode for the electrical performance test was a 2 mm diameter Au electrode.

Characterization. X-ray diffraction (Advance D8), scanning electron microscopy (MIRA4 LMH), piezoelectric force microscopy (Nanoman TM VS), thermogravimetric analysis (TGA, 8000-FTIR-GCMS), transmission electron microscopy (TEM, Titan G2 60-300), and X-ray photoelectron spectroscopy (XPS, ESCALAB250Xi) were employed to investigate the microstructural information of BNT-BST nanofibers. The dielectric properties, displacement hysteresis loops, and pulse discharge performance of nanocomposites were characterized using an Agilent 4990A, TF Analyzer 2000 (aixACT, Germany) at 10 Hz, and dielectric material charge measurement system DCQ-20A (PolyK Technologies, USA), respectively.

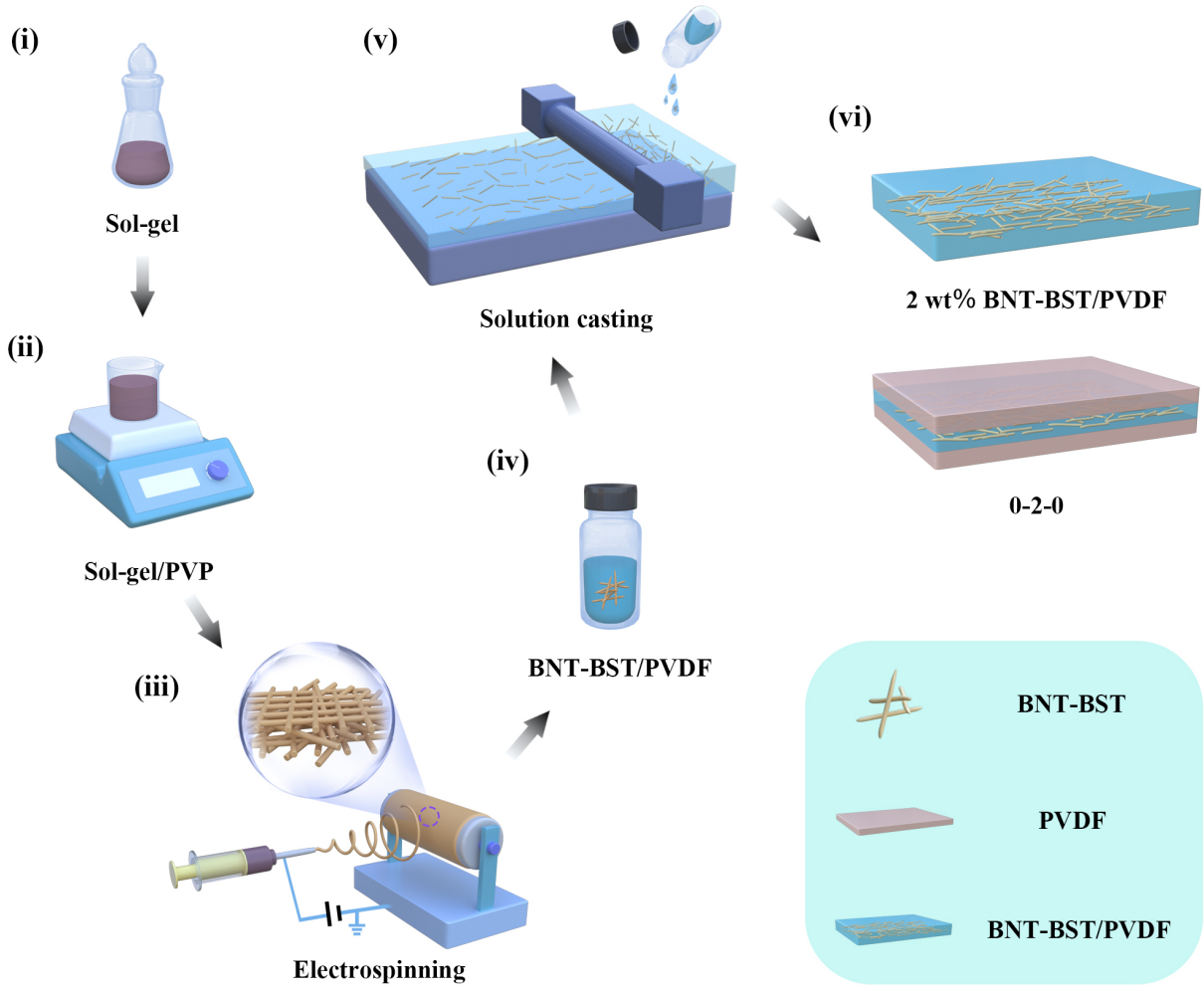

Figure 1. Schematic of the fabrication process for $0.55Bi_{0.5}Na_{0.5}TiO_3$-$0.45(Sr_{0.7}Bi_{0.2})TiO_3$ (BNT-BST)/ polyvinylidene difluoride (PVDF) nanocomposites. (i) Configuring the sol-gel of BNT-BST. (ii) Mixing of polyvinylpyrrolidone and BNT-BST sol-gel. (iii) Electrospinning process. (iv) Dispersion process of BNT-BST nanofibers in PVDF. (v) Solution-casting process. (vi) Schematic of nanocomposites.

RESULTS AND DISCUSSION

The crystallinity of BNT-BST nanofibers is shown in Figure 2A. Refinement of the raw X-ray diffraction data revealed that BNT-BST had a two-phase coexistence with 90.012% of the P4bm (PDF#70-4760) phase and 9.988% of the R3c (PDF#36-0153) phase, respectively. Figure 2B shows the microscopic topography of the electrospun precursors that have nanofibers before sintering. The diameter of the nanofibers obtained from the electrospinning precursors was ~260-650 nm, with an average diameter of 498.8 nm. The precursor nanofibers had a smooth exterior. To further determine the sintering parameters of electrospun nanofibers, the precursor nanofibers were subjected to TGA; the result is shown in Figure 2C. The weight losses were 10.82% (30-180 °C), 38.67% (180-400 °C), and 12.11% (400-800 °C) due to the rapid vaporization of the electrospinning solution, breakdown of the acetate ligand, and pyrolysis of the gel, respectively[30,31]. According to TGA, BNT-BST nanofibers can be produced by maintaining the electrospun nanofibers at 300 °C and 700 °C for 1 h. Figure 2D and E show the morphology and diameter distribution of BNT-BST nanofibers after sintering and crushing. According to the statistical results of the histogram, the diameter distribution and average diameter of BNT-BST nanofibers were 150-380 nm and 280.8 nm, respectively. The ferroelectric response of BNT-BST nanofibers was investigated using piezoelectric force microscopy. To

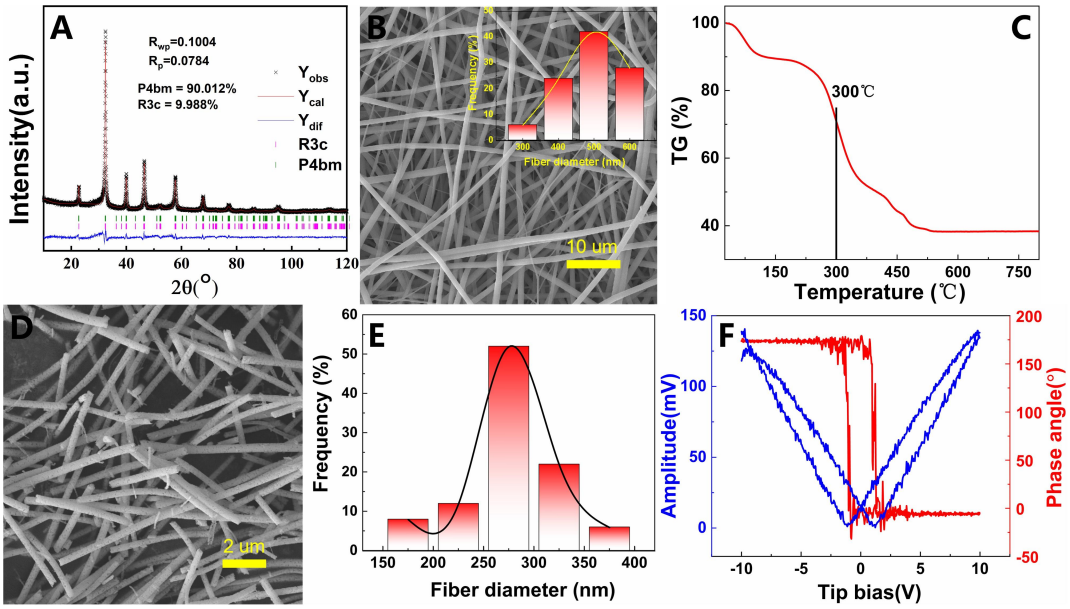

Figure 2. (A) X-ray diffraction pattern of $0.55Bi_{0.5}Na_{0.5}TiO_3$-$0.45(Sr_{0.7}Bi_{0.2})TiO_3$ (BNT-BST) nanofibers. (B) Scanning electron microscopy (SEM) image before sintering. (C) Thermogravimetric analysis of electrospinning nanofibers. (D) SEM image after sintering. (E) Diameter distribution. (F) Piezoelectric force microscopy image of BNT-BST nanofibers.

examine the local polarization reversal of BNT-BST nanofibers, a DC bias voltage of -10 V to +10 V was applied to its surface, and the BNT-BST nanofibers exhibited a 180° change in phase angle, as shown in Figure 2F. Simultaneously, a distinct amplitude-voltage butterfly curve with an amplitude of 140 mV and polarization reversal behavior was observed in this BNT-BST nanofiber.

The structure of the BNT-BST nanofibers was determined via TEM. Figure 3A is a TEM image of a BNT-BST nanofiber. Figure 3B demonstrates that the localized region has a lattice spacing of 0.295 nm, which corresponds to the (110) plane of the BNT-BST nanofiber. Figure 3B demonstrates the presence of distinct lattice fringes in a second region with an interplanar space of 0.390 nm, which is generated by the (101) plane of the BNT-BST nanofibers. The insets of Figure 3B and C show the selected area electron diffraction patterns along the [111] and [110] orientations for the corresponding selected areas, respectively. These results are comparable to those described in the literature, demonstrating further that BNT-BST nanofibers exhibit a pseudocubic phase with polar nano regions[22,32]. Figure 3D shows the element mapping images for O, Na, Ti, Sr, and Bi elements. O, Na, Ti, Sr, and Bi elements appear to be consistently distributed in BNT-BST nanofiber.

Figure 4A shows the XPS survey spectrum of BNT-BST nanofibers, in which the presence of Bi 4f, Na 1s, Ti 2p, Sr 3d, and O 1s is evident. Peak C has a standard binding energy of 284.8 eV. Figure 4B depicts the spectrum of Bi 4f, which reveals two peaks at 164.29 eV and 158.98 eV associated with Bi $4f_{5/2}$ and Bi $4f_{7/2}$, respectively. The binding energy for Na 1s is 1070.94 eV, which corresponds to the Na^+ ion [Figure 4C]. In the high-resolution Ti^{4+} XPS spectra [Figure 4D], the Ti $2p_{1/2}$ and Ti $2p_{3/2}$ appeared at 464.74 and 458.05 eV, respectively[33]. The presence of Sr^{2+} is indicated by the binding energies of Sr $3d_{3/2}$ and Sr $3d_{5/2}$, which are 134.49 eV and 132.76 eV, respectively [Figure 4E][34]. In Figure 4F, the O 1s spectra for BNT-BST nanofibers exhibit the main peaks at 530.34 eV and 529.49 eV corresponding to the bonded oxygen in oxygen-deficient regions and lattice oxygen, respectively[35].

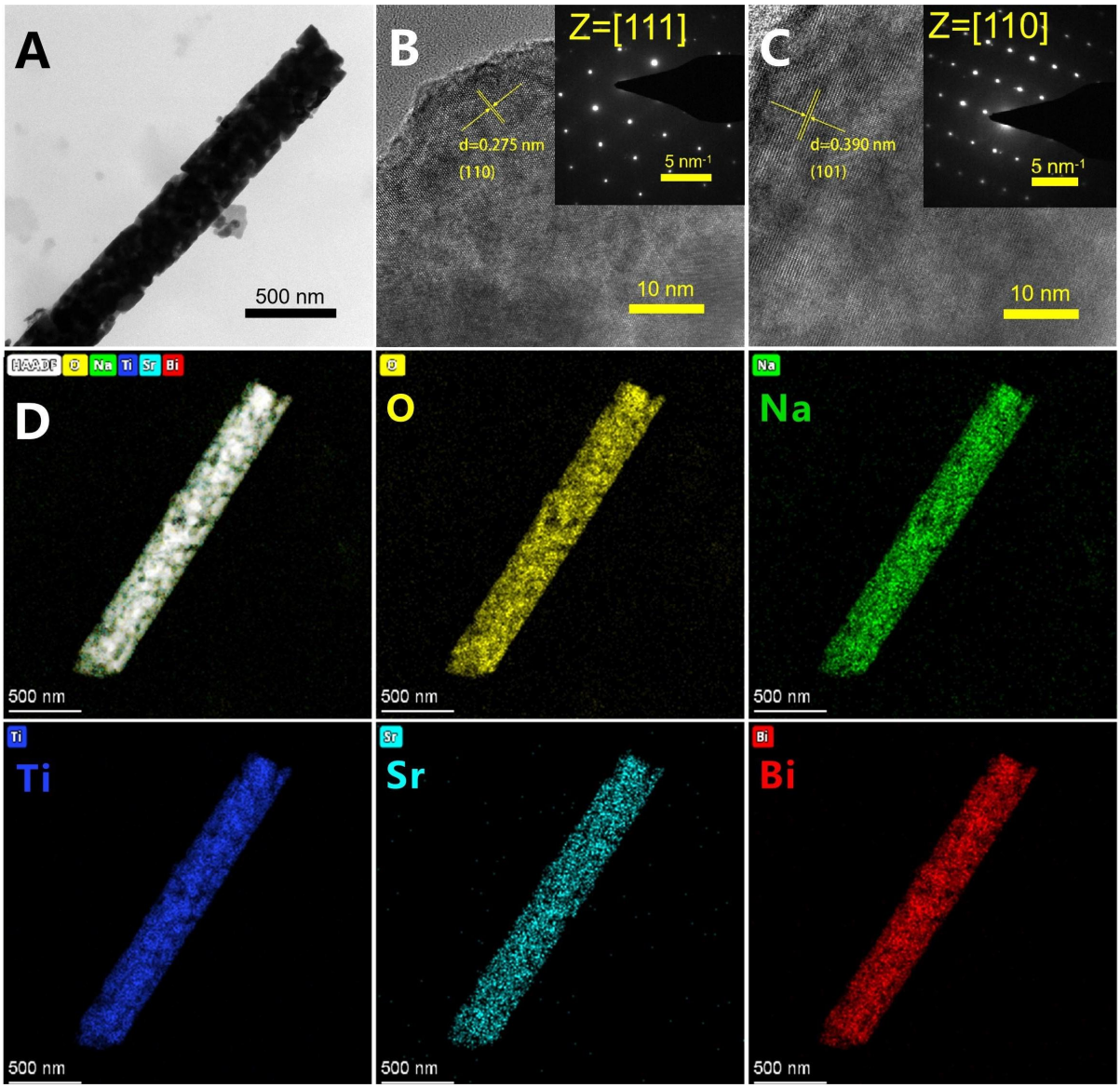

Figure 3. (A) Transmission electron microscopy (TEM) image. (B and C) High-resolution TEM images. (D) Element mapping images of $0.55Bi_{0.5}Na_{0.5}TiO_3$-$0.45(Sr_{0.7}Bi_{0.2})TiO_3$ nanofiber.

Figure 5 depicts dielectric properties as a function of frequency for monolayer and trilayer BNT-BST/PVDF nanocomposites. The dielectric constant (ε) of the monolayer BNT-BST/PVDF nanocomposite decreased steadily with frequency owing to the intrinsic dielectric relaxation of the PVDF polymer[29,33]. For instance, the ε of monolayer BNT-BST/PVDF nanocomposites with 8 wt% BNT-BST nanofibers was 12.12 at 10^3 Hz and 7.28 at 10^7 Hz [Figure 5A]. Figure 5A and B demonstrate that the incorporation of BNT-BST nanofibers may increase the dielectric constant of PVDF-based nanocomposites. At 1 kHz, the ε of pure PVDF, 1 wt%, 2 wt%, 4 wt%, 6 wt%, and 8 wt% monolayer BNT-BST/PVDF nanocomposites, respectively, were 9.53, 10.29, 10.49, 10.86, 11.57, and 12.12. The ε was increased owing to the intrinsically high dipole polarization of BNT-BST nanofibers and the interfacial polarization in the nanocomposites. The interface between the BNT-BST/PVDF layer and the pure PVDF layer must be considered in nanocomposites with a trilayer structure. The electron trap would form at the interface and gather at the region of interface, thus enhancing interfacial polarization and increasing permittivity[36]. Figure 5C shows the frequency-dependent dielectric

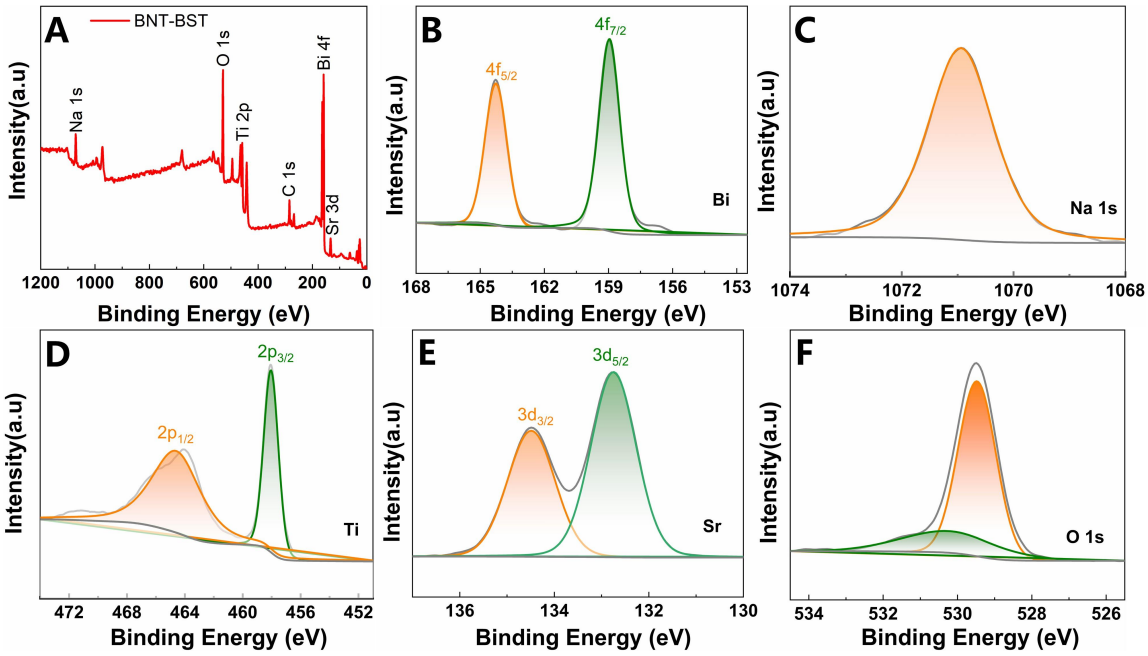

Figure 4. X-ray photoelectron spectroscopy spectra of $0.55Bi_{0.5}Na_{0.5}TiO_3$-$0.45(Sr_{0.7}Bi_{0.2})TiO_3$ nanofibers: (A) survey spectra, (B) Bi, (C) Na, (D) Ti, (E) Sr, and (F) O.

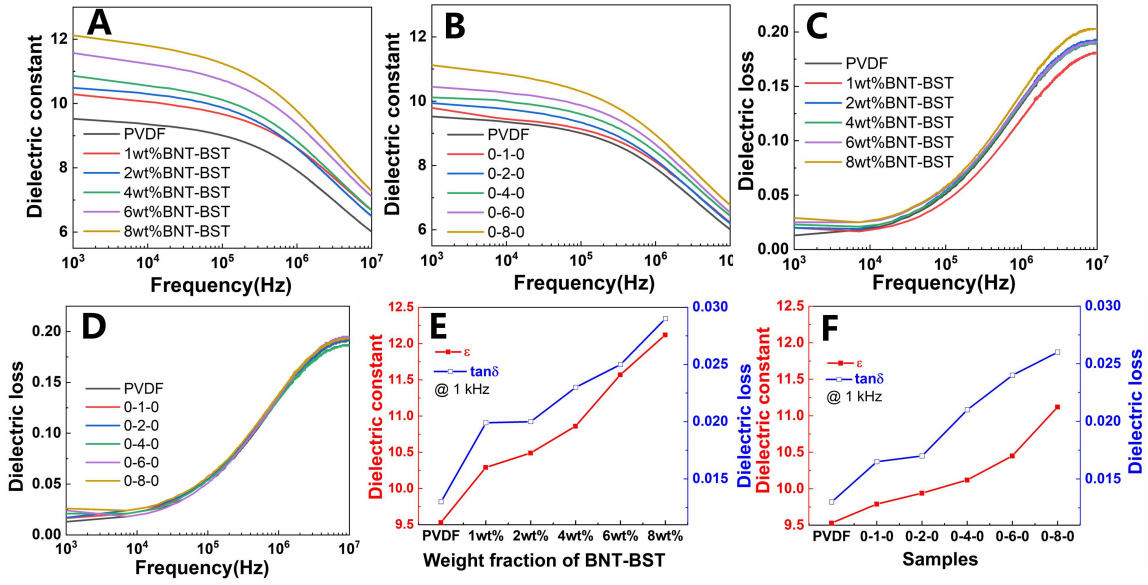

Figure 5. (A and B) ε and (C and D) dielectric loss of monolayer and trilayer nanocomposites. (E and F) ε and dielectric loss at 1 kHz of nanocomposites with various $0.55Bi_{0.5}Na_{0.5}TiO_3$-$0.45(Sr_{0.7}Bi_{0.2})TiO_3$ nanofiber loadings.

loss of monolayer BNT-BST/PVDF nanocomposites. The dielectric loss of nanocomposites is primarily caused by two factors: conduction loss and polarization loss[37].

As shown in Figure 5B and D, the frequency dependence of the dielectric characteristics of the symmetric trilayer nanocomposites is comparable to that of the monolayer BNT-BST/PVDF nanocomposites. The analysis of ε and dielectric loss at 1 kHz of the nanocomposites is shown in Figure 5E and F. Notably, the

most significant enhancement was observed at 8 wt% monolayer BNT-BST/PVDF nanocomposites, i.e., from 9.53 for pure PVDF to 12.12 at 1 kHz, which is a 27% improvement. It is important to note that the dielectric loss of monolayer BNT-BST/PVDF nanocomposites was consistently larger than that of trilayer nanocomposites at the same mass fractions. The dielectric loss of 1 wt%, 2 wt%, 4 wt%, 6 wt%, and 8 wt% monolayer BNT-BST/PVDF nanocomposites was 0.0199, 0.0201, 0.0228, 0.0253, and 0.0288, respectively, as shown in Figure 5E. Figure 5F shows the dielectric loss at 1 kHz for 0-1-0, 0-2-0, 0-4-0, 0-6-0, and 0-8-0 trilayer BNT-BST nanocomposites to be 0.0165, 0.0172, 0.0206, 0.0243, and 0.0261, respectively. This is primarily attributable to the trilayer structure. Compared to the BNT-BST/PVDF nanocomposite layer, the pure PVDF outer layer in the symmetric trilayer nanocomposites had lower electron mobility and greater insulation, as well as limited charge injection at the dielectric/dielectric interface. In addition, a high number of deep traps existed at the interlayer interface of the trilayer structure, thereby impeding the long-distance migration of electrons and reducing the leakage current considerably[15,29,38].

Figure 6A and B show the corresponding P-E loops for each nanocomposite at the maximum breakdown electric field. The BNT-BST nanofibers can enhance saturation polarization at high electric fields due to the wide enclosed area between the P-E loop and the vertical P axis, which is advantageous for attaining a larger discharge energy density in the nanocomposite. In addition to high saturation polarization, achieving high breakdown strength (E_b) is crucial for obtaining a high discharge energy density. The effect of BNT-BST nanofibers with a high aspect ratio on the breakdown strength of nanocomposites is effectively illustrated here using the Weibull statistical Equation (1):

$$P(E)=1-\exp\left(-(E/E_b)^{\beta}\right) \tag{1}$$

where $P(E)$, E, E_b, and β are the cumulative failure probability, breakdown electric field of the experimental test sample, breakdown strength with a nanocomposite breakdown probability of 63.2%, and shape parameter or slope obtained by fitting, respectively. As shown in Figure 6C and D, the breakdown electric field was measured at least nine times for each nanocomposite, and the results were calculated using Weibull statistics. The Weibull distribution breakdown electric field for each nanocomposite sample is displayed in Figure 6E and F. For example, the E_b of pure PVDF, 1 wt%, 2 wt%, 4 wt%, 6 wt%, and 8 wt% monolayer BNT-BST/PVDF nanocomposites was 431.3 kV/mm, 432.5 kV/mm, 445.7 kV/mm, 401.1 kV/mm, 344.6 kV/mm, and 332.5 kV/mm, respectively. In monolayer BNT-BST/PVDF nanocomposites, the BNT-BST nanofibers with a high aspect ratio and small specific surface area were easily dispersed and distributed along the plane during the solution-casting process. When oriented perpendicular to the direction of the electric field, BNT-BST nanofibers can provide an ordered electron scattering center[39]. The BNT-BST nanofibers extended a tortuous breakdown path in the growth of the electrical tree over the breakdown process, thereby limiting the transfer of charges to the electrode, hindering the extension of the electrical tree, and resulting in an increase in E_b[39,40]. However, the overlapping interfaces between PVDF and BNT-BST nanofibers, particularly when the overloaded BNT-BST nanofibers aggregate in the PVDF matrix, result in an uneven distribution of the electric field, thus providing conducting routes for carriers. In addition, the incorporation of BNT-BST nanofibers leads to defects such as air porosity and inorganic-organic interface, which increases the leakage current of BNT-BST/PVDF nanocomposites and decreases E_b. Contrary to monolayer nanocomposites, trilayer nanocomposites may spatially modify the distribution of the electric field and have a higher E_b despite a high filler loading. Specifically, the E_b and β of pure PVDF, 0-1-0, 0-2-0, 0-4-0, 0-6-0, and 0-8-0 samples are 431.3 kV/mm (β~20.7), 535.5 kV/mm (β~25.3), 568.0 kV/mm (β~33.3), 524.0 kV/mm (β~28.8), 516.7 kV/mm (β~20.5), and 494.7 kV/mm (β~16.1), respectively. The justifications are as follows: first, the BNT-BST nanofibers aligned perpendicular to the direction of the electric field increase the electron

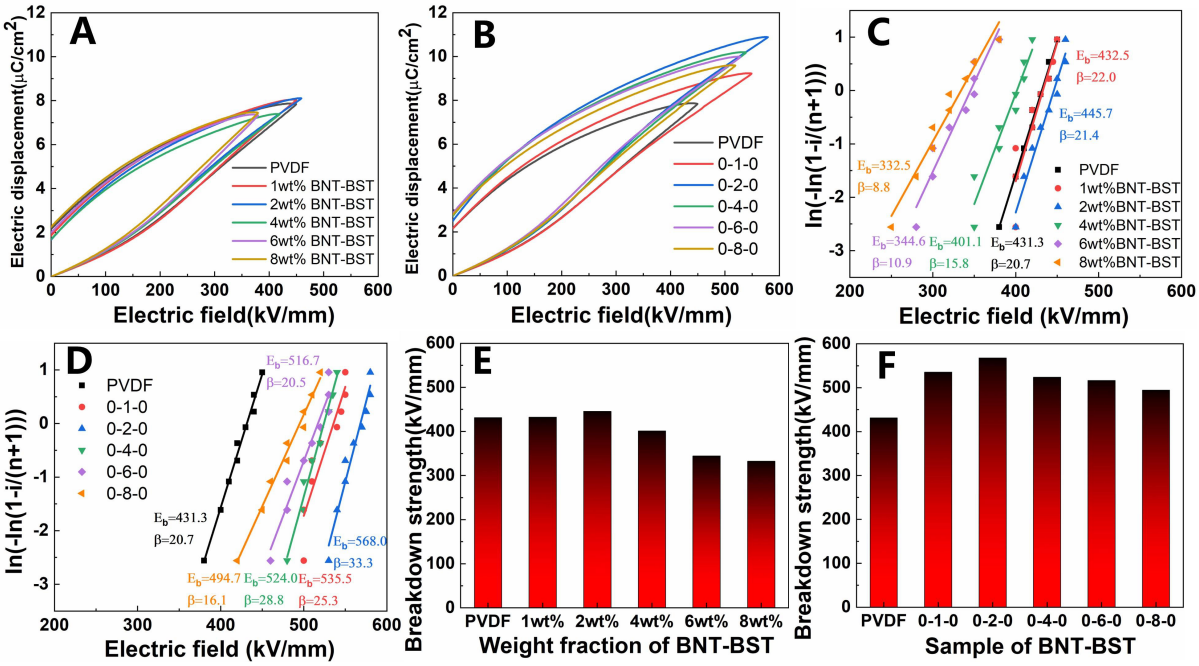

Figure 6. (A and B) P-E loops. (C and D) Weibull plots. (E and F) E_b from Weibull plots of monolayer and trilayer nanocomposites.

tortuosity of the path for electrons, hinder the growth of the electric tree, and raise the breakdown electric field of nanocomposites. Second, the pure PVDF outer layer with low conductivity contained in the trilayer structure limits the charge injection of the electrode and the electric field concentration impact, as well as hinders the extension of the electric tree during the breakdown process. Third, trilayer nanocomposites can alleviate the electric field concentration effect, and the introduction of electron traps increases breakdown path, further hinders the transport of carriers, and minimizes losses, thereby improving the breakdown electric field and discharge energy density[15,26-28].

Figure 7 shows the variation curves of discharge energy density (U_{dis}) and energy efficiency (η) for each sample with varying electric fields as determined by the integration of P-E loops. Figure 7A and B show that the U_{dis} value of the same sample increases monotonically with the applied electric field. In the same electric field, the introduction of BNT-BST nanofibers and interfacial polarization results in an increase in electrical displacement with increasing BNT-BST nanofiber loading. The electric field is high, as is the integral value of the effective area, and U_{dis} are large. However, Figure 7C and D show that η first decreases and then increases with an electric field, which is mostly attributable to the ferroelectric conversion in PVDF[41]. Under the same electric field, η first increases and then decreases with the increased loading of BNT-BST nanofibers. As the outermost layer, pure PVDF can sustain a greater external electric field, mitigating the effect of electric field concentration within the nanocomposite. The interface between BNT-BST nanofibers and pure PVDF matrix, as well as the interlayer interface of the trilayer structure, inhibited the extension and growth of the electrical tree and reduced the increase in leakage current, both of which are advantageous for preventing early dielectric breakdown and promoting the improvement of E_b and η. Therefore, the synergy between the outer insulating layer and the central composite layer is key to concurrently improving U_{dis} and η[27,28]. However, the overloaded BNT-BST nanofibers lead to an increase in defects and leakage current, which reduces U_{dis} and η. Figure 7E and F show the corresponding U_{dis} and η for each sample at the maximum breakdown electric field. For example, the U_{dis} and η of pure PVDF and symmetric trilayer nanocomposites were 9.12 J/cm³ (45.72%), 14.05 J/cm³ (51.63%), 17.37 J/cm³ (52.93%),

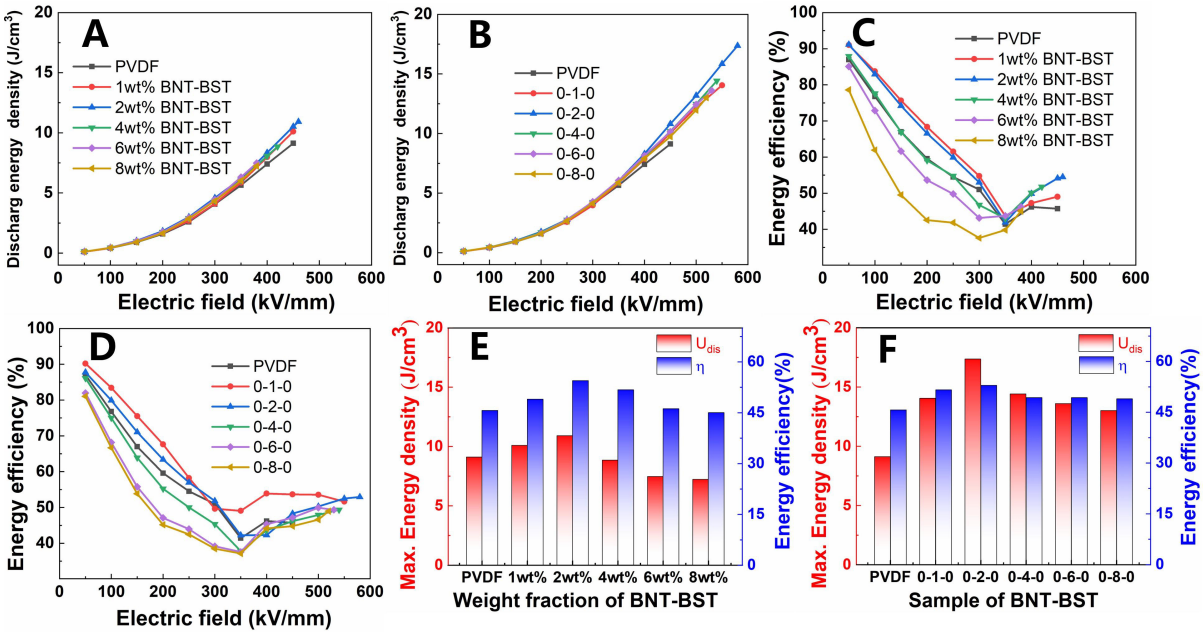

Figure 7. (A and B) U_{dis}, (C and D) η, (E and F) U_{dis} and η at each E_{Max} of monolayer and trilayer nanocomposites.

14.43 J/cm³ (49.34%), 13.61 J/cm³ (49.34%), and 13.01 J/cm³ (48.98%), respectively. Figure 7F reveals that the U_{dis} and η of the 0-2-0 sample are 17.37 J/cm³ and 52.93%, respectively, at 580 kV/mm, which are 90.5% and 7.2% more than those of pure PVDF (9.12 J/cm³ and 45.72% at 450 kV/mm).

To better characterize the uniform stability of the 0-2-0 sample, the average values of U_{dis} and η of the 0-2-0 sample in several places with varying electric fields were measured, as shown in Figure 8A and B. The variation patterns of U_{dis} and η for the electric field were consistent, as shown in Figure 7. In addition, the radar chart emphasized the overall performance of the 0-2-0 sample. The larger the area of the radar chart, the better the overall performance of the nanocomposites. The five parameters of U_{dis}, η, β, ε, and E_b of pure PVDF, 2 wt% monolayer BNT-BST/PVDF nanocomposites, and the symmetric trilayer 0-2-0 sample are compared in Figure 8C. The results show that the area encompassed by the 0-2-0 sample is the largest, indicating that the 0-2-0 sample has superior performance in all respects. Finally, the overdamped discharge curve of the 0-2-0 sample in various electric fields was examined using a dielectric material charge measurement system with a resistance of 10 kΩ [Figure 8D and E]. The peak current reached 0.505 A for 0.228 μs. Figure 8F shows that the pulse discharge energy density (W_d) of the 0-2-0 sample is 5.30 J/cm³ at 400 kV/mm and 10 μs compared with 3.10 J/cm³ for pure PVDF.

CONCLUSIONS

In conclusion, BNT-BST nanofibers with high aspect ratios were prepared using the electrospinning method. Monolayer and symmetric trilayer PVDF-based nanocomposites with varied BNT-BST nanofiber loadings were prepared using the solution-casting method. It was proved that trilayer nanocomposites are more effective than monolayer nanocomposites at enhancing the energy storage performance of dielectric nanocomposites. The reason is that a pure PVDF layer with excellent insulating properties helps prevent charge injection and current leakage by inhibiting the development of electrical trees. Therefore, a high energy density of 17.37 J/cm³ and an efficiency of 52.93% are simultaneously achieved in the optimized 0-2-0 sample. We believe that the trilayer design strategy is crucial for investigating dielectric capacitors with high energy density.

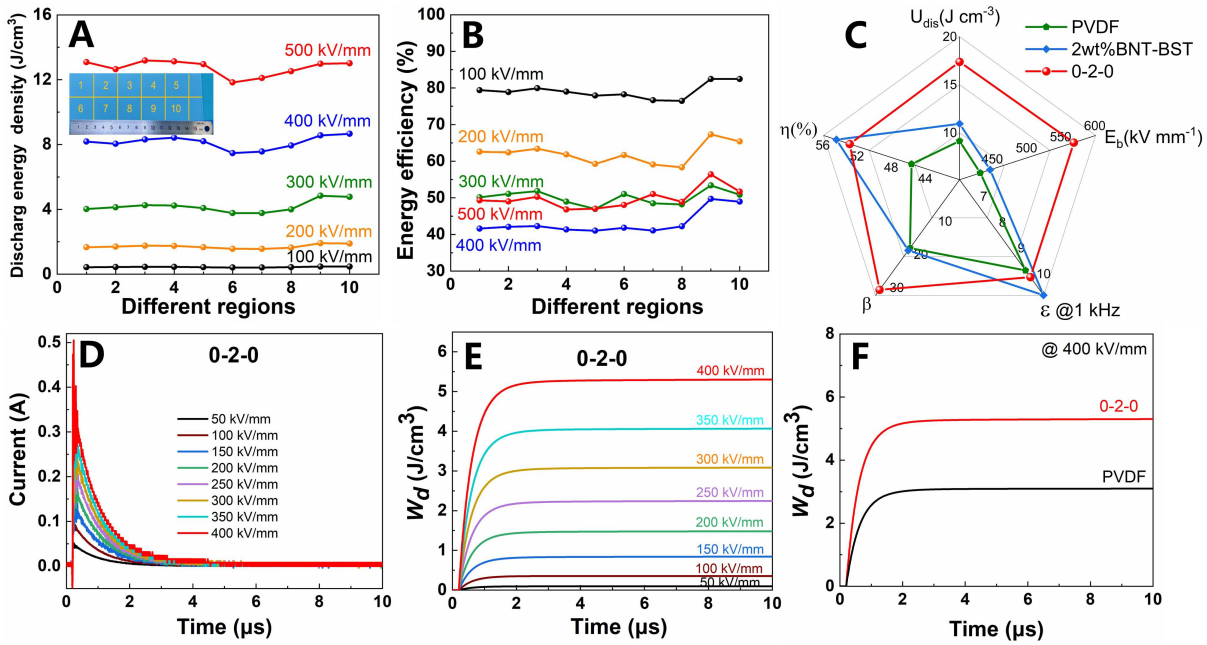

Figure 8. (A) U_{dis} and (B) η of different regions of the 0-2-0 sample tested with different electric fields. (C) Radar plots of pure polyvinylidene difluoride (PVDF), 2 wt% monolayer $0.55Bi_{0.5}Na_{0.5}TiO_3$-$0.45(Sr_{0.7}Bi_{0.2})TiO_3$ (BNT-BST)/PVDF and trilayer 0-2-0 sample. (D) Overdamped discharge curves. (E) Time dependence of W_d with different electric fields of the 0-2-0 sample. (F) Variation rule of W_d with time for pure PVDF and the 0-2-0 sample at 400 kV/mm.

DECLARATIONS

Authors' contributions

Conception, design, writing and editing: Liu Y, Luo H, Zhang D
Materials synthesis and structural characterizations: Liu Y, Zhou X, Jiang X
Data analysis and interpretation: Liu Y, Xie H, Xiao Z, Wang F
All authors contributed to the manuscript and were involved in discussion.

Availability of data and materials

Not applicable.

Financial support and sponsorship

The authors acknowledge the support of National Natural Science Foundation of China (52172265 and 52002404), Scientific research project of Hunan Provincial Department of Education (21B0009), Hunan Excellent Youth Science Foundation (2022JJ20067), The science and technology innovation Program of Hunan Province(2022RC1074), Central South University Innovation-Driven Research Program (2023CXQD010) and State Key Laboratory of Powder Metallurgy, Central South University, Changsha, China.

Conflicts of interest

All authors declared that there are no conflicts of interest.

Ethical approval and consent to participate

Not applicable.

Consent for publication

Not applicable.

REFERENCES

1. Ren X, Meng N, Ventura L, et al. Ultra-high energy density integrated polymer dielectric capacitors. *J Mater Chem A* 2022;10:10171-80. DOI
2. Feng QK, Zhong SL, Pei JY, et al. Recent progress and future prospects on all-organic polymer dielectrics for energy storage capacitors. *Chem Rev* 2022;122:3820-78. DOI PubMed
3. Liu S, Kang L, Hu J, et al. Realizing superior redox kinetics of hollow bimetallic sulfide nanoarchitectures by defect-induced manipulation toward flexible solid-state supercapacitors. *Small* 2022;18:e2104507. DOI PubMed
4. Kang L, Zhang M, Zhang J, et al. Dual-defect surface engineering of bimetallic sulfide nanotubes towards flexible asymmetric solid-state supercapacitors. *J Mater Chem A* 2020;8:24053-64. DOI
5. Yang L, Kong X, Li F, et al. Perovskite lead-free dielectrics for energy storage applications. *Prog Mater Sci* 2019;102:72-108. DOI
6. Luo H, Wang F, Guo R, et al. Progress on polymer dielectrics for electrostatic capacitors application. *Adv Sci* 2022;9:e2202438. DOI PubMed PMC
7. Thakur VK, Gupta RK. Recent progress on ferroelectric polymer-based nanocomposites for high energy density capacitors: synthesis, dielectric properties, and future aspects. *Chem Rev* 2016;116:4260-317. DOI PubMed
8. Li H, Ai D, Ren L, et al. Scalable polymer nanocomposites with record high-temperature capacitive performance enabled by rationally designed nanostructured inorganic fillers. *Adv Mater* 2019;31:e1900875. DOI PubMed
9. Zhou Y, Luo H, Chen S, Han X, Zhang D. Optimising the dielectric property of carbon nanotubes/P(VDF-CTFE) nanocomposites by tailoring the shell thickness of liquid crystalline polymer modified layer. *IET Nanodielectr* 2019;2:142-50. DOI
10. Cheng R, Wang Y, Men R, et al. High-energy-density polymer dielectrics via compositional and structural tailoring for electrical energy storage. *iScience* 2022;25:104837. DOI PubMed PMC
11. Dong J, Hu R, Niu Y, et al. Enhancing high-temperature capacitor performance of polymer nanocomposites by adjusting the energy level structure in the micro-/meso-scopic interface region. *Nano Energy* 2022;99:107314. DOI
12. Luo H, Zhou X, Ellingford C, et al. Interface design for high energy density polymer nanocomposites. *Chem Soc Rev* 2019;48:4424-65. DOI PubMed
13. Li L, Cheng J, Cheng Y, et al. Significant improvements in dielectric constant and energy density of ferroelectric polymer nanocomposites enabled by ultralow contents of nanofillers. *Adv Mater* 2021;33:e2102392. DOI PubMed
14. Cheng Y, Pan Z, Bai H, et al. Two-dimensional fillers induced superior electrostatic energy storage performance in trilayered architecture nanocomposites. *ACS Appl Mater Interfaces* 2022;14:8448-57. DOI PubMed
15. Liu Y, Luo H, Zhai D, et al. Symmetric trilayer dielectric composites with high energy density using a low loading of $KNbO_3$ nanosheets. *ACS Sustain Chem Eng* 2021;9:15983-94. DOI
16. Zhang H, Marwat MA, Xie B, et al. Polymer matrix nanocomposites with 1D ceramic nanofillers for energy storage capacitor applications. *ACS Appl Mater Interfaces* 2020;12:1-37. DOI PubMed
17. Pan Z, Yao L, Zhai J, Yang K, Shen B, Wang H. Ultrafast discharge and high-energy-density of polymer nanocomposites achieved via optimizing the structure design of barium titanates. *ACS Sustain Chem Eng* 2017;5:4707-17. DOI
18. Song Y, Shen Y, Liu H, Lin Y, Li M, Nan C. Improving the dielectric constants and breakdown strength of polymer composites: effects of the shape of the $BaTiO_3$ nanoinclusions, surface modification and polymermatrix. *J Mater Chem* 2012;22:16491. DOI
19. Zhou X, Xue G, Luo H, Bowen CR, Zhang D. Phase structure and properties of sodium bismuth titanate lead-free piezoelectric ceramics. *Prog Mater Sci* 2021;122:100836. DOI
20. Shen Y, Wu L, Zhao J, et al. Constructing novel binary $Bi_{0.5}Na_{0.5}TiO_3$-based composite ceramics for excellent energy storage performances via defect engineering. *Chem Eng J* 2022;439:135762. DOI
21. Ma Y, Xie H, Sun Y, et al. Topochemical synthesis and structural characteristics of orientation-controlled $(Bi_{0.5}Na_{0.5})_{0.94}Ba_{0.06}TiO_3$ perovskite microplatelets. *Microstructures* 2022;2:2022006. DOI
22. Li J, Li F, Xu Z, Zhang S. Multilayer lead-free ceramic capacitors with ultrahigh energy density and efficiency. *Adv Mater* 2018;30:e1802155. DOI PubMed
23. You D, Tan H, Yan Z, et al. Enhanced dielectric energy storage performance of $0.45Na_{0.5}Bi_{0.5}TiO_3$-$0.55Sr_{0.7}Bi_{0.2}TiO_3$/AlN 0-3 type lead-free composite ceramics. *ACS Appl Mater Interfaces* 2022;14:17652-61. DOI PubMed
24. Ang C, Yu Z. High remnant polarization in $Sr_{0.7}Bi_{0.2}TiO_3$-$Na_{0.5}Bi_{0.5}TiO_3$ solid solutions. *Appl Phys Lett* 2009;95:232908. DOI
25. Xue J, Wu T, Dai Y, Xia Y. Electrospinning and electrospun nanofibers: methods, materials, and applications. *Chem Rev* 2019;119:5298-415. DOI PubMed PMC
26. Chen J, Zhang X, Wang Z, Chen W, Yuan Q, Wang Y. Laminated ferroelectric polymer composites exhibit synchronous ultrahigh discharge efficiency and energy density via utilizing multiple-interface barriers. *J Mater Chem A* 2022;10:20402-13. DOI

27. Feng M, Feng Y, Zhang T, et al. Recent advances in multilayer-structure dielectrics for energy storage application. *Adv Sci* 2021;8:e2102221. DOI PubMed PMC
28. Wang Y, Yao M, Ma R, et al. Design strategy of barium titanate/polyvinylidene fluoride-based nanocomposite films for high energy storage. *J Mater Chem A* 2020;8:884-917. DOI
29. Guo R, Luo H, Yan M, Zhou X, Zhou K, Zhang D. Significantly enhanced breakdown strength and energy density in sandwich-structured nanocomposites with low-level $BaTiO_3$ nanowires. *Nano Energy* 2021;79:105412. DOI
30. Zhang Y, Jeong CK, Yang T, et al. Bioinspired elastic piezoelectric composites for high-performance mechanical energy harvesting. *J Mater Chem A* 2018;6:14546-52. DOI
31. Liu Y, Luo H, Gao Z, et al. Electrospinning synthesis of $Na_{0.5}Bi_{0.5}TiO_3$ nanofibers for dielectric capacitors in energy storage application. *Nanomaterials* 2022;12:906. DOI PubMed PMC
32. Li J, Shen Z, Chen X, et al. Grain-orientation-engineered multilayer ceramic capacitors for energy storage applications. *Nat Mater* 2020;19:999-1005. DOI PubMed
33. Liu Y, Luo H, Zhai D, et al. Improved energy density and energy efficiency of poly(vinylidene difluoride) nanocomposite dielectrics using $0.93Na_{0.5}Bi_{0.5}TiO_3$-$0.07BaTiO_3$ nanofibers. *ACS Appl Mater Interfaces* 2022;14:19376-87. DOI PubMed
34. Ma Y, Luo H, Zhou X, et al. Suppressed polarization by epitaxial growth of $SrTiO_3$ on $BaTiO_3$ nanoparticles for high discharged energy density and efficiency nanocomposites. *Nanoscale* 2020;12:8230-6. DOI PubMed
35. Zhou X, Sun Q, Zhai D, Xue G, Luo H, Zhang D. Excellent catalytic performance of molten-salt-synthesized Bi0.5Na0.5TiO3 nanorods by the piezo-phototronic coupling effect. *Nano Energy* 2021;84:105936. DOI
36. Wang Y, Cui J, Yuan Q, Niu Y, Bai Y, Wang H. Significantly enhanced breakdown strength and energy density in sandwich-structured barium titanate/poly(vinylidene fluoride) nanocomposites. *Adv Mater* 2015;27:6658-63. DOI PubMed
37. Pei JY, Yin LJ, Zhong SL, Dang ZM. Suppressing the loss of polymer-based dielectrics for high power energy storage. *Adv Mater* 2022:e2203623. DOI PubMed
38. Jiang J, Shen Z, Qian J, et al. Synergy of micro-/mesoscopic interfaces in multilayered polymer nanocomposites induces ultrahigh energy density for capacitive energy storage. *Nano Energy* 2019;62:220-9. DOI
39. Lin Y, Zhang Y, Zhan S, et al. Synergistically ultrahigh energy storage density and efficiency in designed sandwich-structured poly(vinylidene fluoride)-based flexible composite films induced by doping $Na_{0.5}Bi_{0.5}TiO_3$ whiskers. *J Mater Chem A* 2020;8:23427-35. DOI
40. Wang Z, Feng Z, Tang H, et al. Effects of Nanofibers orientation and aspect ratio on dielectric properties of nanocomposites: a phase-field simulation. *ACS Appl Mater Interfaces* 2022;14:42513-21. DOI PubMed
41. Yuan M, Li B, Zhang S, Rajagopalan R, Lanagan MT. High-field dielectric properties of oriented poly(vinylidene fluoride-co-hexafluoropropylene): structure-dielectric property relationship and implications for energy storage applications. *ACS Appl Polym Mater* 2020;2:1356-68. DOI

AUTHOR INSTRUCTIONS

1. Submission Overview

Before you decide to publish with *Microstructures*, please read the following items carefully and make sure that you are well aware of Editorial Policies and the following requirements.

1.1 Topic Suitability

The topic of the manuscript must fit the scope of the journal. Please refer to Aims and Scope for more information.

1.2 Open Access and Copyright

The journal adopts Gold Open Access publishing model and distributes content under the Creative Commons Attribution 4.0 International License. Copyright is retained by authors. Please make sure that you are well aware of these policies.

1.3 Publication Fees

Microstructures is an open access journal. When a paper is accepted for publication, authors are required to pay Article Processing Charges (APCs) to cover its editorial and production costs. The APC for each submission is $600. There are no additional charges based on color, length, figures, or other elements. For more details, please refer to OAE Publication Fees.

1.4 Language Editing

All submissions are required to be presented clearly and cohesively in good English. Authors whose first language is not English are advised to have their manuscripts checked or edited by a native English speaker before submission to ensure the high quality of expression. A well-organized manuscript in good English would make the peer review even the whole editorial handling more smoothly and efficiently.

If needed, authors are recommended to consider the language editing services provided by Charlesworth to ensure that the manuscript is written in correct scientific English before submission. Authors who publish with OAE journals enjoy a special discount for the services of Charlesworth via the following two ways.

Submit your manuscripts directly at http://www.charlesworthauthorservices.com/~OAE;

Open the link http://www.charlesworthauthorservices.com/, and enter Promotion Code “OAE” when you submit.

1.5 Work Funded by the National Institutes of Health

If an accepted manuscript was funded by National Institutes of Health (NIH), the author may inform editors of the NIH funding number. The editors are able to deposit the paper to the NIH Manuscript Submission System on behalf of the author.

2. Submission Preparation

2.1 Cover Letter

A cover letter is required to be submitted accompanying each manuscript. It should be concise and explain why the study is significant, why it fits the scope of the journal, and why it would be attractive to readers, etc.

Here is a guideline of a cover letter for authors’ consideration:

In the first paragraph: include the title and type (e.g., Research Article, Review Article, etc.) of the manuscript, a brief on the background of the study, the question the author sought out to answer and why;

In the second paragraph: concisely explain what was done, the main findings and why they are significant;

In the third paragraph: indicate why the manuscript fits the Aims and Scope of the journal, and why it would be attractive to readers;

In the fourth paragraph: confirm that the manuscript has not been published elsewhere and not under consideration of any other journal. All authors have approved the manuscript and agreed on its submission to the journal. Journal’s specific requirements have been met if any.

If the manuscript is contributed to a special issue, please also mention it in the cover letter.

If the manuscript was presented partly or entirely in a conference, the author should clearly state the background information of the event, including the conference name, time and place in the cover letter.

2.2 Types of Manuscripts

There is no restriction on the length of manuscripts, number of figures, tables and references, provided that the manuscript is concise and comprehensive. The journal publishes Research Article, Review Article, Editorial, Perspective etc. For more details about paper type, please refer to the following table.

Manuscript Type	Definition	Abstract	Keywords	Main Text Structure
Research Article	A Research Article describes detailed results from novel research. All findings are extensively discussed.	Structured abstract including Aim, Methods, Results and Conclusion. No more than 250 words.	3-8 keywords	The main content should include four sections: Introduction, Materials and Methods, Results and Discussion.
Review Article	A Review Article summarizes the literature on previous studies. It usually does not present any new information on a subject.	Unstructured abstract. No more than 250 words.	3-8 keywords	The main text may consist of several sections with unfixed section titles. We suggest that the author include an "Introduction" section at the beginning, several sections with unfixed titles in the middle part, and a "Conclusion" section in the end.
Meta-Analysis	A Meta-Analysis is a statistical analysis combining the results of multiple scientific studies. It is often an overview of clinical trials.	Structured abstract including Aim, Methods, Results and Conclusion. No more than 250 words.	3-8 keywords	The main content should include four sections: Introduction, Methods, Results and Discussion.
Technical Note	A Technical Note is a short article giving a brief description of a specific development, technique or procedure, or it may describe a modification of an existing technique, procedure or device applied in research.	Unstructured abstract. No more than 250 words.	3-8 keywords	/
Commentary	A Commentary is to provide comments on a newly published article or an alternative viewpoint on a certain topic.	Unstructured abstract. No more than 250 words.	3-8 keywords	/
Editorial	An Editorial is a short article describing news about the journal or opinions of senior editors or the publisher.	None required.	None required.	/
Letter to Editor	A Letter to Editor is usually an open post-publication review of a paper from its readers, often critical of some aspect of a published paper. Controversial papers often attract numerous Letters to Editor.	Unstructured abstract (optional). No more than 250 words.	3-8 keywords (optional)	/
Opinion	An Opinion usually presents personal thoughts, beliefs, or feelings on a topic.	Unstructured abstract (optional). No more than 250 words.	3-8 keywords	/
Perspective	A Perspective provides personal points of view on the state-of-the-art of a specific area of knowledge and its future prospects. Links to areas of intense current research focus can also be made. The emphasis should be on a personal assessment rather than a comprehensive, critical review. However, comments should be put into the context of existing literature. Perspectives are usually invited by the Editors.	Unstructured abstract. No more than 150 words.	3-8 keywords	/

2.3 Manuscript Structure

2.3.1 Front Matter

2.3.1.1 Title

The title of the manuscript should be concise, specific and relevant, with no more than 16 words if possible. When gene or protein names are included, the abbreviated name rather than full name should be used.

2.3.1.2 Authors and Affiliations

Authors' full names should be listed. The initials of middle names can be provided. Institutional addresses and email addresses for all authors should be listed. At least one author should be designated as corresponding author. In addition, corresponding authors are suggested to provide their Open Researcher and Contributor ID upon submission. Please note that any change to authorship is not allowed after manuscript acceptance.

2.3.1.3 Highlights

Highlights are mandatory because they can help increase the discoverability of your article through search engines. They consist of a short collection of bullet points that capture the novel results of your research as well as new methods that were used during the study (if any). They should be submitted in a separate editable file in the online submission system. Please use 'Highlights' in the file name and include 3 to 5 bullet points (maximum 85 characters per bullet point, including spaces).

2.3.1.4 Abstract

The abstract should be a single paragraph with word limitation and specific structure requirements (for more details please refer to Types of Manuscripts). It usually describes the main objective(s) of the study, explains how the study was done, including any model organisms used, without methodological detail, and summarizes the most important results and their significance. The abstract must be an objective representation of the study: it is not allowed to contain results which are not presented and substantiated in the manuscript, or exaggerate the main conclusions. Citations should not be included in the abstract.

2.3.1.5 Graphical Abstract

The graphical abstract is essential as this can catch first view of your publication by readers. We recommend you to submit an eye-catching figure. It should summarize the content of the article in a concise graphical form. It is recommended to use it because this can make online articles get more attention. The graphic abstract should be submitted as a separate document in the online submission system. Please provide an image with a minimum of 730 × 1,228 pixels (h × w) or proportionally more. The image should be readable at a size of 7 × 12 cm using a regular screen resolution of 96 dpi. Preferred file types: TIFF, PSD, AI, JPG, JPEG, EPS, PNG, ZIP and PDF files.

2.3.1.6 Keywords

Three to eight keywords should be provided, which are specific to the article, yet reasonably common within the subject discipline.

2.3.2 Main Text

Manuscripts of different types are structured with different sections of content. Please refer to Types of Manuscripts to make sure which sections should be included in the manuscripts.

2.3.2.1 Introduction

The introduction should contain background that puts the manuscript into context, allow readers to understand why the study is important, include a brief review of key literature, and conclude with a brief statement of the overall aim of the work and a comment about whether that aim was achieved. Relevant controversies or disagreements in the field should be introduced as well.

2.3.2.2 Materials and Methods

Materials and Methods should contain sufficient details to allow others to fully replicate the study. New methods and protocols should be described in detail while well-established methods can be briefly described or appropriately cited. Experimental participants selected, the drugs and chemicals used, the statistical methods taken, and the computer software used should be identified precisely. Statistical terms, abbreviations, and all symbols used should be defined clearly. Protocol documents for clinical trials, observational studies, and other non-laboratory investigations may be uploaded as supplementary materials.

2.3.2.3 Results and Discussion

This section should contain the findings of the study and discuss the implications of the findings in context of existing research and highlight limitations of the study. Future research directions may also be mentioned. Results of statistical analysis should also be included either as text or as tables or figures if appropriate. Authors should emphasize and summarize

only the most important observations. Data on all primary and secondary outcomes identified in the section Methods should also be provided. Extra or supplementary materials and technical details can be placed in supplementary documents.

2.3.2.4 Conclusions

It should state clearly the main conclusions and include the explanation of their relevance or importance to the field.

2.3.3 Back Matter

2.3.3.1 Acknowledgments

Anyone who contributed towards the article but does not meet the criteria for authorship, including those who provided professional writing services or materials, should be acknowledged. Authors should obtain permission to acknowledge from all those mentioned in the Acknowledgments section. This section is not added if the author does not have anyone to acknowledge.

2.3.3.2 Authors' Contributions

Each author is expected to have made substantial contributions to the conception or design of the work, or the acquisition, analysis, or interpretation of data, or the creation of new software used in the work, or have drafted the work or substantively revised it.

Please use Surname and Initial of Forename to refer to an author's contribution. For example: made substantial contributions to conception and design of the study and performed data analysis and interpretation: Salas H, Castaneda WV; performed data acquisition, as well as provided administrative, technical, and material support: Castillo N, Young V.

If an article is single-authored, please include "The author contributed solely to the article." in this section.

2.3.3.3 Availability of Data and Materials

In order to maintain the integrity, transparency and reproducibility of research records, authors should include this section in their manuscripts, detailing where the data supporting their findings can be found. Data can be deposited into data repositories or published as supplementary information in the journal. Authors who cannot share their data should state that the data will not be shared and explain it. If a manuscript does not involve such issue, please state "Not applicable." in this section.

2.3.3.4 Financial Support and Sponsorship

All sources of funding for the study reported should be declared. The role of the funding body in the experiment design, collection, analysis and interpretation of data, and writing of the manuscript should be declared. Any relevant grant numbers and the link of funder's website should be provided if any. If the study is not involved with this issue, state "None." in this section.

2.3.3.5 Conflicts of Interest

Authors must declare any potential conflicts of interest that may be perceived as inappropriately influencing the representation or interpretation of reported research results. If there are no conflicts of interest, please state "All authors declared that there are no conflicts of interest." in this section. Some authors may be bound by confidentiality agreements. In such cases, in place of itemized disclosures, we will require authors to state "All authors declare that they are bound by confidentiality agreements that prevent them from disclosing their conflicts of interest in this work.". If authors are unsure whether conflicts of interest exist, please refer to the "Conflicts of Interest" of *Microstructures* Editorial Policies for a full explanation.

2.3.3.6 Copyright

Authors retain copyright of their works through a Creative Commons Attribution 4.0 International License that clearly states how readers can copy, distribute, and use their attributed research, free of charge. A declaration "© The Author(s) 2023." will be added to each article. Authors are required to sign License to Publish before formal publication.

2.3.3.7 References

References should be numbered in order of appearance at the end of manuscripts. In the text, reference numbers should be placed in square brackets and the corresponding references are cited thereafter. If the number of authors is less than or equal to six, we require to list all authors' names. If the number of authors is more than six, only the first three authors' names are required to be listed in the references, other authors' names should be omitted and replaced with "et al.". Abbreviations of the journals should be provided on the basis of Index Medicus. Information from manuscripts accepted but not published should be cited in the text as "Unpublished material" with written permission from the source.

References should be described as follows, depending on the types of works:

Types	Examples
Journal articles by individual authors	Weaver DL, Ashikaga T, Krag DN, et al. Effect of occult metastases on survival in node-negative breast cancer. *N Engl J Med* 2011;364:412-21. [DOI: 10.1056/NEJMoa1008108]

Organization as author	Diabetes Prevention Program Research Group. Hypertension, insulin, and proinsulin in participants with impaired glucose tolerance. *Hypertension* 2002;40:679-86. [DOI: 10.1161/01.hyp.0000035706.28494.09]
Both personal authors and organization as author	Vallancien G, Emberton M, Harving N, van Moorselaar RJ; Alf-One Study Group. Sexual dysfunction in 1,274 European men suffering from lower urinary tract symptoms. *J Urol* 2003;169:2257-61. [DOI: 10.1097/01.ju.0000067940.76090.73]
Journal articles not in English	Zhang X, Xiong H, Ji TY, Zhang YH, Wang Y. Case report of anti-N-methyl-D-aspartate receptor encephalitis in child. *J Appl Clin Pediatr* 2012;27:1903-7. (in Chinese)
Journal articles ahead of print	Odibo AO. Falling stillbirth and neonatal mortality rates in twin gestation: not a reason for complacency. *BJOG* 2018; Epub ahead of print [DOI: 10.1111/1471-0528.15541]
Books	Sherlock S, Dooley J. Diseases of the liver and billiary system. 9th ed. Oxford: Blackwell Sci Pub; 1993. pp. 258-96.
Book chapters	Meltzer PS, Kallioniemi A, Trent JM. Chromosome alterations in human solid tumors. In: Vogelstein B, Kinzler KW, editors. The genetic basis of human cancer. New York: McGraw-Hill; 2002. pp. 93-113.
Online resource	FDA News Release. FDA approval brings first gene therapy to the United States. Available from: https://www.fda.gov/NewsEvents/Newsroom/PressAnnouncements/ucm574058.htm. [Last accessed on 30 Oct 2017]
Conference proceedings	Harnden P, Joffe JK, Jones WG, editors. Germ cell tumours V. Proceedings of the 5th Germ Cell Tumour Conference; 2001 Sep 13-15; Leeds, UK. New York: Springer; 2002..
Conference paper	Christensen S, Oppacher F. An analysis of Koza's computational effort statistic for genetic programming. In: Foster JA, Lutton E, Miller J, Ryan C, Tettamanzi AG, Editors. Genetic programming. EuroGP 2002: Proceedings of the 5th European Conference on Genetic Programming; 2002 Apr 3-5; Kinsdale, Ireland. Berlin: Springer; 2002. pp. 182-91.
Unpublished material	Tian D, Araki H, Stahl E, Bergelson J, Kreitman M. Signature of balancing selection in Arabidopsis. *Proc Natl Acad Sci U S A*. Forthcoming 2002.

For other types of references, please refer to U.S. National Library of Medicine.

The journal also recommends that authors prepare references with a bibliography software package, such as EndNote to avoid typing mistakes and duplicated references.

2.3.3.8 Supplementary Materials

Additional data and information can be uploaded as Supplementary Materials to accompany the manuscripts. The supplementary materials will also be available to the referees as part of the peer-review process. Any file format is acceptable, such as data sheet (word, excel, csv, cdx, fasta, pdf or zip files), presentation (powerpoint, pdf or zip files), image (cdx, eps, jpeg, pdf, png or tiff), table (word, excel, csv or pdf), audio (mp3, wav or wma) or video (avi, divx, flv, mov, mp4, mpeg, mpg or wmv). All information should be clearly presented. Supplementary materials should be cited in the main text in numeric order (e.g., Supplementary Figure 1, Supplementary Figure 2, Supplementary Table 1, Supplementary Table 2, etc.). The style of supplementary figures or tables complies with the same requirements on figures or tables in main text. Videos and audios should be prepared in English, and limited to a size of 500 MB.

2.4 Manuscript Format

2.4.1 File Format

Manuscript files can be in DOC and DOCX formats and should not be locked or protected.

2.4.2 Length

There are no restrictions on paper length, number of figures, or number of supporting documents. Authors are encouraged to present and discuss their findings concisely.

2.4.3 Language

Manuscripts must be written in English.

2.4.4 Multimedia Files

The journal supports manuscripts with multimedia files. The requirements are listed as follows:

Video or audio files are only acceptable in English. The presentation and introduction should be easy to understand. The frames should be clear, and the speech speed should be moderate.

A brief overview of the video or audio files should be given in the manuscript text.

The video or audio files should be limited to a size of up to 500 MB.

Please use professional software to produce high-quality video files, to facilitate acceptance and publication along with the submitted article. Upload the videos in mp4, wmv, or rm format (preferably mp4) and audio files in mp3 or wav format.

2.4.5 Figures

Figures should be cited in numeric order (e.g., Figure 1, Figure 2) and placed after the paragraph where it is first cited;
Figures can be submitted in format of TIFF, PSD, AI, EPS or JPEG, with resolution of 300-600 dpi;
Figure caption is placed under the Figure;
Diagrams with describing words (including, flow chart, coordinate diagram, bar chart, line chart, and scatter diagram, etc.) should be editable in word, excel or powerpoint format. Non-English information should be avoided;
Labels, numbers, letters, arrows, and symbols in figure should be clear, of uniform size, and contrast with the background;
Symbols, arrows, numbers, or letters used to identify parts of the illustrations must be identified and explained in the legend;
Internal scale (magnification) should be explained and the staining method in photomicrographs should be identified;
All non-standard abbreviations should be explained in the legend;
Permission for use of copyrighted materials from other sources, including re-published, adapted, modified, or partial figures and images from the internet, must be obtained. It is authors' responsibility to acquire the licenses, to follow any citation instruction requested by third-party rights holders, and cover any supplementary charges.

2.4.6 Tables

Tables should be cited in numeric order and placed after the paragraph where it is first cited;
The table caption should be placed above the table and labeled sequentially (e.g., Table 1, Table 2);
Tables should be provided in editable form like DOC or DOCX format (picture is not allowed);
Abbreviations and symbols used in table should be explained in footnote;
Explanatory matter should also be placed in footnotes;
Permission for use of copyrighted materials from other sources, including re-published, adapted, modified, or partial tables from the internet, must be obtained. It is authors' responsibility to acquire the licenses, to follow any citation instruction requested by third-party rights holders, and cover any supplementary charges.

2.4.7 Abbreviations

Abbreviations should be defined upon first appearance in the abstract, main text, and in figure or table captions and used consistently thereafter. Non-standard abbreviations are not allowed unless they appear at least three times in the text. Commonly-used abbreviations, such as DNA, RNA, ATP, etc., can be used directly without definition. Abbreviations in titles and keywords should be avoided, except for the ones which are widely used.

2.4.8 Italics

General italic words like vs., et al., etc., in vivo, in vitro; t test, F test, U test; related coefficient as r, sample number as n, and probability as P; names of genes; names of bacteria and biology species in Latin.

2.4.9 Units

SI Units should be used. Imperial, US customary and other units should be converted to SI units whenever possible. There is a space between the number and the unit (i.e., 23 mL). Hour, minute, second should be written as h, min, s.

2.4.10 Numbers

Numbers appearing at the beginning of sentences should be expressed in English. When there are two or more numbers in a paragraph, they should be expressed as Arabic numerals; when there is only one number in a paragraph, number < 10 should be expressed in English and number > 10 should be expressed as Arabic numerals. 12345678 should be written as 12,345,678.

2.4.11 Equations

Equations should be editable and not appear in a picture format. Authors are advised to use either the Microsoft Equation Editor or the MathType for display and inline equations.

2.5 Submission Link

Submit an article via https://oaemesas.com/login?JournalId=microstructures.

Microstructures

Los Angeles Office
245 E Main Street ste122, Alhambra,
CA 91801, USA
Tel: +1 323 9987086
E-mail: editorialoffice@microstructj.com
Website: https://www.oaepublish.com/microstructures